Aeroelastic Studies on a High Aspect Ratio Wing

by

Linda M. Mendenhall

B. S., Aeronautics and Astronautics

B. S., Astronomy and Astrophysics,

The Pennsylvania State University, University Park, Pennsylvania (1997)

Submitted to the Department of Aeronautics and Astronautics

in partial fulfillment of the requirements for the degree of

MASTER OF SCIENCE IN AERONAUTICS AND ASTRONAUTICS

at the

MASSACHUSETTS INSTITUTE OF TECHNOLOGY

February 2003

Author_____

Department of Aeronautics and Astronautics

January 31, 2003

Certified by_____

Carlos E. S. Cesnik

Visiting Associate Professor of Aeronautics and Astronautics

Thesis Supervisor

Accepted by_____

Edward M. Greitzer

H.N. Slater Professor of Aeronautics and Astronautics

Chair, Committee on Graduate Students

Aeroelastic Studies on a High Aspect Ratio Wing

by

Linda M. Mendenhall

Submitted to the Department of Aeronautics and Astronautics
on January 31, 2003, in partial fulfillment of the
requirements for the degree of
Master of Science in Aeronautics and Astronautics

Abstract

A high aspect ratio (10.56) composite wing was designed and fabricated in order to verify a new analysis code developed to predict dynamic behavior of high-aspect-ratio wings. The chosen wing design was manufactured and tested (both bench-top and wind tunnel testing), and its dynamic behavior was characterized. Strain gauges and accelerometers were embedded within the wing at various distances along the span to record wing natural frequency information during bench-top 'tap' testing, and frequency changes as a function of wind speed and root angle of attack during wind tunnel testing. Bench-top natural frequencies and mode shapes for the 1^{st} and 2^{nd} Bending, 1^{st} Chordwise Bending, and 1^{st} Torsion modes are in good agreement with the analytical model. Mode shapes with frequencies exceeding 100 Hz were not considered. Within the tunnel, the wing was studies at 1°, 2°, and 5° root angles of attack. The 2° root angle of attack configuration was flown to the flutter point by observing of the wing behavior. This was within 99% of the predicted flutter speed.

Thesis Supervisor: Carlos E. S. Cesnik
Title: Visiting Associate Professor of Aeronautics and Astronautics

Acknowledgments

The completion of this research required the assistance of many people and institutions. I would first like to thank MIT Lincoln Laboratory for allowing me to go back to school to further my education. In particular, the Lincoln Scholars Commitee for the financial support and time away from work necessary to complete such an endevor. Also my Group leaders, Bob Davis and Steve Forman, who were extremely understanding about my absence. A special thank-you to my Lincoln Tor-mentor (I mean Mentor), John Sultana, who always provided something to laugh about! Also, thanks to all the people in my group and through out the laboratory who have helped, especially Dennis Burianek, Vinny Cerrati, Charlie Nickerson, and Anne Vogel.

A giant thank you goes to my family for putting up with the neglect and all of my moodiness. Especially my husband, Dr Jeffrey Mendenhall, who took over all the household and farm duties and still found time to pick me up at the train station. Special thanks to Rajah, Angie, Jack, Ian, Betty, and Sierra, for providing the devotion and unconditional love that every graduate student needs. To my parents, Charles and Marion Baker, for instilling in me the importance of education. Thanks to all my friends who allowed me to drop out of existance for awhile!

I would also like to thank many people on MIT campus, who provided necessary assitance along the way. John Kane, Dave Roberts, and Donald Weiner for providing invaluable assistance during the manufacturing process. Also Dick Perdichizzi for his assistance in the tunnel. A special thanks to Professor John Dugundji for taking such an interest in my work and helping me through all of the difficult times. Thanks also to my advisor, Carlos Cesnik, for providing me with such an interesting topic.

Partial funding for this work was provided by NASA Langley Research Center, under grant NAG-1-01102, and monitored by Dr. W. Keats Wilkie. Such support does not constitute an endorsement by NASA of the views expressed herein.

This work was also performed for the Air Force under Air Force Contract F19628-00-C-002. The opinions, interpretations, conclusions, and recommendations are solely those of the author and are not necessarily endorsed by the United States Government.

" I know where the pieces fit "

-*Schism,* Tool 2001

Contents

List of Figures

List of Tables

Chapter 1

Introduction

1.1 Motivation

Many industries consider using High Altitude Long Endurance (HALE) aircraft to perform autonomous sensing (environmental, urban, and reconnaissance), or to assist in civilian or military communication as a relay [1]. The wings of these vehicles are typically of high aspect ratio. Long slender wings result in large deflections during flight, especially when flown at high angles of attack. These large deflections cannot be ignored when analyzing the wing's flight characteristics. The change in the wing's stiffness, due to nonlinear geometric behavior, requires new methods of modeling [2]. This change in stiffness results in changes to the wing's dynamic behavior. There has been considerable research in this area by numerous groups, resulting in new modeling techniques and codes which need to be validated through experimentation. One such computational modeling tool is being developed by Cesnik and Brown [3]. This research is a follow-on of work performed by Cesnik and Ortega-Morales [4]. The ground work for this was set forth by Patil, Hodges, and Cesnik [1], [5], and [6].

1.2 Objective

The primary objective of this research is to design and test an experimental wind tunnel model wing. This test wing should present nonlinear aeroelastic behavior. The collected

data will then support the validation of the MATLAB computer code being developed by Cesnik and Brown [3]. Originally this would encompass all portions of the code, including the ability to model active materials embedded within the layers of the composite wing. However, due to reasons beyond the control of the author, no active structural tests are included in this study.

1.3 Background

As mentioned above, there has been substantial effort towards developing analytical models which accurately depict the behavior of high aspect ratio wings undergoing large deflections. This work is summarized in the next two sections.

1.3.1 Previous Work

In the late 1980s, Minguet and Dugundji studied the effects of deflection on dynamic behavior of thin composite strips [7]. In their study, it was shown that deflection has significant effect on the torsion and chordwise bending frequencies. Their beam analysis obtained a set of linearized equations about a deflected position. The experiments for this research utilized flat composite beams of various composite orientations and thicknesses. This study showed that deflections of as little as 3% of the total length affected the torsional and chordwise bending modes, while the normal bending modes remained relatively uneffected. They also showed that tip bending deflections between 5% and 10% of the total beam length resulted in a mix between the 1^{st} torsion and 1^{st} chordwise bending modes.

Patil, Hodges and Cesnik [8] have worked to improve modeling capabilities for high aspect ratio wings, which include geometrical non-linearities for structural and aerodynamic analyses. Their research has shown that accurate modeling of geometric non-linearities is necessary to fully understand the torsion/bending coupling observed during flutter of wings with large deflections [8]. Their modeling of nonlinear aeroelasticity is based on a mixed variational formulation for the dynamics of beams in moving reference frames and finite-state airloads to accommodate deformable airfoil effects [1].

Tang and Dowell have studied various ways of modeling high aspect ratio wing aeroelastic behavior and correlated their work with wind tunnel tests. In the late 1990's, they built a 45-cm wing with an aspect ratio of 8.89 [9]. The wing was flown into the flutter domain to study limit cycle oscillation behavior. They also used this wing to study the modeling of gust response [10].

Ortega-Morales and Cesnik created a framework for implementing active aeroelastic tailoring of high aspect ratio wings, as well as gust mitigation [4]. The active tailoring was implemented through embedded piezoelectric actuators within the composite skin of the wing. This work implemented many of the analysis techniques studied in [1], [8], [2], [5], and [6], and consisted of an asymptotically correct active cross-section formulation, geometrically-exact mixed formulation for dynamics of moving beams, and finite-state unsteady aerodynamics.

1.3.2 Present Work

Cesnik and Brown are continuing the work done in [4]. This work formulated the MATLAB code used within this thesis, which employs a strain-based finite element representation of a nonlinear, large deflection beam model experiencing finite-state unsteady airloads [11]. This program has the capability to model active materials embedded within the composite lay-up of the wing and to take into account effects from the fuselage and tail [3]. The basic formulation behind this modeling effort is summarized in Appendix A.

Two different wing designs were generated using the code from [11] and are presented in Chapter 2 of this thesis. These designs were chosen for their torsional flexibility and interesting flutter characteristics. Chapter 3 discusses the manufacture and instrumentation of the wing. The benchtop and wind tunnel experiments, as well as the experimental results are discussed in Chapter 4. Along with these results is a modified numerical model which replicates the results of the tests. Finally, conclusions and suggestions for further work are presented in Chapter 5. This thesis contains three Appendices. Appendix A provides a summary of the mathematical formulation for the code, Appendix B contains relevant material properties, and Appendix C provides the preliminary studies for a future active wing build-up.

Chapter 2

Design and Analysis of High Aspect Ratio Wing

This chapter describes the design and analysis of the static flexible wing that was built to validate the model of [3] for subsonic speeds. Some of the design parameters were set by the wind tunnel limitations and others by ease of fabrication.

2.1 Design Criteria

Since this study targets large deflection aeroelastic response, a high aspect ratio flexible wing was needed. To reduce the risk of damage to the wind tunnel during the dynamic portion of testing, the design flutter speed for this wing should be in the range of 40 m/s. This relatively low flutter speed reduces the amount of momentum the wing would have in case it becomes unstable and brakes away from the mounting fixture. As a result, a very flexible wing design, soft in torsion, is expected. Although the wing needed to be as long as possible to increase the aspect ratio, the span of the wing was also limited by the wind tunnel test section dimension. The minimum chord of the wing also has limitations. It could not be too small, as that would significantly increase the complexity of manufacturing. With these constraints in mind, the length of the wing was set to 1.13 meters (44.5 inches) and the chord length was set to 0.107 meters (4.22 inches). This yielded an aspect ratio of 10.56.

The airfoil shape chosen is the NACA 0012. Safety to the wing tunnel was a major concern, so the wing needed to possess margins of safety for strain within the E-glass/epoxy of at least 1. For added safety this requirement needed to be met when the wing was analyzed at 10% above the predicted flutter speed. Also, the wing needed to exhibit limit cycle oscillation at speeds up to 10% above the predicted flutter values.

After several preliminary layup considerations, two basics ones were selected for detailed studies: a so-called "two-layer" design and a "three-layer" design. They represent flexible designs, with flutter speeds within the appropriate range. They also demonstrate interesting flutter characteristics.

2.2 Two-Layer Design

2.2.1 Basic Characteristics

The two-layer design is composed of two-layers of E-glass/epoxy fabric oriented at 0° around an inner foam core. A table of the material properties is provided in Appendix B. There is no spar in this design. This design provides a very flexible wing while still maintaining closed cell properties. A cross-sectional representation is given in Figure 2-1.

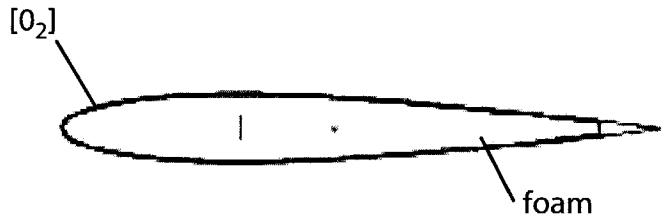

Figure 2-1: Cross section of two-layer wing (NACA 0012)

The cross-sectional properties for the two-layer design are provided below. The stiffness matrix terms for this cross-section are given in Table 2.1. Detailed definition of the elements of this matrix are provided in Appendix A. The inertia matrix for this cross-section is provided in Table 2.2. The center of gravity for the cross-section is located 0.0182 m aft of the reference line (located at 30% chord). This places the center of gravity at 47% of the chord.

Table 2.1: Non-zero stiffness matrix terms for two-layer design: 1 = Extension, 2 = Torsion, 3 = Flatwise Bending, 4 = Chordwise Bending

K_{11}	$9.55 * 10^5$ N
K_{14}= K_{41}	$-1.68 * 10^4$ N*m
K_{22}	14.24 N*m^2
K_{33}	22.25 N*m^2
K_{44}	$1.18 * 10^3$ N*m^2

Table 2.2: Non-zero inertial matrix terms for two-layer design

I_{11}	$0.10 * 10^{-3}$ m^4
I_{22}	$0.22 * 10^{-5}$ m^4
I_{33}	$0.98 * 10^{-4}$ m^4

The dynamic properties of the wing are important to its aeroelastic response. The first six natural frequencies of the wing are summarized in Table 2.3. The corresponding mode shapes are provided in Figure 2-2.

Table 2.3: Natural frequencies of the two-layer design in vacuum

Mode	Frequency	Mode Shape
1	8 Hz	1^{st} Bending
2	50 Hz	1^{st} Chordwise Bending
3	52 Hz	2^{nd} Bending
4	95 Hz	1^{st} Torsion
5	153 Hz	3^{rd} Bending
6	292 Hz	2^{nd} Torsion

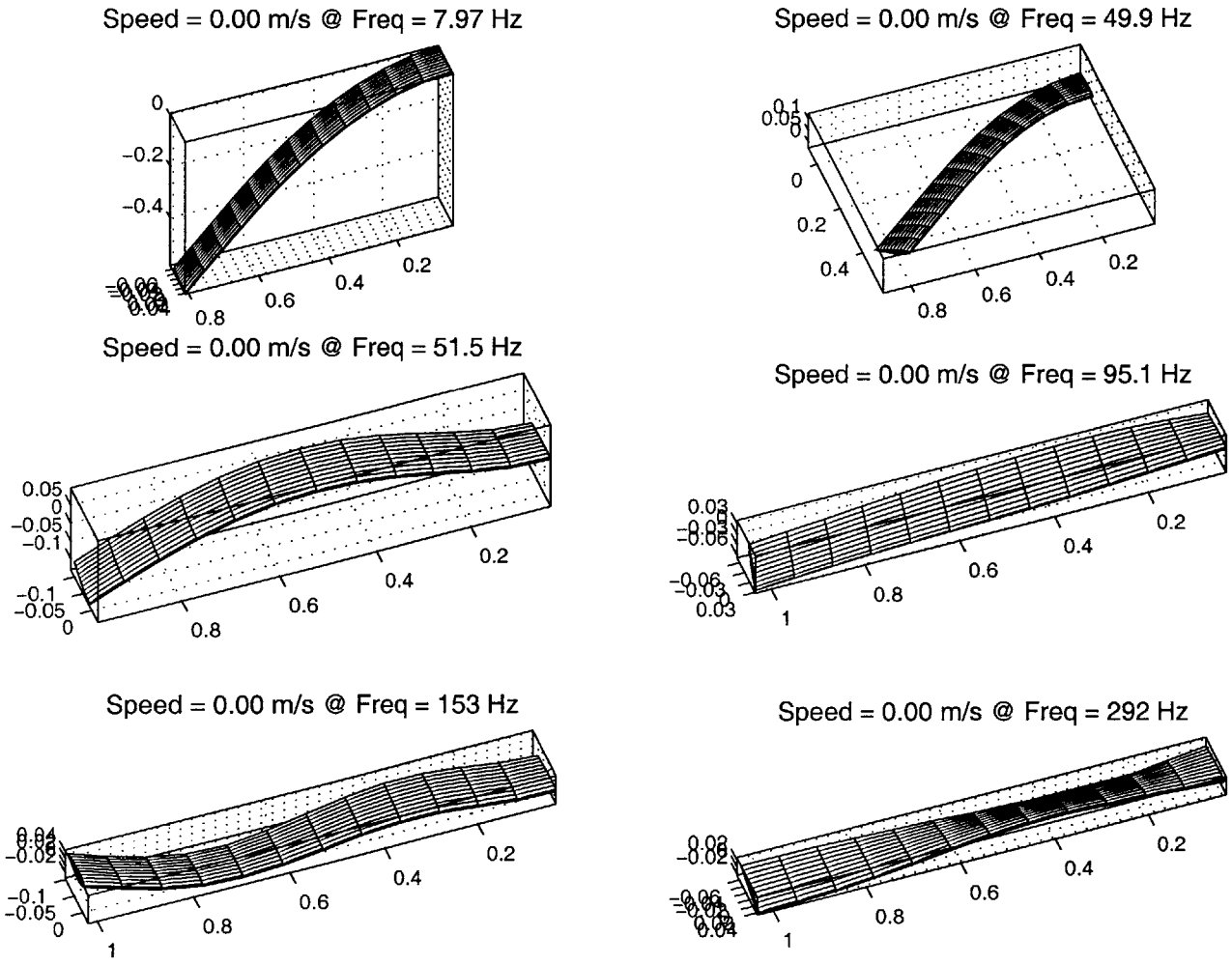

Figure 2-2: First six normal modes for two-layer wing (in vacuum)

2.2.2 Wing Non-linear Characteristics

Different root angles of attack of the wing result in different wing tip deflections once the wing is exposed to airloads. The change in tip deflection is graphed in Figure 2-3 for the range of angles of attack of interest: 0° to 5°. The tip deflection increases with increased angle of attack. This is to be expected, since the aerodynamic load is directly proportional to the angle of attack.

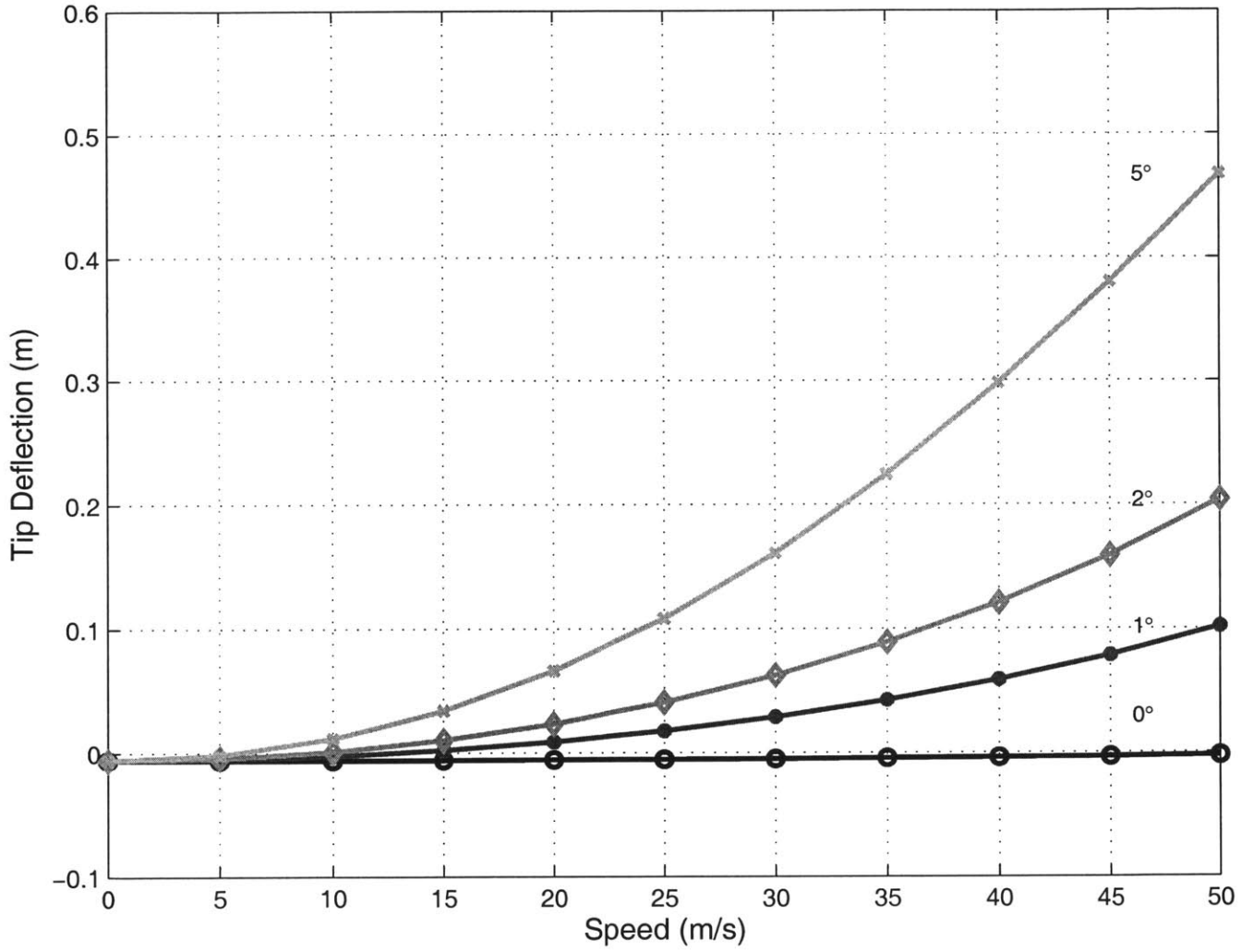

Figure 2-3: Static tip deflection for increasing speed at different root angles of attack

The wing tip twist also changes with increased root angle of attack. This data is provided in Figure 2-4. To better illustrate this effect, the initial root angle of attack has been subtracted from the total tip twist, yielding only the elastic angle change due to gravitational

and aero-loading.

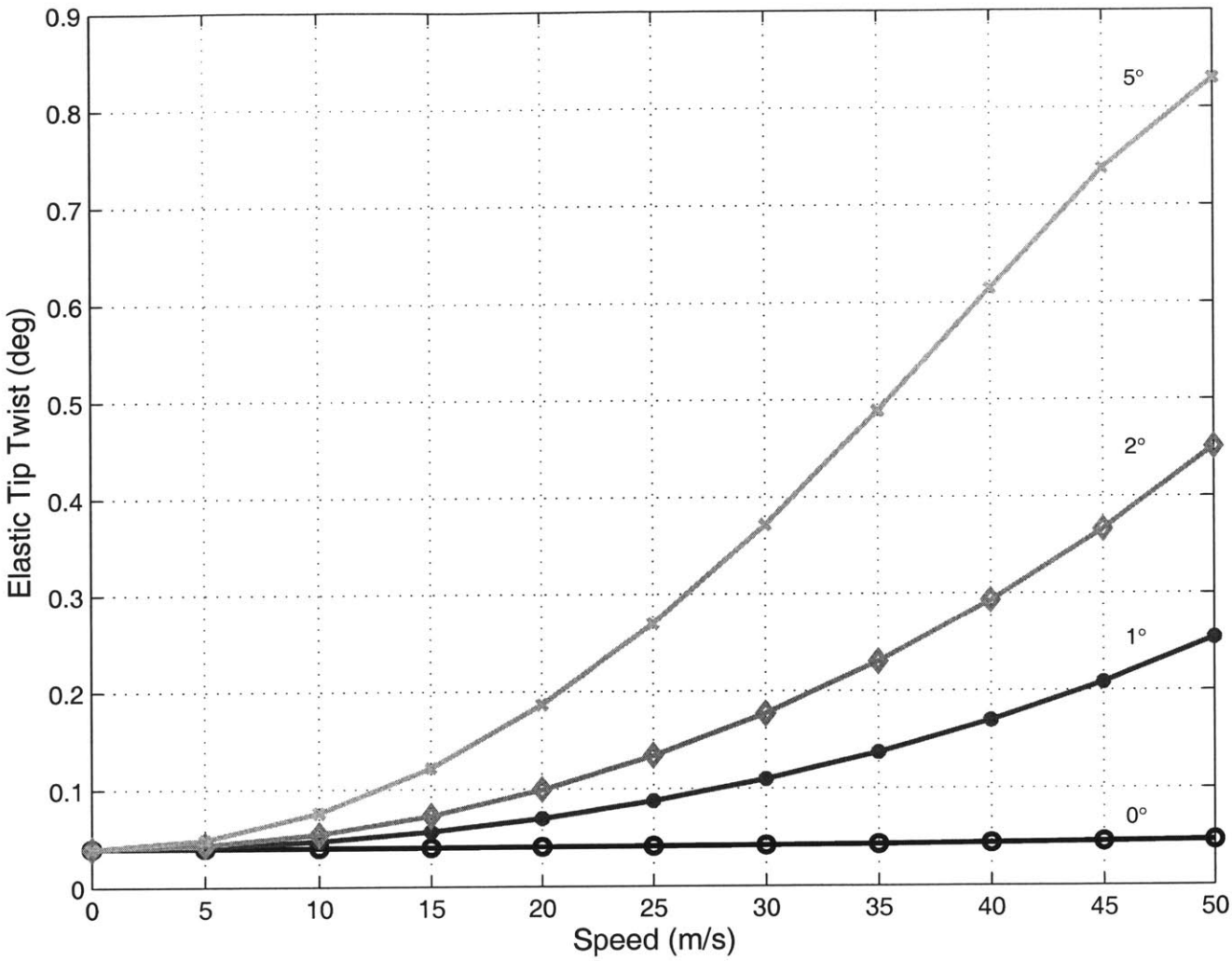

Figure 2-4: Elastic tip twist for increasing speed at different root angles of attack

The changes in tip deflection and twist result in a change in the dynamic behavior of the wing, and ultimately a change in the wing stability. This is illustrated by the change in the mode shapes and their corresponding frequencies for the wing at different root angles of attack at 30 m/s. Table 2.4 gives the frequencies of the first six modes for 0°, 1°, 2° and 5°. Figure 2-5 contains the first four modes graphically.

It is interesting to note that as the wing is bent upwards due to the force of air pressure, the natural frequencies of the second mode decrease and the fourth mode increase. This effect will cause some different behaviors in the wing as the different modes interact.

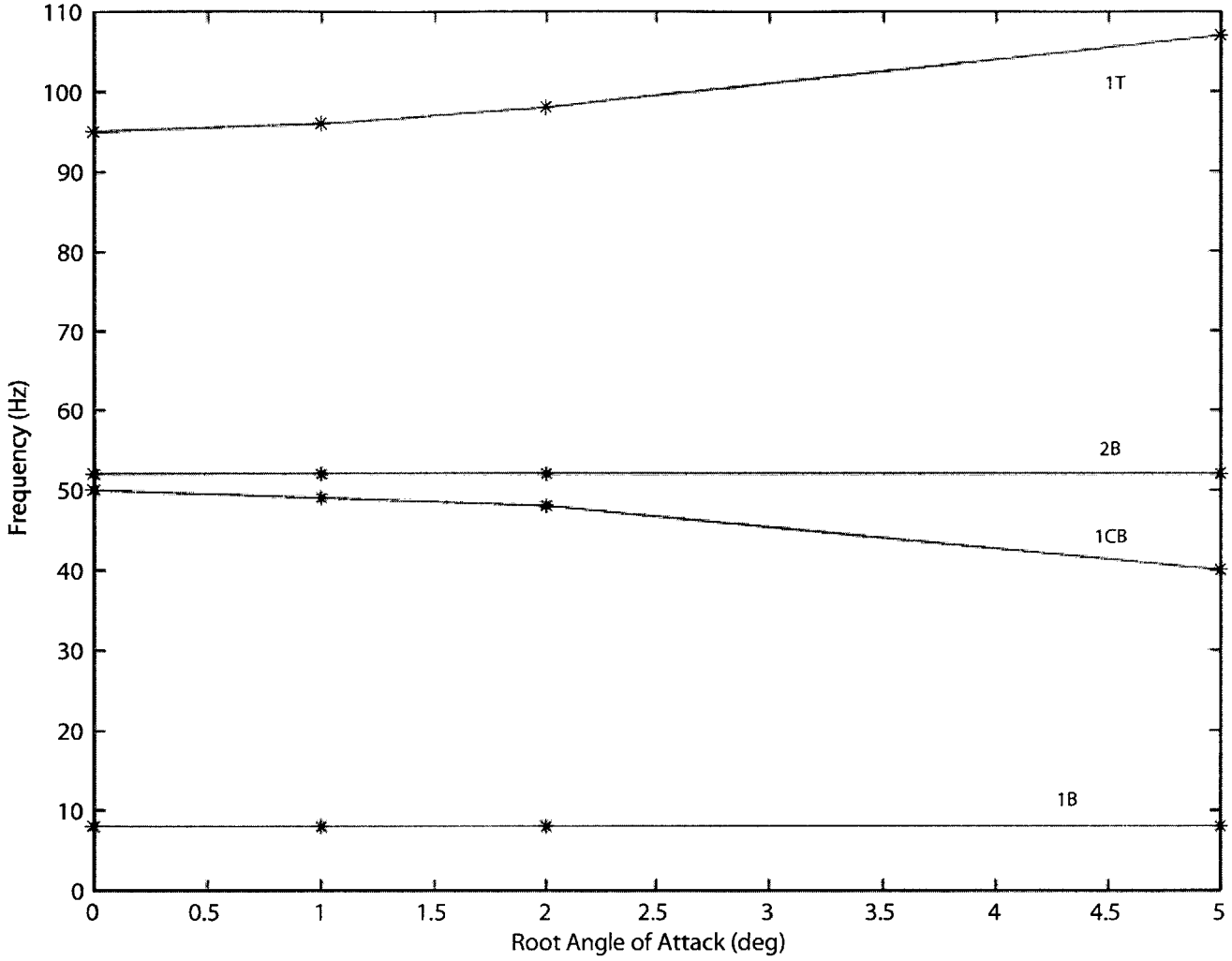

Figure 2-5: Frequency change due to root angle of attack change at U = 30 m/s

Table 2.4: Dynamic properties at U = 30 m/s

Angle of Attack		0°	1°	2°	5°
Tip Deflection		-0.005 m	0.03 m	0.06 m	0.16 m
Mode Shapes	1^{st} Bending	8	8	8	8
	1^{st} Chordwise Bending	50	49	48	40
	2^{nd} Bending	52	52	52	52
	1^{st} Torsional	95	96	98	107
	3^{rd} Bending	153	153	153	153
	2^{nd} Torsional	292	293	295	303

A similar behavior is also seen when the speed increases for a set angle of attack. This behavior is illustrated in Table 2.5 and Table 2.6. The first four modes for each of these examples is presented graphically in Figure 2-6 and Figure 2-7, respectively.

Table 2.5: Dynamic properties at angle of attack = 2°

Speed		30 m/s	35 m/s	40 m/s	45 m/s
Tip Deflection		0.06 m	0.09 m	0.12 m	0.16 m
Mode Shapes	1^{st} Bending	8	8	8	8
	1^{st} Chordwise Bending	48	46	43	40
	2^{nd} Bending	52	52	52	52
	1^{st} Torsional	98	100	103	107
	3^{rd} Bending	153	153	153	153
	2^{nd} Torsional	295	297	300	303

This change in the dynamic behavior of the wing results in changes in its flutter speed. This is shown in Figures 2-9, 2-11, 2-18 and 2-24, which present the root locus plots for the wing at root angles of attack of 0°, 1°, 2° and 5°. The flutter speeds as function of root angle of attack determined from these plots are summarized in Figure 2-8.

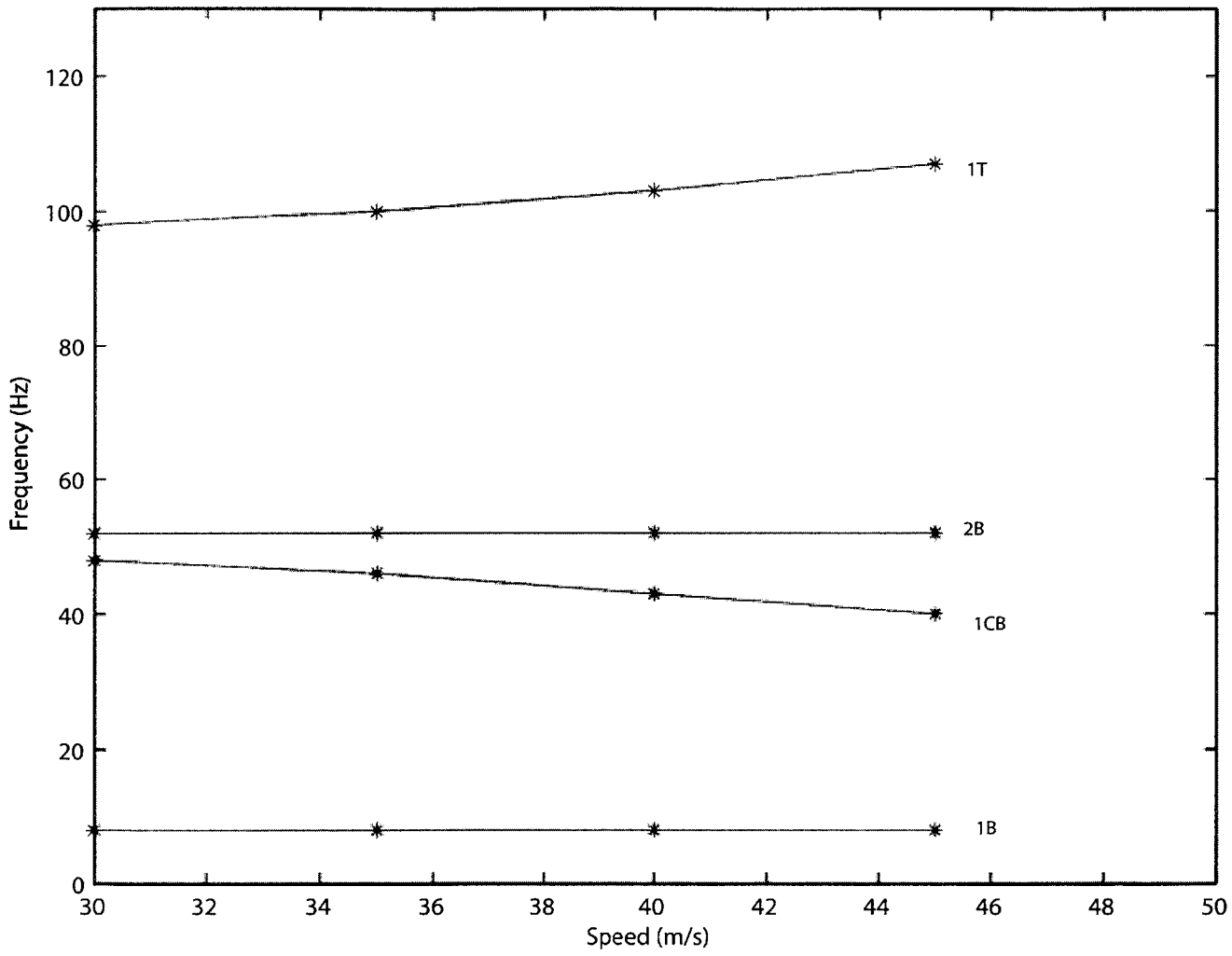

Figure 2-6: Frequency change due to change in speed for 2° root angle of attack

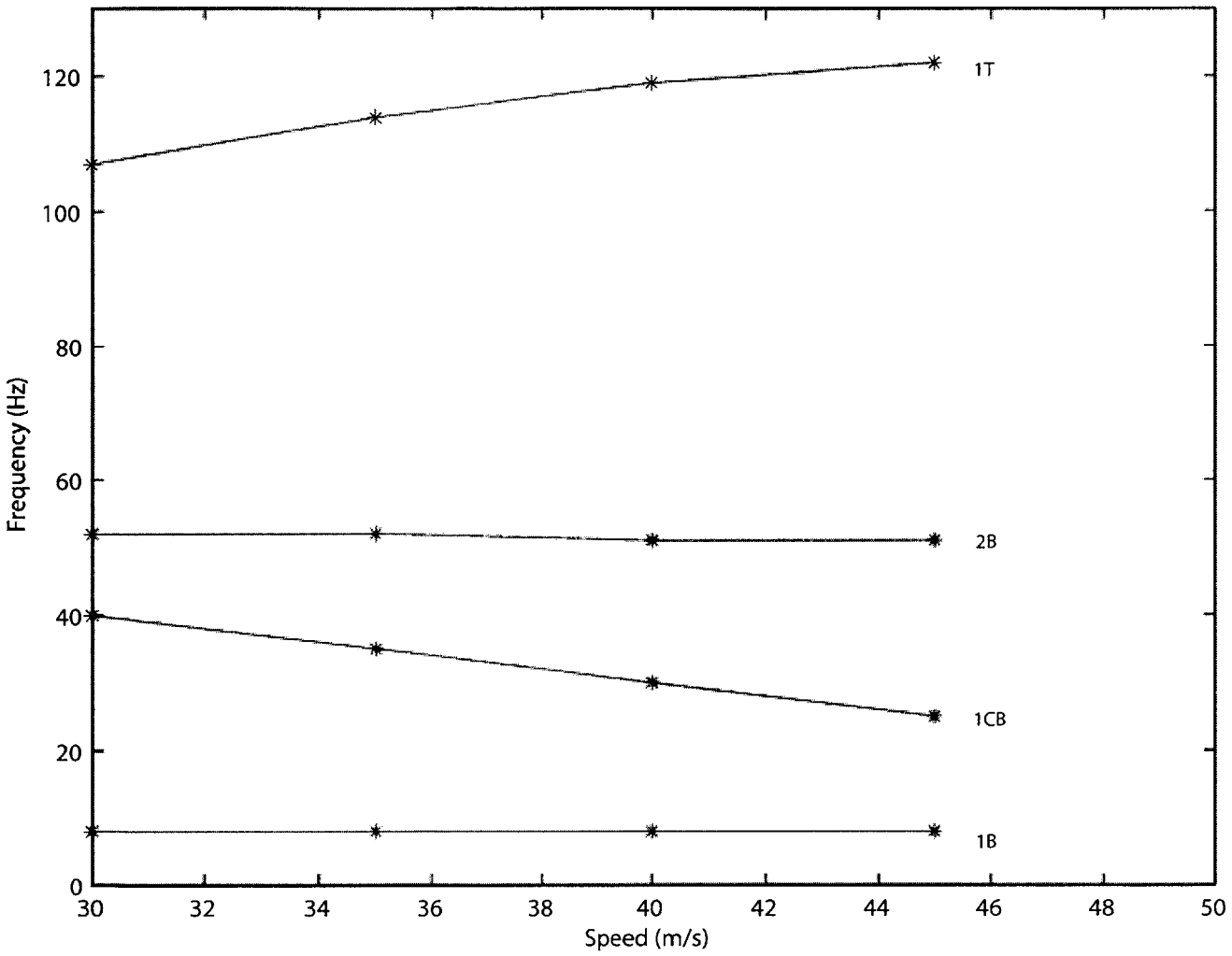

Figure 2-7: Frequency change due to change in speed for 5° root angle of attack

Table 2.6: Dynamic properties at angle of attack = 5°

Speed		30 m/s	35 m/s	40 m/s	45 m/s
Tip Deflection		0.16 m	0.22 m	0.30 m	0.38 m
Mode Shapes	1^{st} Bending	8	8	8	8
	1^{st} Chordwise Bending	40	35	30	25
	2^{nd} Bending	52	52	51	51
	1^{st} Torsional	107	114	119	122
	3^{rd} Bending	153	153	152	151
	2^{nd} Torsional	303	300	293	284

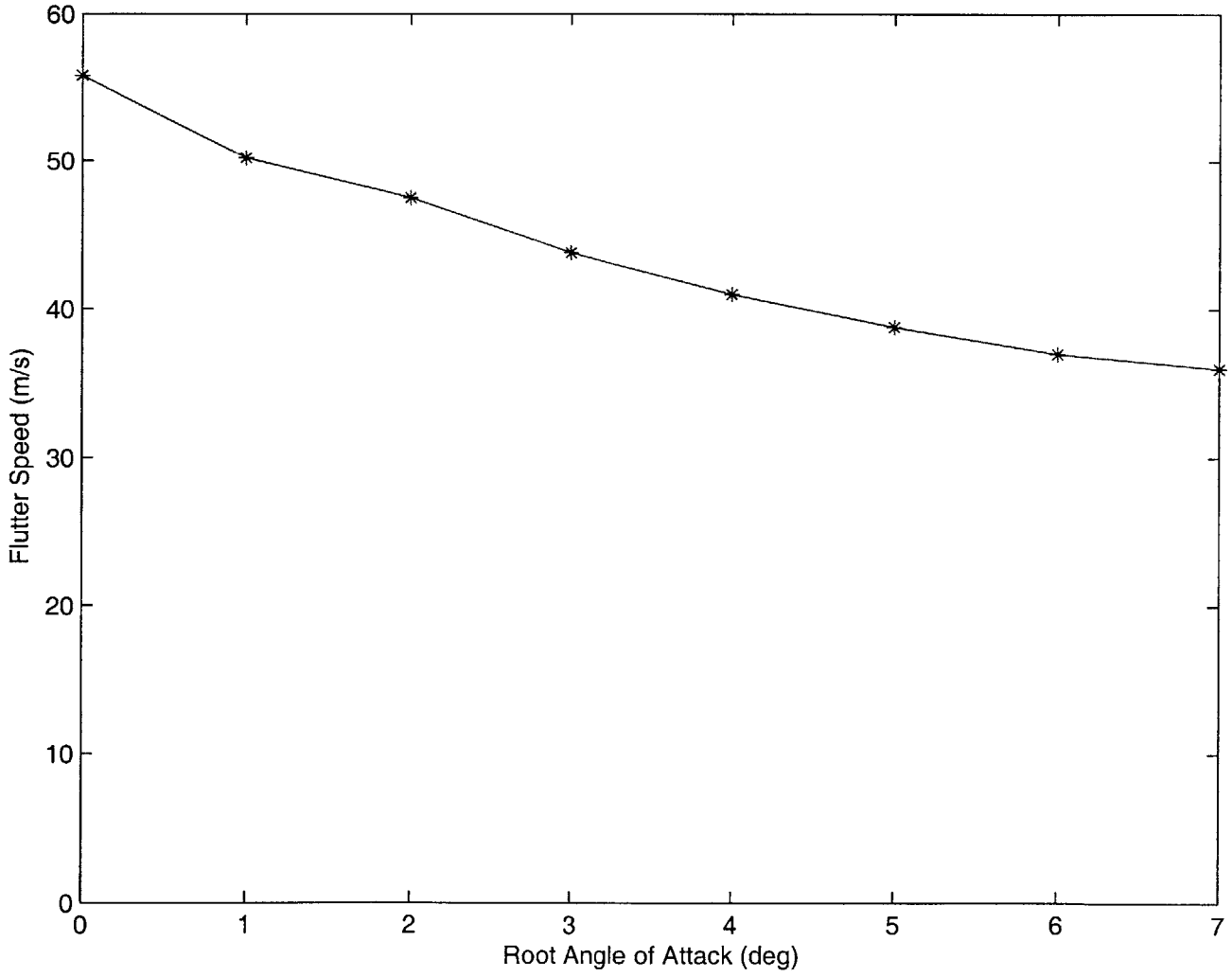

Figure 2-8: Flutter speeds for two-layer design

Zero-Degree Root Angle of Attack

The flutter speed for zero degree root angle of attack is determined to be 55.8 m/s from the root locus plot, given in Figure 2-9. The unstable mode is the fourth mode, which is primarily the first torsion mode. There is some chordwise bending present as well. The mode shapes for the wing at this speed are given in Figure 2-10.

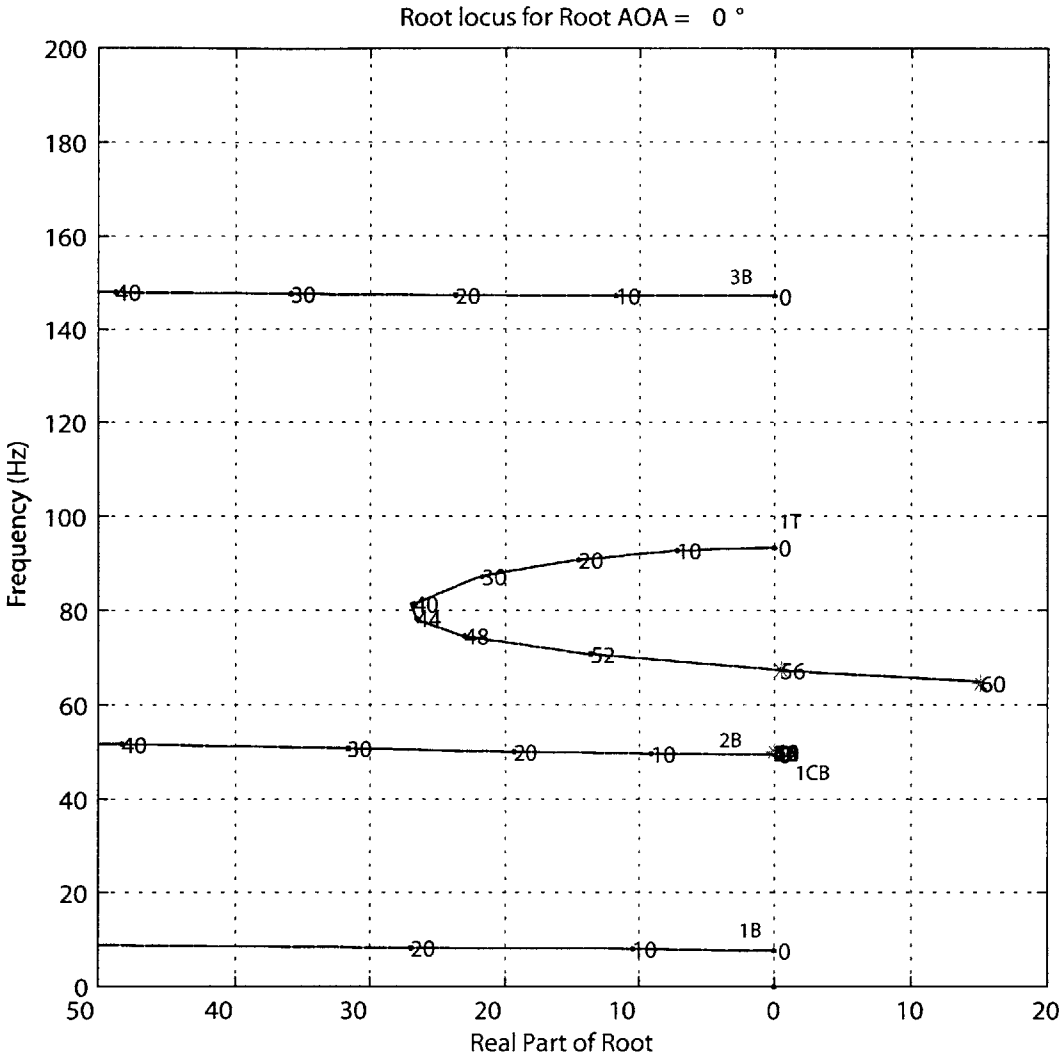

Figure 2-9: Root locus plot for 0° root angle of attack

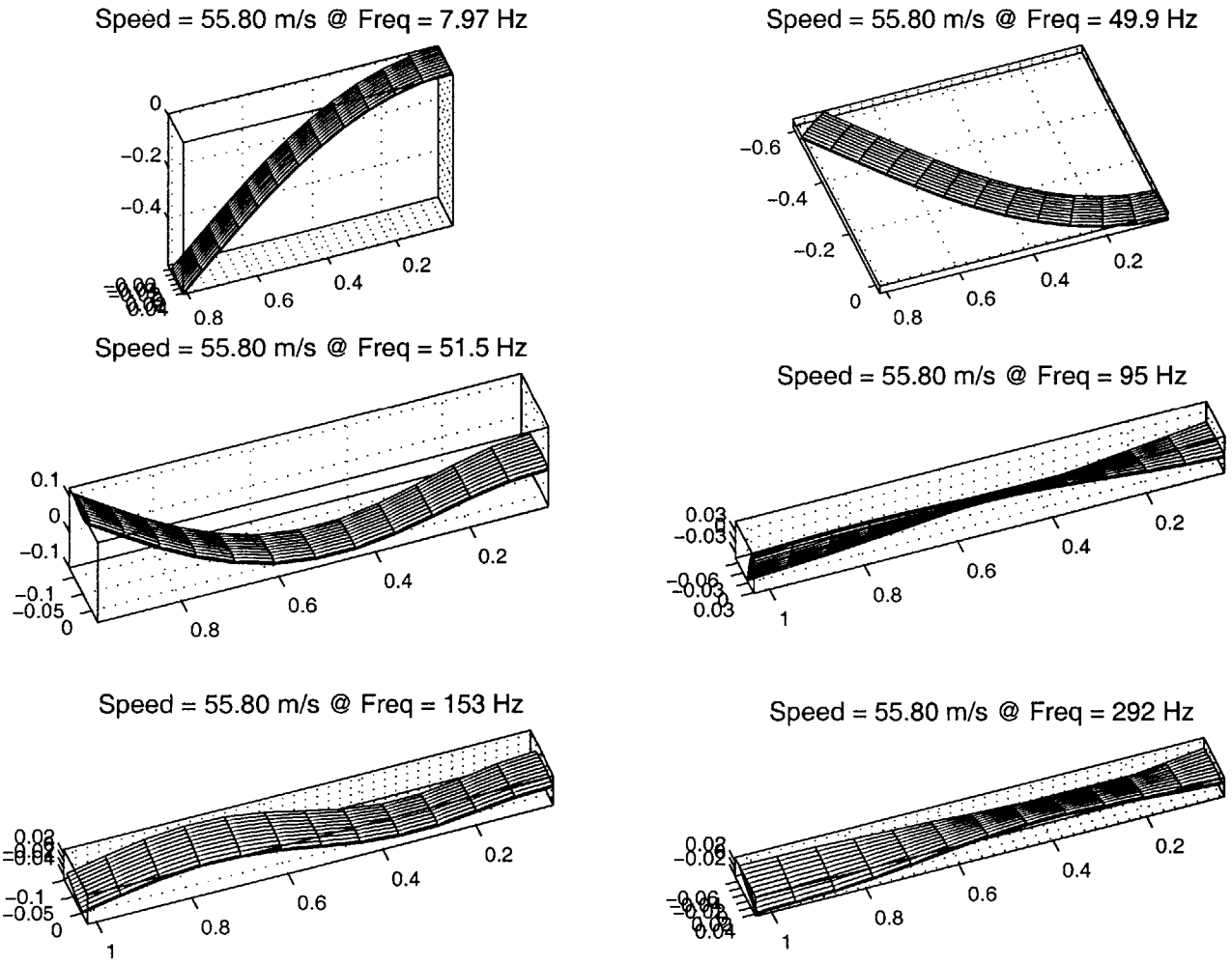

Figure 2-10: Mode shapes for two-layer design at 0° root angle of attack and its corresponding flutter speed of 55.8 m/s

One-Degree Root Angle of Attack

The flutter speed for one-degree root angle of attack is determined to be 50.2 m/s, shown in Figure 2-11. The mode of instability is the second mode. A magnification of this mode is provided in Figure 2-12. This mode is primarily the first chordwise bending. However, the forces due to air pressure on the tilted wing result in some torsion being present as well. The first six mode shapes at this speed are given in Figure 2-13.

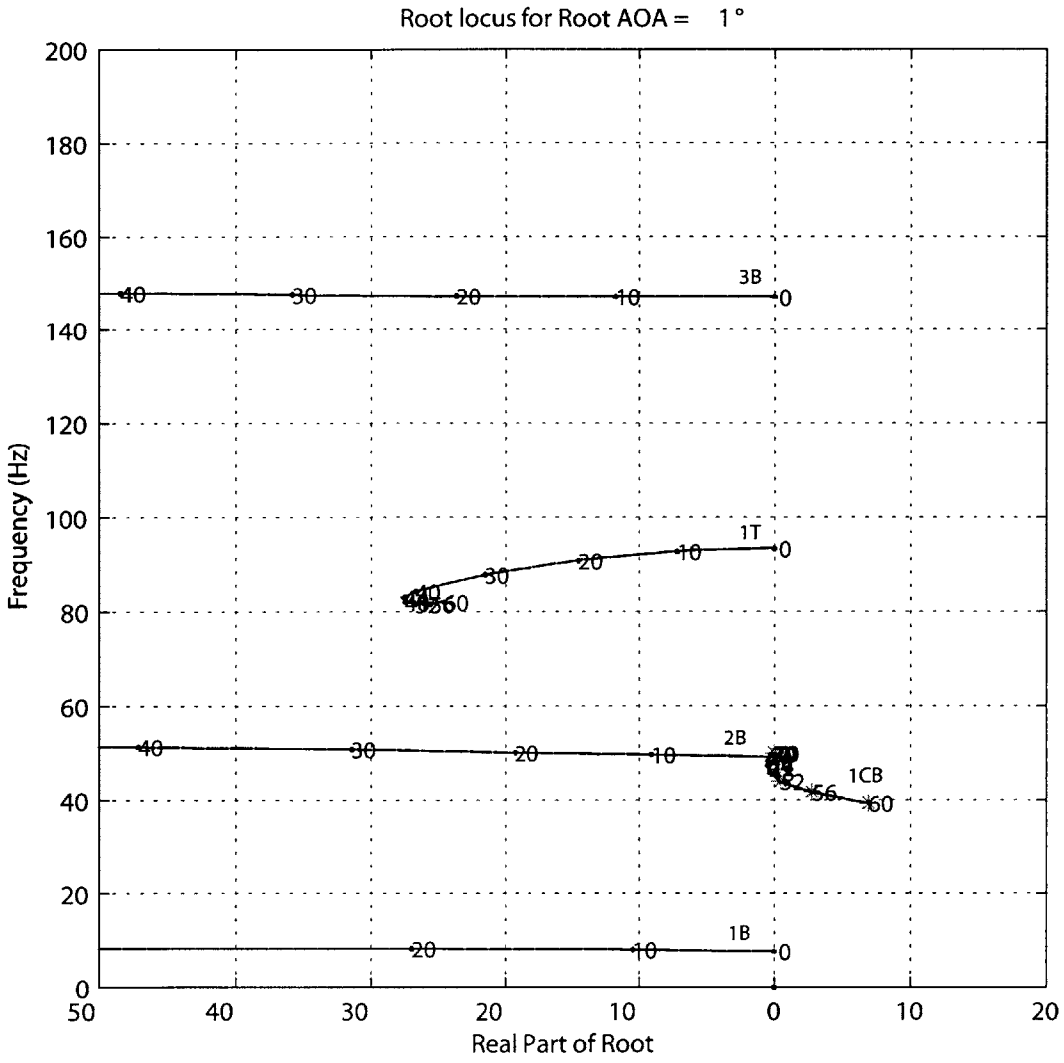

Figure 2-11: Root locus plot for 1° root angle of attack

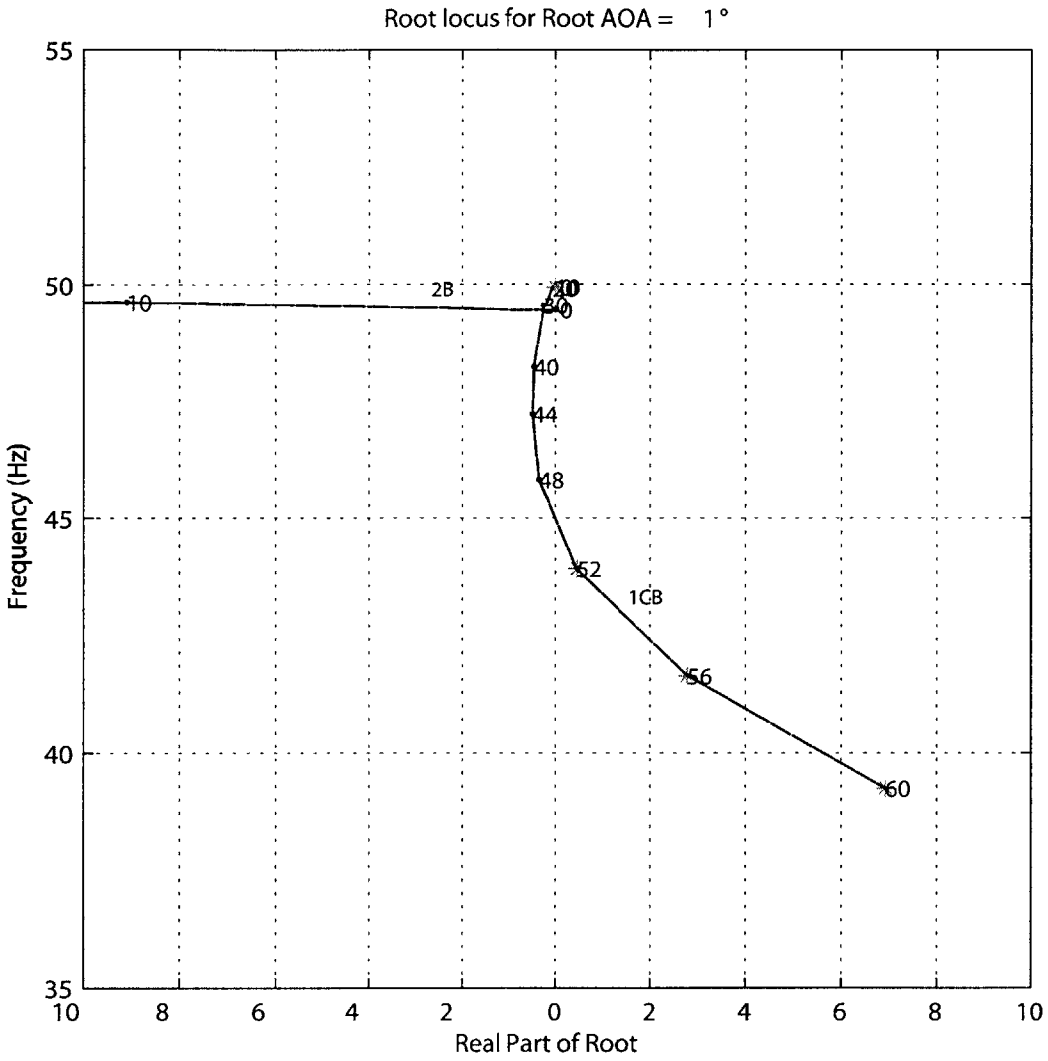

Figure 2-12: Magnification of root locus plot for 1° root angle of attack

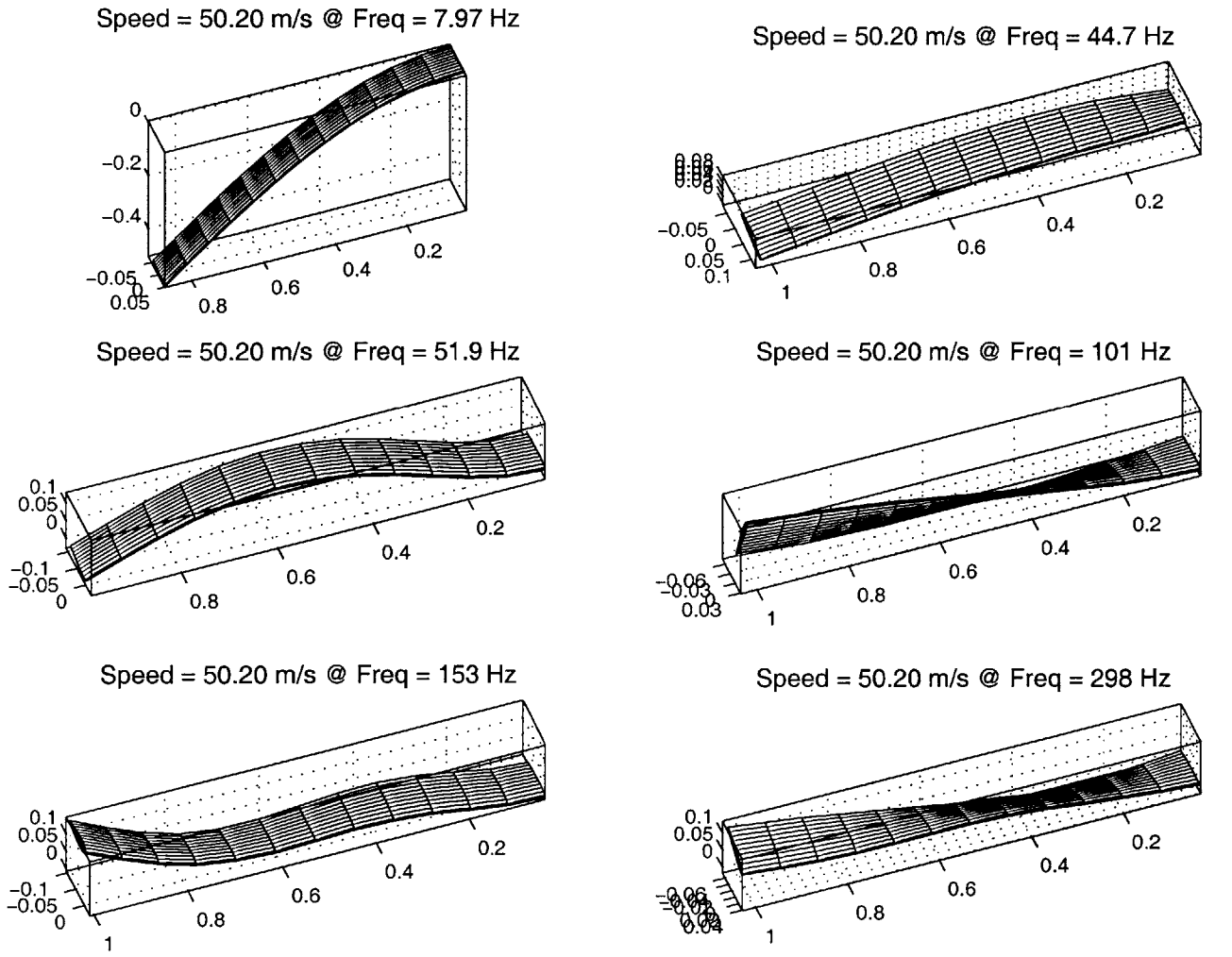

Figure 2-13: Mode shapes for two-layer design at 1° root angle of attack and its corresponding flutter speed of 50.2 m/s

When the wing is flown at 10% above the flutter speed for a 1° root angle of attack, the wing enters into a Limit Cycle Oscillation (LCO). The tip deflections and the tip twist are plotted for this case up to 1 second. These plots are given in Figure 2-14 thru Figure 2-16.

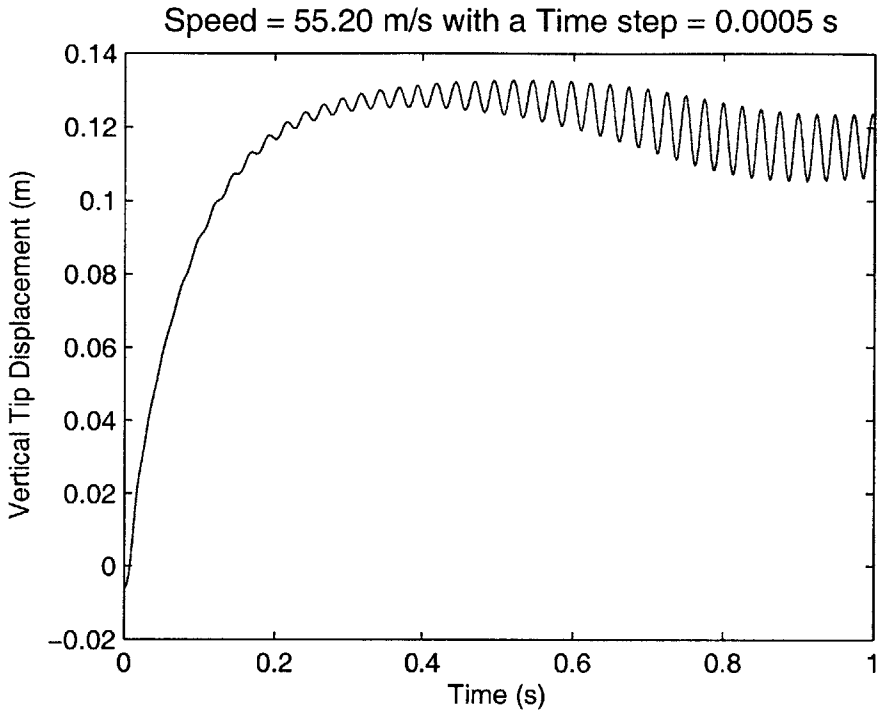

Figure 2-14: Nonlinear time simulation of the wing vertical tip displacement at 10% above its flutter speed (1° root angle of attack) for the two-layer design

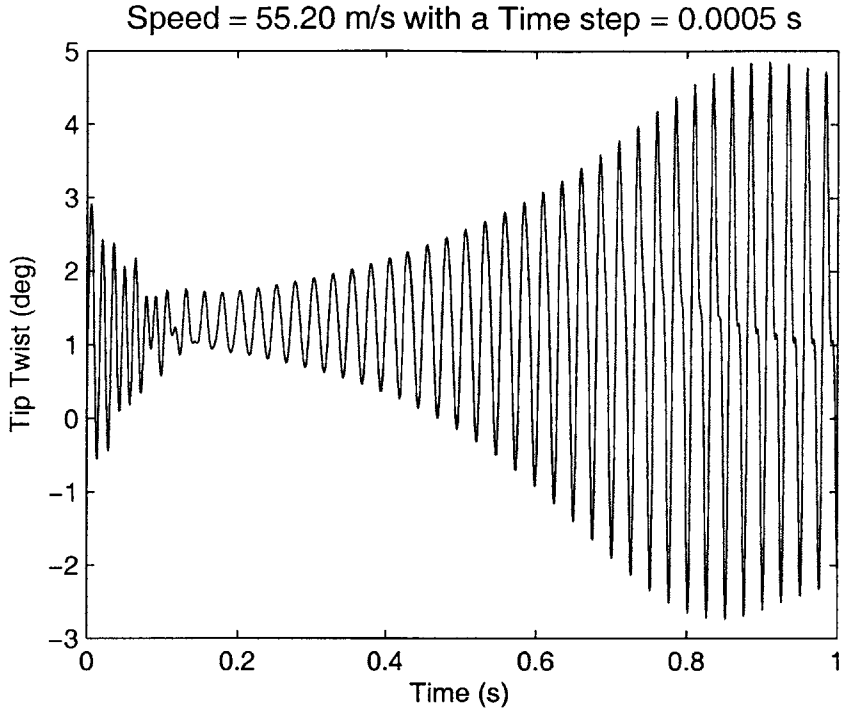

Figure 2-15: Nonlinear time simulation of the wing tip twist at 10% above its flutter speed (1° root angle of attack) for the two-layer design

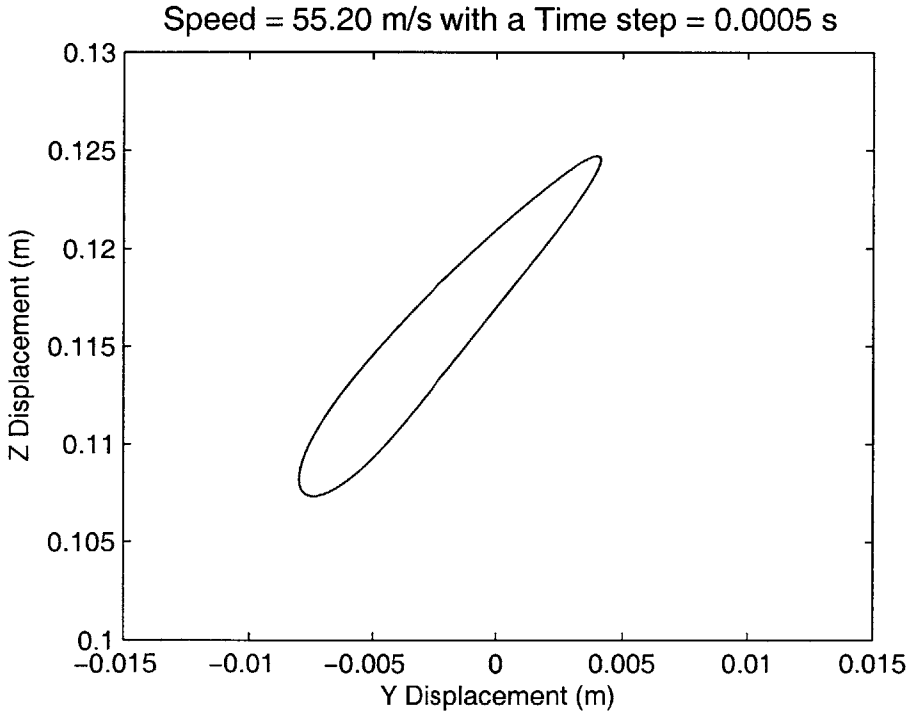

Figure 2-16: Nonlinear time simulation of the wing tip displacement motion at 10% above its flutter speed (1° root angle of attack) for the two-layer design

A strain analysis was performed on the wing when it was at its maximum deflection. This occurs during the initial rise shown in Figure 2-14. The maximum tensile strain is 2660 μm/m and the maximum shear strain is -769 μm/m. Both occur at the bottom of the root of the wing in the outer ply. These results are summarized in Figure 2-17. From Appendix B, the maximum allowable strain for E-glass/epoxy is 10000 μm/m in tension and 15000 μm/m in shear. This results in a margin of safety (Equation 2.1) of 2.76 for tension and 18.5 for shear.

$$MS(\%) = \frac{Allowable}{Actual} - 1 \tag{2.1}$$

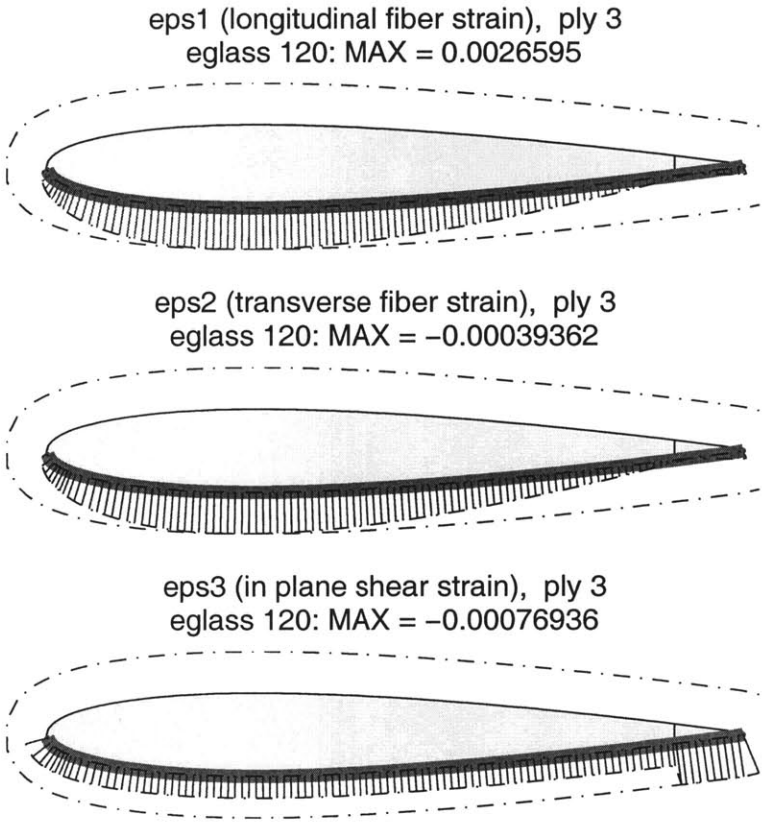

Figure 2-17: Maximum ply strain reached at 10% above flutter speed of 1° root angle of attack for the two-layer design

Two-Degree Root Angle of Attack

The flutter speed for two-degree root angle of attack is determined to be 47.5 m/s from the root locus plot shown in Figure 2-18. The instability mode is the same as for 1°, except the amount of torsion present has increased. Also, by the time the angle of attack is 2°, the effects of the large deflections on the wing cause the natural frequency of the fourth mode to increase with increasing speed instead of decrease as it did in the 0° and 1° cases. The drop in the second natural frequency due to the increased upward bend also causes the second mode to turn over faster and amplifies the effects of flow over the wing. The first six modes at flutter speed are provided in Figure 2-19.

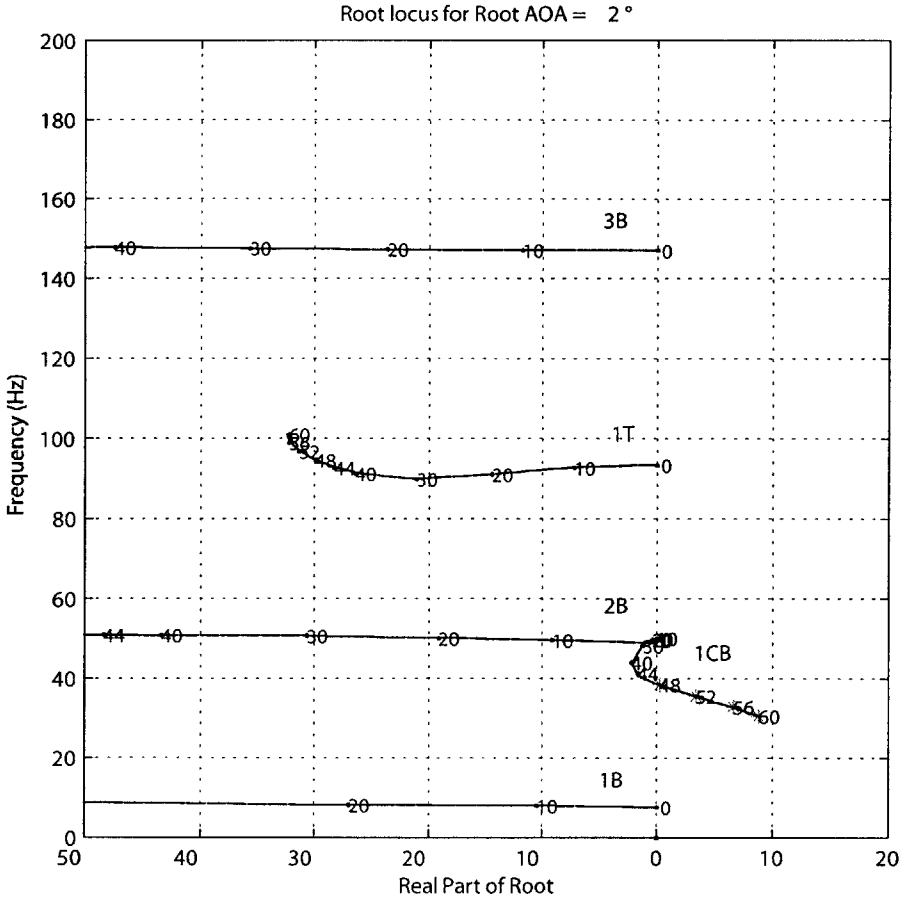

Figure 2-18: Root locus plot for 2° root angle of attack

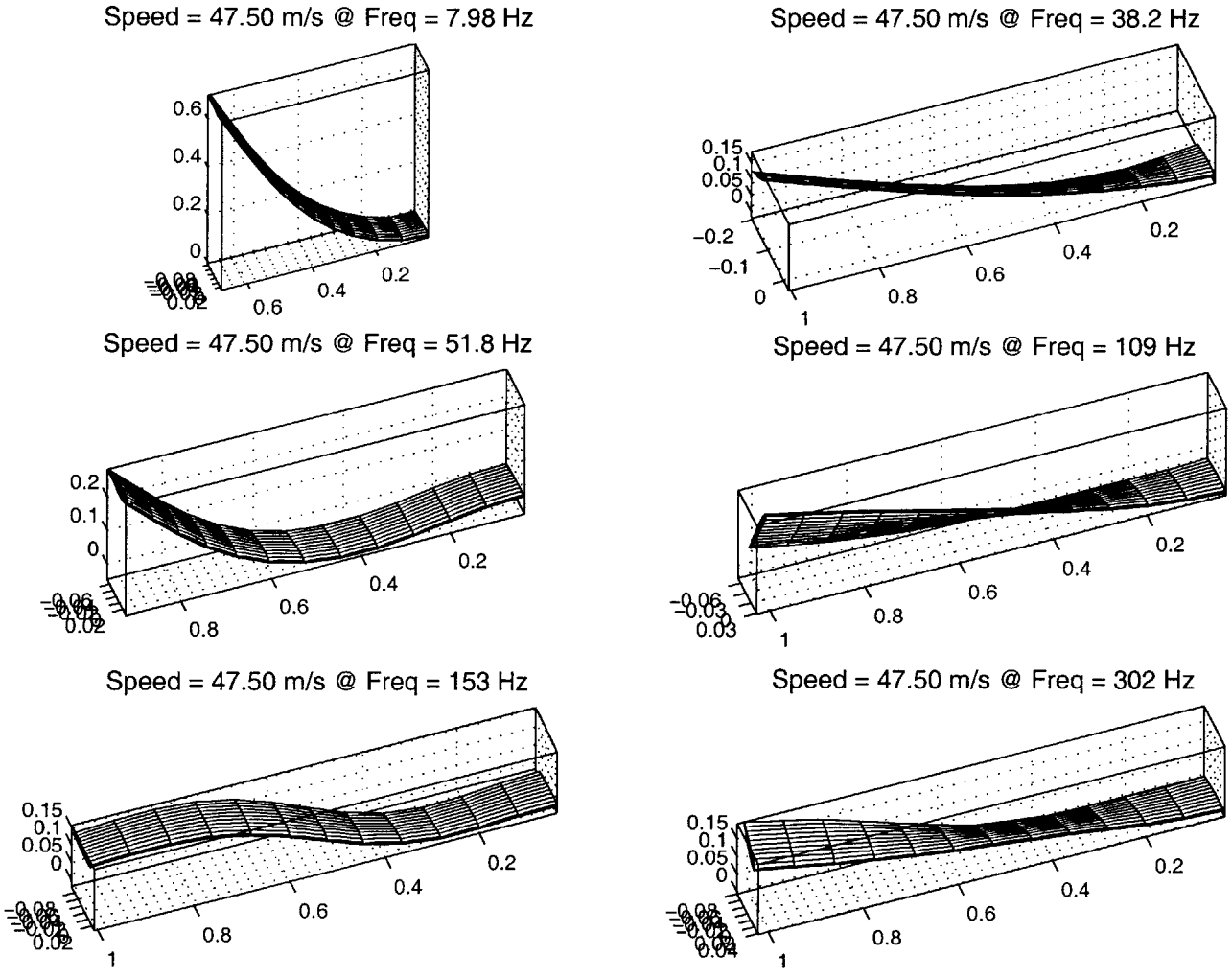

Figure 2-19: Mode shapes for two-layer design at 2° root angle of attack and at its corresponding flutter speed of 47.5 m/s

For 2° angle of attack, the wing also enters a LCO when flown at 10% above its flutter speed. The tip deflections and the tip twist are plotted for this case up to 1 second. These plots are given in Figure 2-20 thru Figure 2-22. Notice from Figure 2-22 that the LCO now has more than one frequency (no single ellipse on the plot), indicating potentially chaotic response.

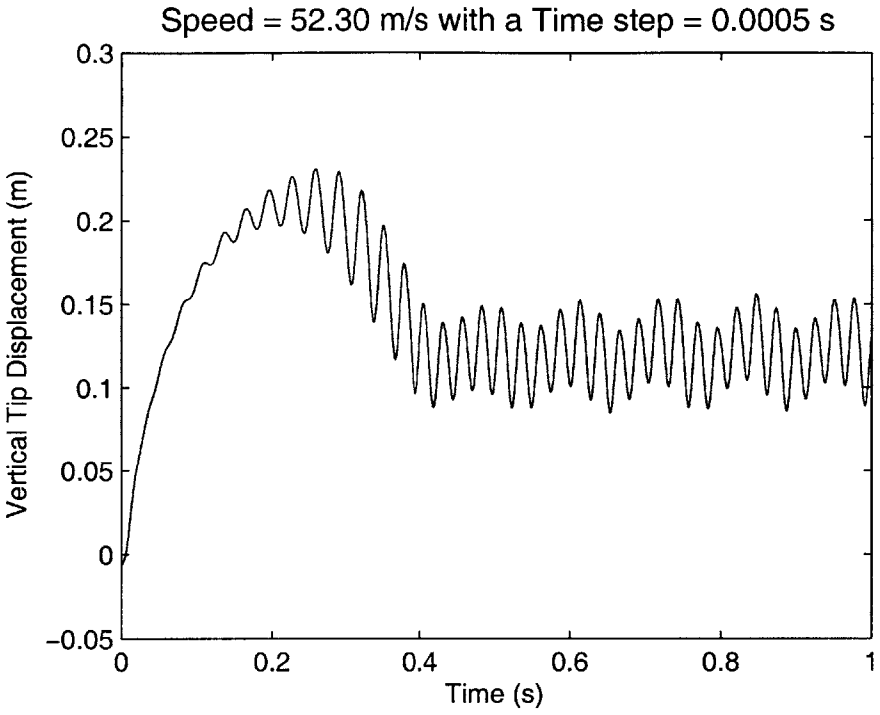

Figure 2-20: Nonlinear time simulation of the wing vertical tip displacement at 10% above its flutter speed (2° root angle of attack) for the two-layer design

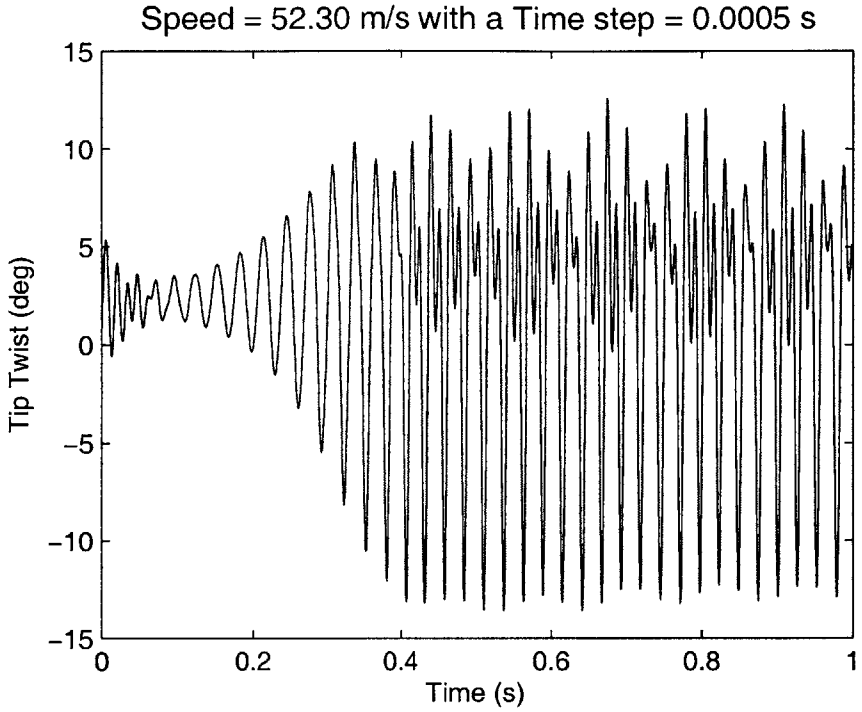

Figure 2-21: Nonlinear time simulation of the wing tip twist at 10% above its flutter speed (2° root angle of attack) for the two-layer design

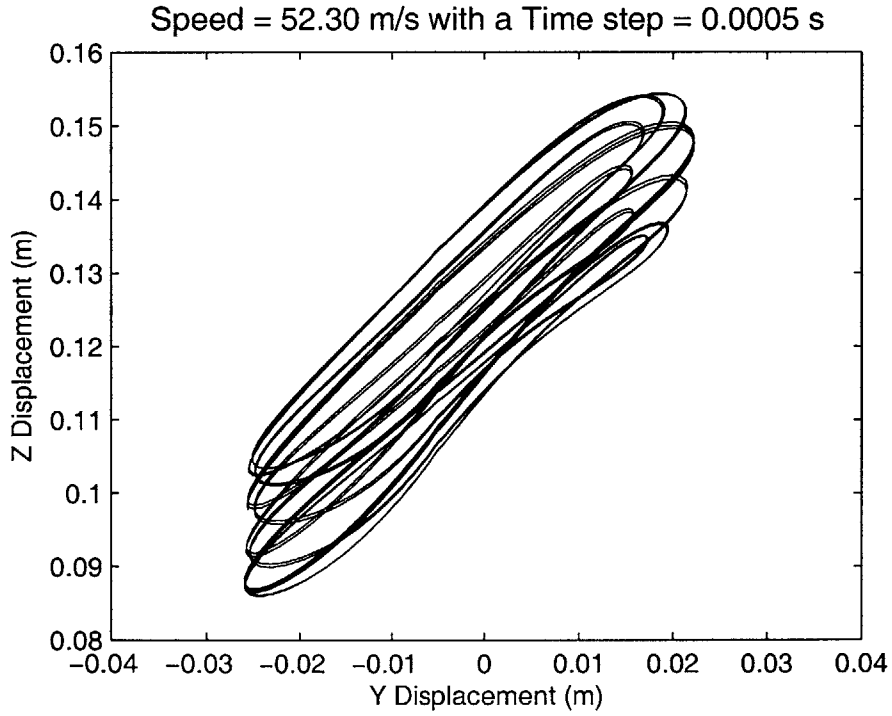

Figure 2-22: Nonlinear time simulation of the wing tip motion at 10% above its flutter speed (2° root angle of attack) for the two-layer design

A strain analysis was performed on the wing when it was at its maximum deflection. This occurs during the transient rise shown in Figure 2-20. The maximum tensile strain is 4484 μm/m and the maximum shear strain is -2726 μm/m. Both occur at the bottom of the root of the wing in the outer ply. These details are summarized in Figure 2-23. These strains result in a margin of safety of 1.23 and 4.5, respectively.

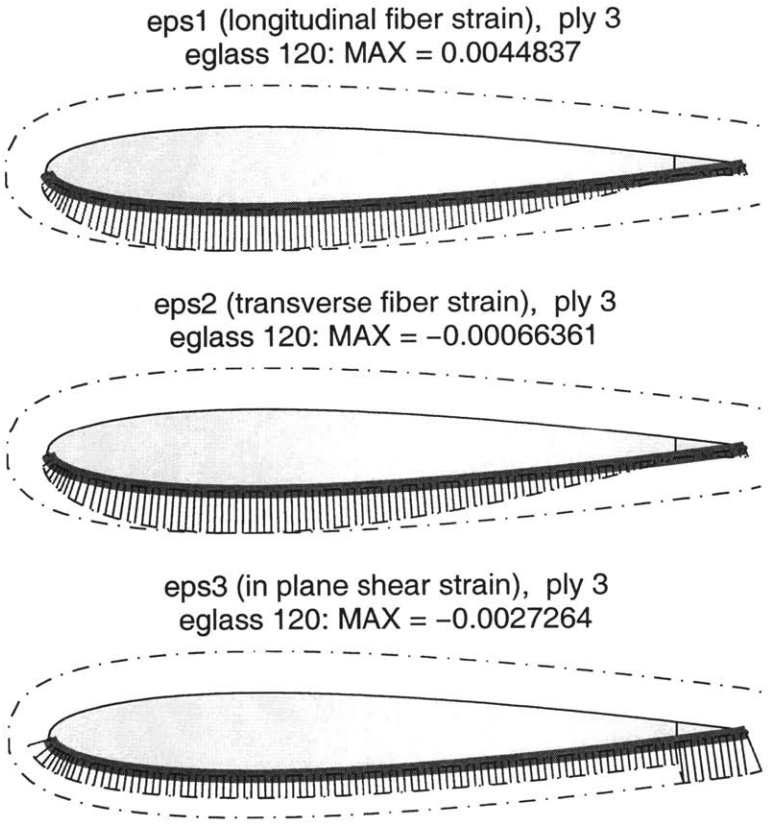

Figure 2-23: Maximum ply strain reached at 10% above flutter speed of 2° root angle of attack for the two-layer design

Five-Degree Root Angle of Attack

The flutter speed for five-degree root angle of attack is determined to be 38.8 m/s from the root locus plot provided in Figure 2-24. As with the 1° and 2° cases, the mode of instability is the second mode, which is the 1^{st} chordwise bending with some torsional effects. As was seen in the 2° case, the changes in the dynamic behavior due to the increased upward bend result in the second mode rolling over faster to the positive dampening axis and the fourth

mode to further curve upward. Although with the fourth mode, we see an interaction with the fifth mode (3^{rd} bending) starting to cause the fourth mode to turn towards the instability line as well. The first six mode shapes for this case are provided in Figure 2-25.

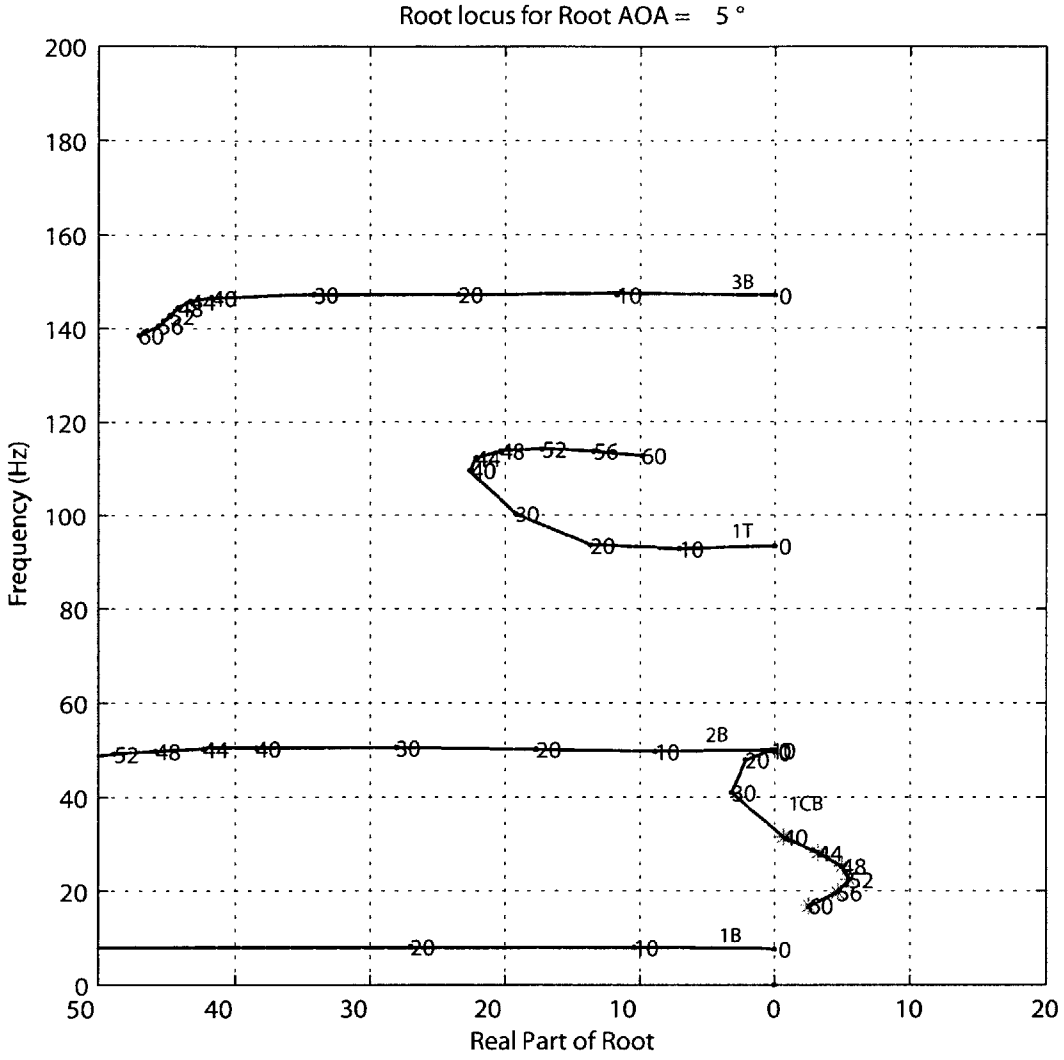

Figure 2-24: Root locus plot for 5° root angle of attack

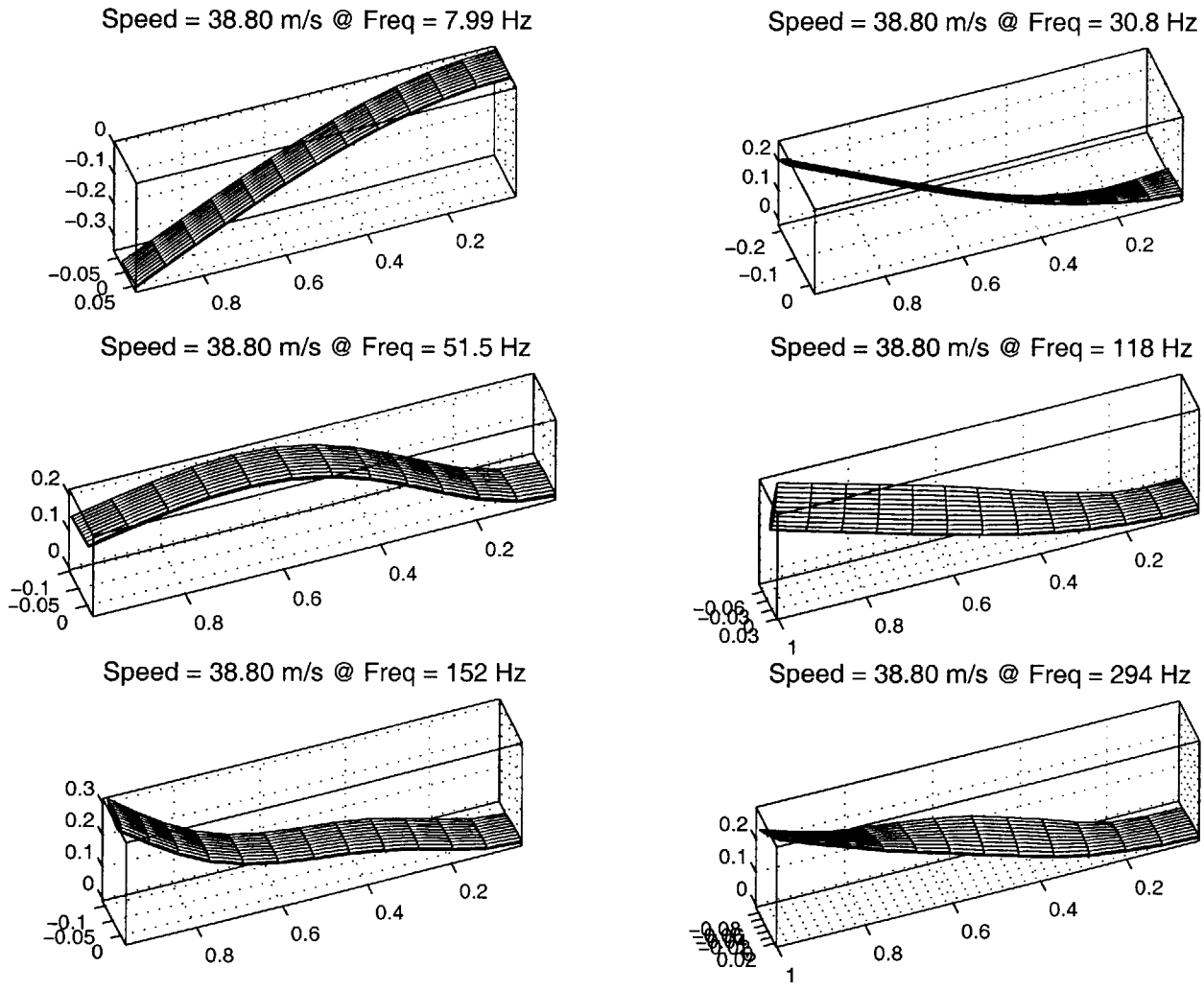

Figure 2-25: Mode shapes for two-layer design at 5° root angle of attack and at its corresponding flutter speed of 38.8 m/s

For 5° root angle of attack, the wing also enters a LCO when flown at 10% above the flutter speed. The tip deflections and the tip twist are plotted for this case up to 1 second. These plots are given in Figure 2-26 thru Figure 2-28.

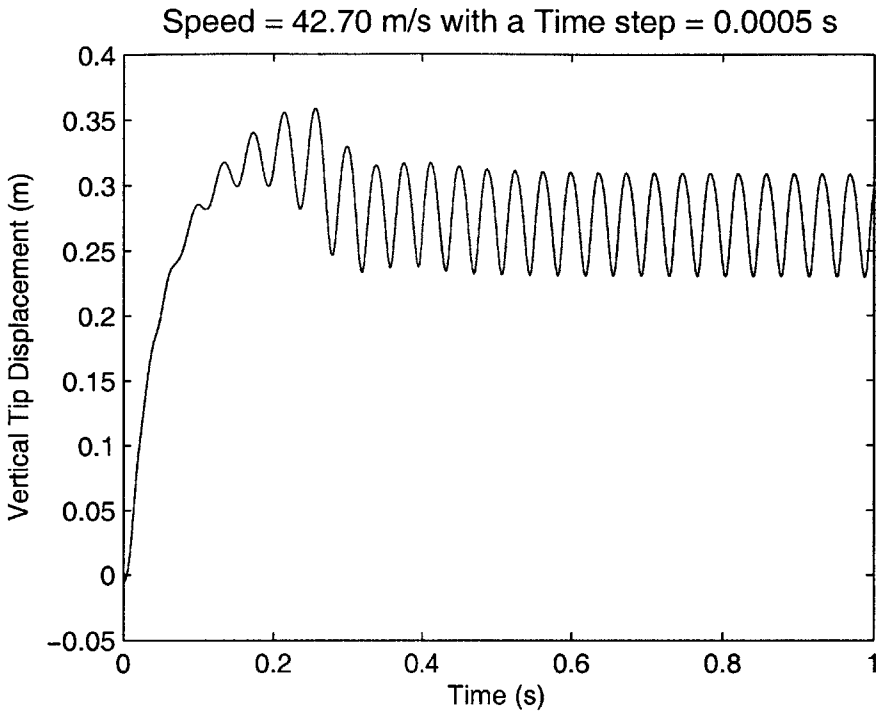

Figure 2-26: Nonlinear time simulation of the wing vertical tip displacement at 10% above its flutter speed (5° root angle of attack) for the two-layer design

A strain analysis was performed on the wing when it was at its maximum deflection. This occurs during the initial rise shown in Figure 2-26. The maximum tensile strain is 7405 μm/m and the maximum shear strain is -5018 μm/m. Both occur at the bottom of the root of the wing in the outer ply. These details are summarized in Figure 2-29. These strains result in a margin of safety of 0.35 and 1.99, respectively.

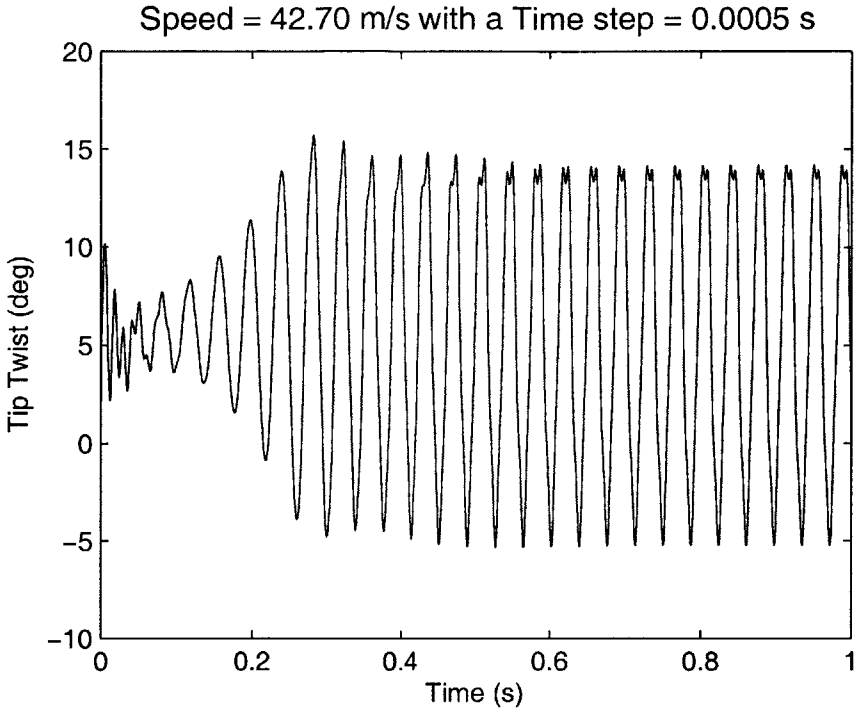

Figure 2-27: Nonlinear time simulation of the wing tip twist at 10% above its flutter speed (5° root angle of attack) for the two-layer design

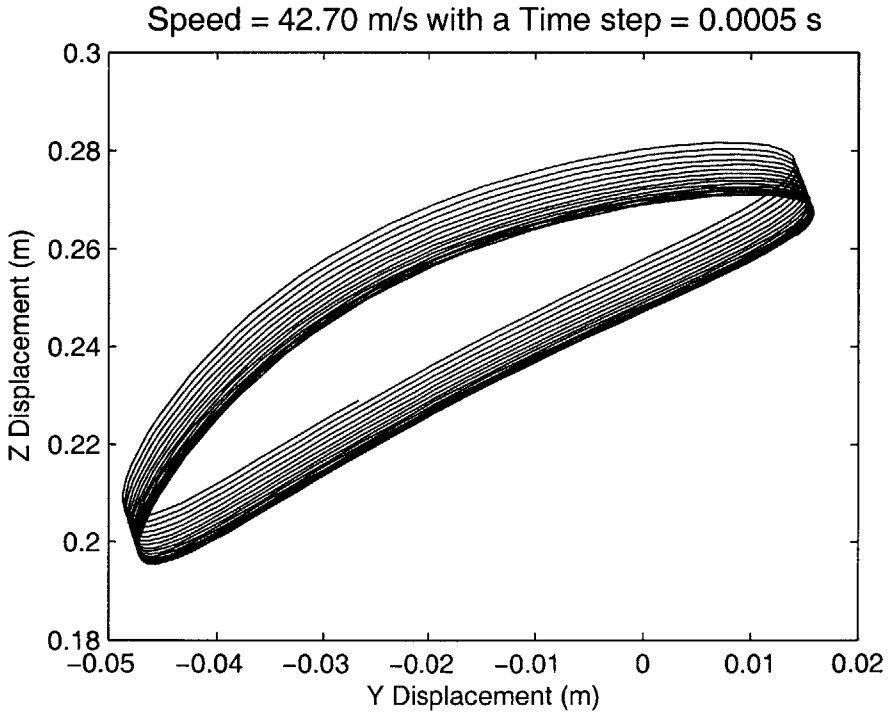

Figure 2-28: Nonlinear time simulation of the wing tip motion at 10% above its flutter speed (5° root angle of attack) for the two-layer design

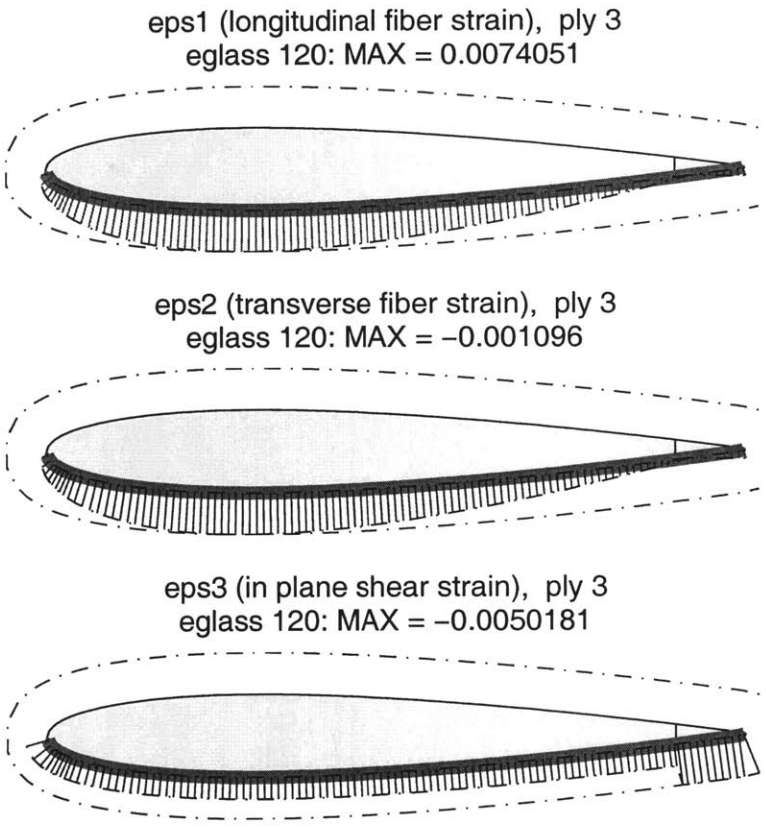

Figure 2-29: Maximum ply strain at reached at 10% above flutter speed of 5° root angle of attack for the two-layer design

2.3 Three-Layer Design

2.3.1 Basic Characteristics

The three-layer design resembles the previous one with the exception of an added layer of E-glass/epoxy fabric, also oriented at 0° (Figure 2-30.

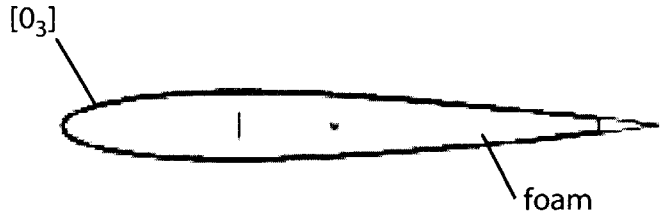

Figure 2-30: Cross section of three-layer wing (NACA 0012)

The cross sectional stiffness properties for this design are provided in Table 2.7. A detailed definition of the terms for this matrix are provided in Appendix A. The inertia matrix for

Table 2.7: Non-zero stiffness matrix terms for three-layer design: 1 = Extension, 2 = Torsion, 3 = Flatwise Bending, 4 = Chordwise Bending

K_{11}	$1.39 * 10^6$ N
K_{14}= K_{41}	$-2.35 * 10^4$ N*m
K_{22}	19.66 N*m^2
K_{33}	33.19 N*m^2
K_{44}	$1.63 * 10^3$ N*m^2

this cross-section is provided in Table 2.8. The center of gravity for the cross-section is

Table 2.8: Non-zero inertial matrix terms for two-layer design

I_{11}	$0.13 * 10^{-3}$ m^4
I_{22}	$0.32 * 10^{-5}$ m^4
I_{33}	$0.13 * 10^{-3}$ m^4

located 0.0173 m aft of the reference line (located at 30% chord). This places the center of gravity at 46% of the chord.

The first six normal modes (in vacuum) and their corresponding frequencies are provided in Table 2.9. It is interesting that the values for the normal modes have changed very little from the two layer case. This can be explained by the fact that the increase in stiffness is comparable to the increase in inertia. The corresponding mode shapes are provided in Figure 2-31.

Table 2.9: Natural frequencies of the three-layer design in vacuum

Mode	Frequency	Mode Shape
1	8 Hz	1^{st} Bending
2	51 Hz	1^{st} Chordwise Bending
3	54 Hz	2^{nd} Bending
4	97 Hz	1^{st} Torsion
5	161 Hz	3^{rd} Bending
6	299 Hz	2^{nd} Torsion

2.3.2 Wing Nonlinear Characteristics

The effects from changes in root angle of attack are similar to those seen in the two-layer design. The tip deflection again increases with increase root angle of attack. This is plotted in Figure 2-32. The tip twist also increases with increased root angle of attack, as shown in Figure 2-33. As with the two-layer data, the root angle of attack was subtracted from the tip angle to better illustrate the effects to do gravity and aero-loading only. It should also be noted that although the trends are the same, the values of deflection and twist are smaller. This is expected as the stiffness of the wing is increased with the additional layer of E-glass/epoxy.

Deflection and twist changes versus angle of attack also result in changes in the dynamic behavior of the wing. The wing's mode shapes and natural frequencies were computed for a wind speed of 30 m/s. The results are summarized in Table 2.10. This data is presented

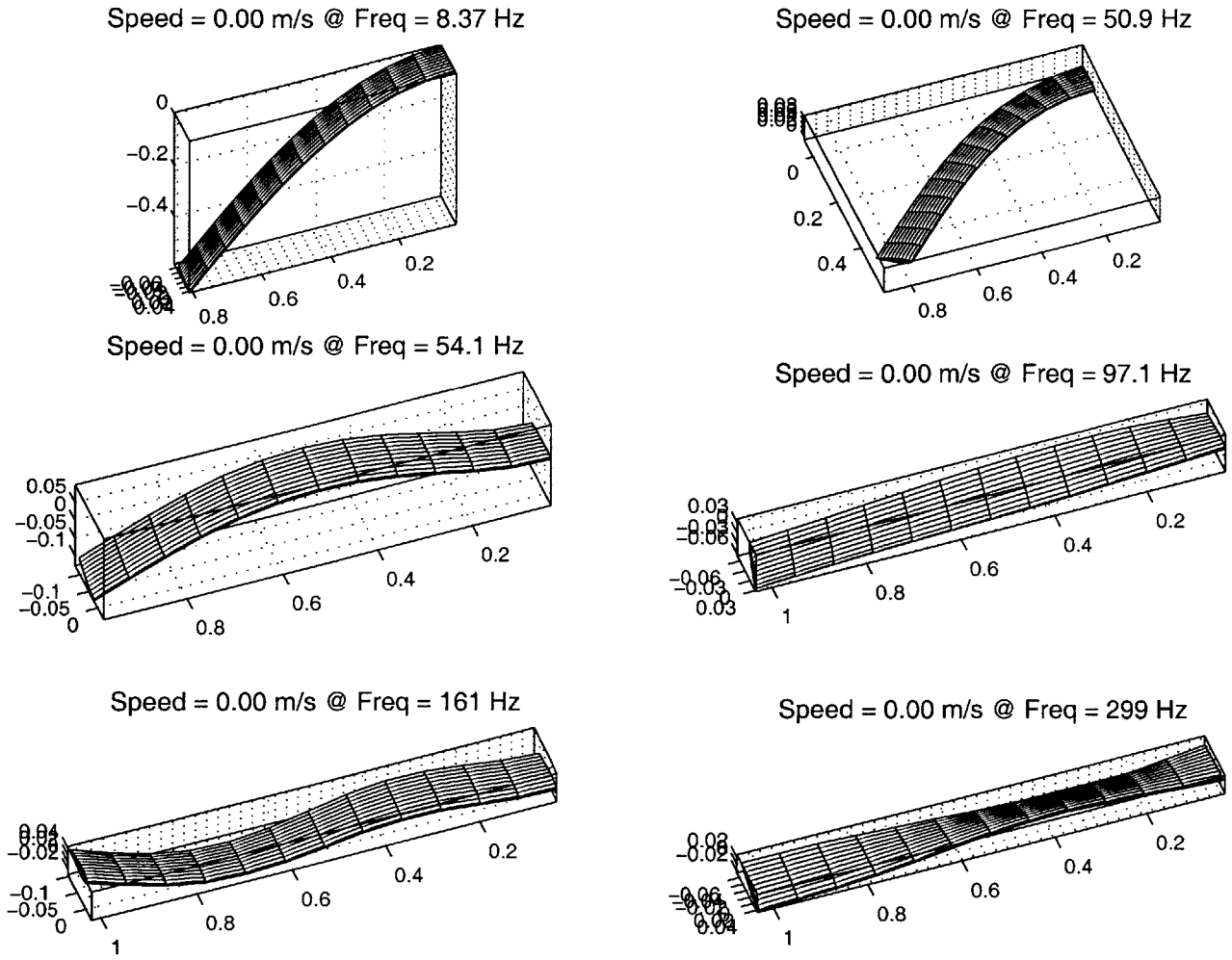

Figure 2-31: First six modes shapes for the three-layer wing (in vacuum)

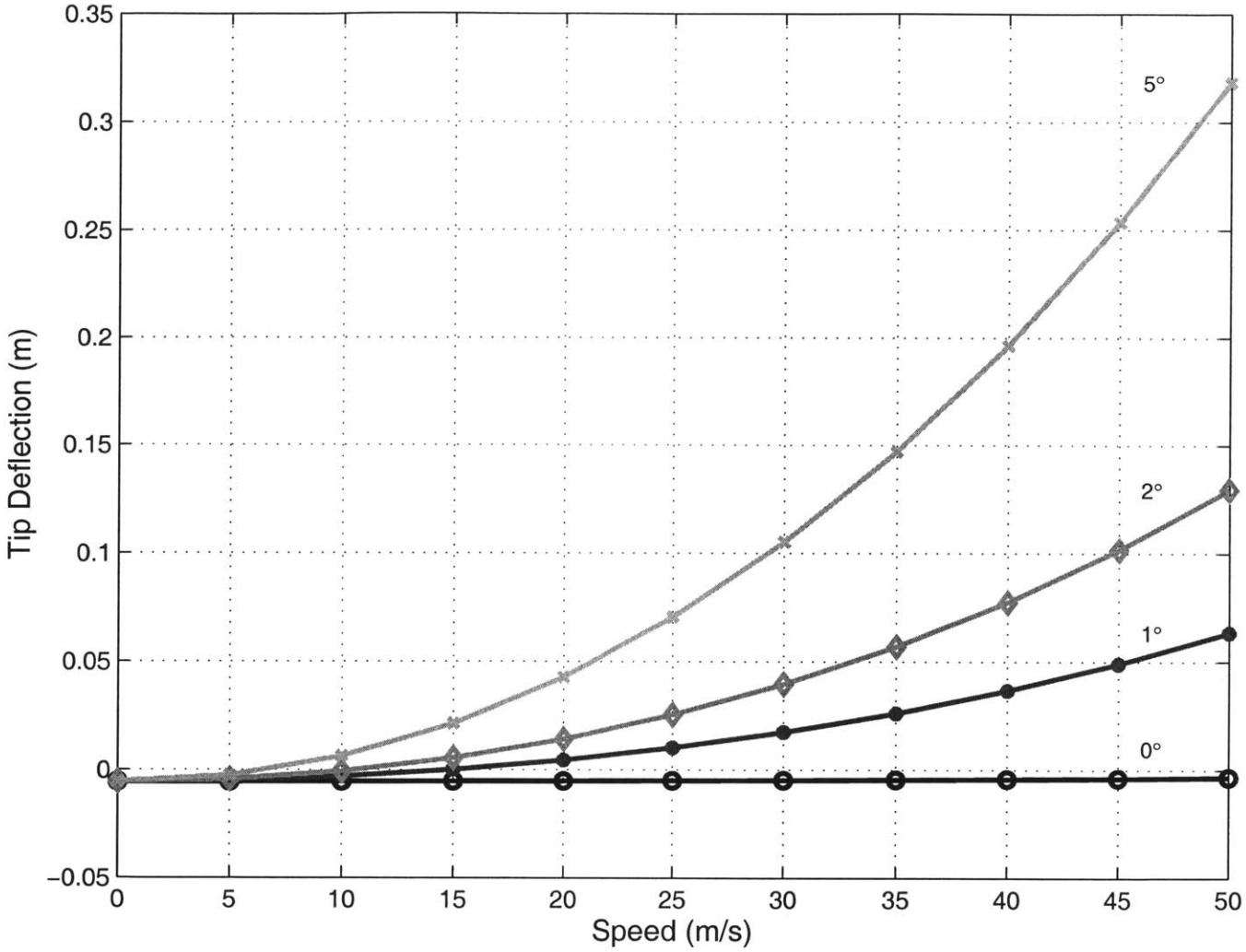

Figure 2-32: Static tip deflection for increasing speed at different root angles of attack

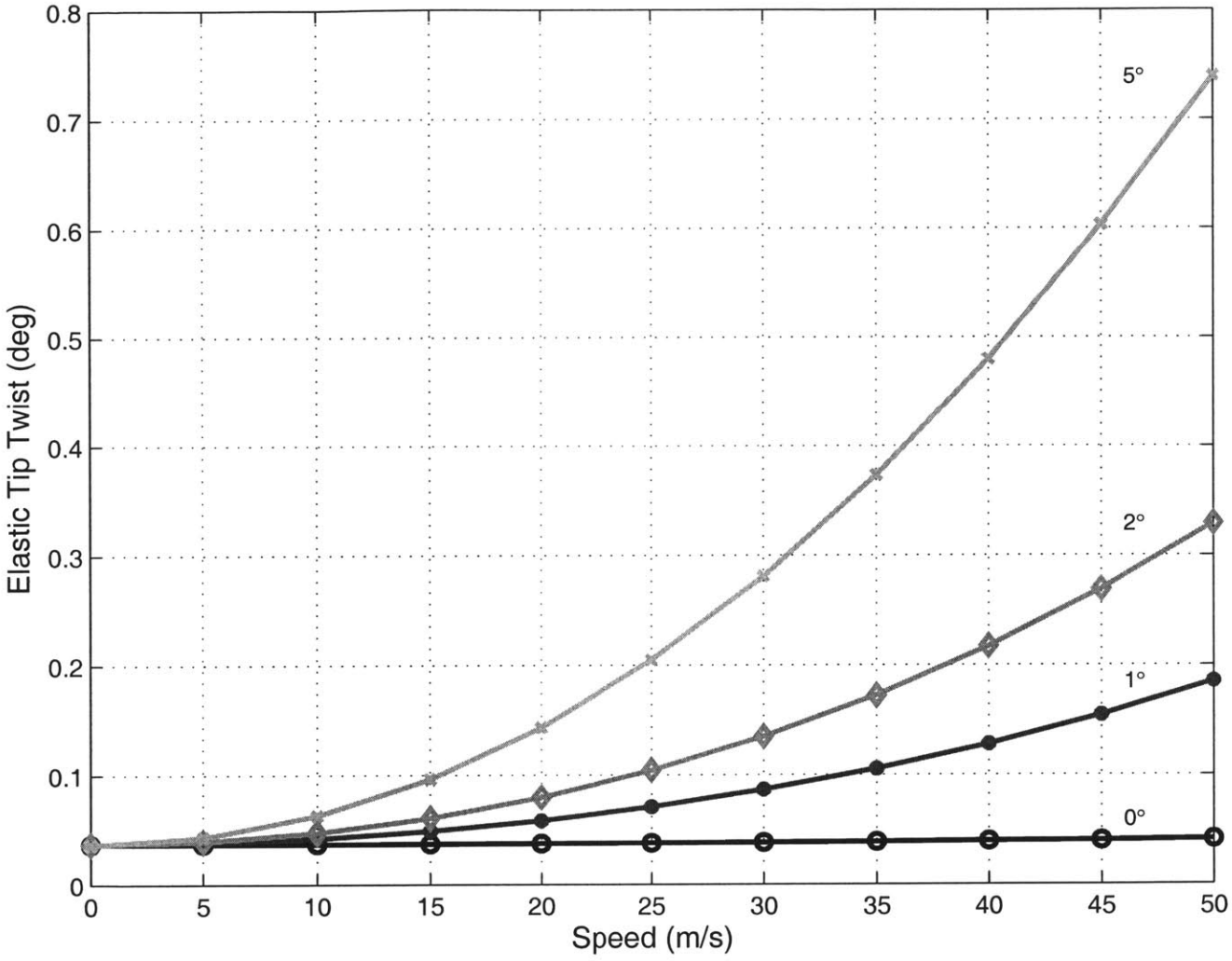

Figure 2-33: Elastic tip twist for increasing speed at different root angles of attack

graphically for the first four modes in Figure 2-34.

Table 2.10: Dynamic properties at $U = 30$ m/s

Angle of Attack		0°	1°	2°	5°
Tip Deflection		-0.005 m	0.02 m	0.04 m	0.10 m
Mode Shapes	1^{st} Bending	8	8	8	8
	1^{st} Chordwise Bending	51	51	50	45
	2^{nd} Bending	54	54	54	54
	1^{st} Torsional	97	97	98	104
	3^{rd} Bending	161	161	161	161
	2^{nd} Torsional	299	299	300	305

The three-layer design also shows a change in the chordwise bending and torsional modes for changes in root angle of attack. As the root angle of attack is increased the frequencies for the 1^{st} chordwise bending mode decrease and the frequencies for the 1^{st} torsional mode increase. The bending modes remain unchanged.

A similar behavior is seen when the speed is varied for a constant root angle of attack. This is illustrated in Table 2.11 and Table 2.12. This data is also provided graphically for the first four modes in Figure 2-35 and Figure 2-36.

Table 2.11: Dynamic properties at root angle of attack = 2°

Speed		$30m/s$	$35m/s$	$40m/s$	$45m/s$
Tip Deflection		0.04 m	0.06 m	0.08 m	0.10 m
Mode Shapes	1^{st} Bending	8	8	8	8
	1^{st} Chordwise Bending	50	49	48	46
	2^{nd} Bending	54	54	54	54
	1^{st} Torsional	98	99	101	103
	3^{rd} Bending	161	161	161	161
	2^{nd} Torsional	300	301	302	305

The flutter speeds for varying angles of attack are given in Figure 2-37. As expected, the addition of the third layer of E-glass resulted in an increase in the flutter speed.

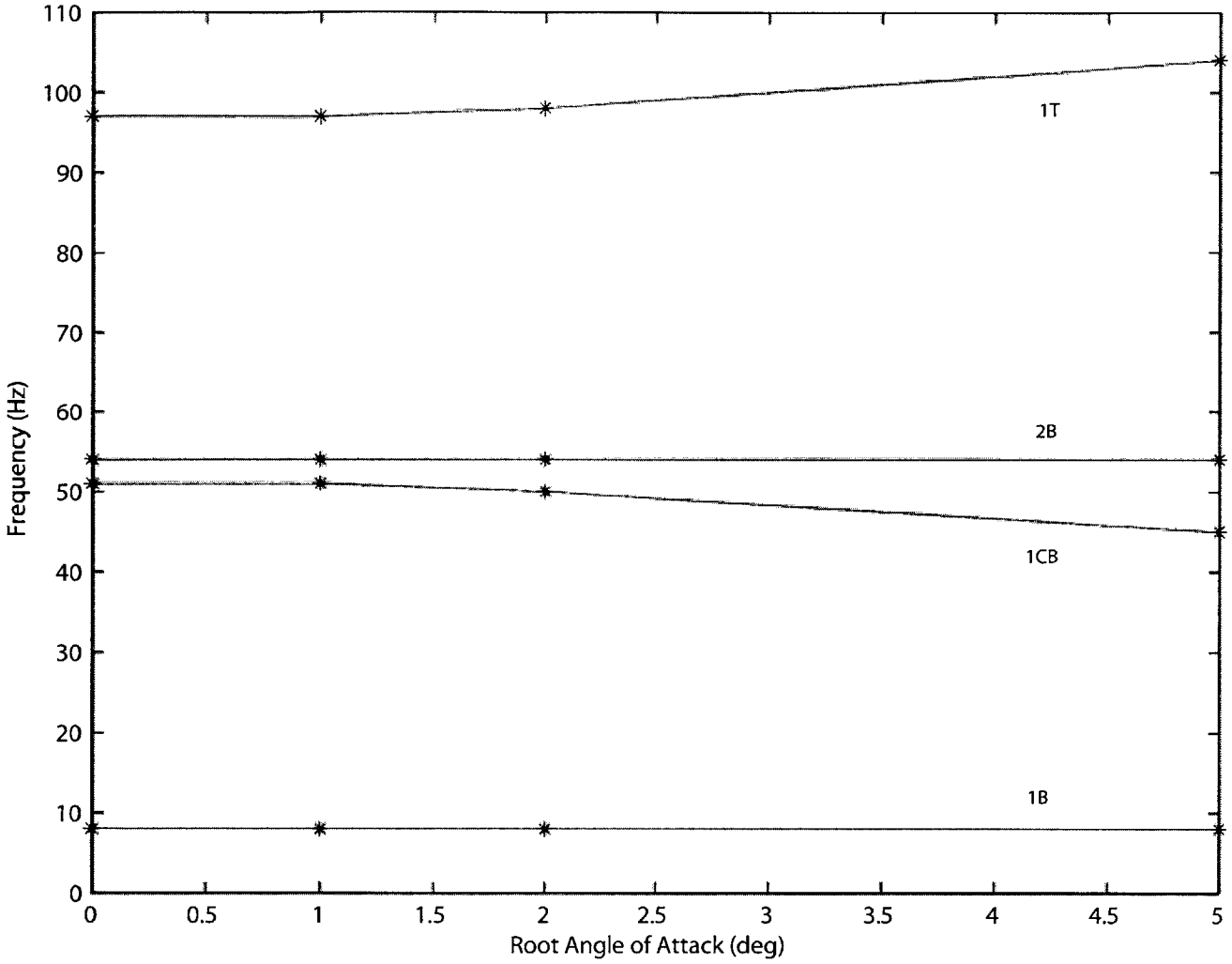

Figure 2-34: Frequency change due to root angle of attack change at U = 30 m/s

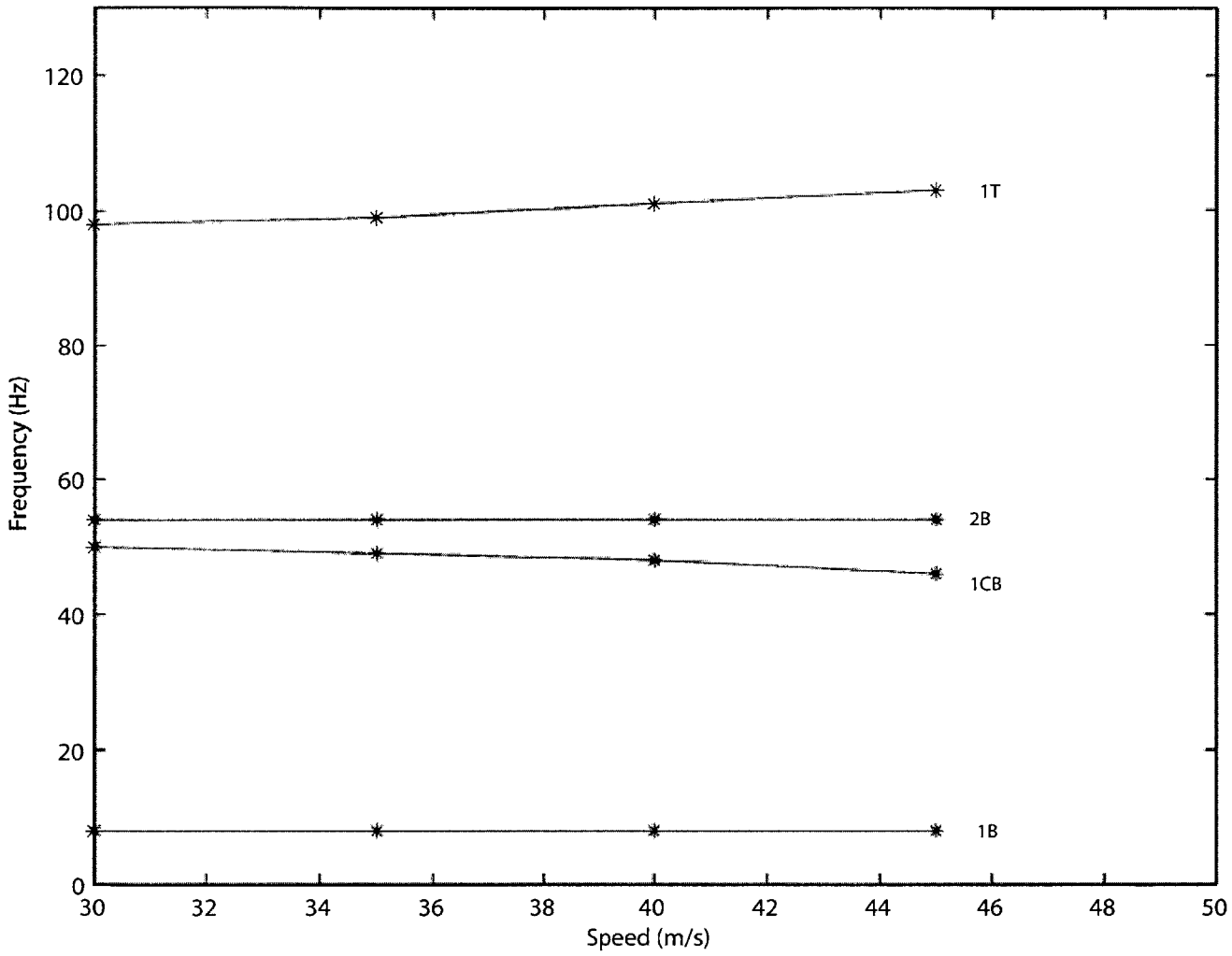

Figure 2-35: Frequency change due to change in speed for 2° root angle of attack

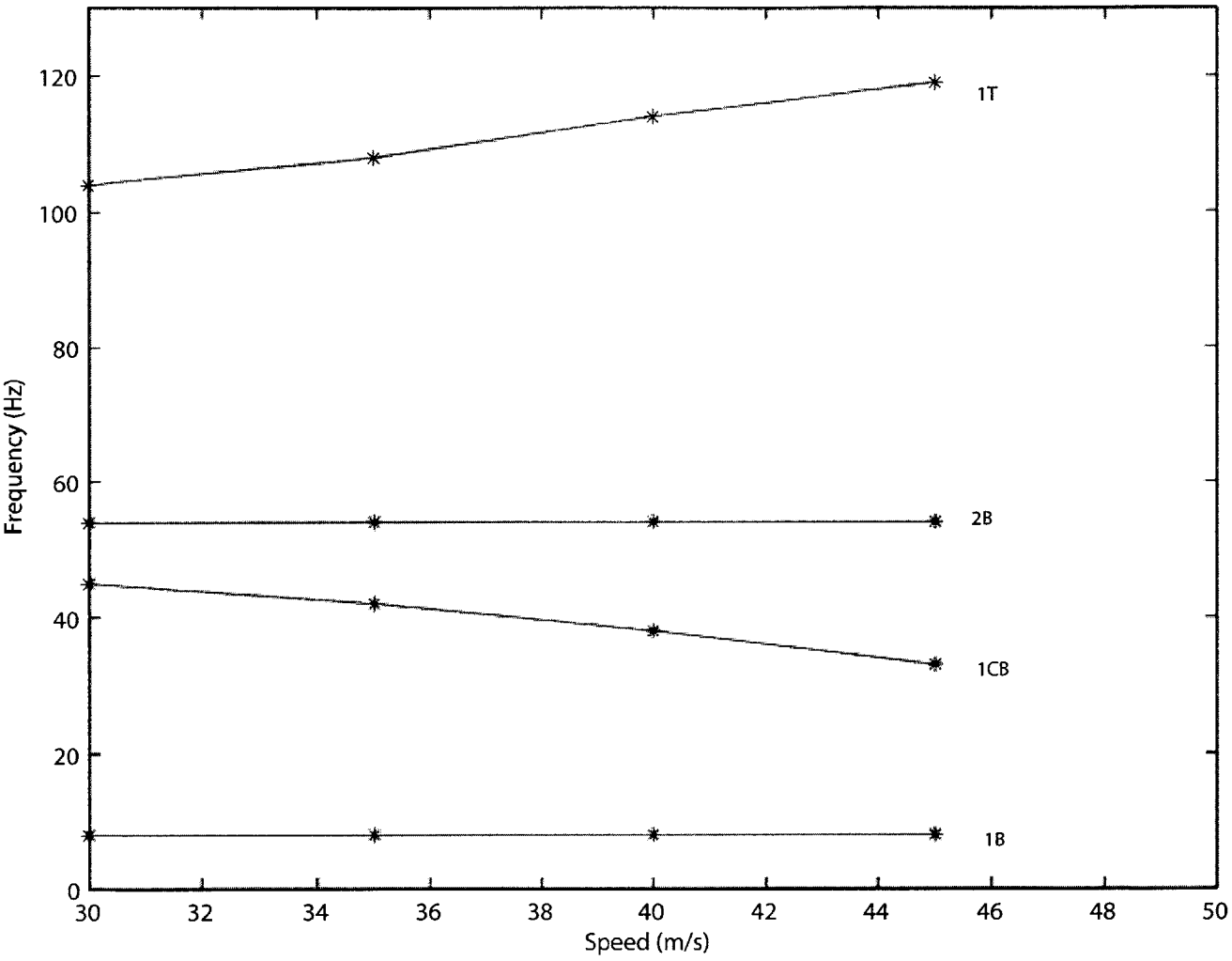

Figure 2-36: Frequency change due to change in speed for 5° root angle of attack

Table 2.12: Dynamic properties at root angle of attack = 5°

Speed		$30m/s$	$35m/s$	$40m/s$	$45m/s$
Tip Deflection		0.10 m	0.15 m	0.20 m	0.25 m
Mode Shapes	1^{st} Bending	8	8	8	8
	1^{st} Chordwise Bending	45	42	38	33
	2^{nd} Bending	54	54	54	54
	1^{st} Torsional	104	108	114	119
	3^{rd} Bending	161	161	161	160
	2^{nd} Torsional	305	308	308	303

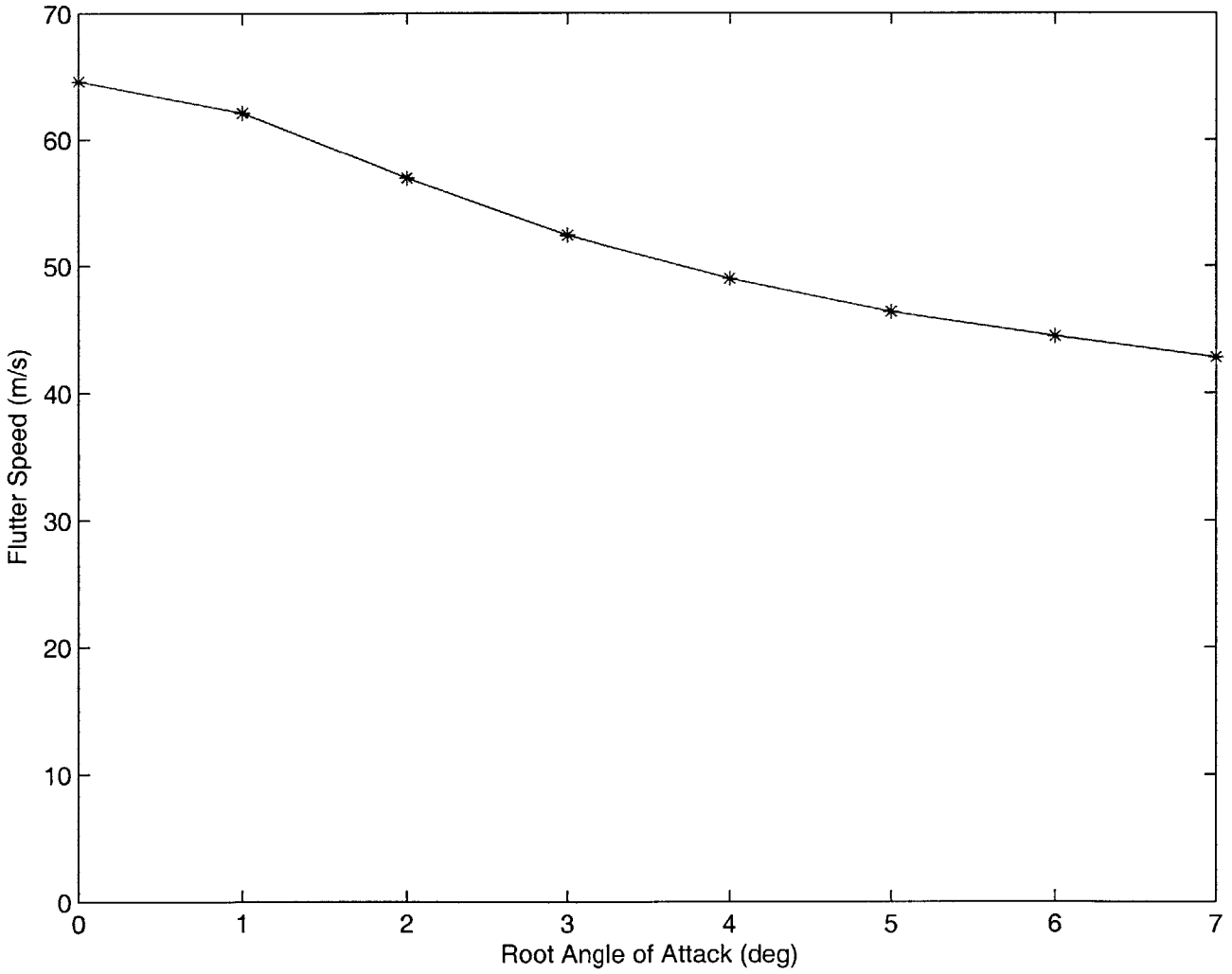

Figure 2-37: Flutter speeds for three-layer design

Zero-Degree Root Angle of Attack

The flutter speed for 0° root angle of attack is determined to be 64.6 m/s from the root locus plot provided in Figure 2-38. The unstable mode is the fourth mode, which cooresponds to the 1^{st} torsional mode. This is the same as was seen in the two-layer case. The first six mode shapes at flutter speed for this wing are shown in Figure 2-39.

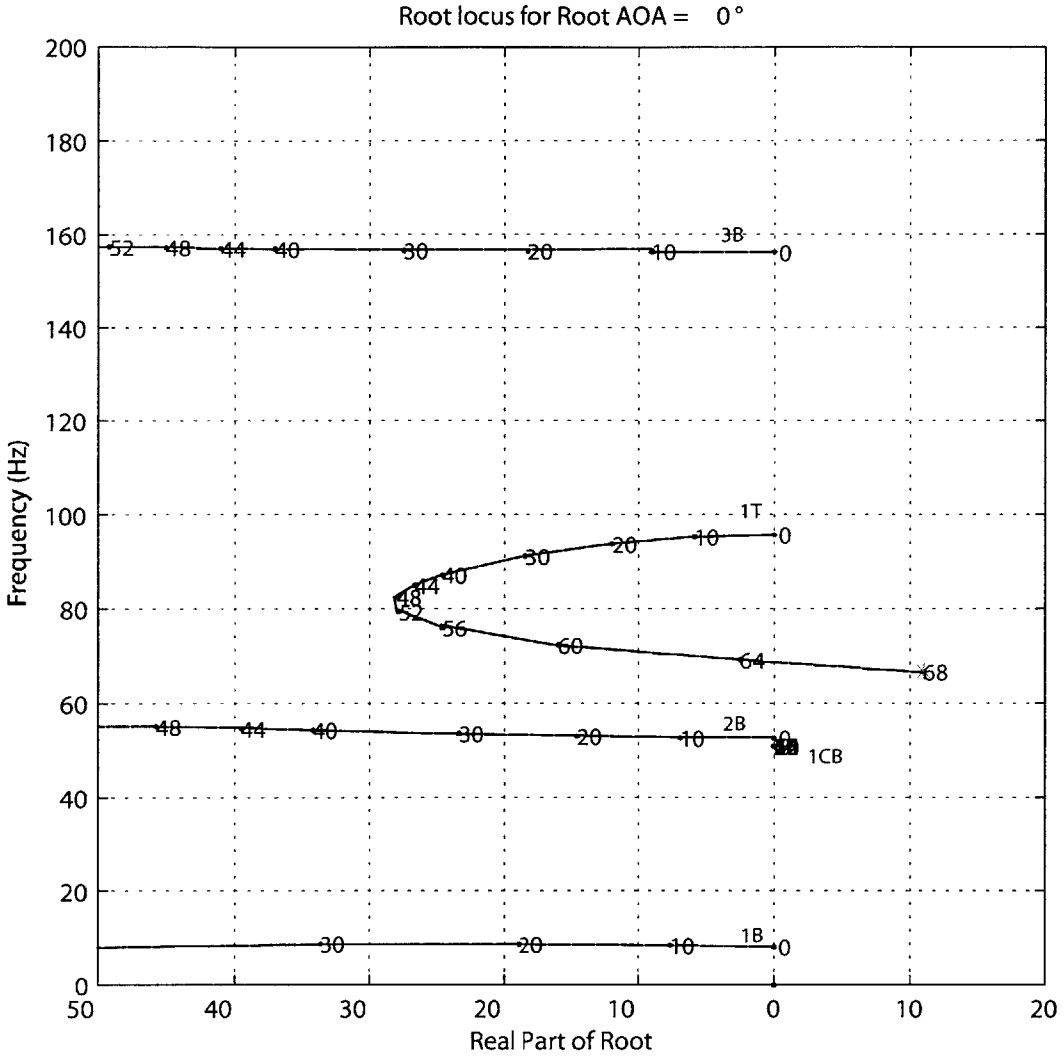

Figure 2-38: Root locus plot for 0° root angle of attack

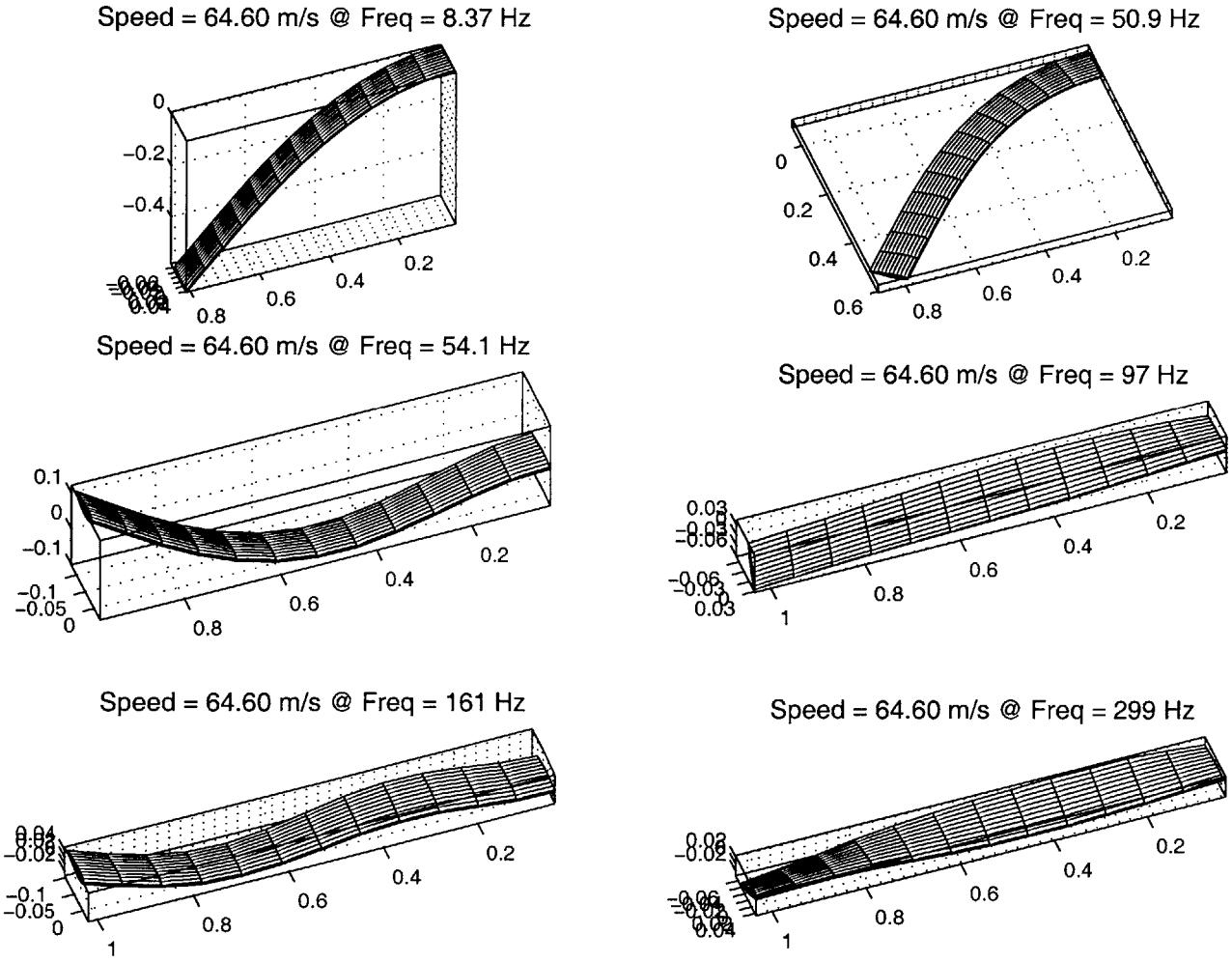

Figure 2-39: Mode shapes for three-layer design at 0° root angle of attack and at its corresponding flutter speed 64.6 m/s

One-Degree Root Angle of Attack

The flutter speed for the 1° root angle of attack is 62.1 m/s. This can be seen on the root locus plot provided in Figure 2-40. The mode of instability is the second mode. This mode is primarily the first chordwise bending. However, the forces due to air pressure on the tilted wing result in some torsion being present as well. The first six mode shapes for this case are provided in Figure 2-41.

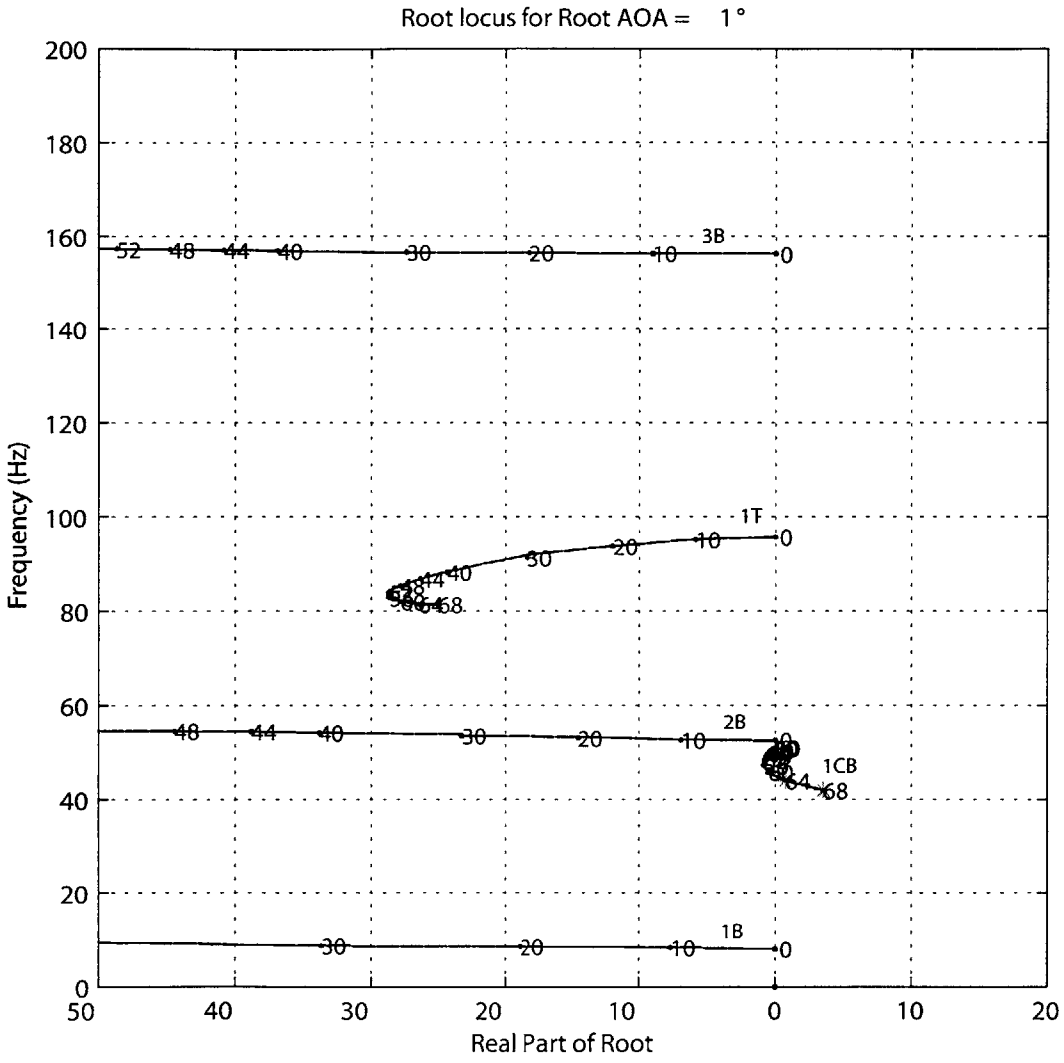

Figure 2-40: Root locus plot for 1° root angle of attack

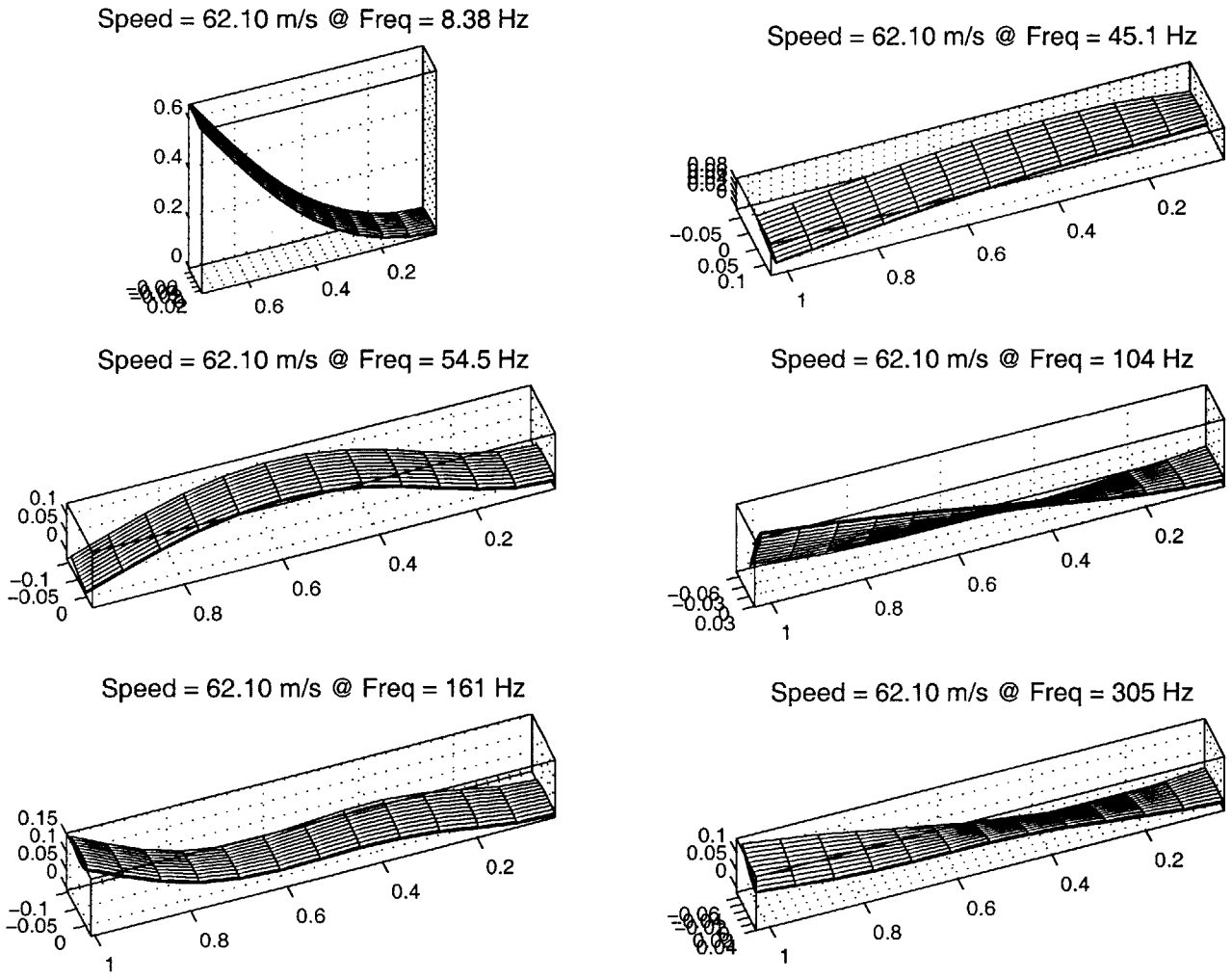

Figure 2-41: Mode shapes for three-layer design at 1° root angle of attack and at its corresponding flutter speed of 62.1 m/s

When this wing is flown at 10% above the predicted flutter speed, the wing enters into a LCO. The tip deflections and the tip twist are plotted for this case up to 1 second. These plots are provided in Figure 2-42 thru Figure 2-44.

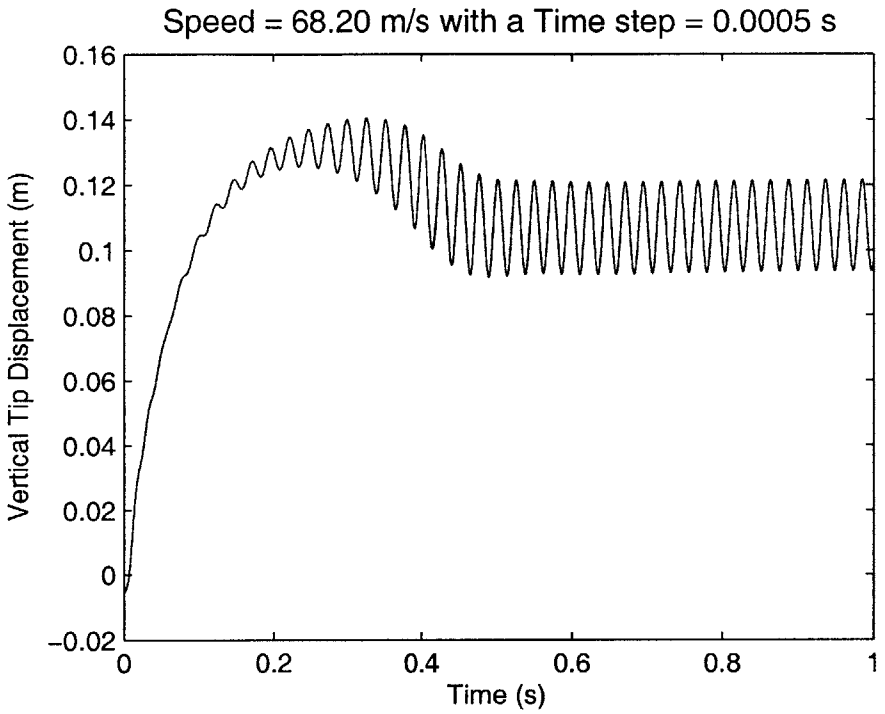

Figure 2-42: Nonlinear time simulation of the wing vertical tip displacement at 10% above its flutter speed (1° root angle of attack) for the three-layer design

A strain analysis was performed on the wing when it was at its maximum deflection. This occurs during the initial rise shown in Figure 2-42. The maximum tensile strain is 2697 μm/m and the maximum shear strain is -1765 μm/m. Both occur at the outer ply of the bottom part of the airfoil at the root of the wing. These results are summarized in Figure 2-45. These strains result in a margin of safety of 2.71 for tension and 7.50 for torsion.

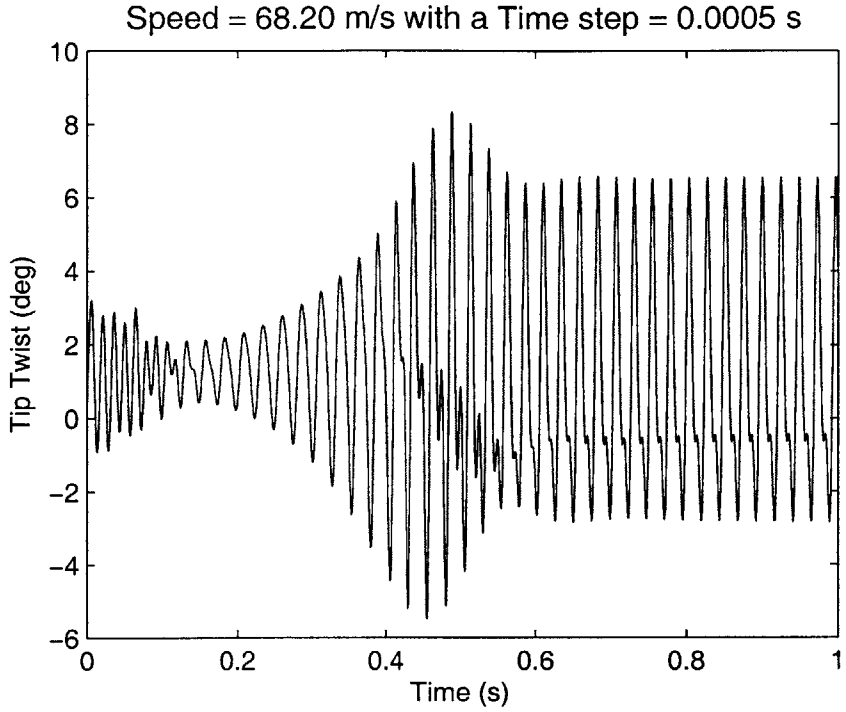

Figure 2-43: Nonlinear time simulation of the wing tip twist at 10% above its flutter speed (1° root angle of attack) for the three-layer design

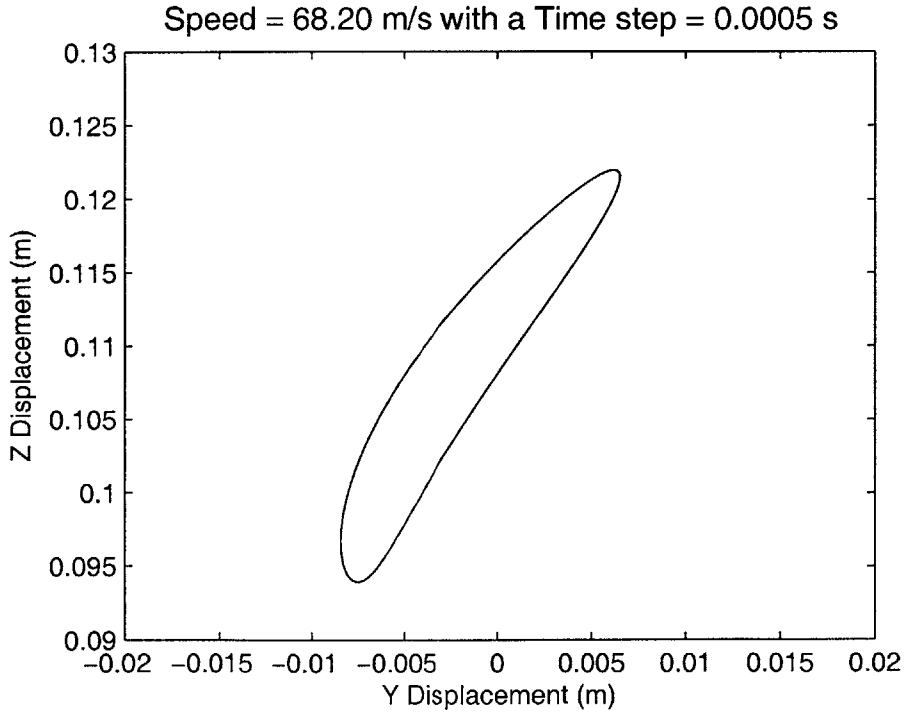

Figure 2-44: Nonlinear time simulation of the wing tip motion at 10% above its flutter speed (1° root angle of attack) for the three-layer design

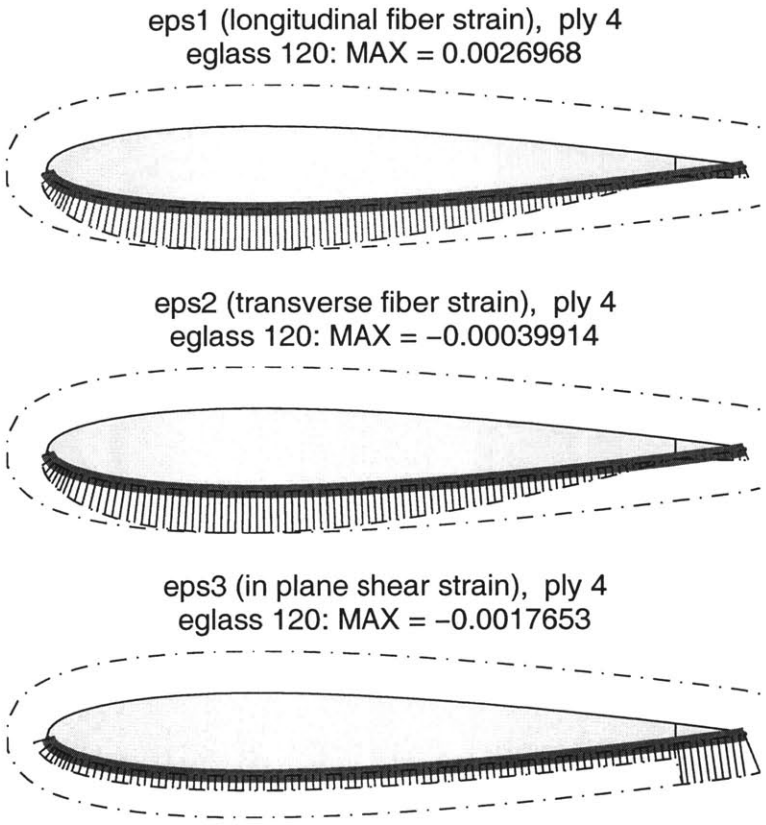

Figure 2-45: Maximum ply strain reached at 10% above flutter speed of 1° root angle of attack for the three-layer design

Two-Degree Root Angle of Attack

The flutter speed for the 2° root angle of attack is 56.9 m/s. This can be seen on the root locus plot provided in Figure 2-46. The second mode is again the mode which crosses the stability axes. The larger tip deflections and tip twists observed for the high angles of attack cause this mode to turn over and go unstable faster. The first six mode shapes for this case are provided in Figure 2-47.

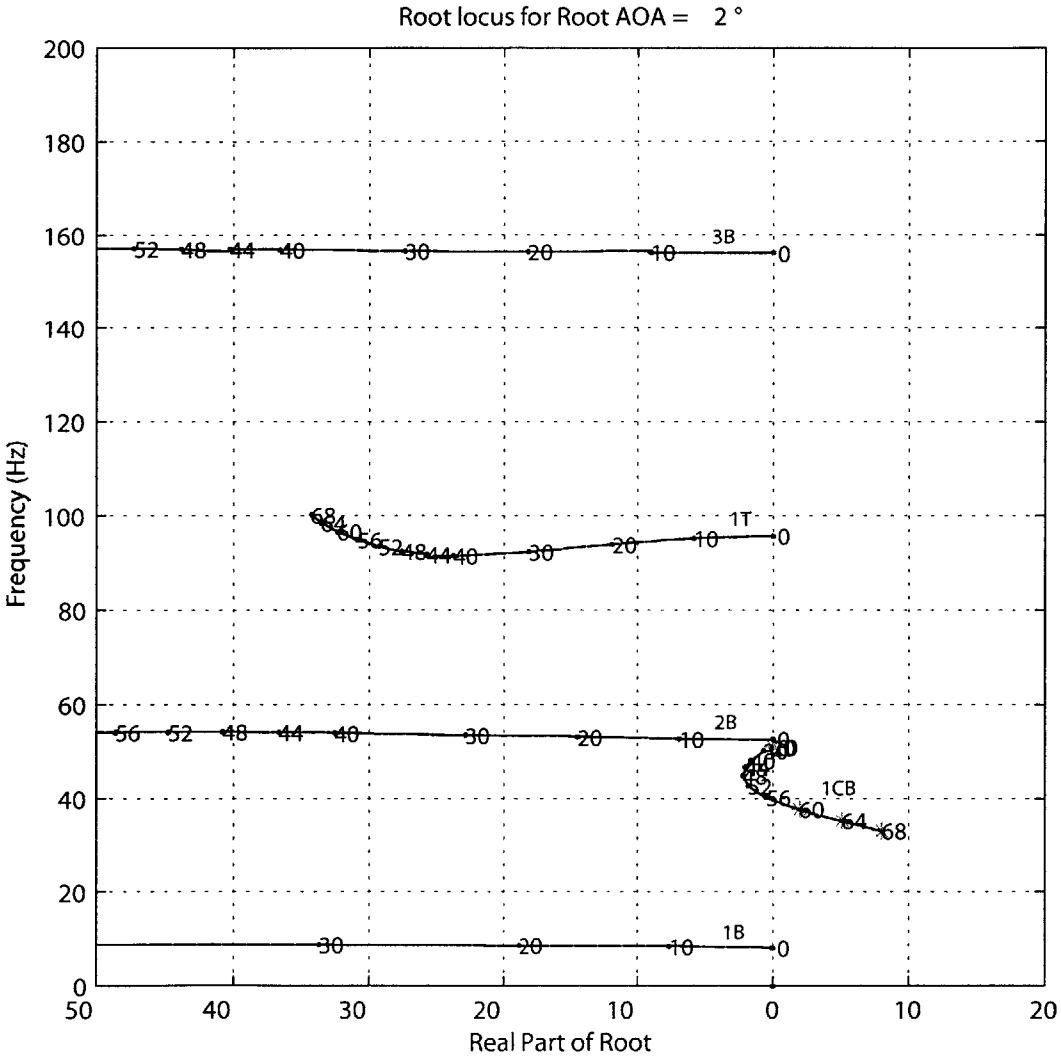

Figure 2-46: Root locus plot for 2° root angle of attack

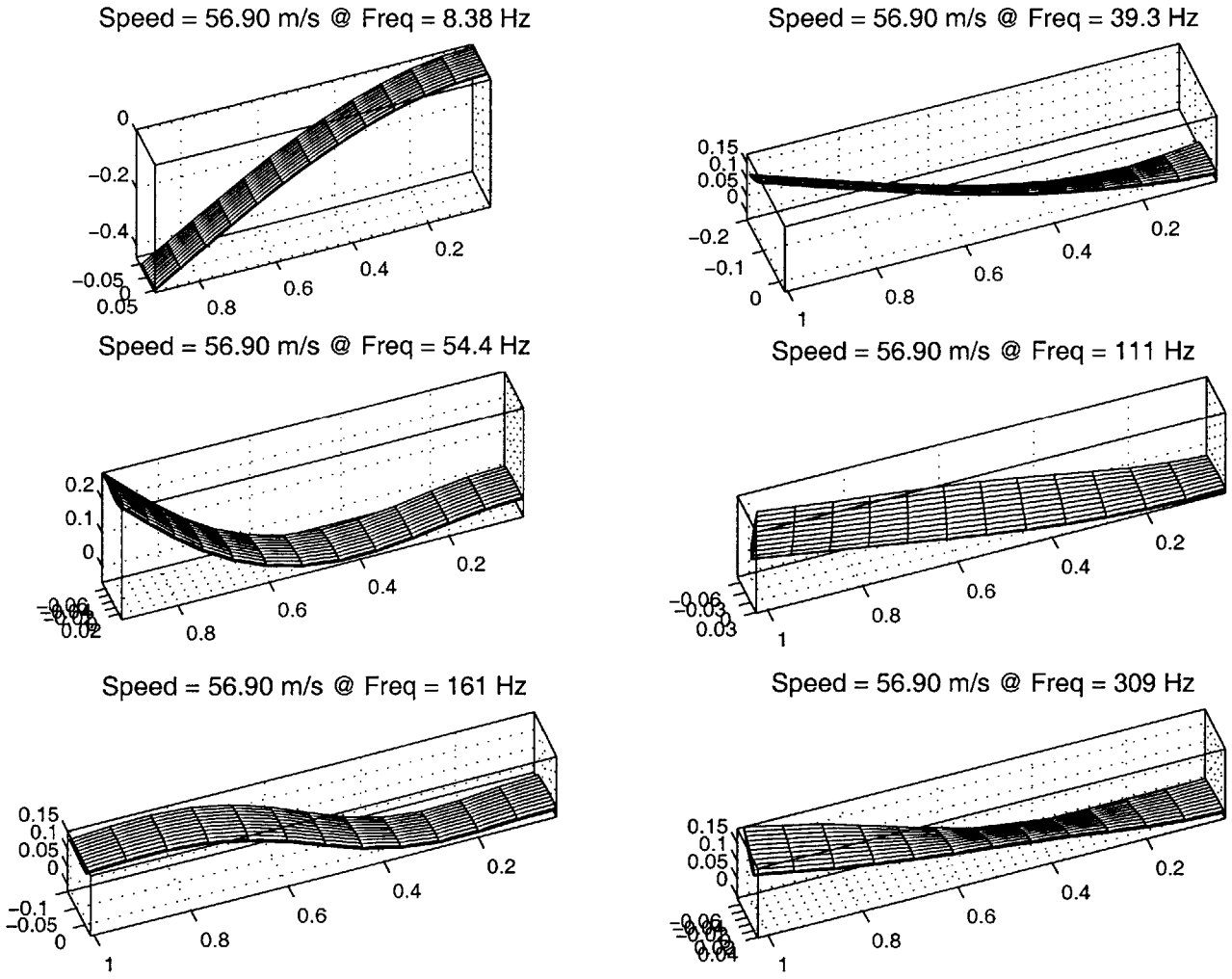

Figure 2-47: Mode shapes for three-layer design at 2° root angle of attack and at its corresponding flutter speed of 56.9 m/s

When this wing is flown at 10% above the predicted flutter speed, the wing enters into a LCO. The tip deflections and the tip twist are plotted for this case up to 1 second. These plots are provided in Figure 2-48 thru Figure 2-50.

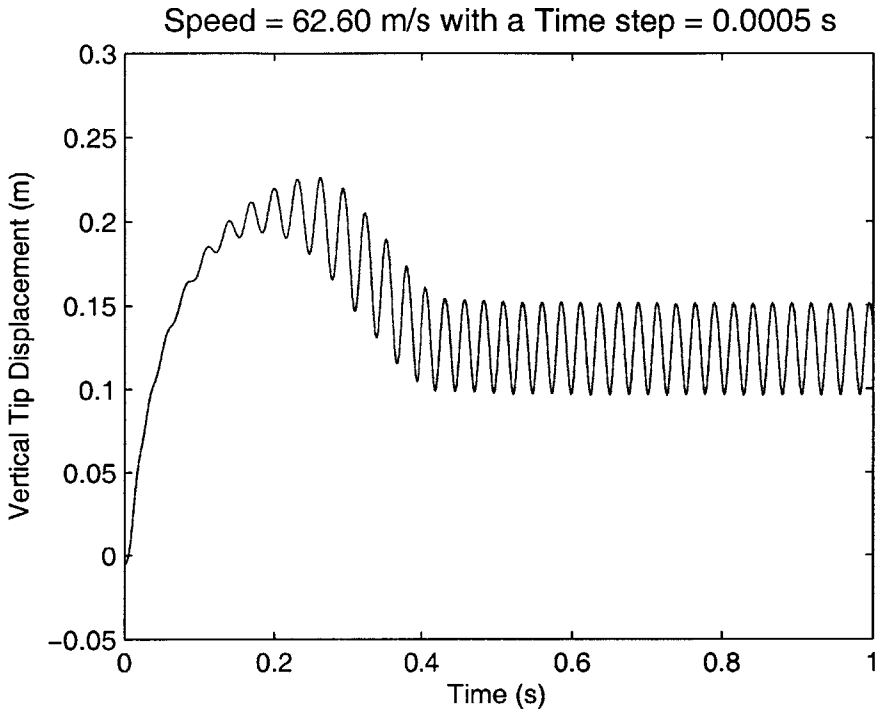

Figure 2-48: Nonlinear time simulation of the wing vertical tip displacement at 10% above its flutter speed (2° root angle of attack) for the three-layer design

A strain analysis was performed on the wing when it was at its maximum deflection. This occurs during the initial rise shown in Figure 2-48. The maximum tensile strain is 4421 μm/m and the maximum shear strain is -4079 μm/m. Both occur at the outer ply of the bottom part of the airfoil at the root of the wing. These results are summarized in Figure 2-51. These strains result in a margin of safety of 1.26 and 2.68, respectively.

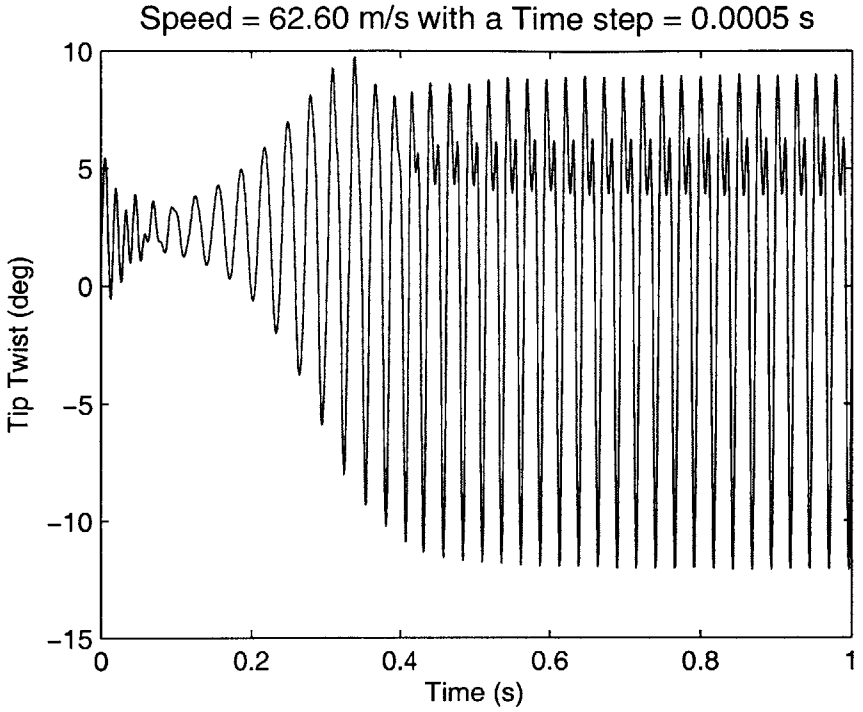

Figure 2-49: Nonlinear time simulation of the wing tip twist at 10% above its flutter speed (2° root angle of attack) for the three-layer design

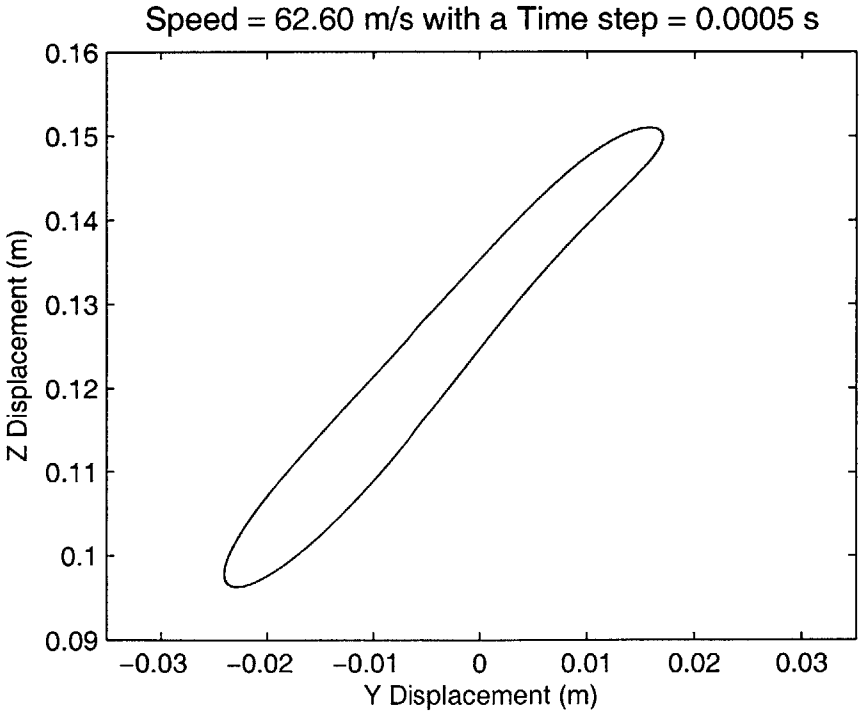

Figure 2-50: Nonlinear time simulation of the wing tip motion at 10% above its flutter speed (2° root angle of attack) for the three-layer design

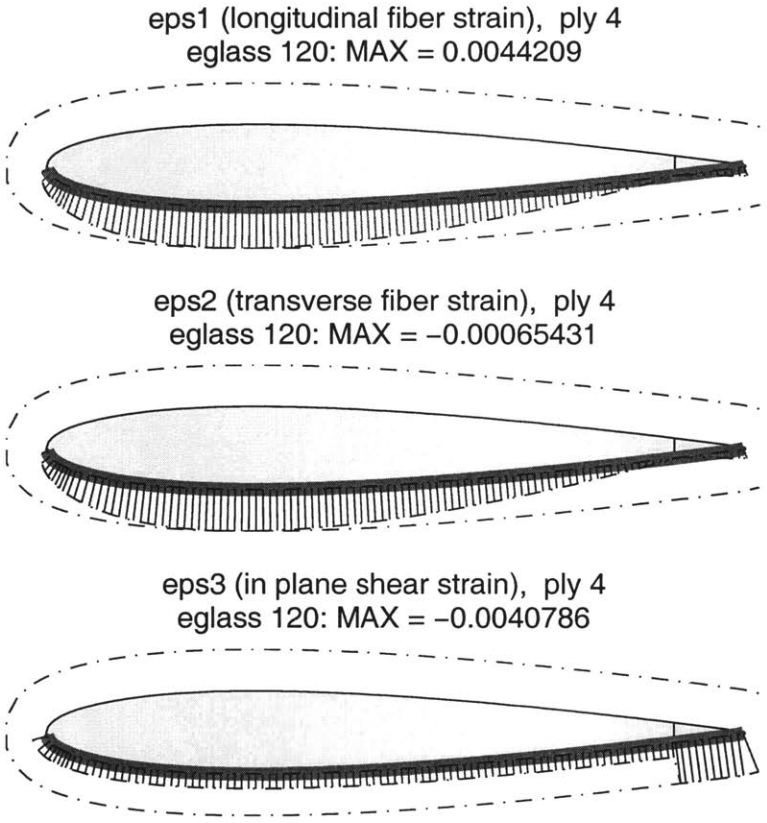

Figure 2-51: Maximum ply strain reached at 10% above flutter speed of 2° root angle of attack for the three-layer design

Five-Degree Root Angle of Attack

The flutter speed for the 5° root angle of attack is 46.4 m/s. This can be seen on the root locus plot provided in Figure 2-52. This plot shows the mode of instability is again the 1^{st} chordwise bending mode (mode 2). Again the increase in angle of attack results in the wing becoming unstable at lower speeds. The 1^{st} torsion (mode 4) and 3^{rd} bending (mode 5) are also starting to interact with each other, causing the torsion mode to head to the instability axes. The first six mode shapes for this case are provided in Figure 2-53.

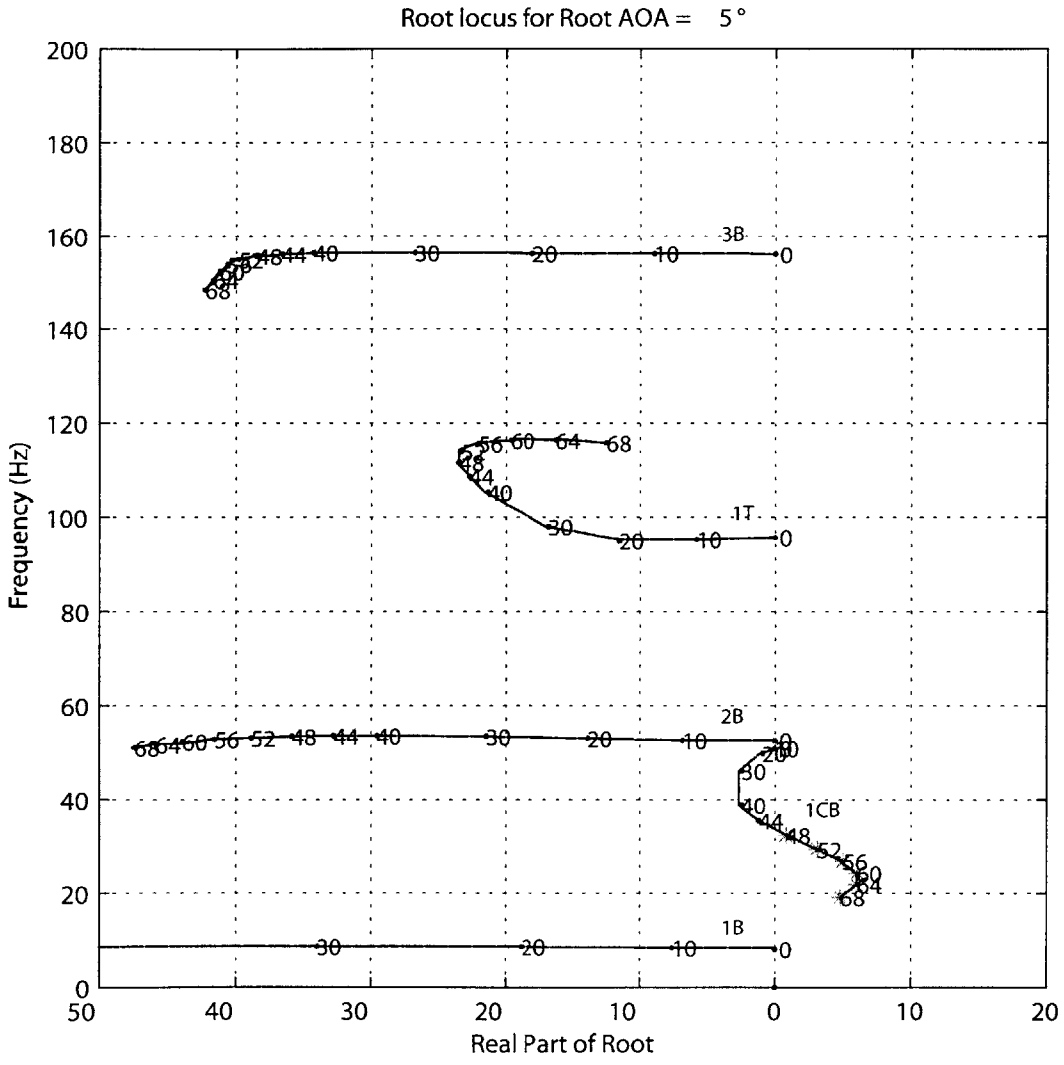

Figure 2-52: Root locus plot for 5° root angle of attack

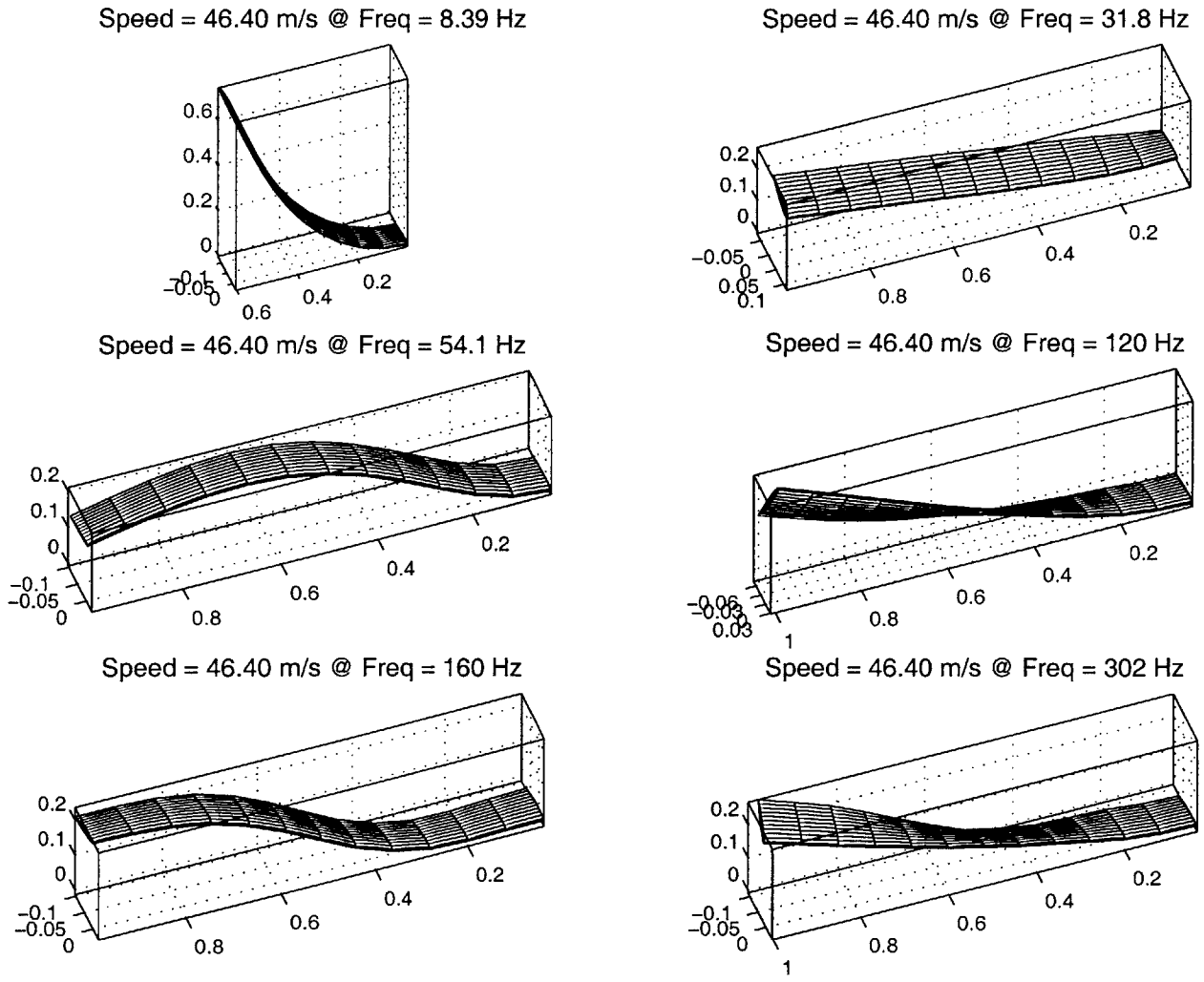

Figure 2-53: Mode shapes for three-layer design at 5° root angle of attack and at its corresponding flutter speed of 46.4 m/s

When this wing is flown at 10% above the predicted flutter speed, the wing enters into a LCO. The tip deflections and the tip twist are plotted for this case up to 1 second. These plots are provided in Figure 2-54 thru Figure 2-56.

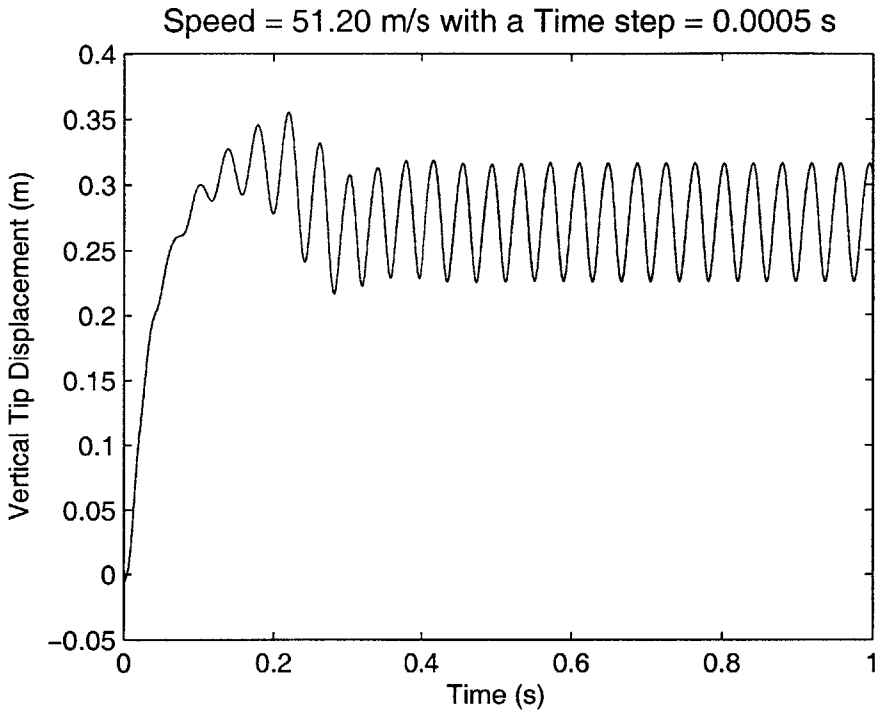

Figure 2-54: Nonlinear time simulation of the wing vertical tip displacement at 10% above its flutter speed (5° root angle of attack) for the three-layer design

A strain analysis was performed on the wing when it was at its maximum deflection. This occurs during the initial rise shown in Figure 2-54. The maximum tensile strain is 7374 μm/m and the maximum shear strain is -6799 μm/m. Both occur at the outer ply of the bottom part of the airfoil at the root of the wing. These details are summarized in Figure 2-57. These strains result in a margin of safety of 0.36 and 1.21, respectively.

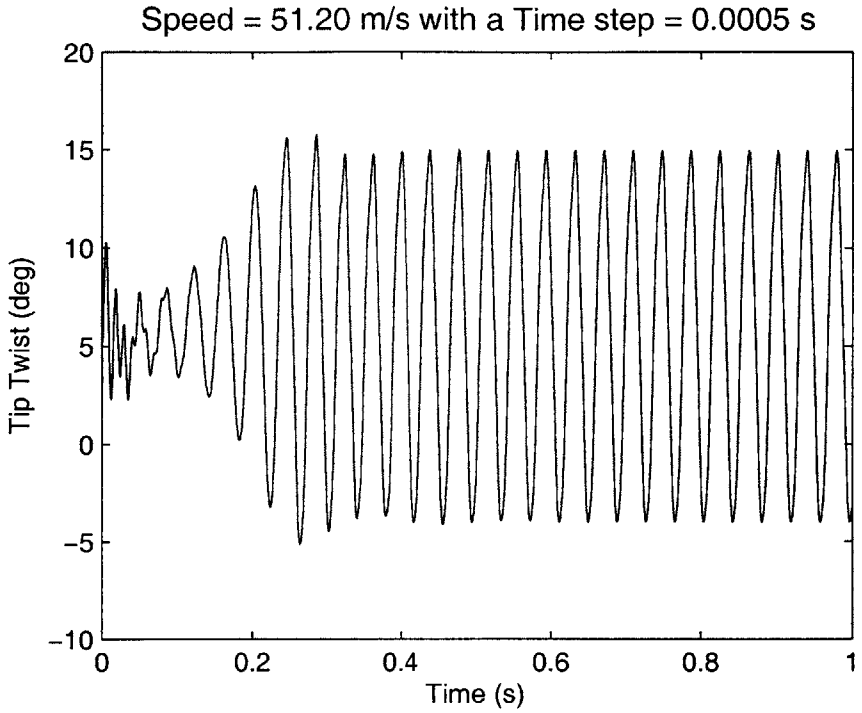

Figure 2-55: Nonlinear time simulation of the wing tip twist at 10% above its flutter speed (5° root angle of attack) for the three-layer design

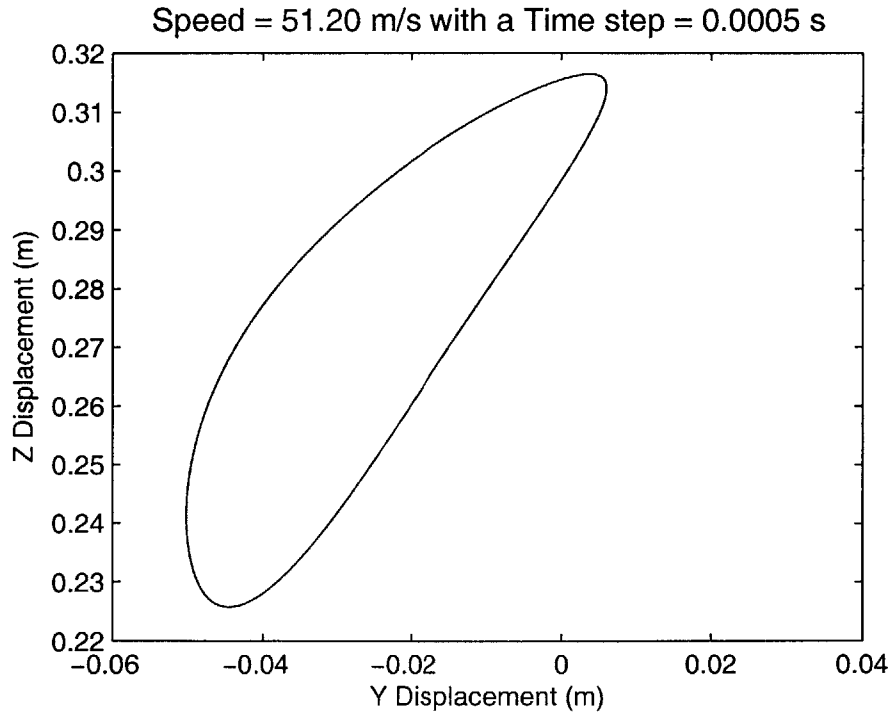

Figure 2-56: Nonlinear time simulation of the wing tip motion at 10% above its flutter speed (5° root angle of attack) for the three-layer design

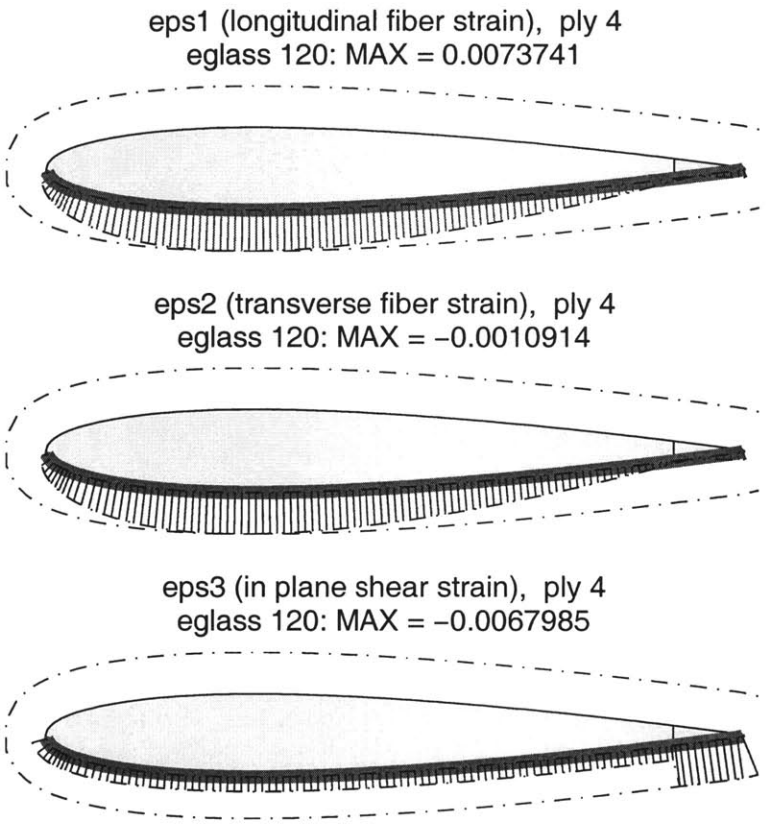

Figure 2-57: Maximum ply strain reached at 10% above flutter speed of 5° root angle of attack

The following is a table to summarize the strain analysis for the different cases.

Table 2.13: Summary of Strain Analysis Results

Angle of Attack		Two-Layer Results	Three-Layer Results
1°	tension	2660 μ m/m	2697 μ m/m
	torsion	-769 μ m/m	-1765 μ m/m
2°	tension	4484 μ m/m	4421 μ m/m
	torsion	-2726 μ m/m	-4079 μ m/m
5°	tension	7405 μ m/m	7374 μ m/m
	torsion	-5018 μ m/m	-6799 μ m/m

2.4 Nastran Comparison

To ensure that the wing would survive the loadings in the tunnel, a stress analysis was performed using MSC.Nastran finite element code. Since the MATLAB code from [3] was not yet validated experimentally, this would provide added assurance that the stress and strain data predicted by the MATLAB code is correct. Figure 2-58 provides a close-up of the finite element model mesh. The wing was discretized using 5550 elements. The foam was modeled as 4-noded solid elements and the composite skin was modeled as 4-noded shell elements.

The worse stress case scenerio for the three-layer design is the 5° root angle of attack case. The MATLAB code was used to provide static deflection values for the wing at 51.15 m/s, which is 10% above the predicted flutter speed. The x,y,z displacements and pitch rotation for the wing were matched for two different cases: maximum vertical (z) displacement and maximum pitch rotation. This was achieved by applying varing forces distributed along the span of the wing at 25% of the chord and then forces to the leading and trailing edges to establish the desired rotation.

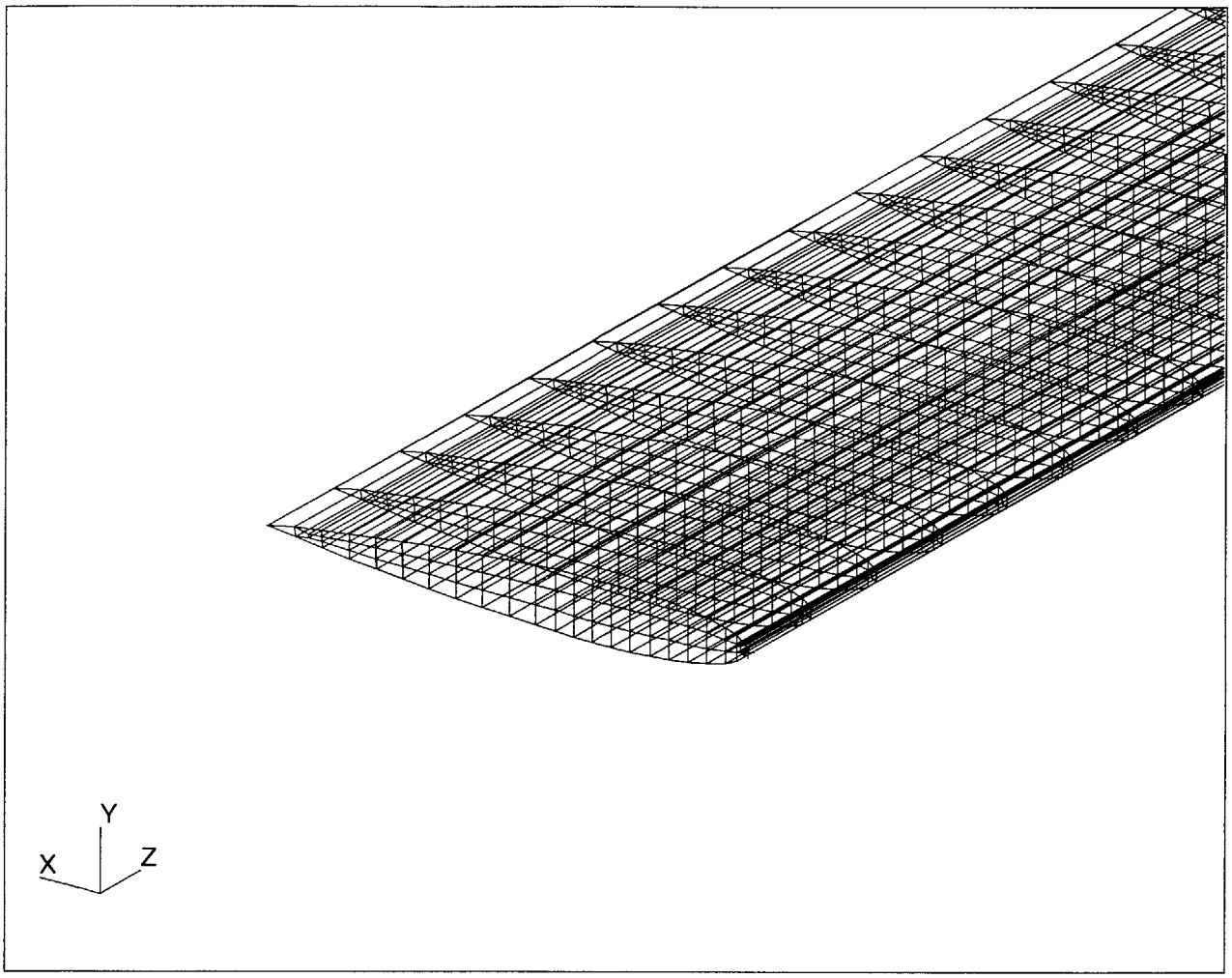

Figure 2-58: Finite element mesh of the three-layer design used in Nastran (5550 elements, 13617 degrees of freedom)

2.4.1 Case 1 - Maximum Vertical Displacement

This case matched the maximum vertical displacement predicted by the MATLAB code during the limit cycle oscillation. The original predicted values and the values determined in Nastran are provided in Table 2.14.

Table 2.14: Nastran Case 1: Displacements and Rotations

	MATLAB Prediction	Nastran Result
chordwise deflection	0.0034 m	0.0199 m
spanwise deflection	0.0603 m	0.0539 m
vertical deflection	0.3159 m	0.3126 m
pitch rotation	$-8.85°$	$-9.11°$

The MATLAB and Nastran displacement results match within 11%, except in the chordwise direction. The overall magnitude of the displacements are equivalent and the major contributors, vertical displacement and pitch rotation, are within 1% and 3%, respectively. Since the results show such high margins of safety (Equation 2.1), the analysis was considered adequate. The results from this case are summarized in Table 2.15 and fringe plots of the stress profiles are provided in Figure 2-59 through Figure 2-61.

Table 2.15: Nastran case 1: summary of results

	Maximum Strain	Margin of Safety
chordwise	2570 μm/m	6.4
spanwise	5430 μm/m	2.5
chord-span shear	-5740 μm/m	8.0

2.4.2 Case 2 - Maximum Pitch Rotation

This case matched the maximum pitch rotation predicted by the MATLAB code during the limit cycle oscillation. The original predicted values and the values determined in Nastran are provided in Table 2.16.

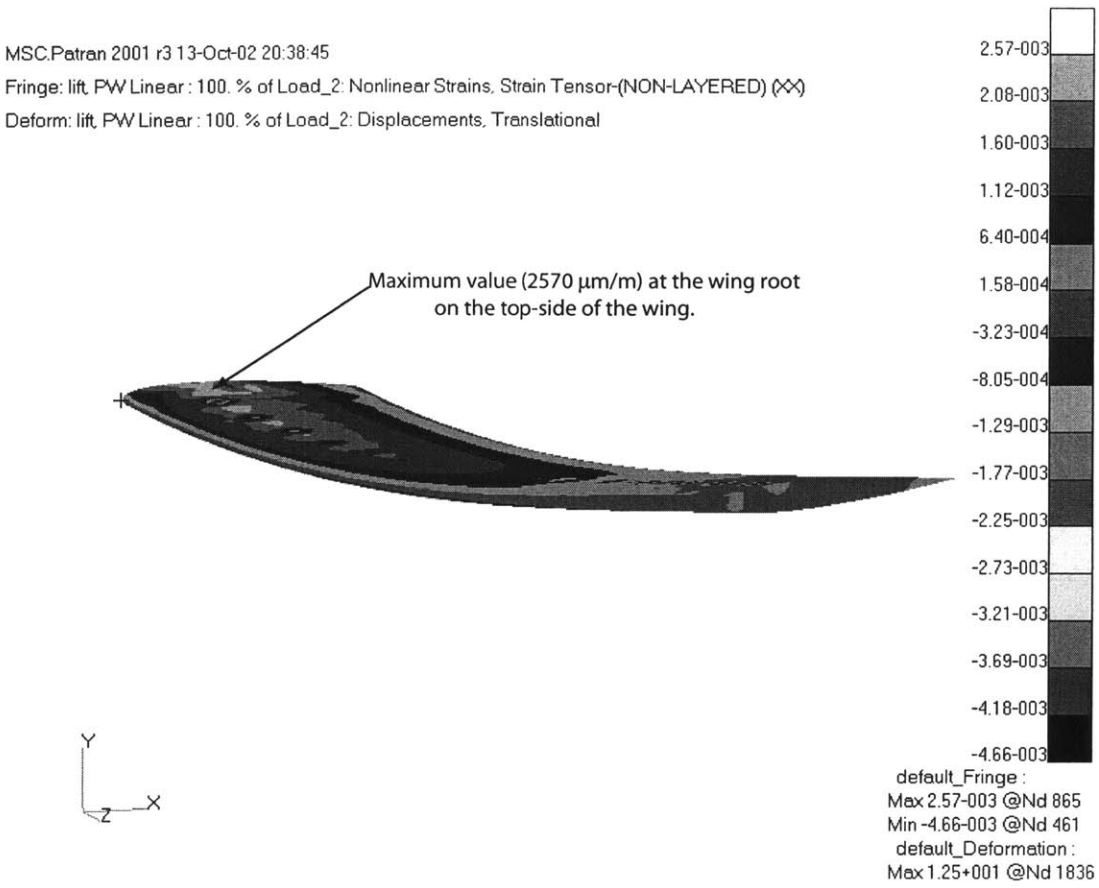

Figure 2-59: Nastran normal (chordwise) strain for 5° root angle of attack

Table 2.16: Nastran case 2: displacements and rotations

	MATLAB Prediction	Nastran Result
chordwise deflection	0.0502 m	0.0176 m
spanwise deflection	0.0370 m	0.0348 m
vertical deflection	0.2391 m	0.2520 m
pitch rotation	9.93°	10.5°

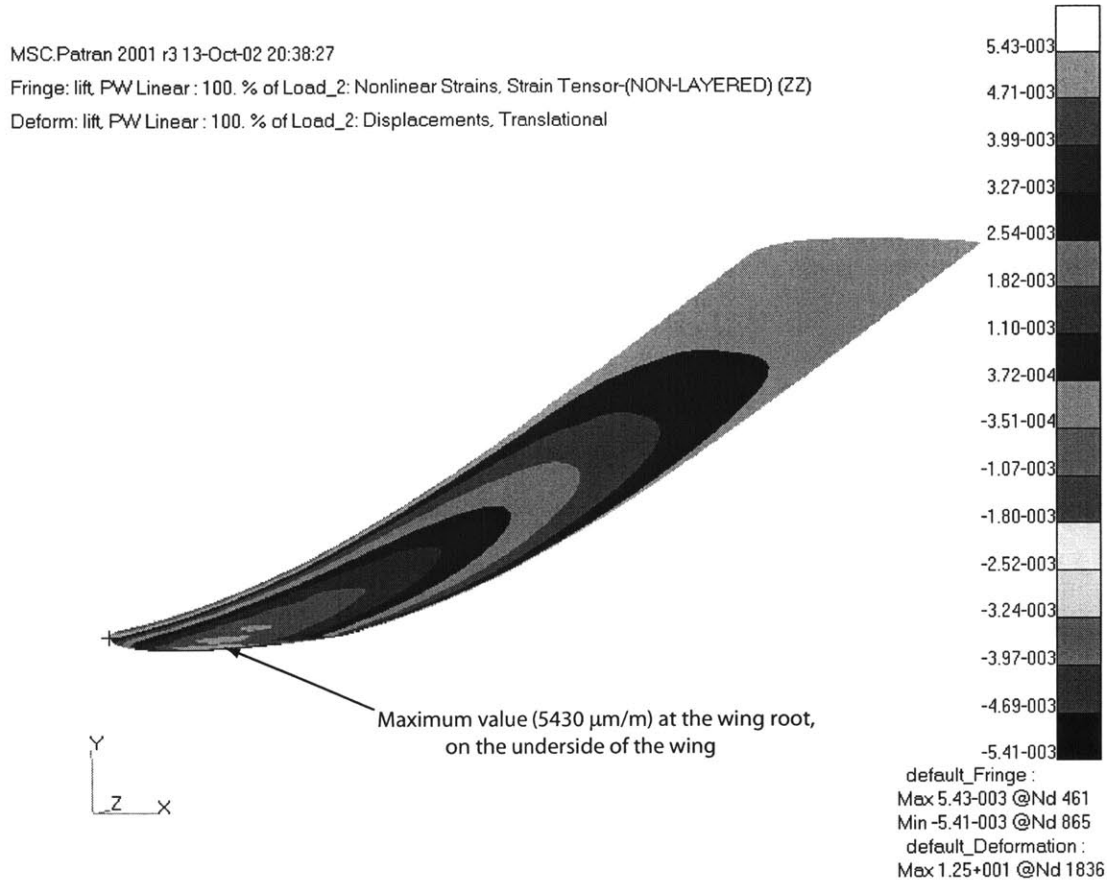

Figure 2-60: Nastran normal (spanwise) strain for 5° root angle of attack

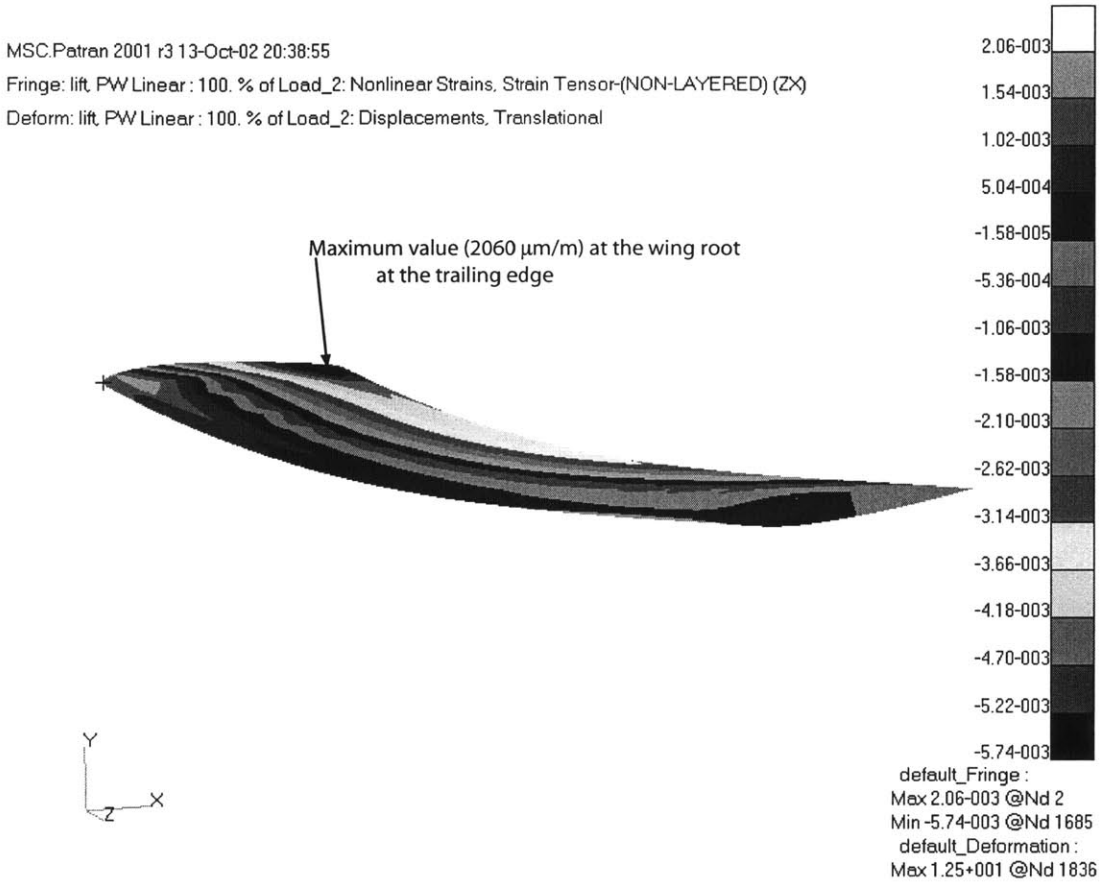

Figure 2-61: Nastran in-plane shear strain for 5° root angle of attack

Similar to the previous case, the MATLAB and Nastran displacements match within 6%. The overall magnitude of displacement is equivalent and the main contributors, vertical displacement and pitch rotation, are over-predicted. Again, although the Nastran displacements do not match the MATLAB exactly, the margins of safety are high enough to consider the values sufficient. The results from this case are summarized in Table 2.17 and fringe plots of the stress profiles are provided in Figure 2-62 through Figure 2-64.

Table 2.17: Nastran case 2: summary of results

	Maximum Strain	Margin of Safety
chordwise	2390 μm/m	6.9
spanwise	4960 μm/m	2.8
chord-span shear	7950 μm/m	5.5

2.5 Design Selection

The three-layer design was chosen for the wind tunnel model. This decision was based on the resulting predicted flutter speeds and on the resulting strains. The flutter speeds for the two-layer case were on average 16% lower than the three-layer design. However, the deflections experienced by the two-layer design ranged from 41% to 61% higher than the three-layer design. This resulted in an increase in the strain levels for the two-layer wing. To be safe, the increase in deflection and strain was considered more detrimental than an increase in the flutter speed. Therefore, the three layer design was chosen.

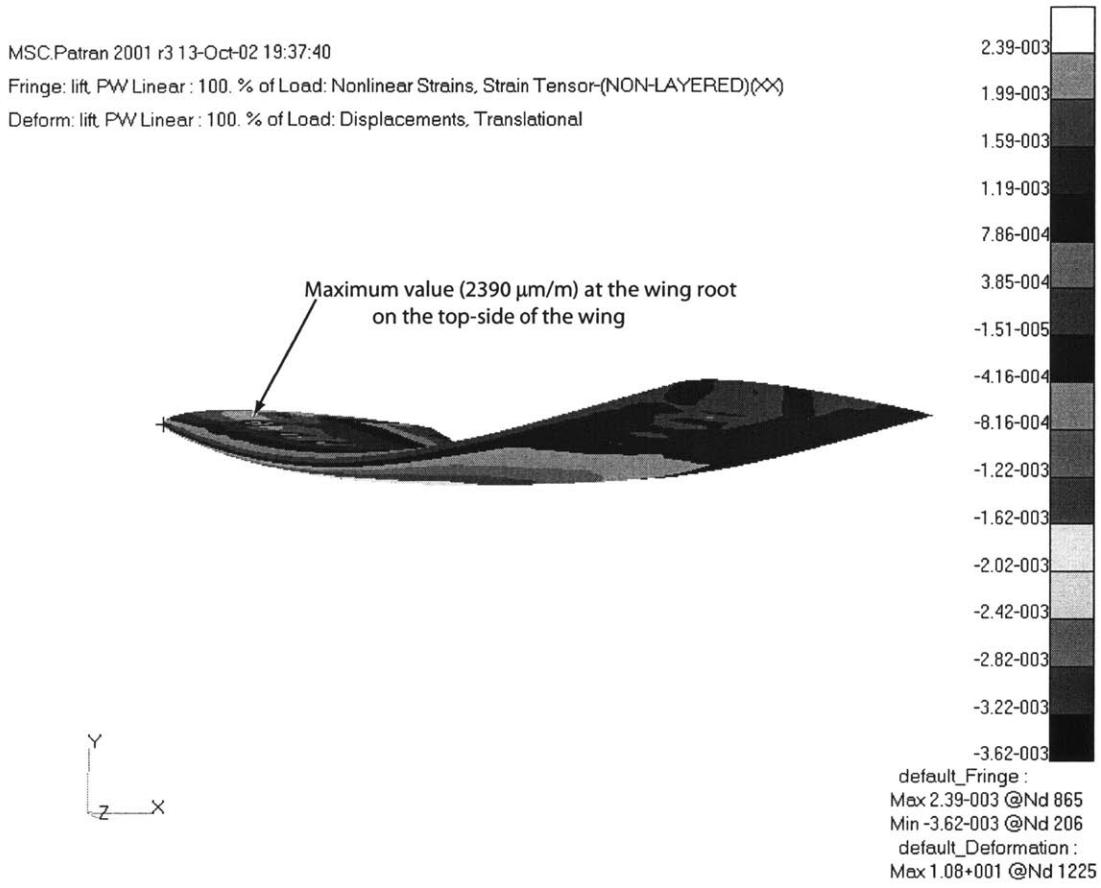

Figure 2-62: Nastran normal (chordwise) strain for 5° root angle of attack

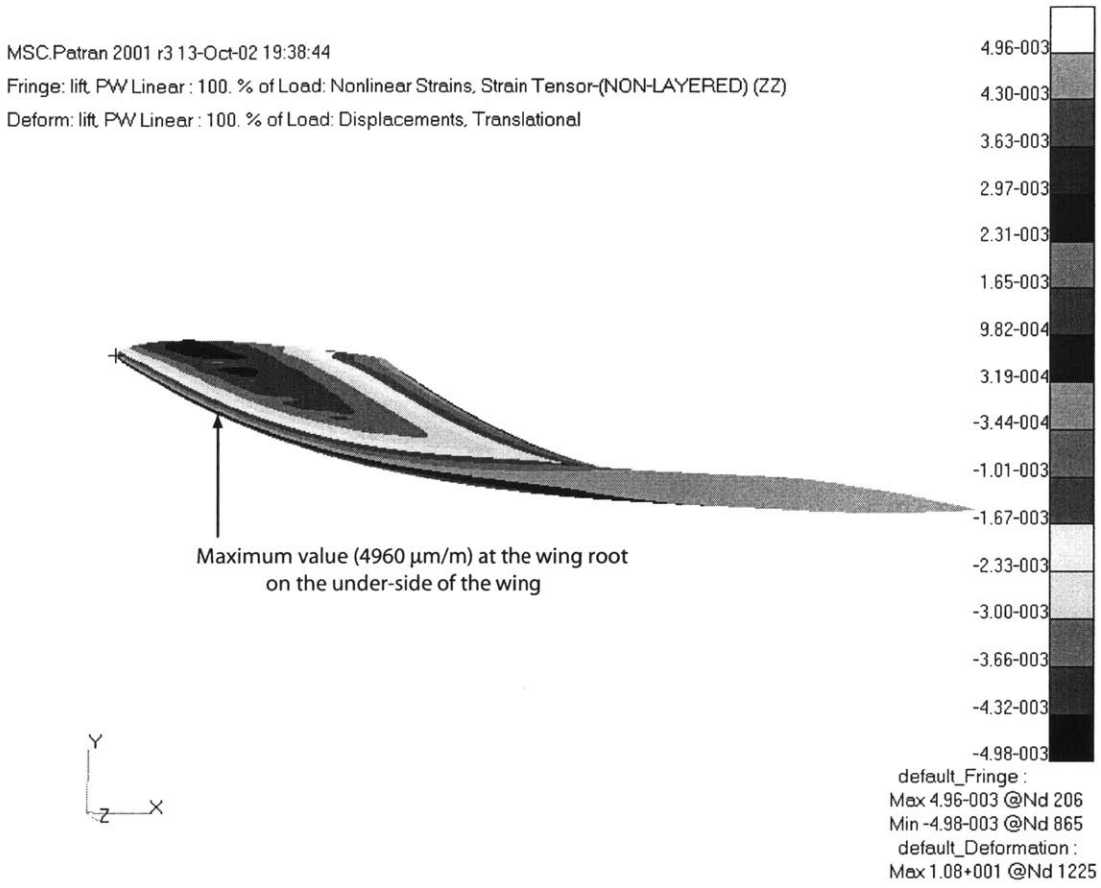

Figure 2-63: Nastran normal (spanwise) strain for 5° root angle of attack

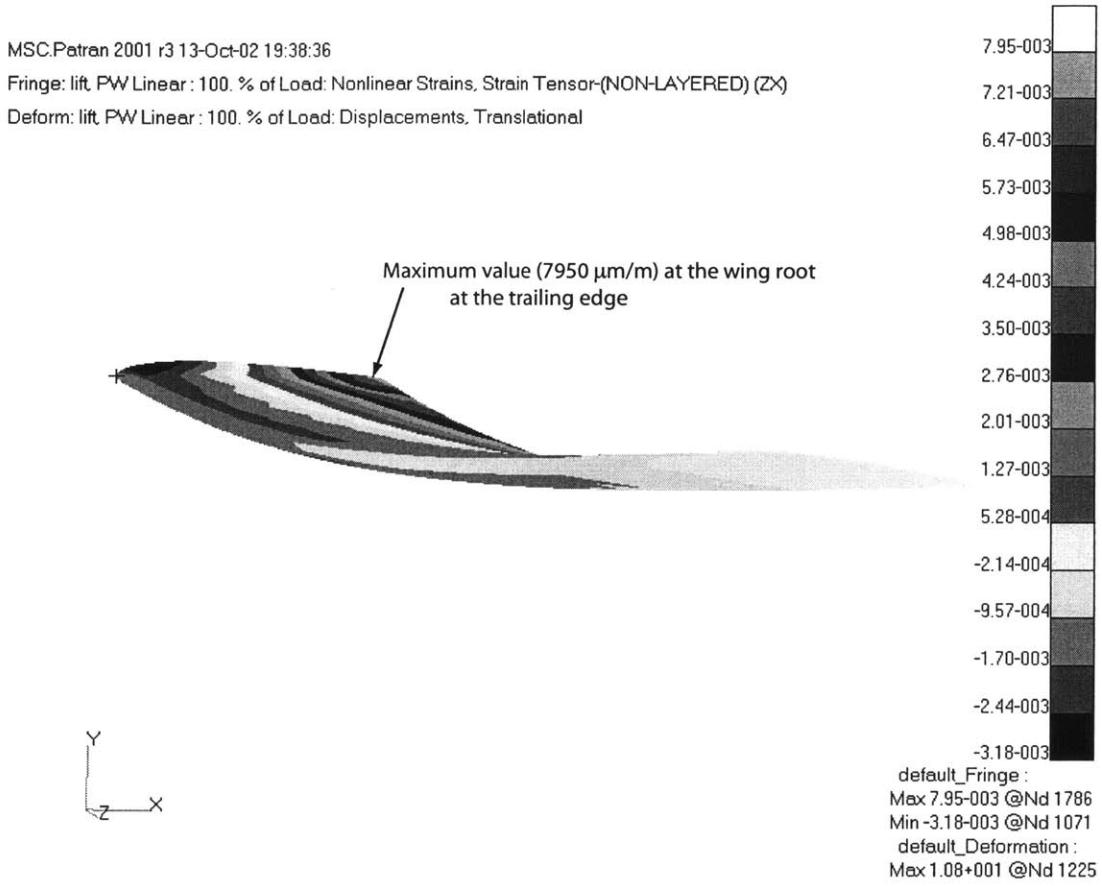

Figure 2-64: Nastran in-plane shear strain for 5° root angle of attack

Chapter 3

Experimental Procedure

This chapter describes the experimental work that took place as part of this project. The manufacturing methods are presented, as are details for instrumentation location and wiring. The chapter also contains the description of the experimental tests: bench top and wind tunnel.

3.1 Wing Manufacture

In this section, different components that make the instrumented wind tunnel model are discussed. The foam cores were machined in the Aeronautics and Astronautics machine shop on the TRAK K3 mill machine with the help of Ricky Watkins and Donald Weiner. The wing lay-up and cure were performed within the TELAC facilities with the support of John Kane. The root clamps for holding the wing during the bench top and wind tunnel characterization were machined at MIT Lincoln Laboratory. The wing mold was provided by NASA Langley.

3.1.1 Foam Core

The foam core of the wing was manufactured out of Rohacell 31. This material was selected to ensure survival of the foam at the elevated temperatures of the wing cure process. The foam for each wing was machined in four seperate pieces, consisting of the top and bottom

of the wing from the root to 0.5715 m and the top and bottom of the wing from 0.5715 m to the tip at 1.13 m. The core is slightly oversized by 0.254 mm (10 mil) to ensure adequate backpressure within the mold during the cure process. After the accelerometers are embedded within the foam at the tip of the wing, the individual pieces are glued together with five minute epoxy. The foam pieced together in the mold is shown in Figure 3-1.

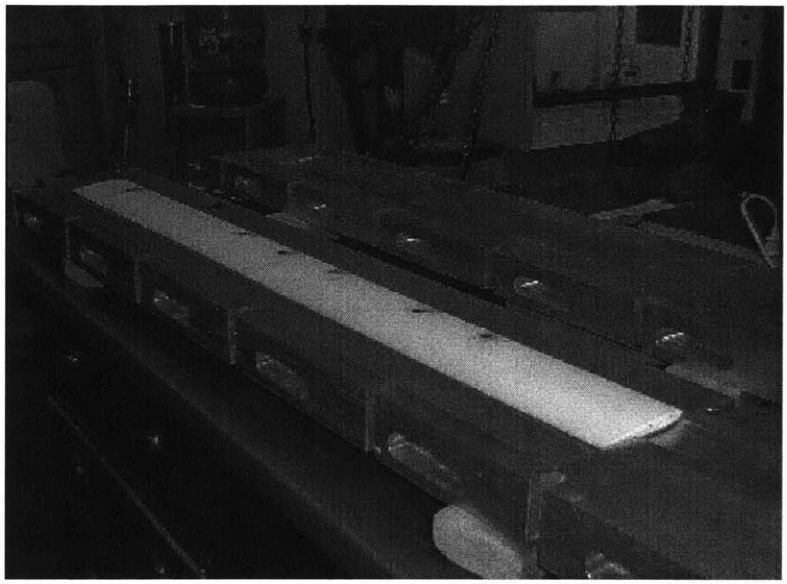

Figure 3-1: Four sections of the foam core pieced together in mold

3.1.2 Instrumentation

Seven full strain gauge bridges and two accelerometers were added on the foam core. The locations of the sensors are provided in Figure 3-2. An additional torsional bridge at the root was attached after the wing was cured and thus is located on the outer surface of the wing. The accelerometers were placed at the tip of the wing where maximum deflection happens. Since the root of the wing experiences the highest strain, one of each of the strain gauge bridge types was placed there. The locations of the other strain gauges along the span of the wing correspond to points of high strain for the higher normal modes, i.e., 2^{nd} and 3^{rd} bending and 2^{nd} torsion.

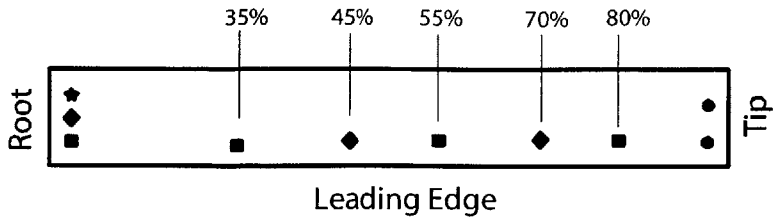

Figure 3-2: Location of sensors: bending gauges are represented by squares, forward/aft gauges by diamonds, torsion gauge by a star, and accelerometers by circles

Strain Gauges

The strain gauges used to make-up the Wheatstone bridges were from the Micro Measurements Division of Measurements Group, Inc. The gauges for the bending bridges were model EA-06-125AD-120 and the gauges for the torsional and forward/aft bending bridges were model CEA-06-125UT-120. Both models consisted of gauges with 120 Ω resistance. The gauges were wired to record spanwise bending and torsion. The four spanwise bending bridges consisted of a pair of gauges oriented in the 0° direction on the top and bottom of the wing. The four torsional bridges consisted of a pair, one in the +45° direction and one in the −45° direction on the top and bottom of the wing [12]. A general Wheatstone bridge wiring diagram is provided in Figure 3-3. The wire diagrams for the specific types of bridges use the same numbering convention. A map of the proper wiring scheme for a spanwise bending bridge is presented in Figure 3-4 and Figure 3-5 details the wiring for the torsional bridges. After some discussion with Professor John Dugundji, MIT, it is believed that the torsional wiring presented in [12] actually refers to a forward and aft motion, as opposed to the twisting motion originally thought. A twist bridge was wired to the outer skin of the wing at the root to measure the twist motion of the wing. The wiring for this bridge is provided in Figure 3-6.

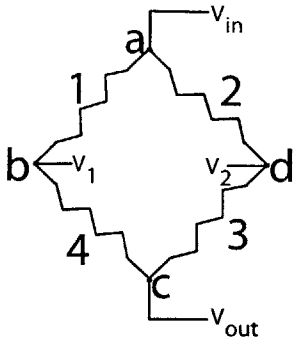

Figure 3-3: General wiring diagram for Wheatstone bridges

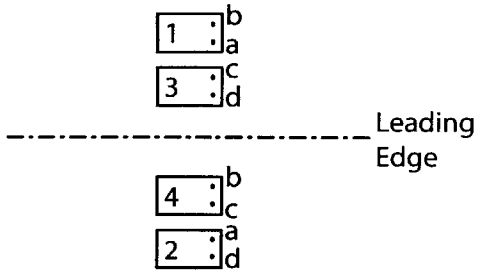

Figure 3-4: Wiring diagram for Wheatstone bridges in bending

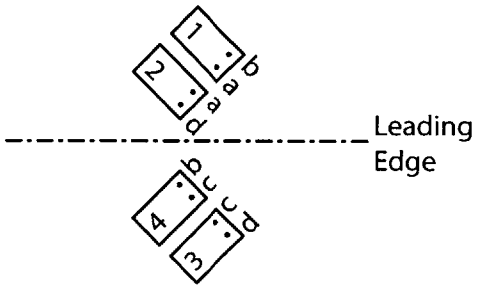

Figure 3-5: Wiring diagram for Wheatstone bridges in forward/aft bending

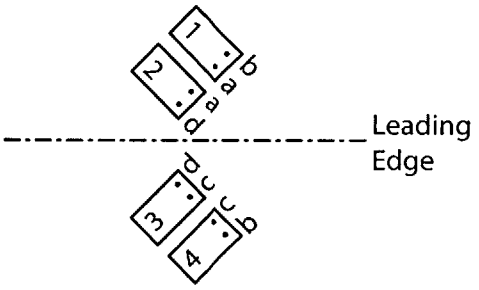

Figure 3-6: Wiring diagram for Wheatstone bridges in twist

The internal strain gauges where attached to a single square layer (25 mm by 25 mm) of pre-cured E-glass/epoxy oriented at 0°/90°. A photo of the internal strain gauges on the wing is provided in Figure 3-7. The squares were glued down with five minute epoxy to the foam. The strain gauges were then also afixed with five minute epoxy. Magnet wire was used to make all of the required electrical connections. The two bridges at the root, with the wiring of both types of bridges, is shown in Figure 3-8.

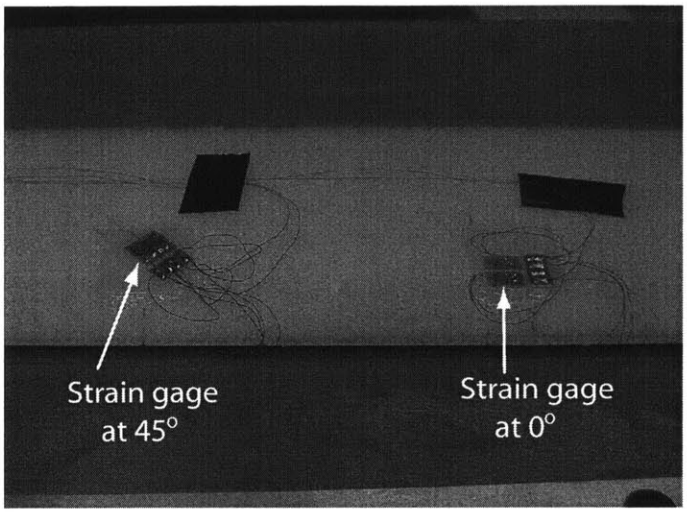

Figure 3-7: Strain gauge at mid-span

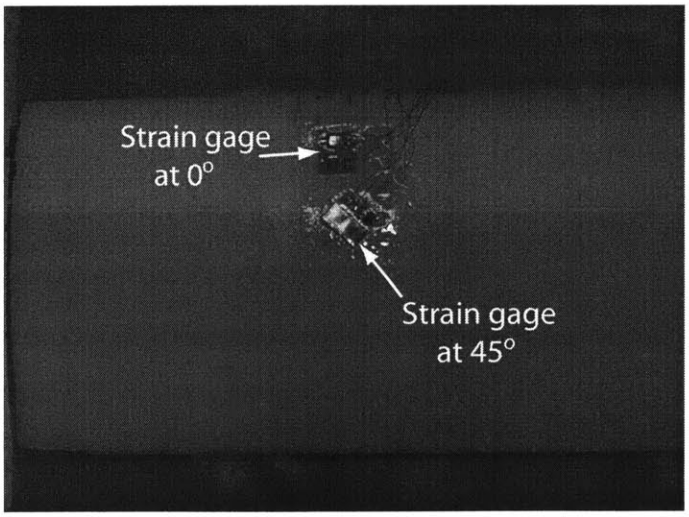

Figure 3-8: Strain gauges wired at the root

Accelerometers

The accelerometers used for this experiment were the Endevco Model 22 piezoelectric accelerometers. These sensors were embedded within the foam core at the wing tip, 14.3 mm from the leading edge and 39.7 mm from the leading edge. The specifications for the accelerometers are provided in Table 3.1. The wires were run parallel to the leading edge in channels between the two halves of foam. The pair of accelerometers is used in combination to calculate the twist and bending frequencies at the wing tip. When the output of one is subtracted from the other, the tip twist response is obtained. The average of the two accelerometers produces the bending response.

Table 3.1: Accelerometers used in the wing model

Gauge	*Location*	*Charge Sensitivity*
CW18-22	14.3 mm from LE	0.374 pC/g
CW13-22	39.7 mm from LE	0.385 pC/g

3.1.3 Lay-Up

In preparation to lay-up the composite on the instrumented foam core, the foam core was put in the oven at 266°F for 24 hours to remove any residual moisture. Moisture has a plasticizer effect on the foam, which causes a decrease in its compressibility strength [13]. If this step is not performed, the foam will collapse under the high temperature and pressure of the curing process.

The required three layers of E-glass/epoxy were cut to 0.305 m by 1.143 m and stacked flat on the table. They were then gathered up and placed into the bottom half of the mold as one piece of cloth. The long edge was placed slightly behind the trailing position and the short end was aligned with the root. At this point, the additional layers of E-glass/epoxy around the root section where wrapped around the foam core. These consisted of a 76-mm strip, a 64-mm strip, a 51-mm strip, and a 38-mm strip, each being two plies thick. These additional plies were added to the root area to provide additional strength where the bolts

from the clamp would be passing through the wing. Once this was done, the foam core was inserted. The rest of the lay-up was then wrapped around the leading edge of the foam and pulled tightly toward the trailing edge. Once the lay-up was smooth on both sides of the wing, a straight edge was placed at the wing trailing edge and the excess was trimmed off. Care was taken to ensure the wires passing out of the root would not interfere with the root clamp. The top of the mold was lifted into position and then the two pieces were clamped together. A thermocouple was attached between the two halves of the mold, as the temperature of the mold is the one which needs to follow the cure profile. With the mold assembly completed, the wing was placed into the autoclave and cured at 250°F for 90 minutes. It was then allowed to cool slowly over 48 hours.

3.1.4 Post Cure

The wing was removed from the mold after slowly cooling and only minor cosmetic touch-ups were required. Some resin had been pulled between the two mold pieces at the leading edge. This resin was scrapped off and then the leading edge was sanded for a smooth finish. This resin was also pulled at the trailing edge, but this is desirable as it creates a smooth taper to the trailing edge, so no modifications were made to the trailing edge. A band saw was used to remove about 6-mm from the wing tip to provide a smooth edge to that side of the wing as well. Finally three holes were drilled into the root of the wing, 28.5-mm behind the leading edge, to accomadate the three bolts from the clamp.

3.1.5 Clamp

The root clamp was made from Aluminum 6061 and was NC machined at MIT Lincoln Laboratory. It consists of two seperate pieces which bolt together through the wing. Drawings of the top and bottom are provided in Figure 3-9 and Figure 3-10. The clamp is designed such that a gap between the two pieces exists at the leading and trailing edge. This allows for some shape mismatch between the final wing and the clamp.

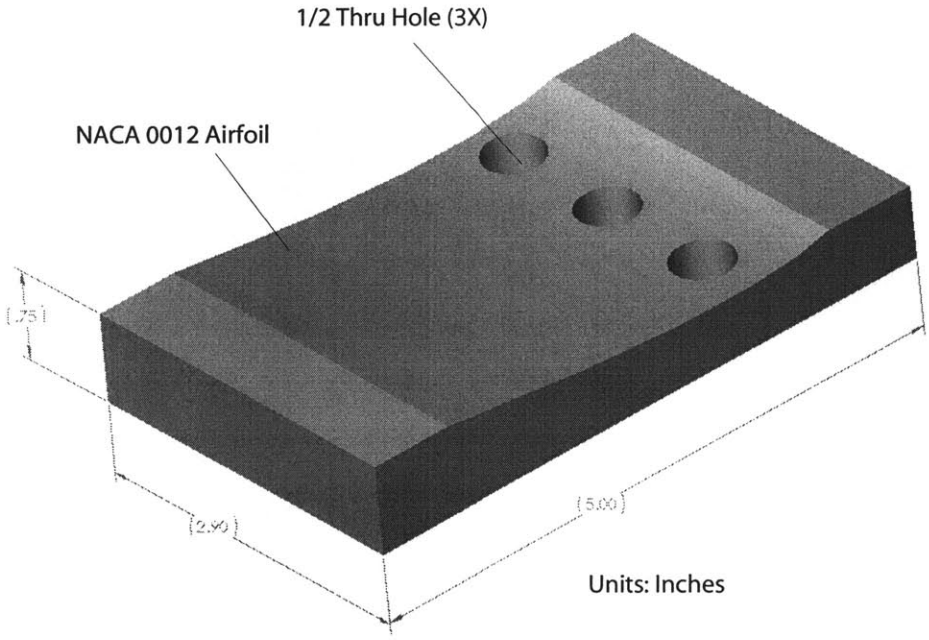

Figure 3-9: Top of root clamp

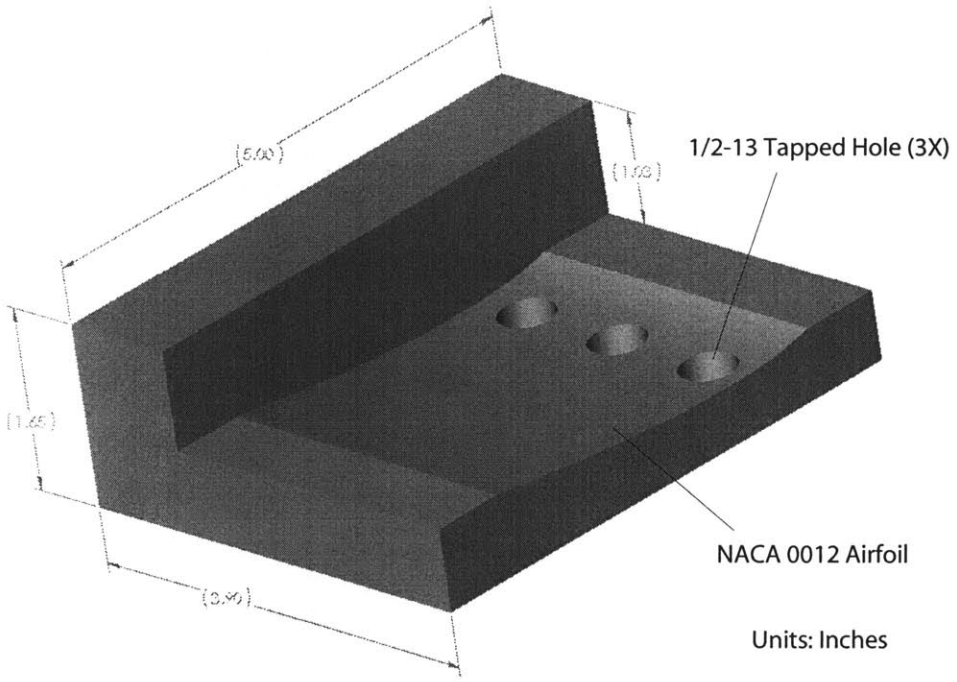

Figure 3-10: Bottom of root clamp

3.2 Data Acquisition Equipment

The strain gauge and accelerometer signals need to be processed through conditioners before they can be sent to a computer to store. Since all of the bridges were full bridges they needed to be connected to the conditioner with the pin readout provided in Figure 3-11. The little letters represent the connections to the strain gauges and the capital letters refer to the pins on the connector. The conditioner box converts the signal to an amplified voltage which is

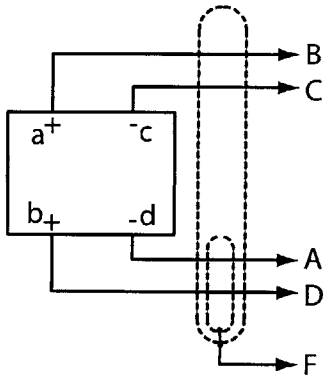

Figure 3-11: Pin diagram for full bridges

sent to the computer via a BNC cable. The accelerometer signal was also processed through a conditioner before the signal voltage was transmitted to the computer. A photo of both conditioners is provided in Figure 3-12. These are the conditioners used for the bench top tests. The wind tunnel tests used similar strain gauge conditioners, but in a different box.

3.3 Wind Tunnel Load Cell

The wind tunnel tests required the use of a load cell. The load cell is the interface between the wing root clamp and the fixed stand in the tunnel. It provides three axis of load data, as well as the yaw moment. For this wing, a 75-lb Multi-Axes Load Cell from JR3, Inc. was used. The load settings and ratings are provided in Table 3.2.

To determine the loads, the voltage channel coming from the load cell must be multiplied by a calibration matrix. The equation for this load cell is:

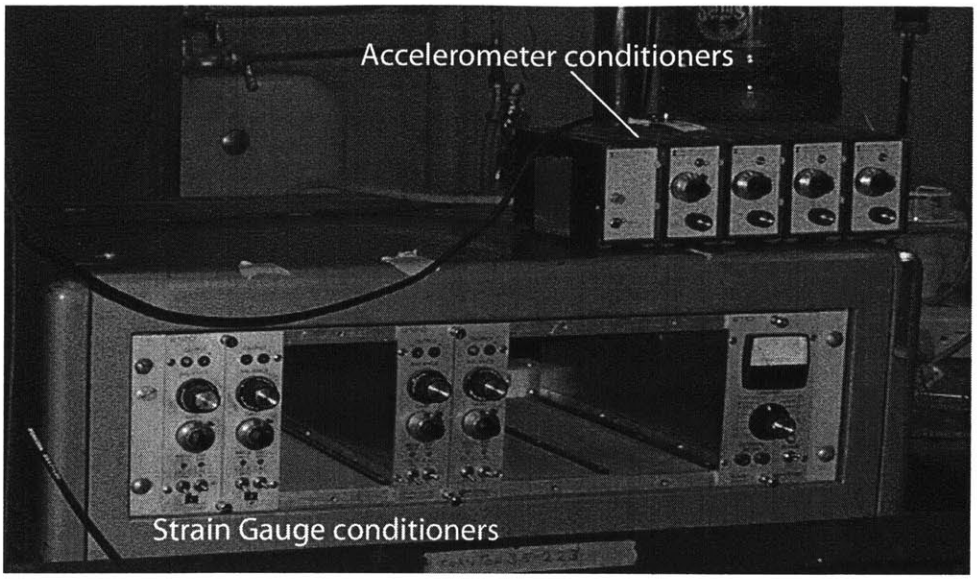

Figure 3-12: Photo of accelerometer and strain gauge conditioners

Table 3.2: Load cell used for the wing tunnel tests

Load Cell Channel	Maximum Load Measurement	Sensor Load Rating
F_x	75 lb	75 lb
F_y	75 lb	75 lb
F_z	150 lb	150 lb
M_x	0 in-lb	225 in-lb
M_y	0 in-lb	225 in-lb
M_z	225 in-lb	225 in-lb

$$\begin{bmatrix} Drag\ (lb) \\ Axial\ (lb) \\ Lift\ (lb) \\ Yaw\ (in\text{-}lb) \end{bmatrix} = \begin{bmatrix} 9.2758 & -0.1770 & -0.0589 & -0.1796 \\ 0.2977 & 9.1166 & 0.0861 & 0.0407 \\ 0.2176 & -0.1894 & 18.2251 & 0.6773 \\ -0.1918 & 0.0131 & -0.0766 & 27.7896 \end{bmatrix} \begin{bmatrix} F_x\ (V) \\ F_y\ (V) \\ F_z\ (V) \\ M_z\ (V) \end{bmatrix} \tag{3.1}$$

Chapter 4

Experimental Studies

This chapter discusses the bench top and the wind tunnel test results. There is also a section on adjustments made to the model to cause the natural frequencies to match those seen in the bench top tests.

4.1 Bench-top Tests

A series of bench top tests were conducted to determine the characteristics of the manufactured wing and to ensure operation of all the sensors. It was discovered that the forward/aft strain gauge bridge at the root was electrically shorted during manufacture. It was not possible to be repaired, so it was not monitored during the tests. Aside from simple functionality tests, only the gauges at the root for bending and torsion were monitored during bench-top tests. These tests were performed in TELAC. A picture of the experimental set-up is provided in Figure 4-1 and a picture of the monitoring equipment is provided in Figure 4-2.

4.1.1 Strain Gauge Calibration

A static calibration of the strain gauges was performed to determine the deflection-voltage relationship. This was performed with the strain gauge conditioners within TELAC. So these results do not correspond with voltages from the wind tunnel tests. This calibration was performed to establish a process to be used later with the tunnel instrumentation. The wing

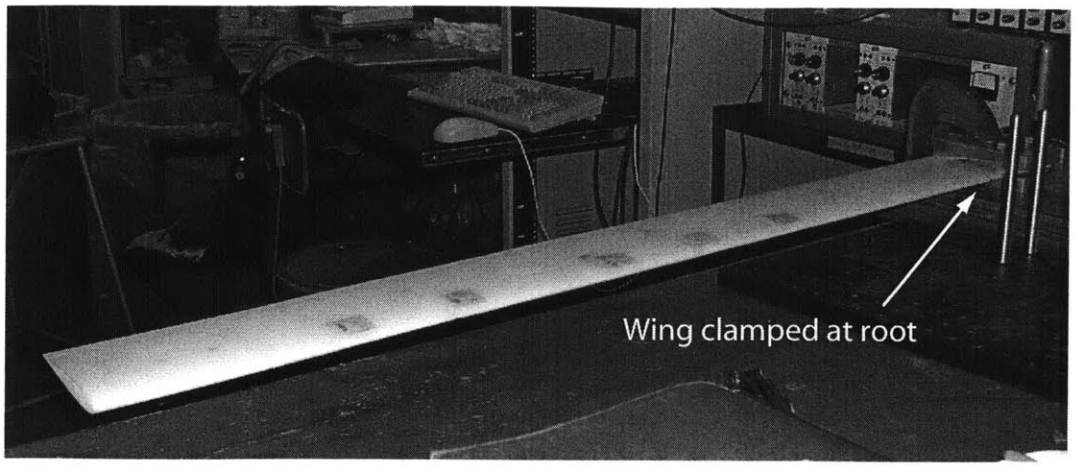

Figure 4-1: Experimental set-up for bench-top tests

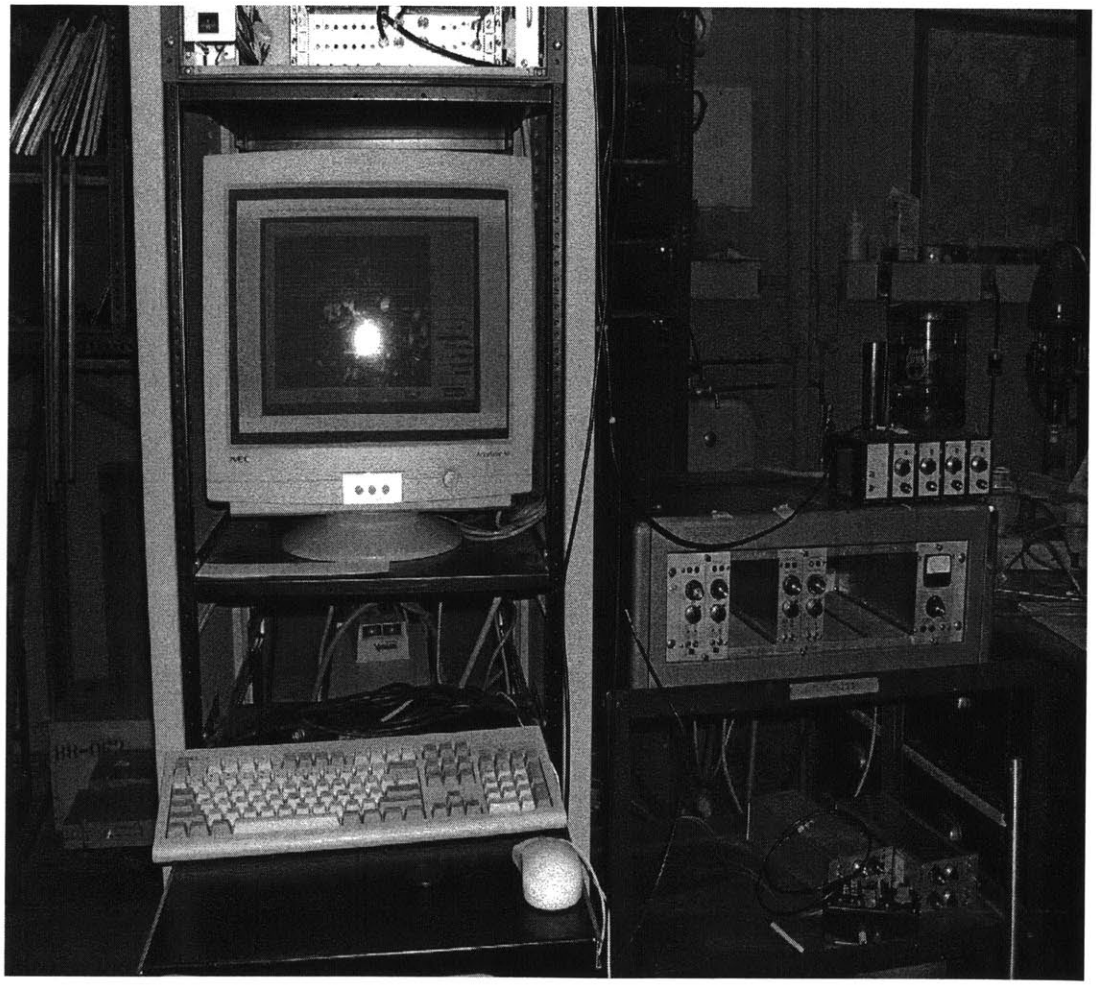

Figure 4-2: Experimental instrumentation for bench-top tests

was displaced in the vertical direction by various pre-established tip displacement values in both directions. This was done by holding the wing tip by hand and aligning it with pre-drawn tick marks on a reference scale. The wing was then held to these locations for a few seconds. This provided data on bending deflections versus voltage. A time trace of this calibration for the root bending strain gauge bridge is provided in Figure 4-3. When

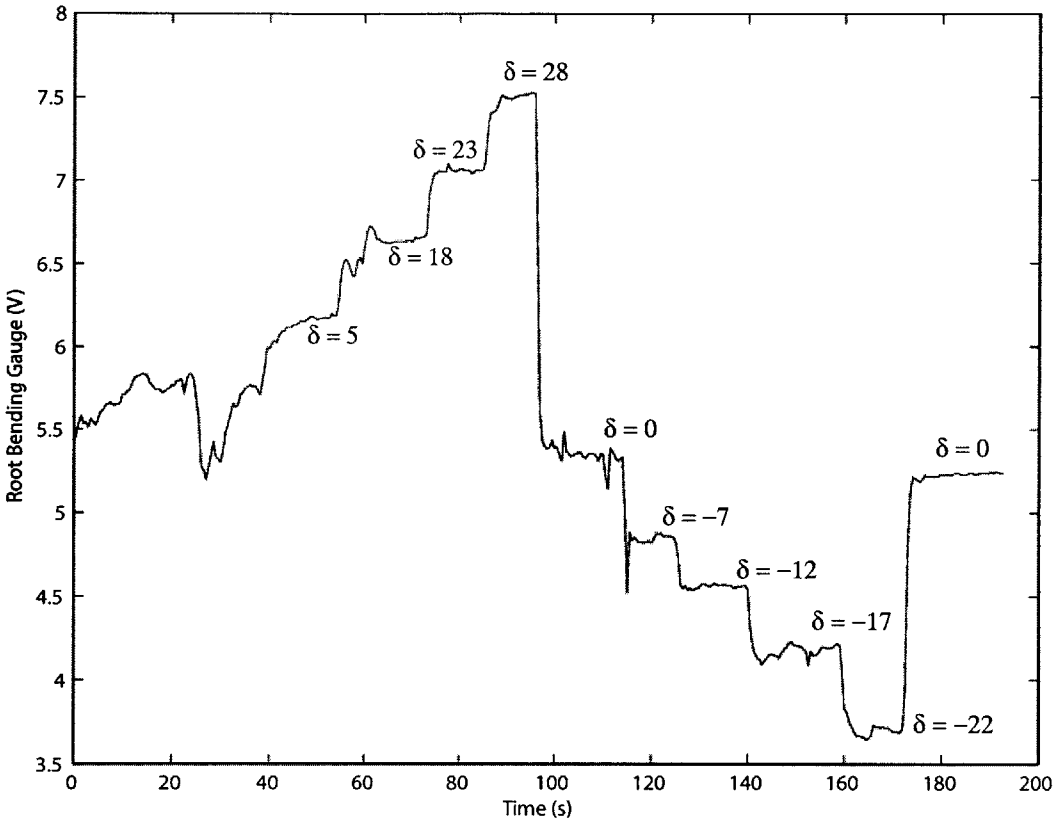

Figure 4-3: Time trace of data from bench-top bending calibration

this data is plotted with the known deflections, a curve of voltage versus tip deflection is generated. This is shown in Figure 4-4.

The wing was also twisted to various amounts at the tip, which provided a calibration for tip twist. For this, the leading edge of the wing was again deflected by hand to pre-drawn tick marks, with the trailing edge held at the original position. A time trace of the data from the root torsion strain gauge bridge is provided in Figure 4-5. This data was plotted

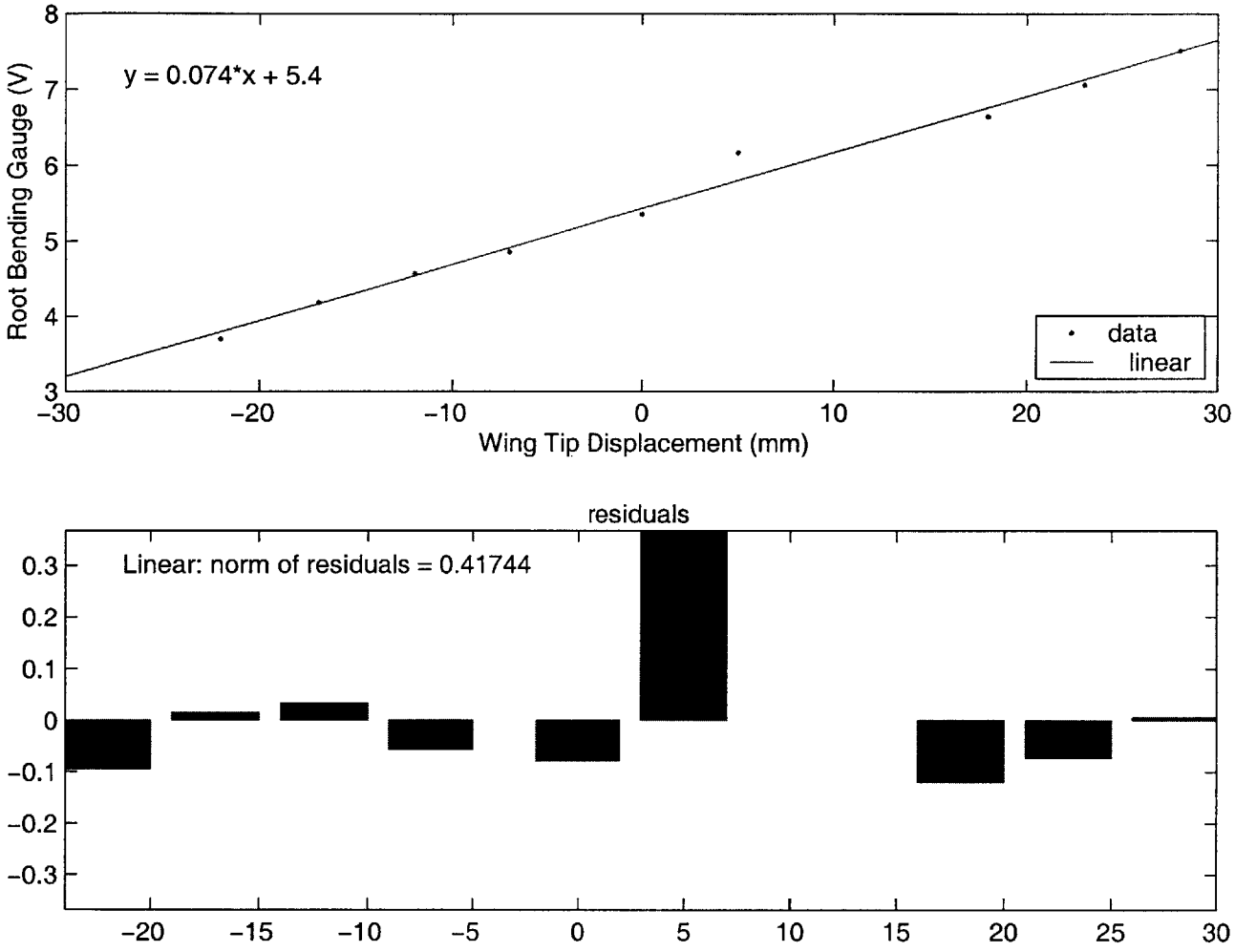

Figure 4-4: Calibration of strain gauge voltage output for bending

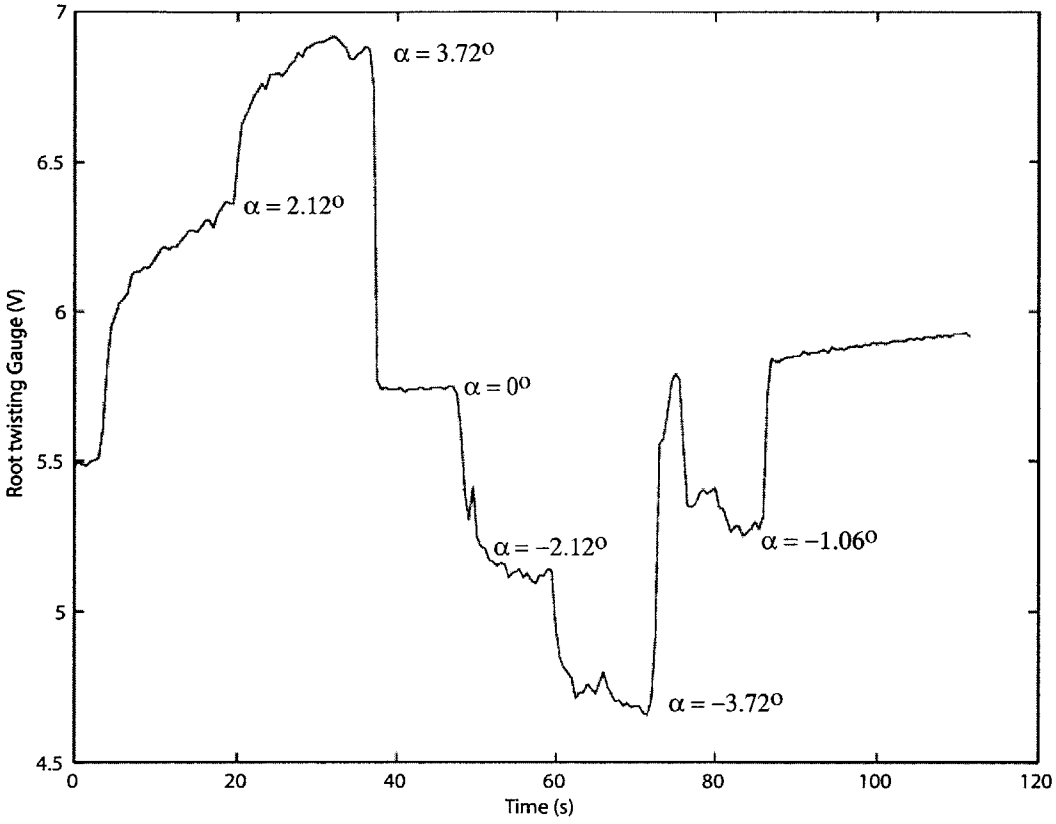

Figure 4-5: Time trace of data from bench-top twist calibration

against the known twist values to provide a curve for the voltage output generated through tip twist. This curve is given in Figure 4-6.

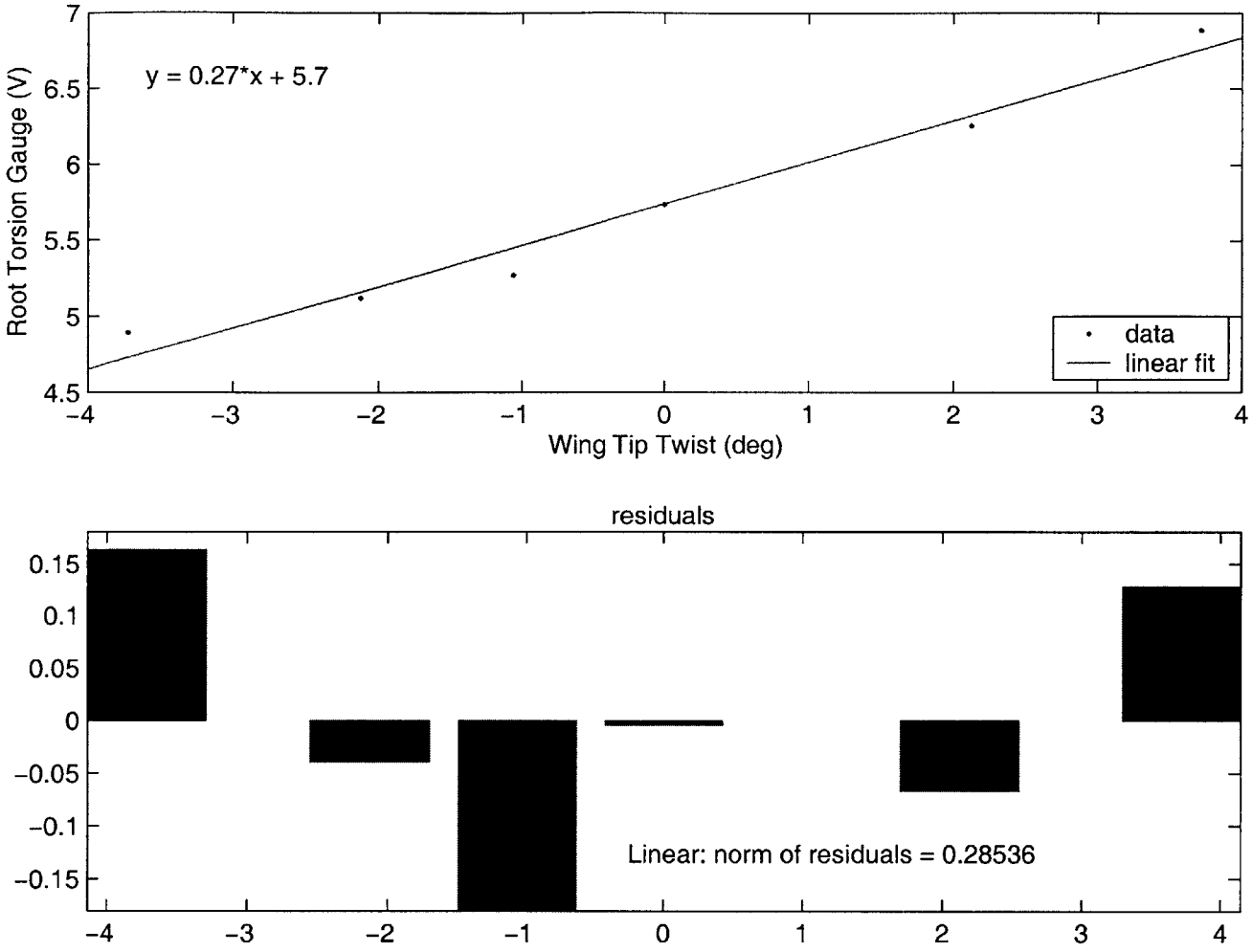

Figure 4-6: Calibration of strain gauge voltage output for tip twist

4.1.2 Tap Tests for Dynamic Properties

Various places on the wing were tapped to excite the different normal modes, so that its natural frequencies could be identified. This data was collected via the strain gauges. The data from various tap tests is given below in Figure 4-7 through Figure 4-9. The top graph of each figure is a time trace of the voltage output from the strain gauges and the bottom is a Fast-Fourier Transform (FFT) of the output. The first tap was to excite the bending modes. The tap was applied to the tip of the wing around 30% chord line. The frequencies

excited were at 6 Hz and at 38 Hz (1^{st} and 2^{nd} bending). The second tap was at the tip but off the elastic axis, at the trailing edge of the wing tip, thus the torsional modes were excited. This plot shows dynamics at 70 Hz (1^{st} torsion), as well as the 6-Hz and 38-Hz bending frequencies. The final tap was on the leading edge of the wing tip in the forward/aft direction. This excited the chordwise bending mode. This plot shows the 1^{st} chordwise bending frequency at 45 Hz. The 6-Hz 1^{st} bending was also excited.

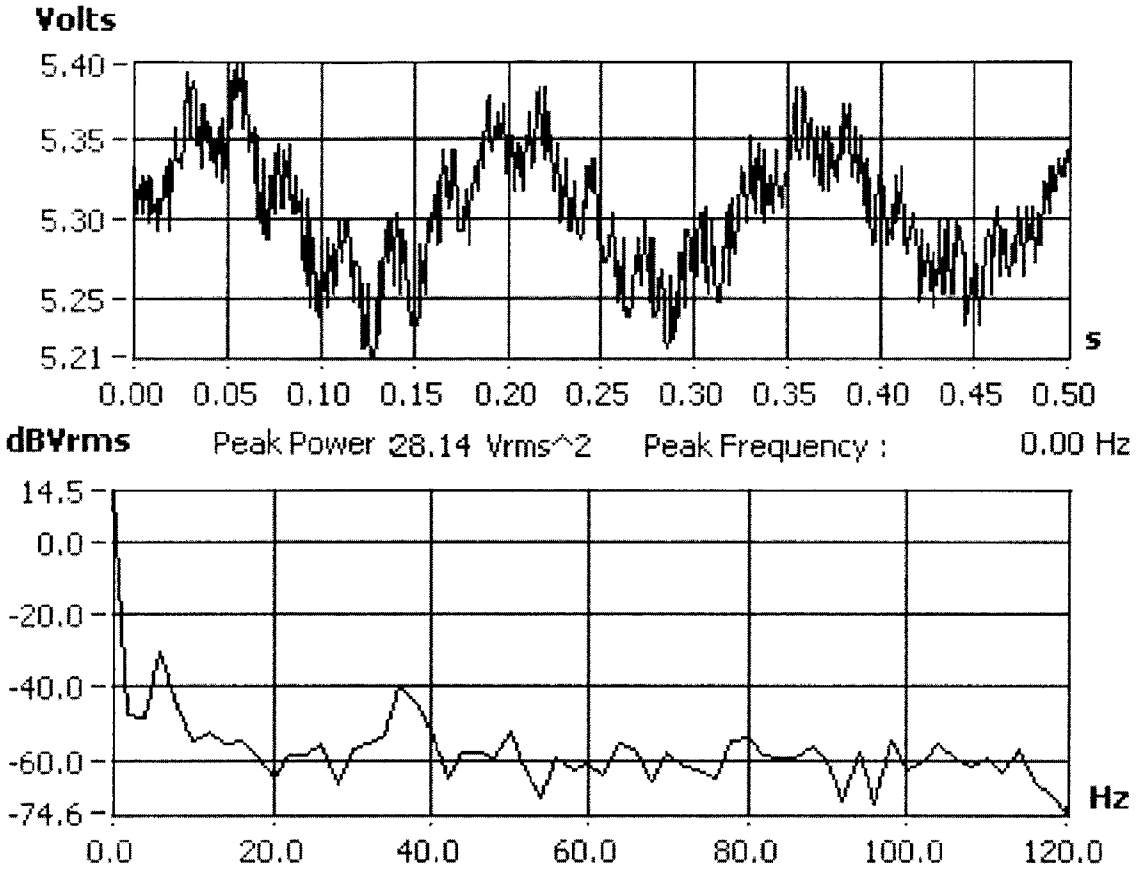

Figure 4-7: Tap test for bending frequencies—root bending gauge

It can be seen through these graphs that tap tests are not perfect, as exciting purely one type of mode is extremely difficult. However, the first four modes of vibration can be determined along with their mode shape. This data is summarized in Table 4.1.

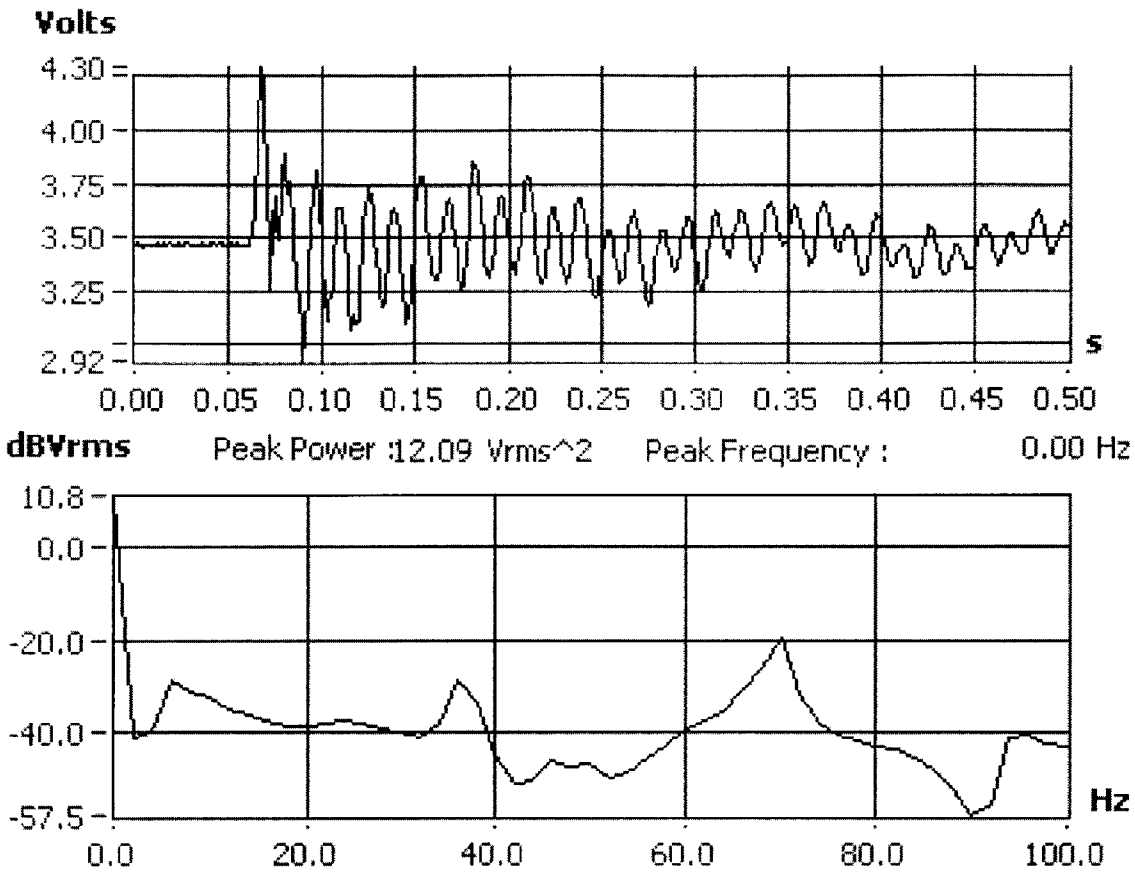

Figure 4-8: Tap test for torsion frequencies—root torsion gauge

Table 4.1: Natural Frequencies From Bench-top Tap Tests

Mode	Frequency	Mode Shape
1	6.4 Hz	1^{st} Bending
2	38 Hz	2^{nd} Bending
3	45.0 Hz	1^{st} Chordwise Bending
4	70.0 Hz	1^{st} Torsional

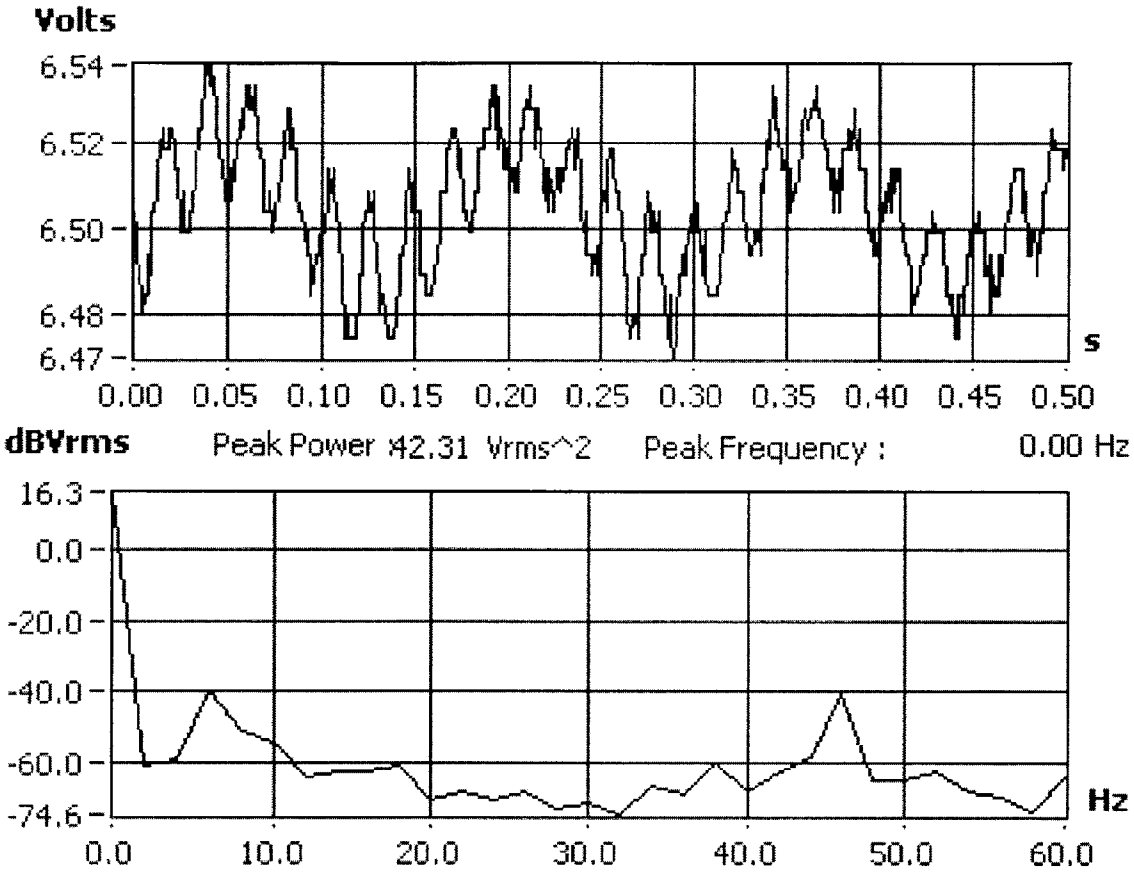

Figure 4-9: Tap test for chordwise bending frequencies—forward/aft gauge

4.1.3 Shaker Tests for Dynamic Properties

Finally, a mini shaker type 4810 from Brüel & Kjaer was applied to different spots on the wing to validate the tap tests and to fully understand the dynamics of the wing. The shaker was first applied to 30% of the chord at about 0.125-m out from the root clamp. The shaker was excited with sine waves of frequencies varing from 1 Hz to 110 Hz. This test was followed by the shaker exciting the leading edge of the wing, as shown in Figure 4-10. Again the shaker was excited with frequencies varing from 1 Hz to 110 Hz. With the shaker

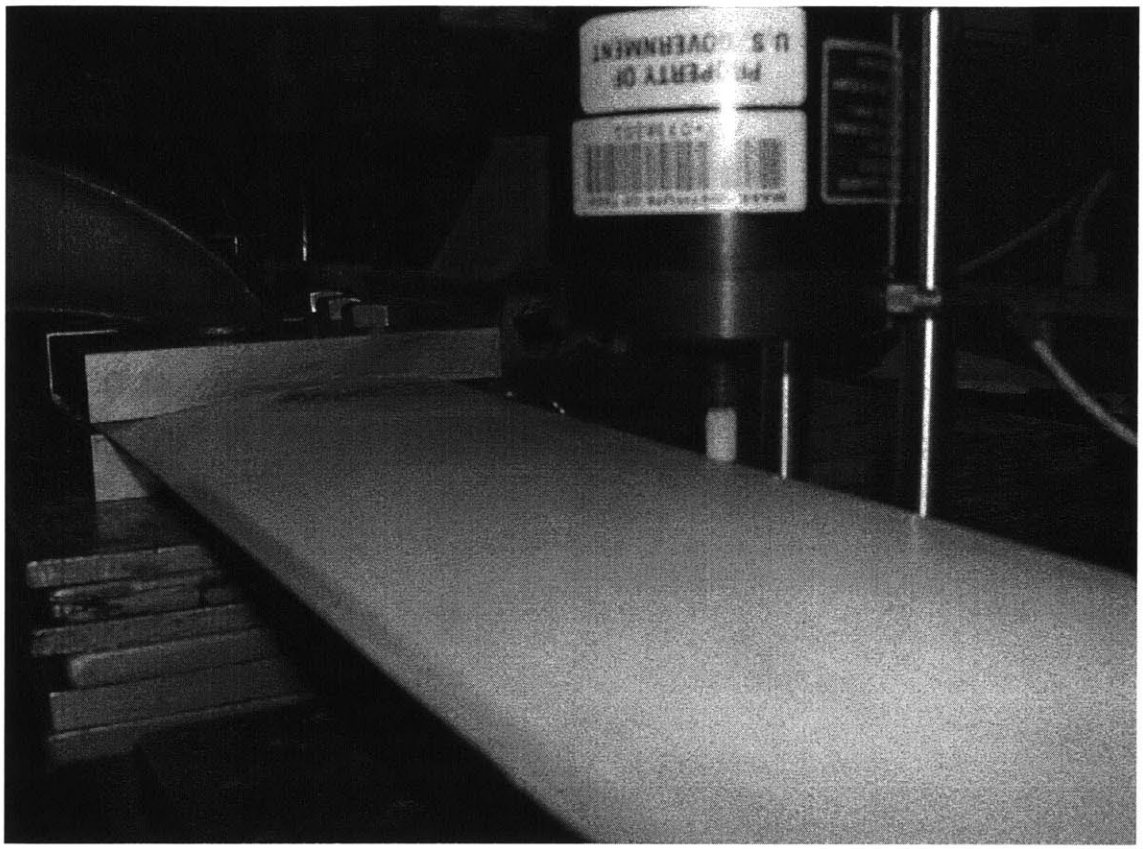

Figure 4-10: Shaker at the wing leading edge for the natural frequency bench test

at the leading edge, the first torsion mode could be excited. The shaker test confirmed the frequencies and mode shapes determined through the tap test, as the node line for the wing could be observed and felt through a light touch. These results support the use of the tap test in the tunnel, where a shaker test would be difficult.

4.2 Re-work of Analytical Model

During the bench top tests the wing was weighed to determine the true cross sectional weight and the final length of the wing. The wing cross-sectional weight is 0.2176 kg/m. The length of the wing outside the clamp is 1.038 m. With these adjusted within the model, the originally calculated natural frequncies for the wing (Table 2.9) changed and the 1^{st} bending mode matches that from the bench-top tests. The first six natural frequencies are given in Table 4.2. A diagram of all the mode shapes is provided in Figure 4-11. The %-error value is calculated with Equation 4.1.

$$\%error = \frac{Calculated - Measured}{Measured} \cdot 100\% \tag{4.1}$$

Table 4.2: Natural frequencies with adjusted weight and length

Mode	Calculated Frequency	Measured Frequency	% Error	Mode Shape
1	6.44 Hz	6.4 Hz	0%	1^{st} Bending
2	39.1 Hz	45 Hz	13%	1^{st} Chordwise Bending
3	41.7 Hz	38 Hz	9.7%	2^{nd} Bending
4	78.4 Hz	70 Hz	12%	1^{st} Torsional
5	124 Hz	-	-	3^{rd} Bending
6	241 Hz	-	-	2^{nd} Torsional

Some adjustment of material properties was made to further modify the wing characterists to match the bench-top results. The shear stiffness, Q_{66} (defined in Appendix B), of the E-glass/epoxy was modified from 4.1 GPa to 3.25 GPa. This changed the first torsional frequency of the modeled wing to 70 Hz without changing the other frequencies. The Young's Modulus of the foam in the chordwise direction was also adjusted from 36.0 MPa to 558 MPa. This changed the first chordwise bending mode to 45 Hz. The discrepancy between the true second bending and the predicted second bending is believed due to the non-uniform distribution of mass along the span of the wing. The cross sectional wing weight takes the weight of the accelerometers, strain gauges, and epoxy which was used to attach the separate

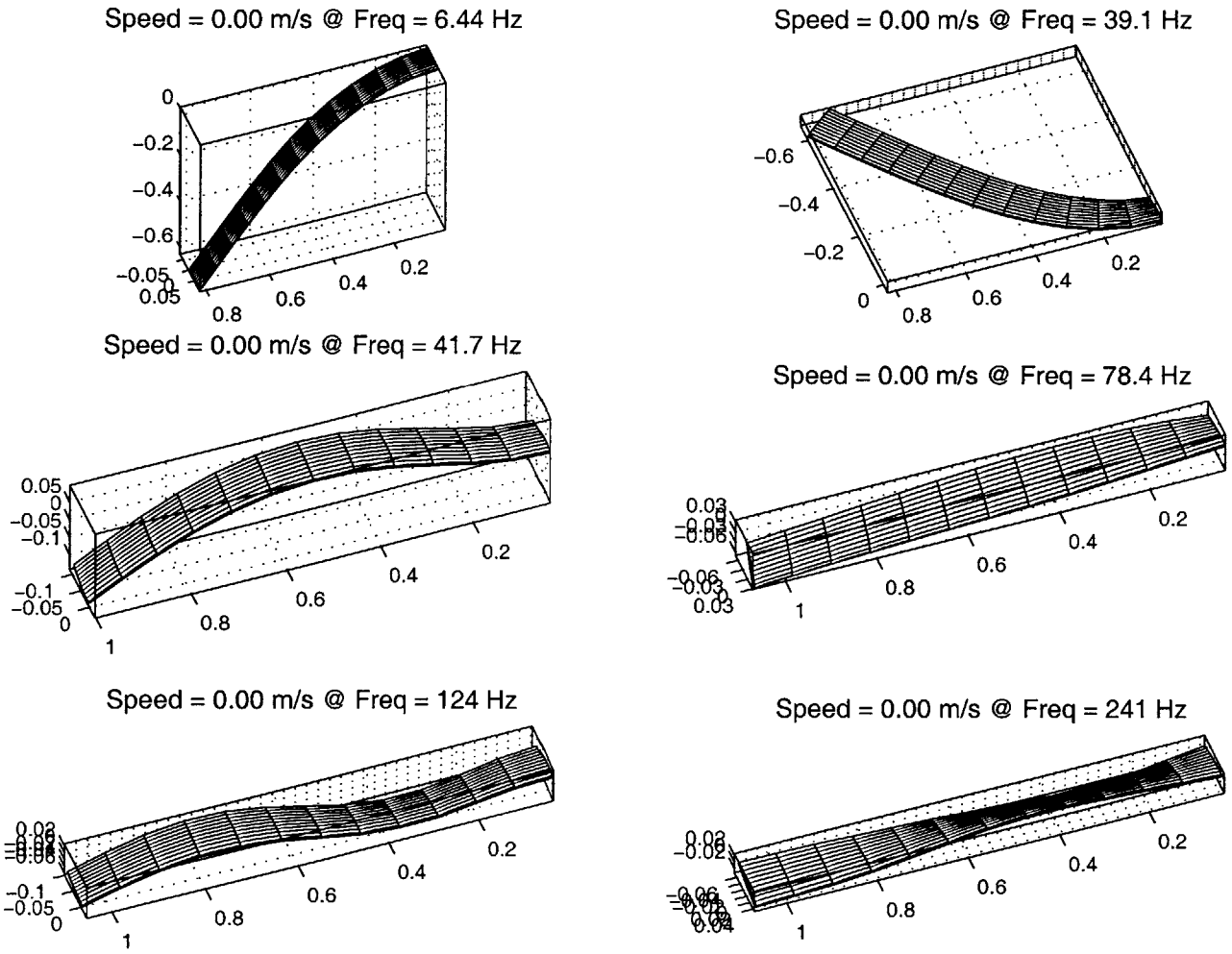

Figure 4-11: Fundamental mode shapes with adjusted weight and length

foam pieces and spreads them evenly across the entire wing. This un-even distribution of mass will cause slight deviations in the second bending, causing the 6.25 times the first bending frequency rule, value for isotropic homogeneous cantilever beams, to not apply.

With these modifications to the wing properties, the model predictions for the wing are close to the measured frequencies. The natural frequencies are given in Table 4.3 and the mode shapes are provided in Figure 4-12.

Table 4.3: Intermediate predicted natural frequencies based on added stiffness corrections

Mode	Calculated Frequency	Measured Frequency	% Error	Mode Shape
1	6.44 Hz	6.4 Hz	0%	1^{st} Bending
2	41.5 Hz	38 Hz	9.2%	2^{nd} Bending
3	45.0 Hz	45 Hz	0%	1^{st} Chordwise Bending
4	70.0 Hz	70 Hz	0%	1^{st} Torsional
5	123 Hz	-	-	3^{rd} Bending
6	216 Hz	-	-	2^{nd} Torsional

These new changes in the model were used to calculate new flutter speeds. The flutter speeds are given in Table 4.4 along with their corresponding root locus plots in Figure 4-13 through Figure 4-17. A portion of the root locus was magnified for 1° and 2°. This data is provided in Figures 4-14 and 4-16.

Table 4.4: Intermediate predicted flutter speeds based on corrected structural properties

Angle of Attack	Flutter Speed
1°	33.0 m/s
2°	52.7 m/s
5°	42.75 m/s

A more indepth study of flutter speed versus angle of attack has provided a graph depicting some strange behavior of the wing between 1° and 2° angle of attack (Figure 4-18). Similar behavior of flutter speed versus angle of attack was discussed in [1]. There, a discontinous jump in the flutter speed was seen between 0° and 1° angle of attack. For this

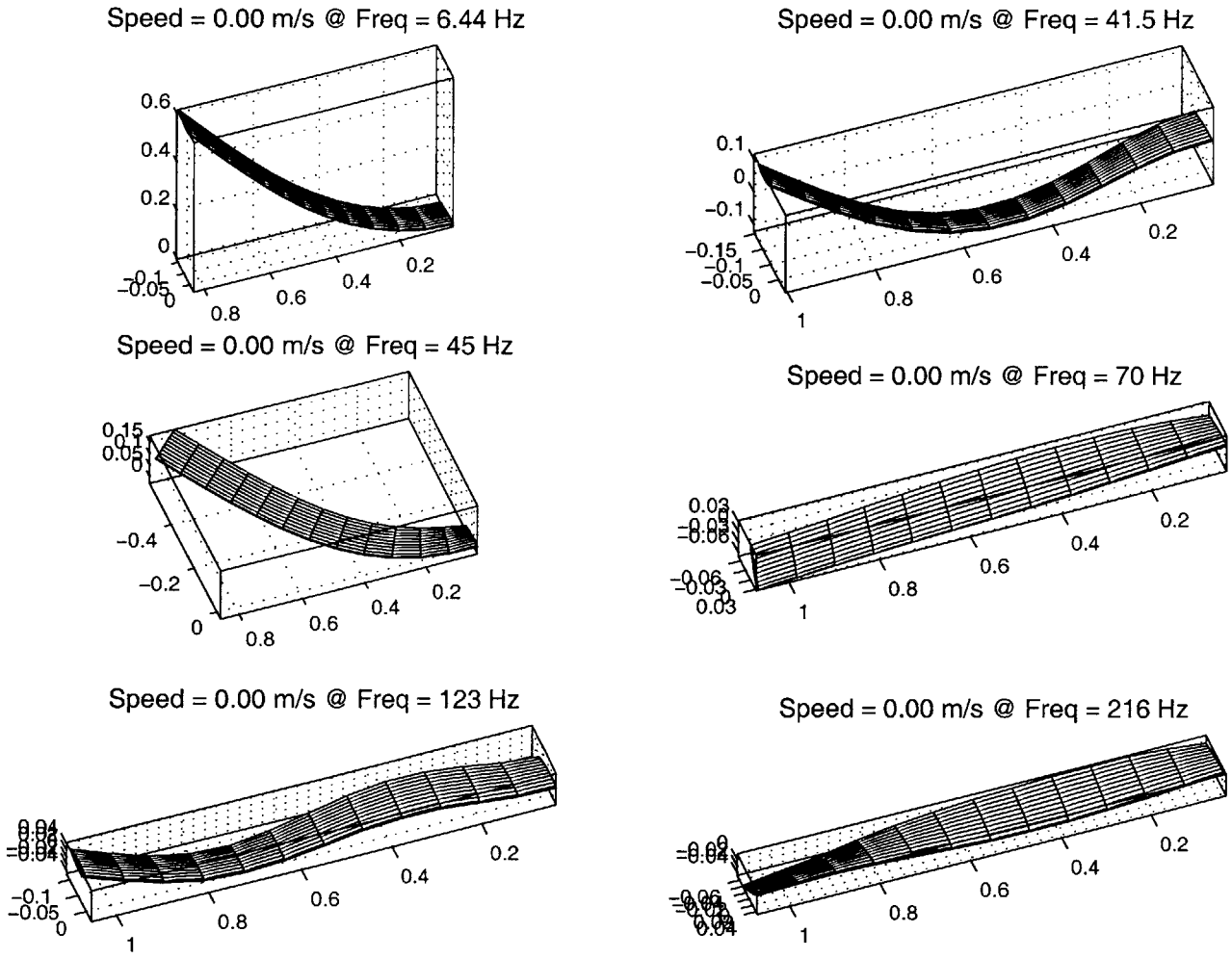

Figure 4-12: Predicted fundamental mode shapes based on added stiffness corrections

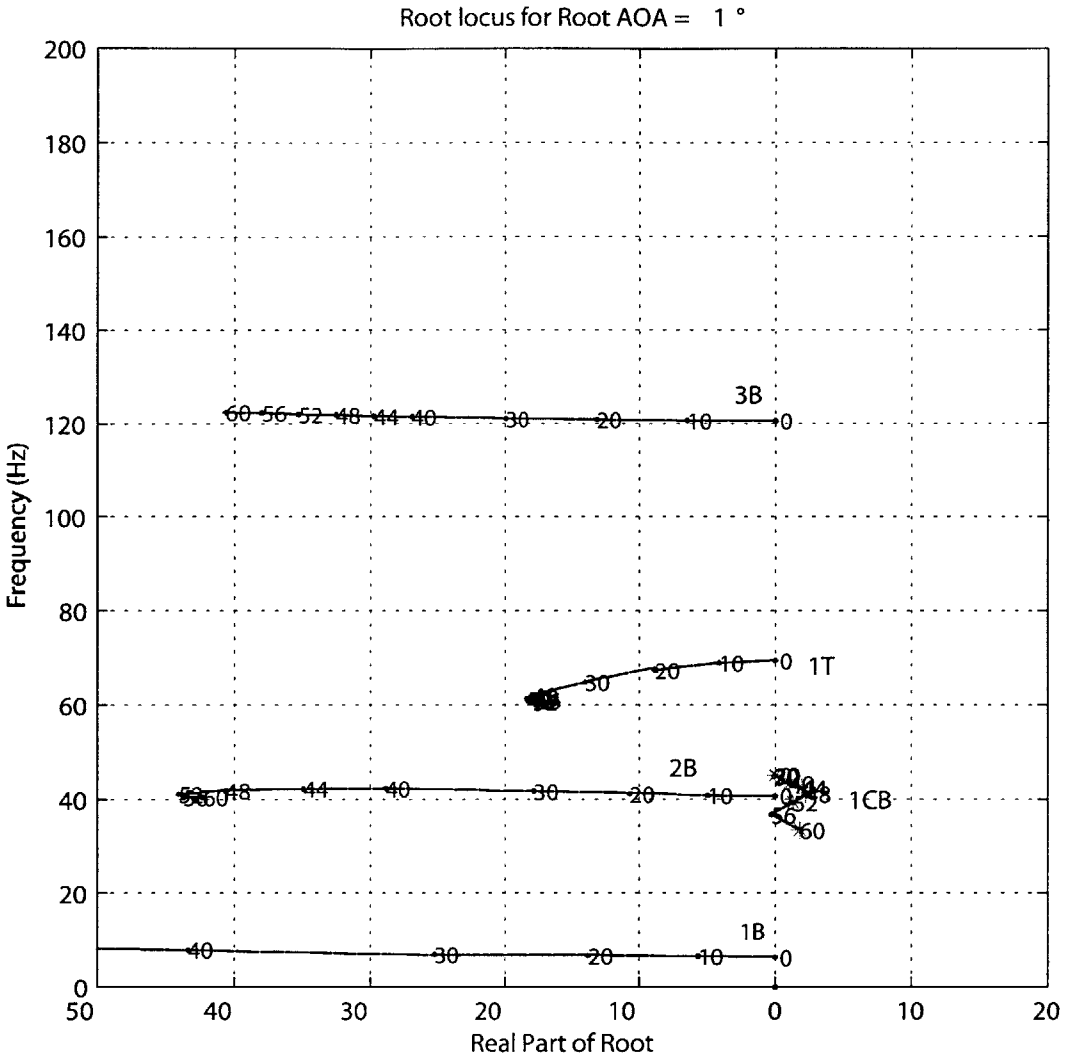

Figure 4-13: Root locus plot for 1° root angle of attack based on modified wing stiffness properties

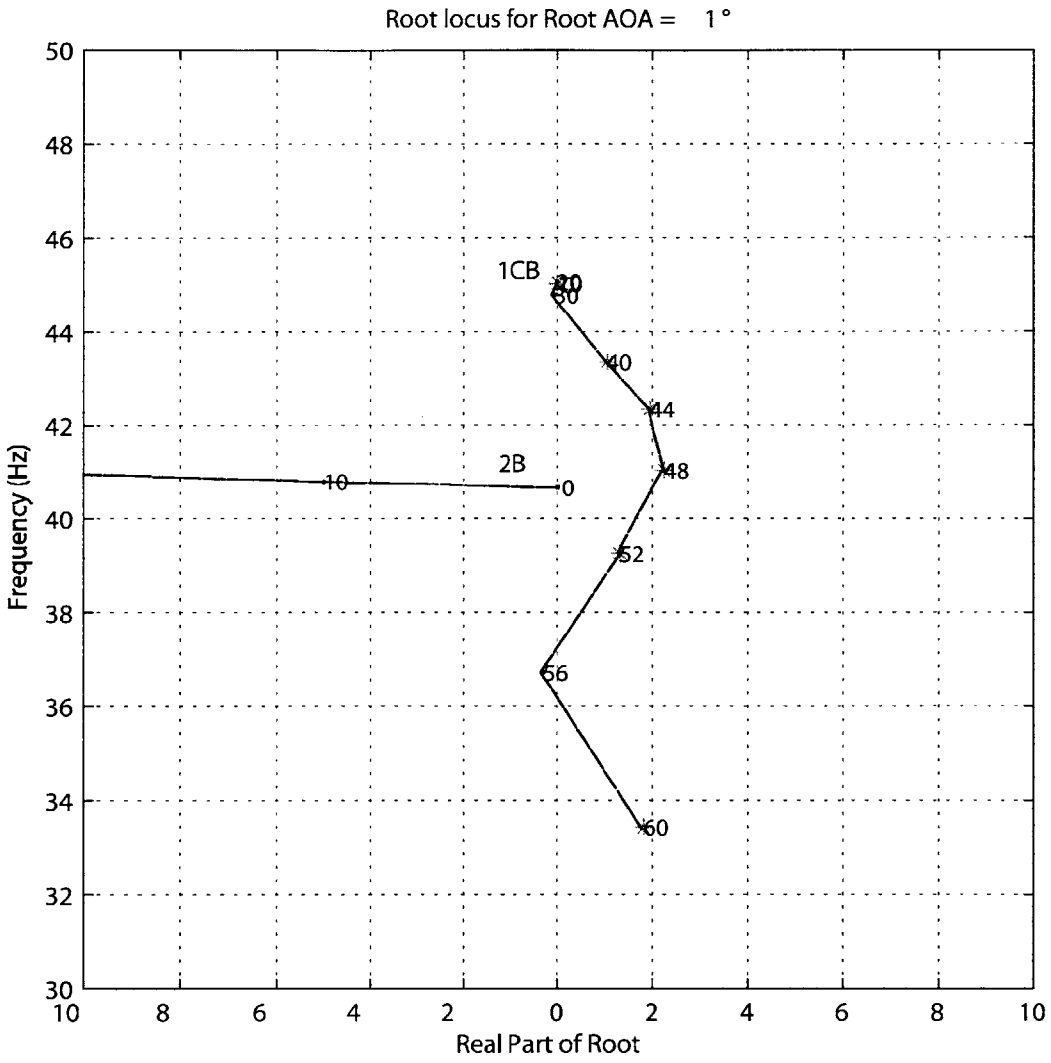

Figure 4-14: Magnified root locus plot for 1° root angle of attack based on modified wing stiffness properties

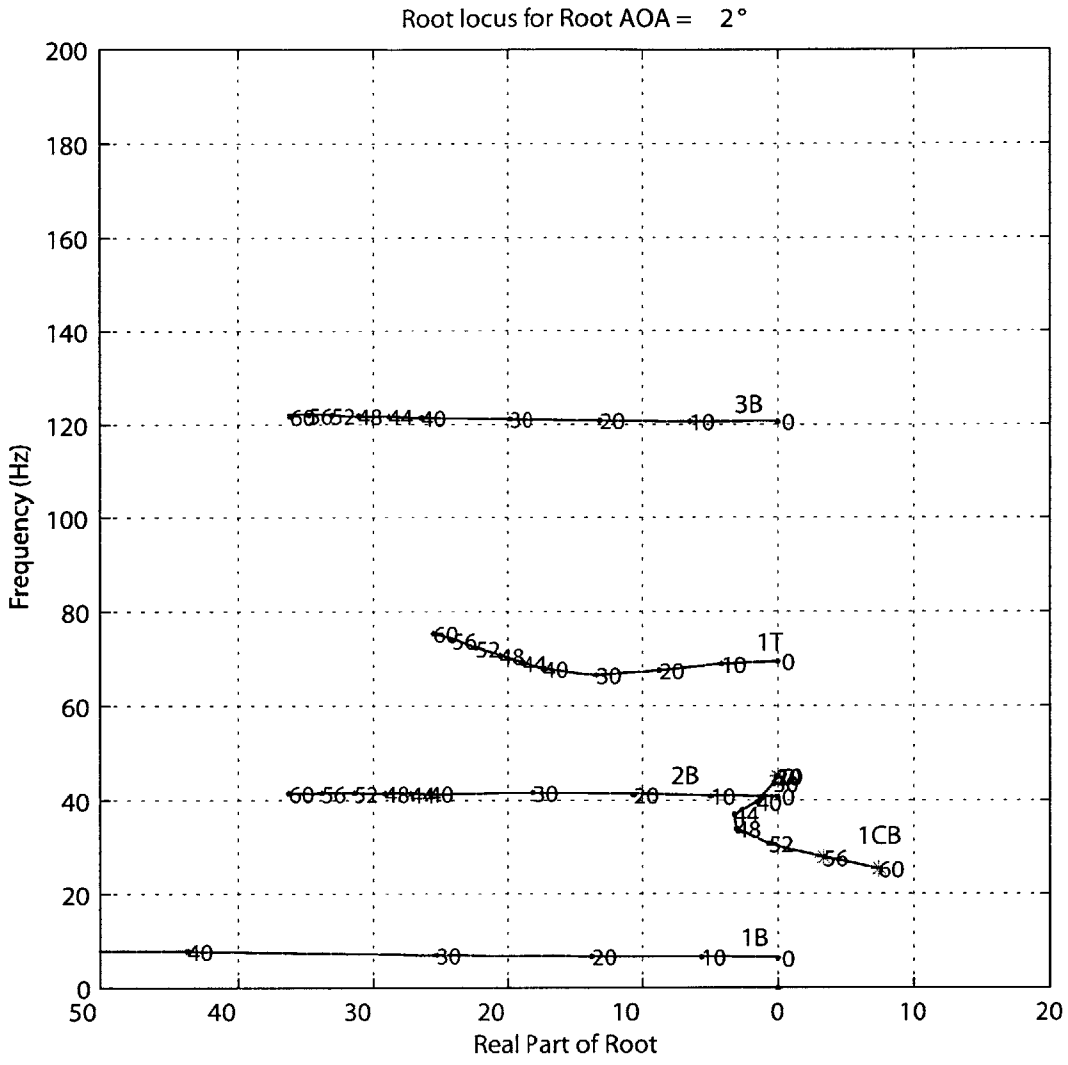

Figure 4-15: Root locus plot for 2° root angle of attack based on modified wing stiffness properties

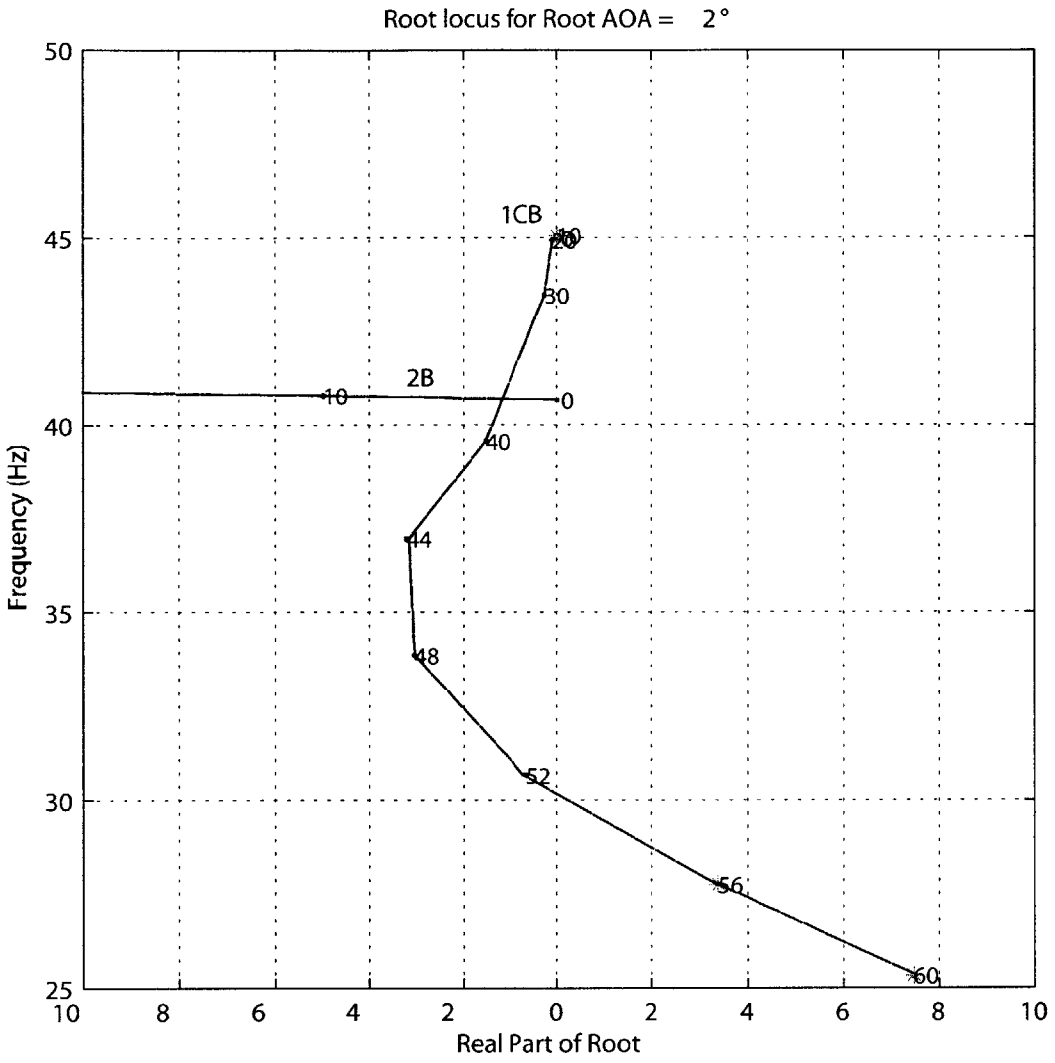

Figure 4-16: Magnified root locus plot for 2° root angle of attack based on modified wing stiffness properties

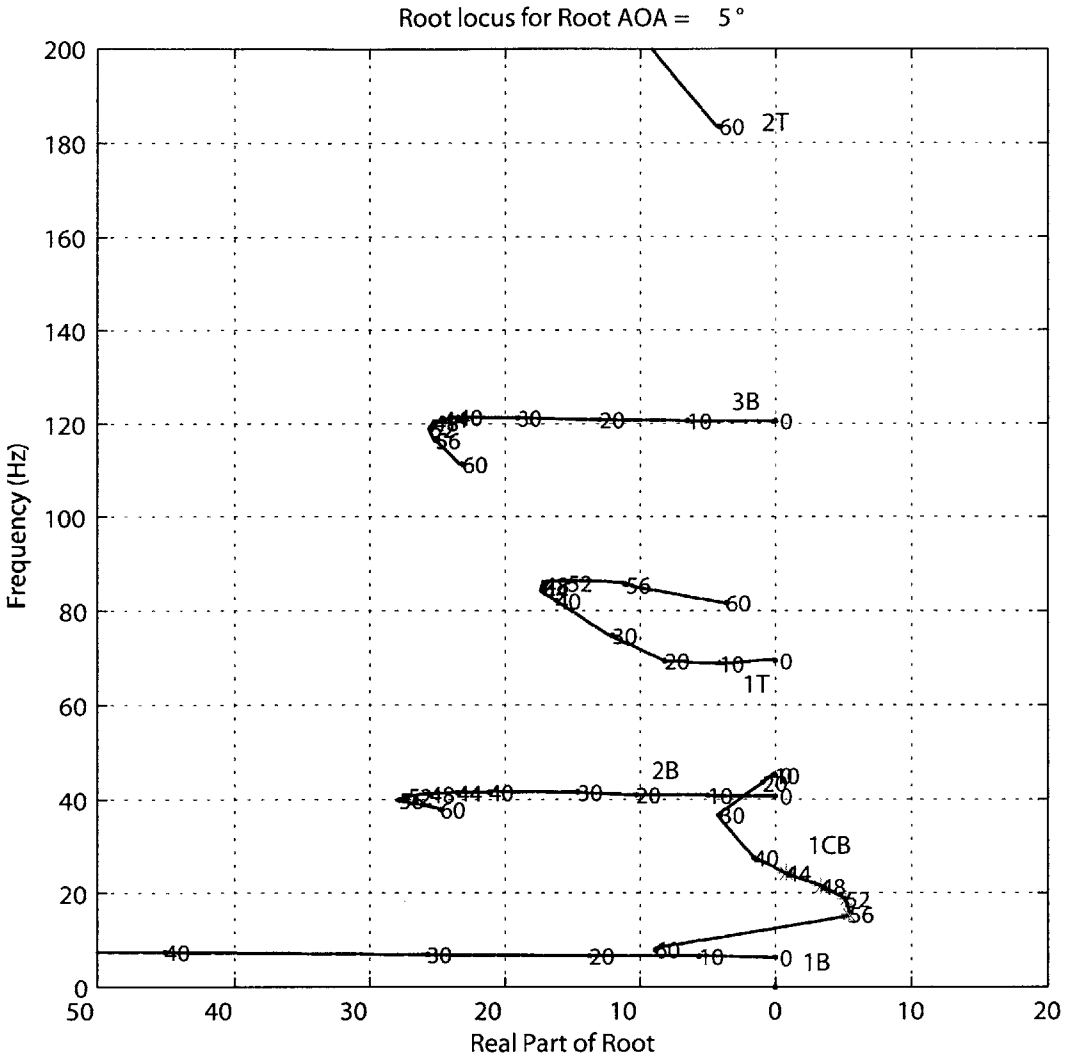

Figure 4-17: Root locus plot for 5° root angle of attack based on modified wing stiffness properties

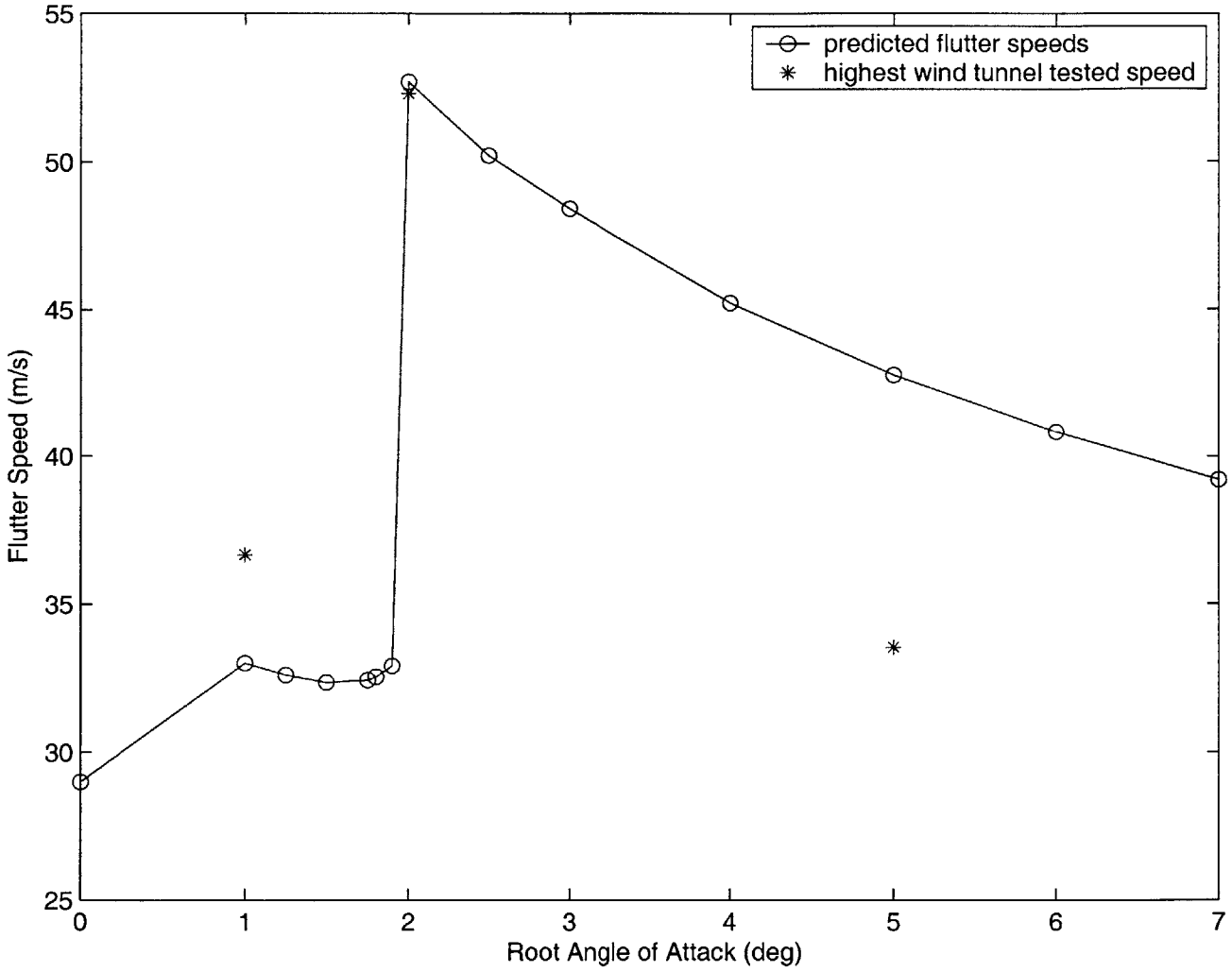

Figure 4-18: Predicted flutter speeds for various root angles of attack based on modified wing stiffness properties

current wing, however, the behavior of the wing at 1° is not believed to be accurate, as is proved during the wind tunnel tests. As will be discussed in more detail later, the wing was flown in the tunnel up to 82 m/s at 1° angle of attack, which is 250% above this predicted flutter speed.

For this reason the analytical model was again adjusted. A point mass was placed at 42% of the span to simulate the line of epoxy which joined the foam. The size of the point mass was adjusted until the second bending frequency matched the measured 38 Hz. The density of the foam was adjusted so that the first bending frequency returned to 6.44 Hz after the addition of this new mass. Table 4.5 provides a summary of the final values for the adjusted parameters.

Table 4.5: Final values of adjusted parameters

Parameter	Original Value	Adjusted Value
wing span	1 m	1.038 m
ρ foam	30 kg/m^3	94.5 kg/m^3
Q_{66} E-glass/epoxy	4.10 GPa	3.265 GPa
E_t foam	36 MPa	558 MPa
Point mass @ 46% span	0 kg	0.0286 kg

With this last adjustment, the first four predicted frequencies match those measured. Table 4.6 shows the frequencies values while Figure 4-19 shows the corresponding mode shapes.

These new dynamic characteristics resulted in a change in the aeroelastic behaviour of the wing. The new stability characteristics are shown in the root locus plots provided in Figure 4-20, Figure 4-24, Figure 4-28, and Figure 4-32. A magnified portion of these graphs for 0°, 1°, and 2° root angles of attack is provided in Figures 4-21, 4-25, and 4-29. The data is also presented in V-g plot format, which is provided in Figure 4-22, Figure 4-23, Figure 4-26, Figure 4-27, Figure 4-30, Figure 4-31, Figure 4-33, and Figure 4-34.

Table 4.6: Final natural frequencies from wing analysis

Mode	Calculated Frequency	Measured Frequency	% Error	Mode Shape
1	6.44 Hz	6.4 Hz	0%	1^{st} Bending
2	38.0 Hz	38 Hz	0%	2^{nd} Bending
3	45.0 Hz	45 Hz	0%	1^{st} Chordwise Bending
4	70.0 Hz	70 Hz	0%	1^{st} Torsional
5	123 Hz	-	-	3^{rd} Bending
6	216 Hz	-	-	2^{nd} Torsional

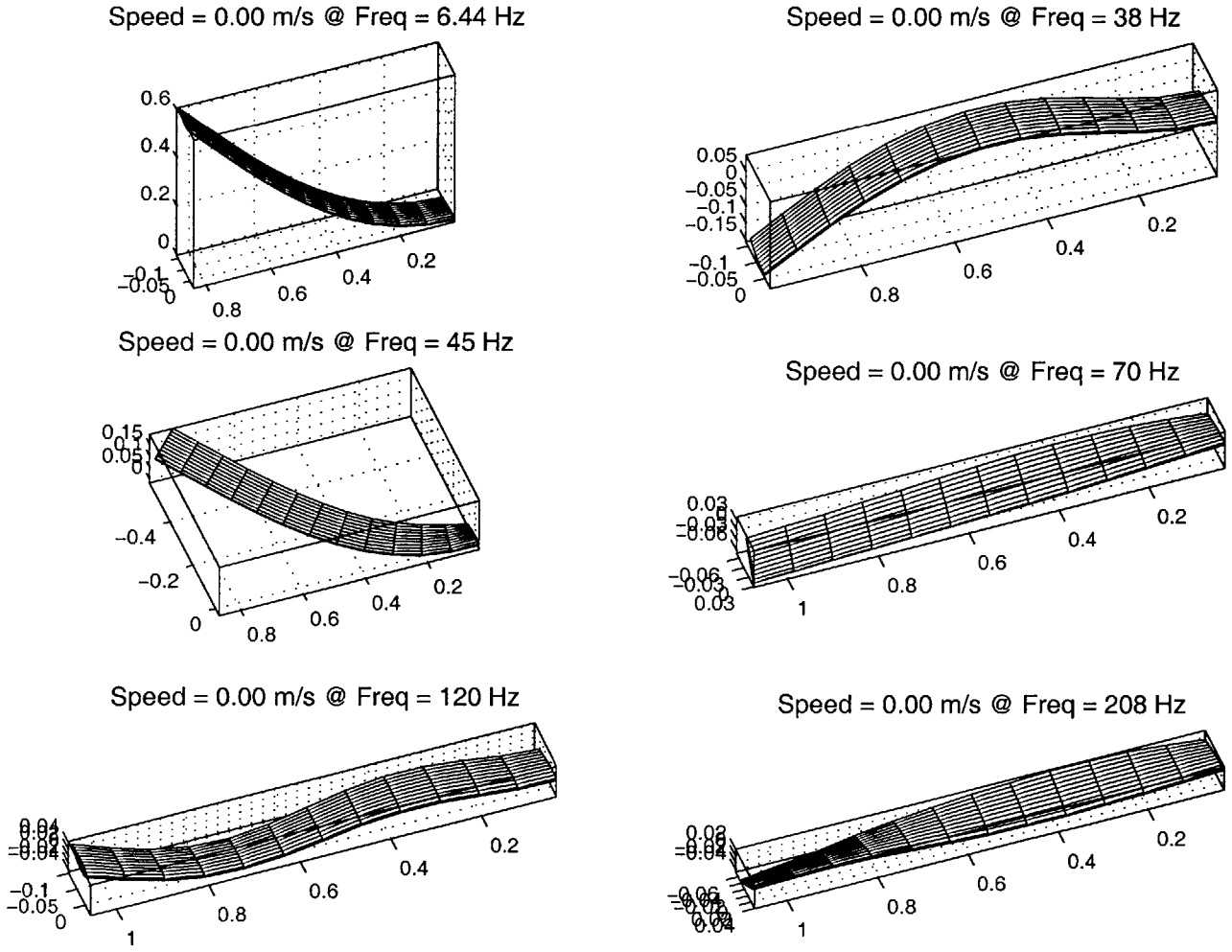

Figure 4-19: Predicted mode shapes after final modifications of different wing properties

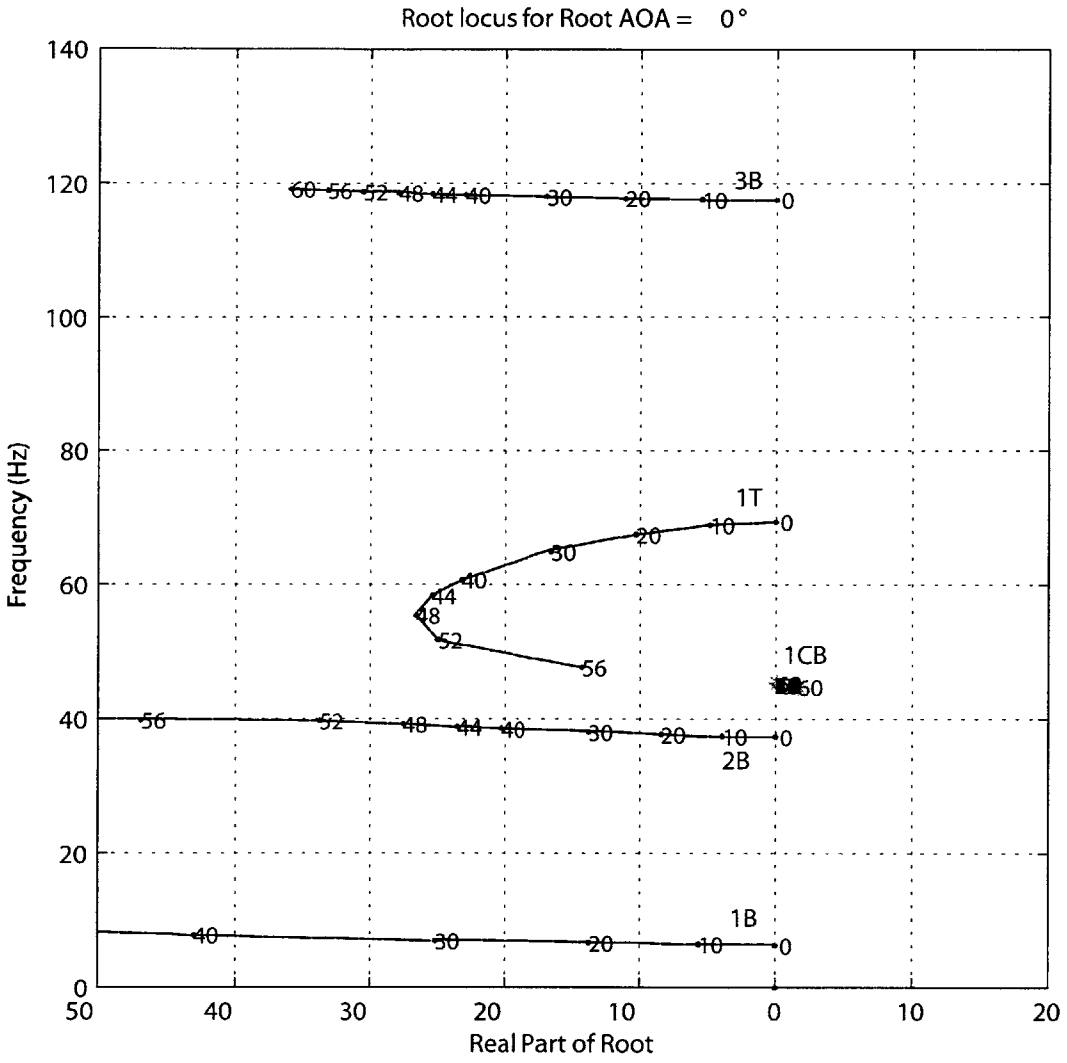

Figure 4-20: Root locus plot for 0° root angle of attack based on final modifications of different wing properties

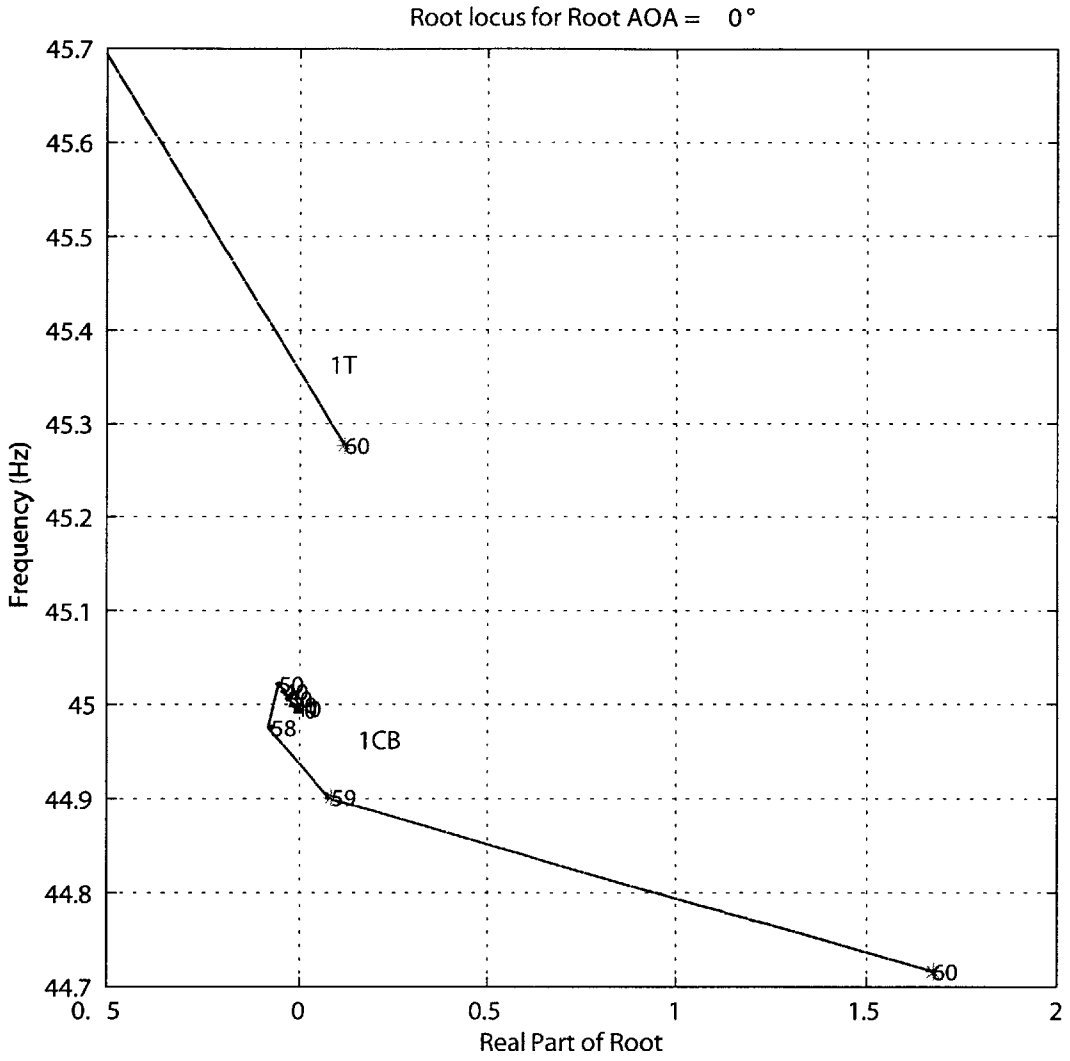

Figure 4-21: Magnified root locus plot for 0° root angle of attack based on final modifications of different wing properties

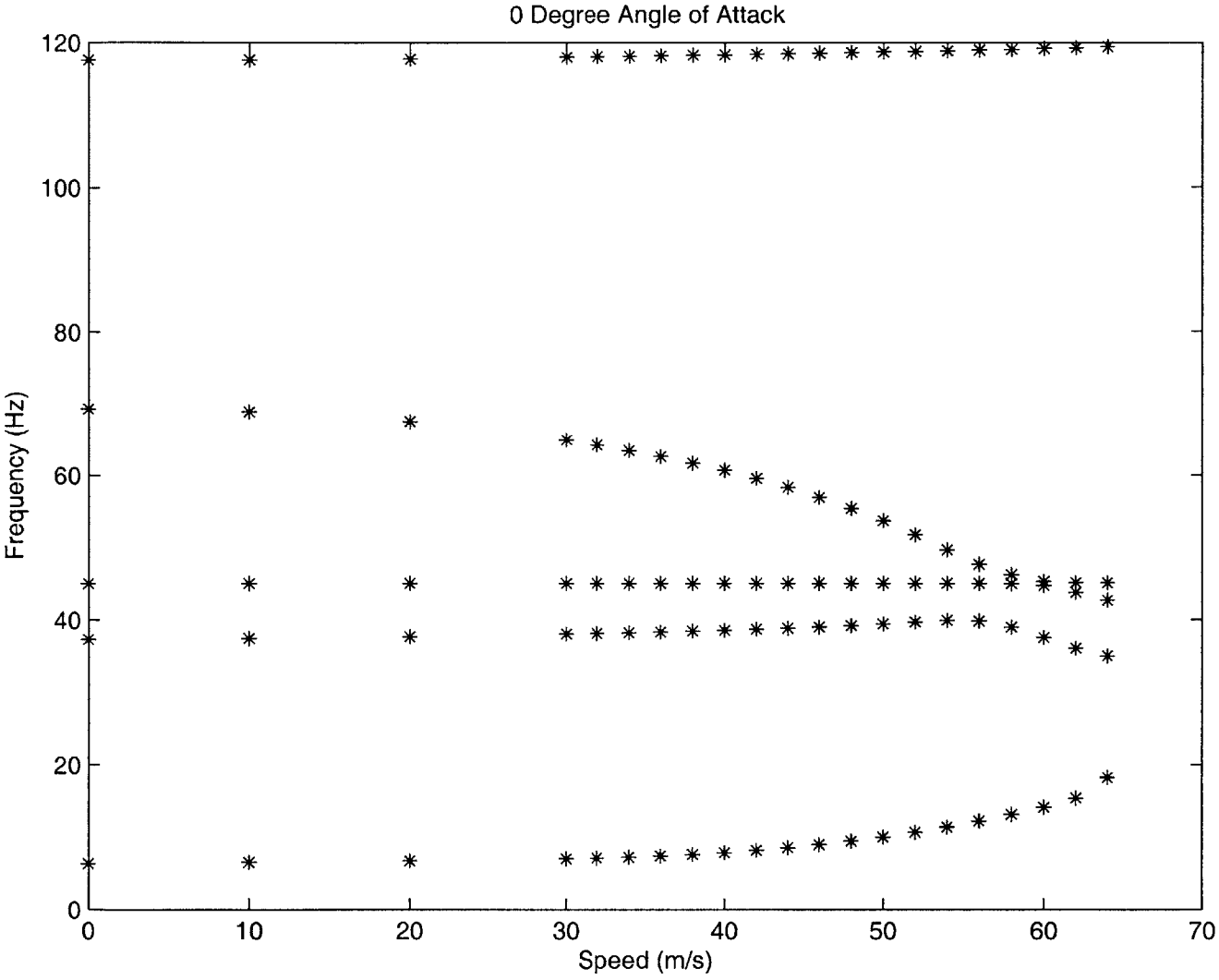

Figure 4-22: V-g (frequency part) for 0° root angle of attack based on final modifications of different wing properties

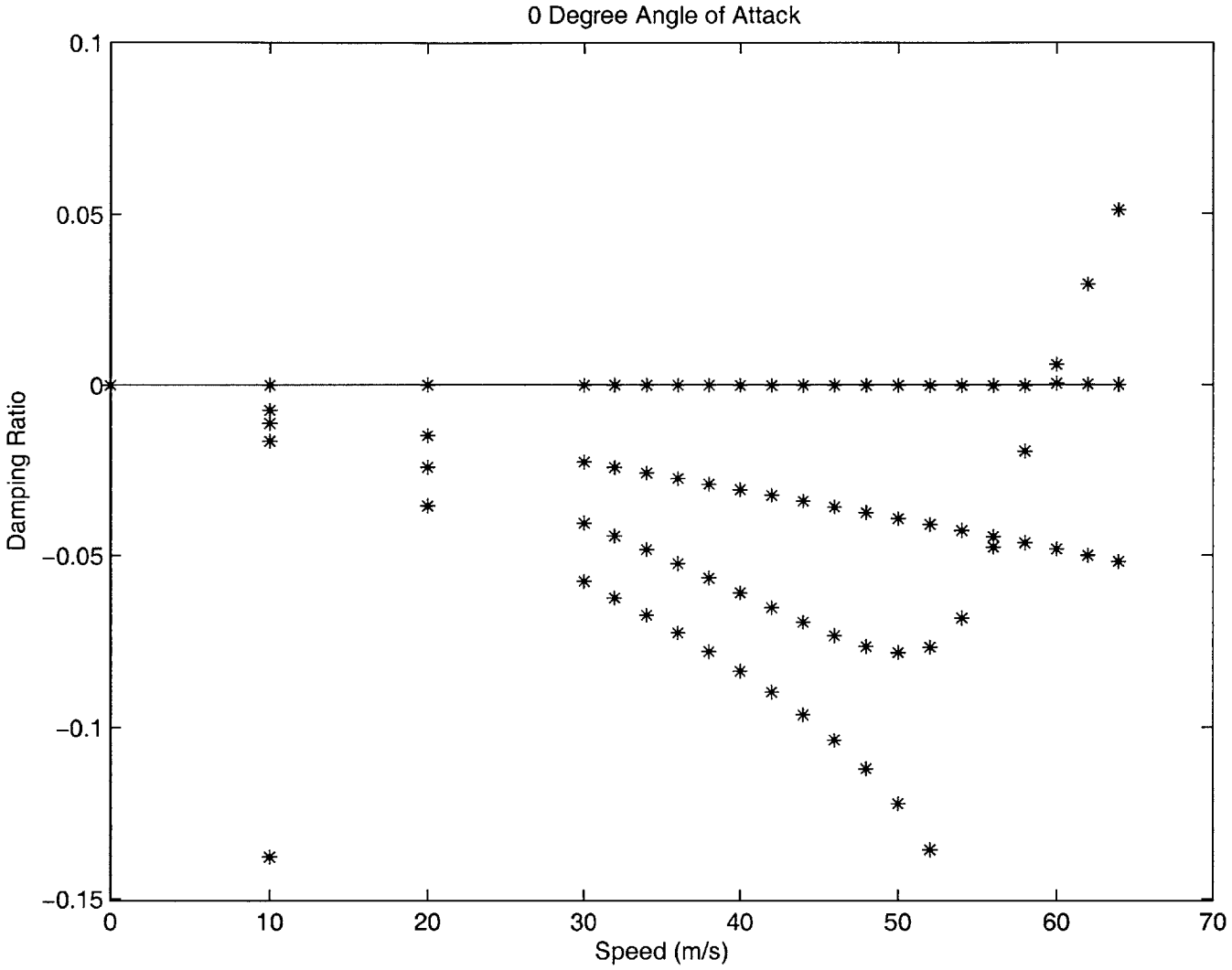

Figure 4-23: V-g (damping part) for 0° root angle of attack based on final modifications of different wing properties

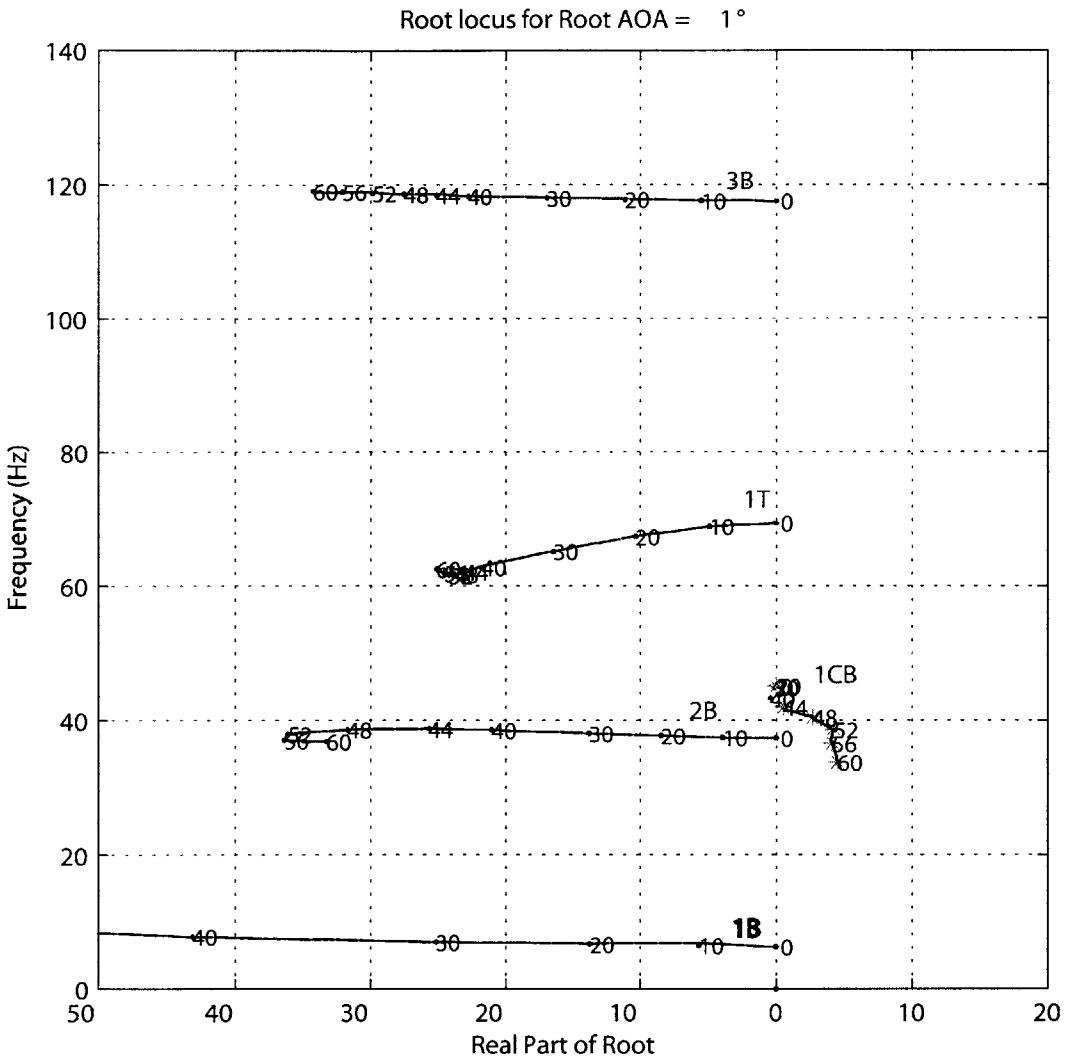

Figure 4-24: Root locus plot for 1° root angle of attack based on final modifications of different wing properties

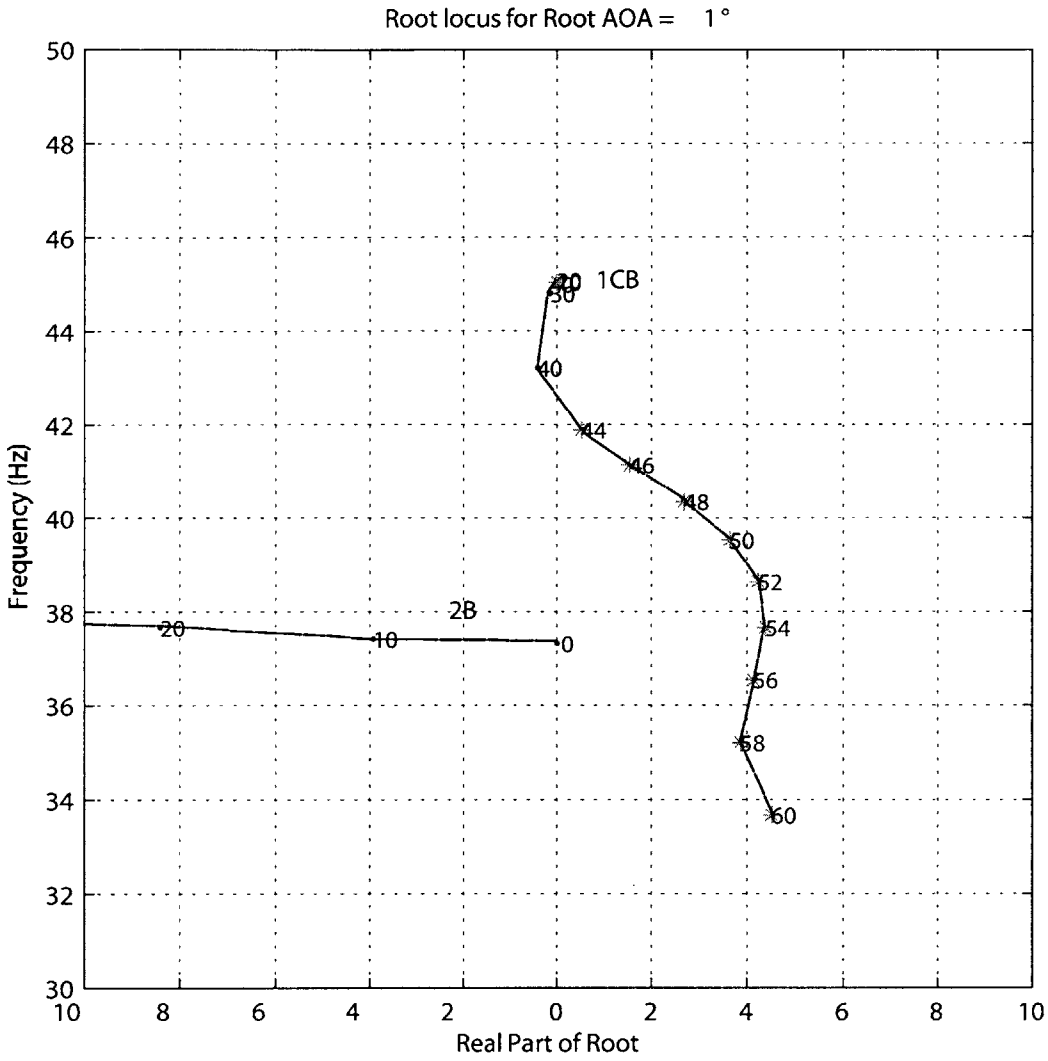

Figure 4-25: Magnified root locus plot for 1° root angle of attack based on final modifications of different wing properties

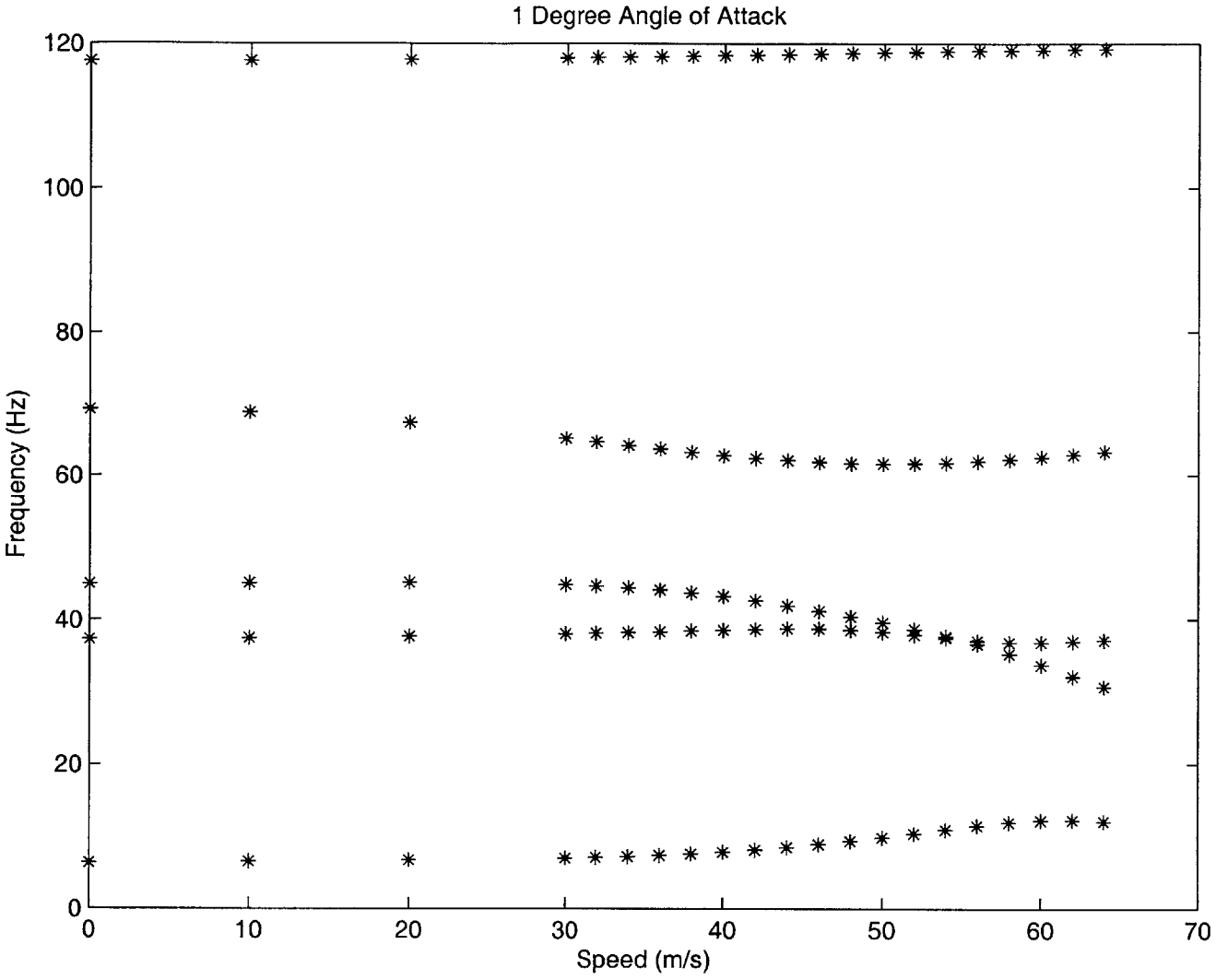

Figure 4-26: V-g (frequency part) for 1° root angle of attack based on final modifications of different wing properties

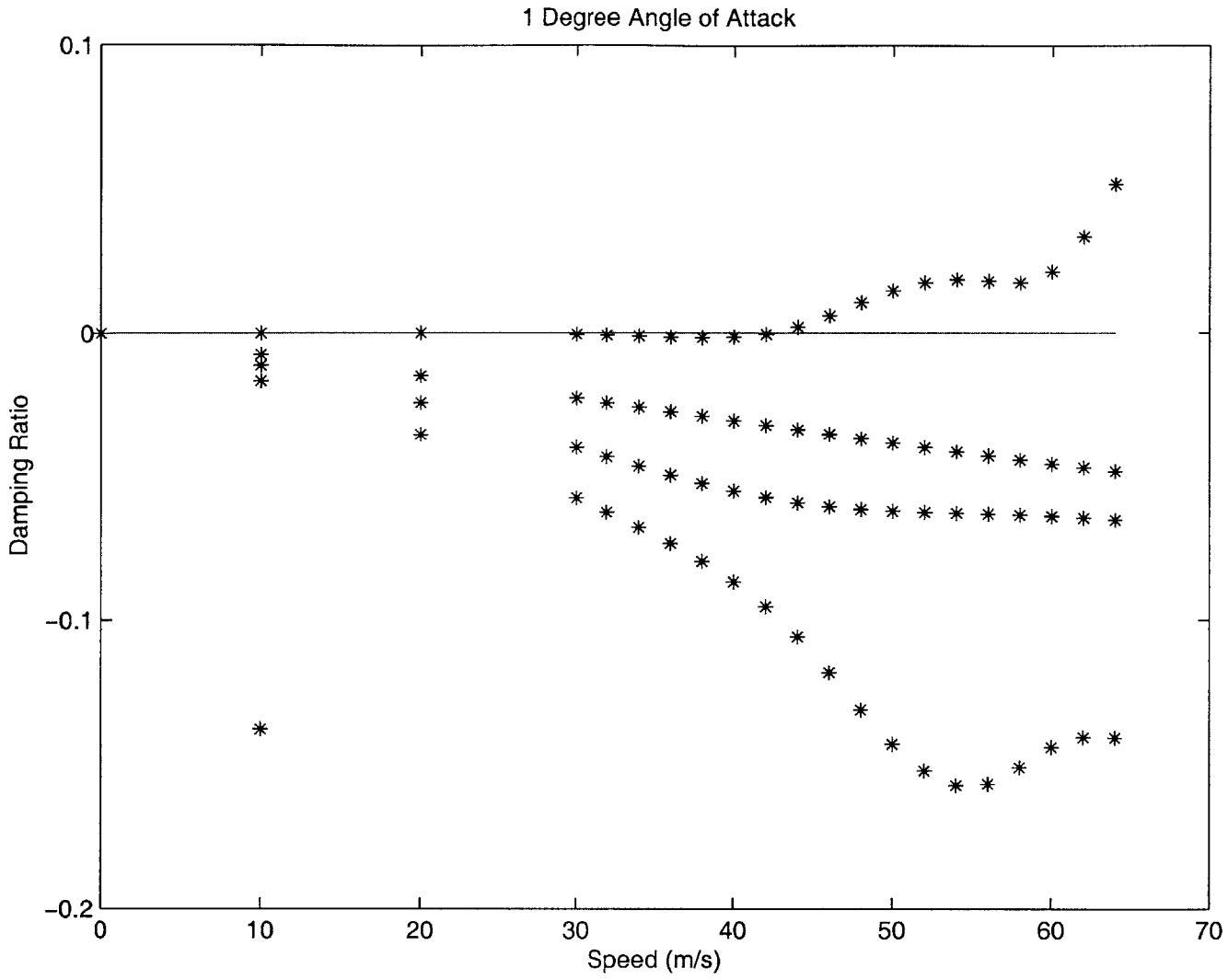

Figure 4-27: V-g (damping part) for 1° root angle of attack based on final modifications of different wing properties

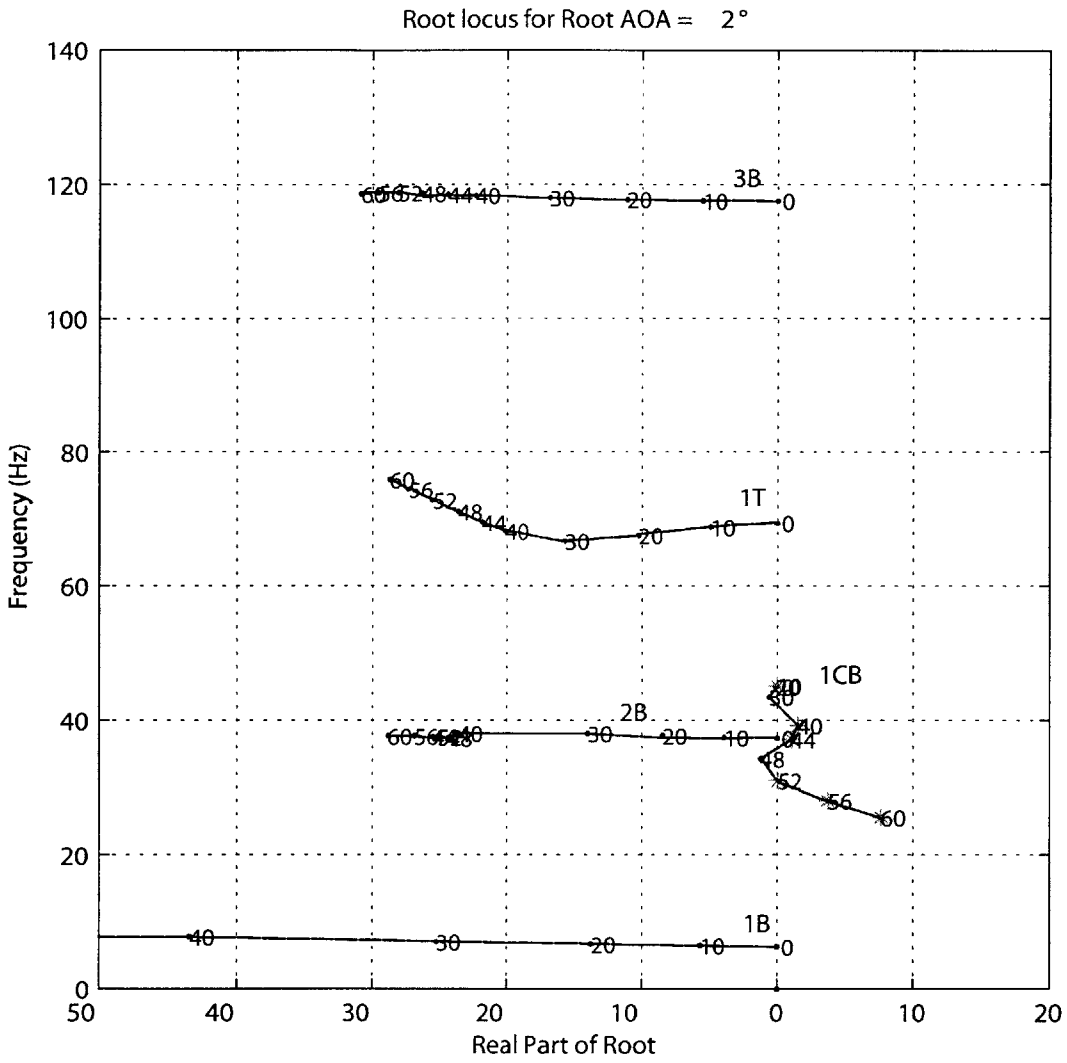

Figure 4-28: Root locus plot for 2° root angle of attack based on final modifications of different wing properties

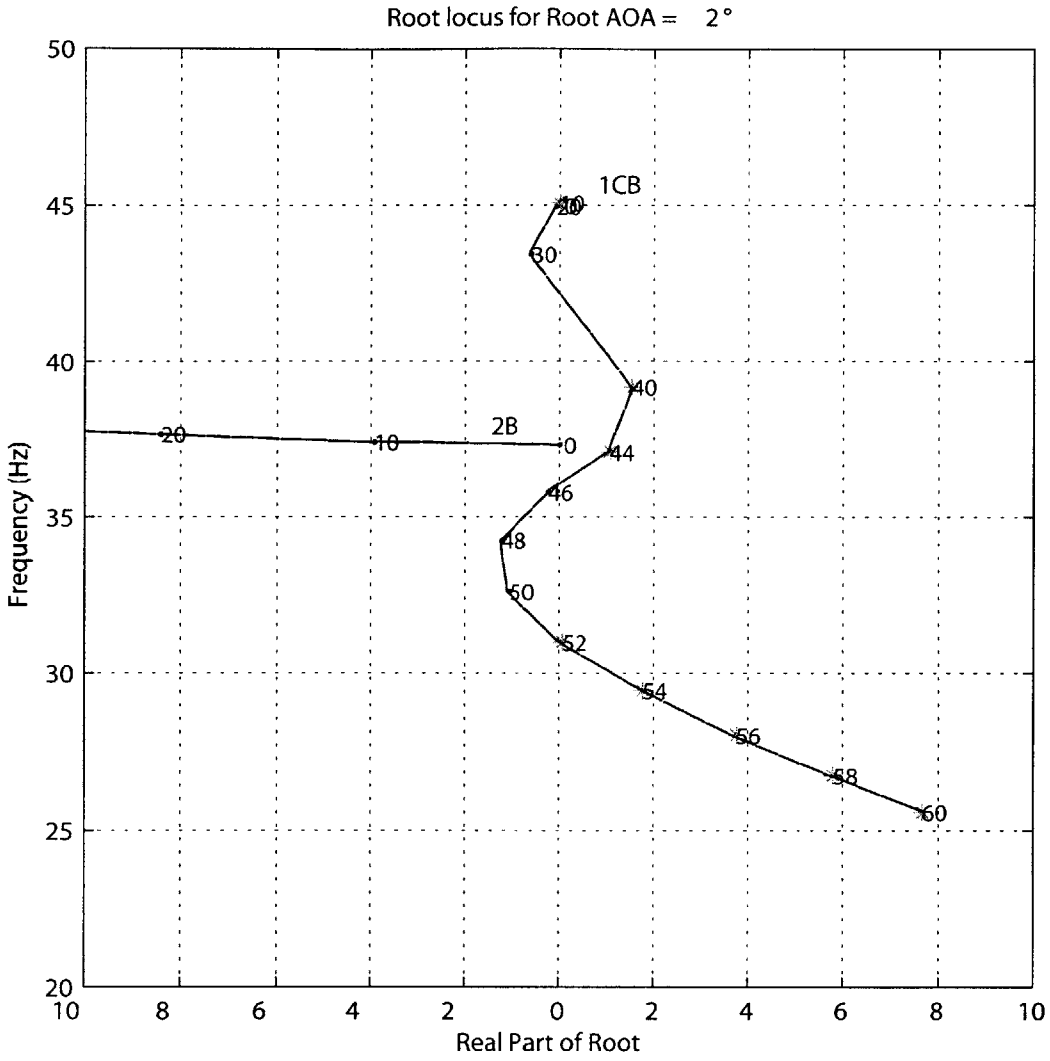

Figure 4-29: Magnified root locus plot for 2° root angle of attack based on final modifications of different wing properties

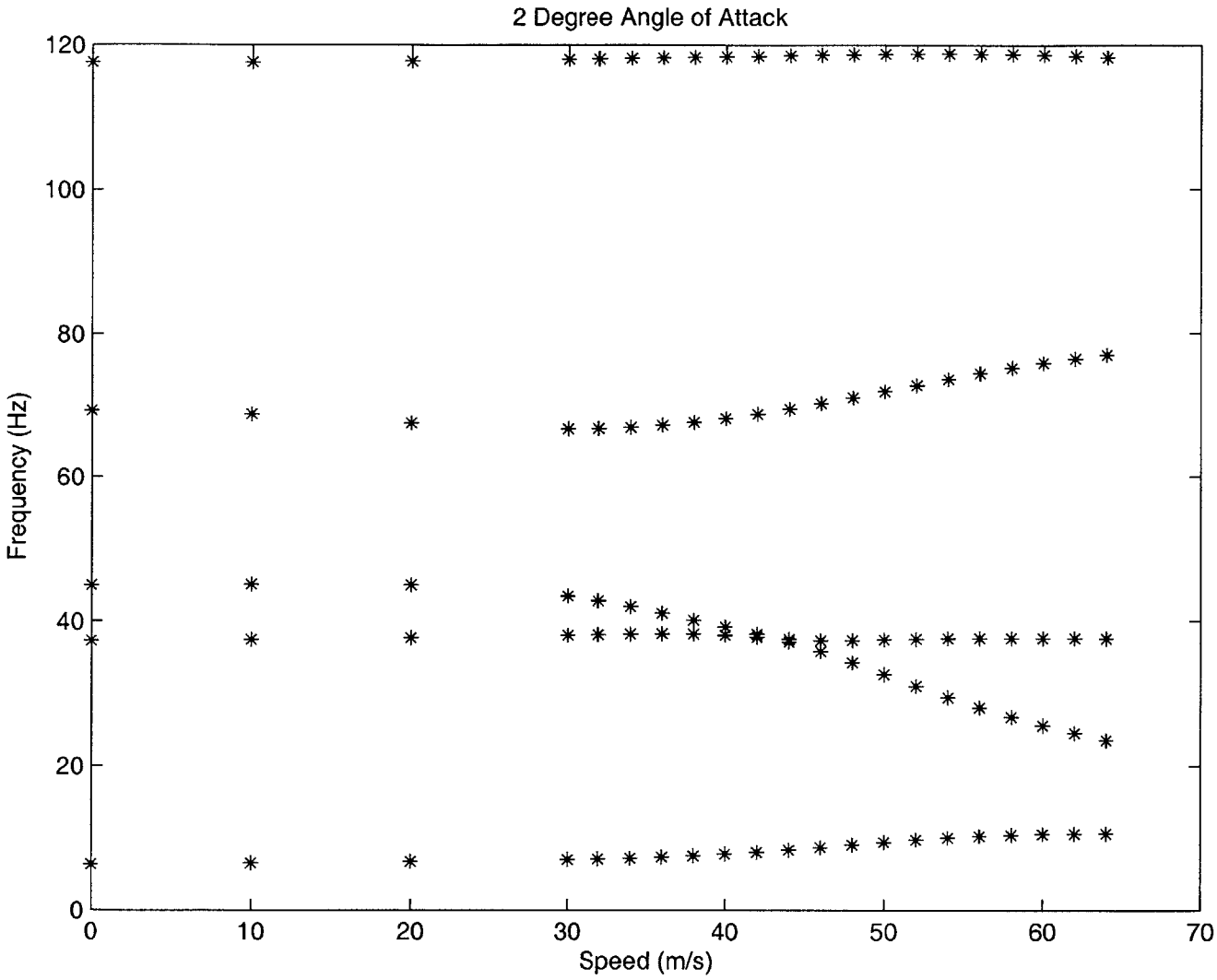

Figure 4-30: V-g plot (frequency part) for 2° root angle of attack based on final modifications of different wing properties

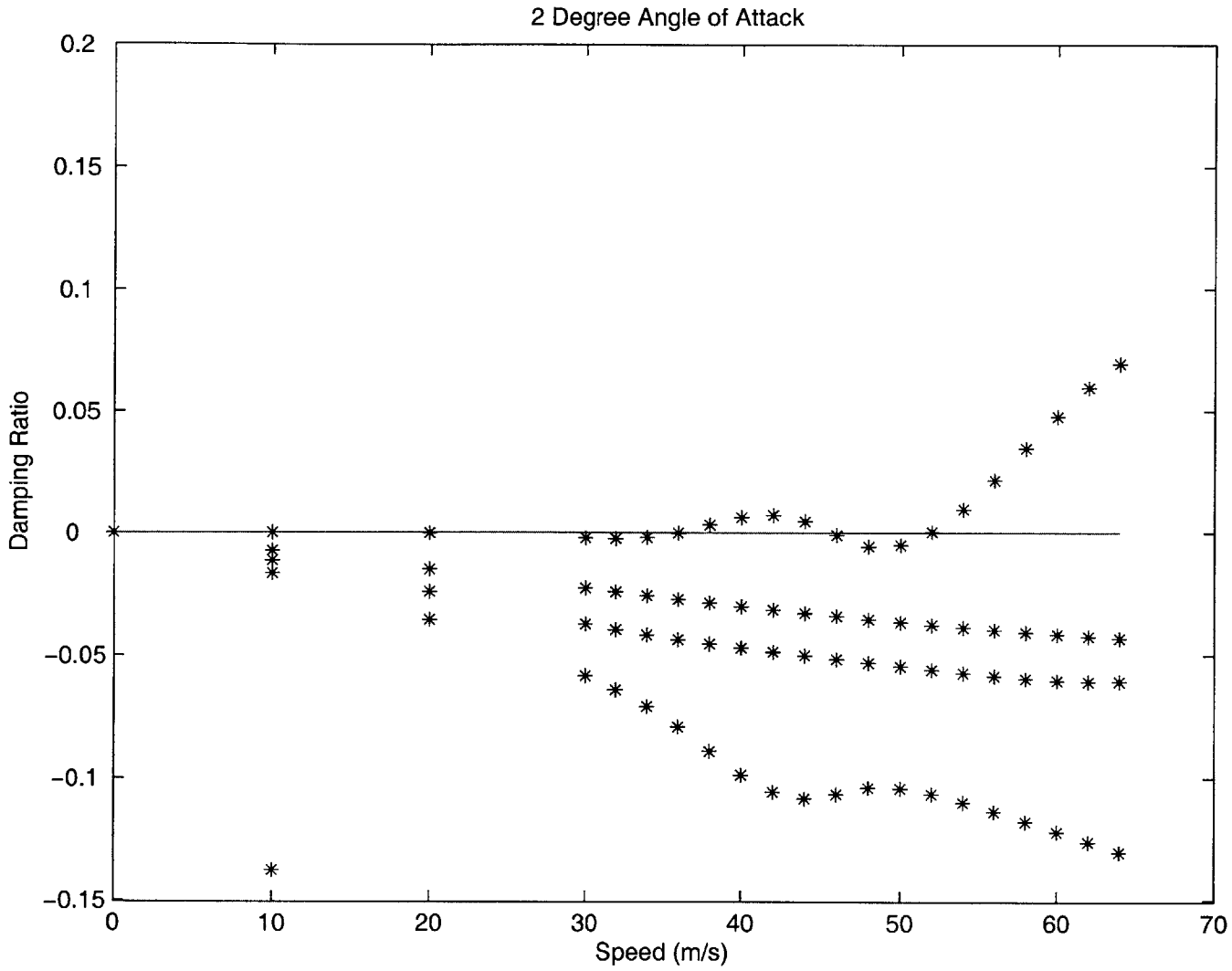

Figure 4-31: V-g plot (damping part) for 2° root angle of Attack based on final modifications of different wing properties

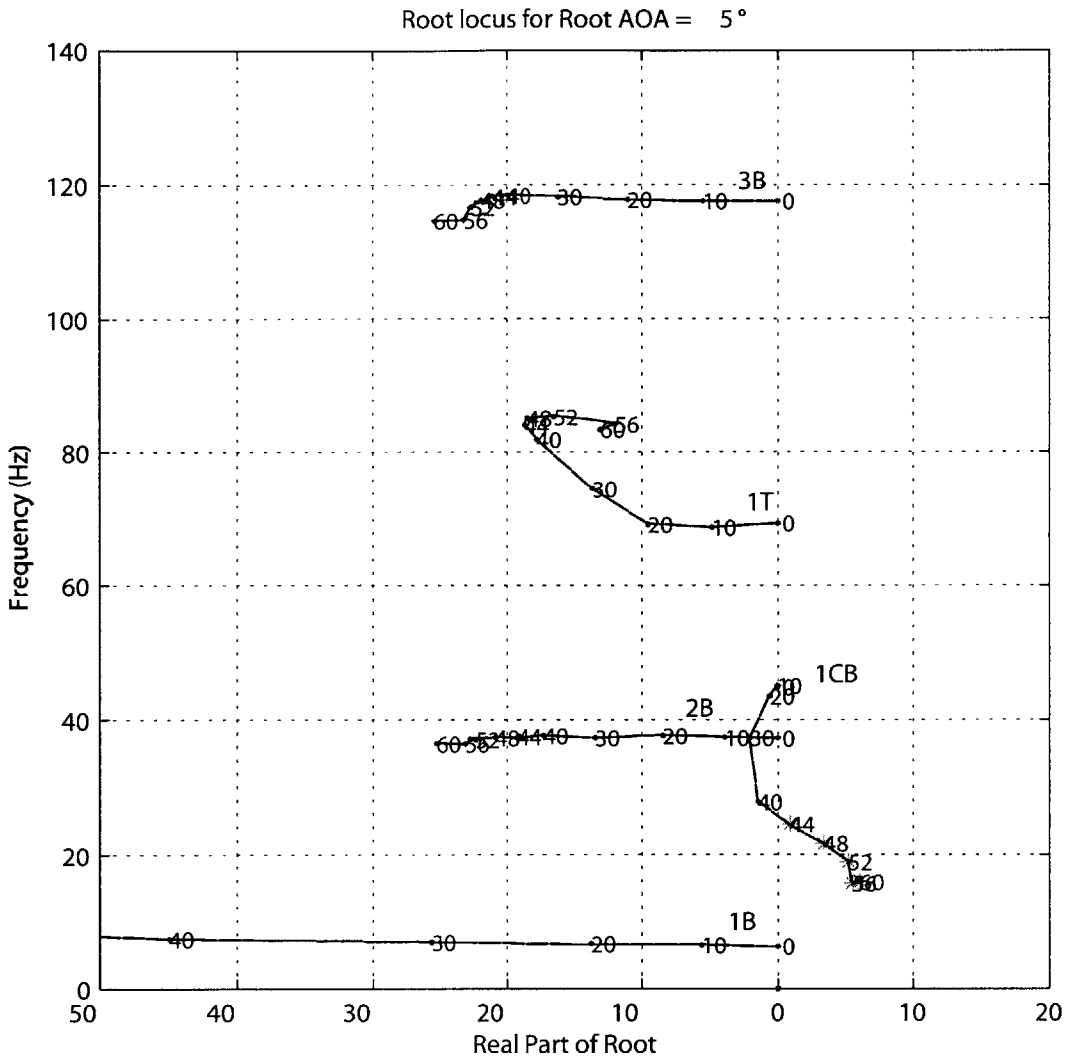

Figure 4-32: Root locus plot for 5° root angle of attack based on final modifications of different wing properties

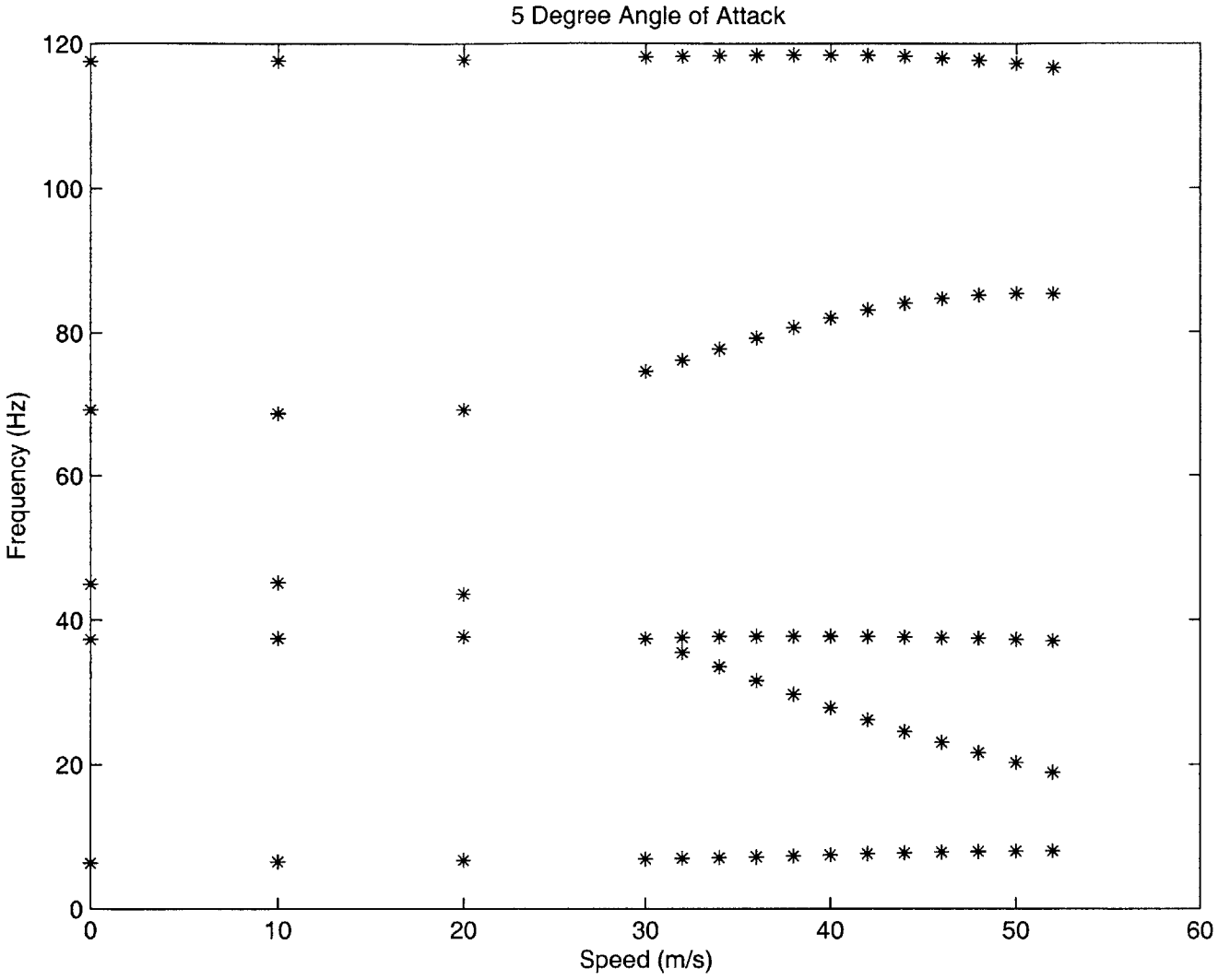

Figure 4-33: V-g (frequency part) for 5° root angle of attack based on final modifications of different wing properties

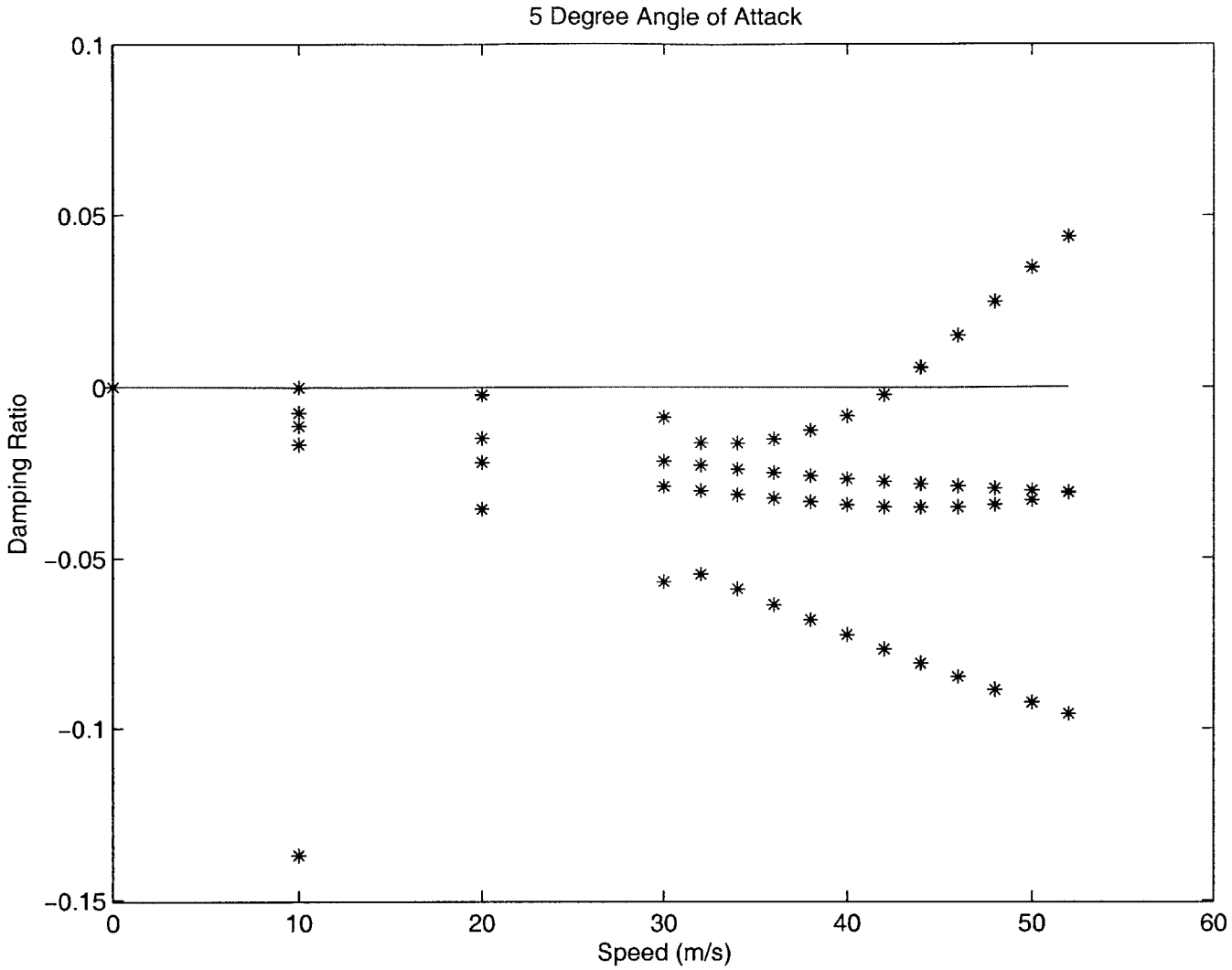

Figure 4-34: V-g (damping part) for 5° root angle of attack based on final modifications of different wing properties

The strange behaviour observed at 1° root angle of attack in the stiffness adjustments has shifted and is now occuring at 2°. By plotting the data in V-g plots, it was determined that the wing is experiencing hump flutter at the lower speed. The mode would not be seen experimentally, as a very small structural damping within the system would have negated the weak flutter seen at the first crossing of the instability axis. The second crossing, at 51.8 m/s for 2° angle of attack, is a much stronger flutter and would manifest itself during experimentation. The predicted flutter speeds for this wing are provided in Table 4.7.

Table 4.7: Predicted flutter speeds with final model adjustments

Angle of Attack	Flutter Speed
1°	42.5 m/s
2°	51.8 m/s
5°	42.7 m/s

The curve for flutter speed versus root angle of attack is provided in Figure 4-35. The solid line represents the final predicted flutter speed. The dotted line shows the speed of the first crossing of the instability axis, or the hump mode speed, and is ignored for reasons mentioned above. The three individual points represent the maximum wind tunnel tested speeds.

4.3 Wind Tunnel Tests

The experimental portion of this thesis culminated with the wind tunnel tests. A photo of the wing in the tunnel is provided in Figure 4-36. Once the set-up was completed, calibration tests were performed before starting the actual tunnel tests. During the wind tunnel tests, four strain gauges were monitored—root bending, root torsion, forward/aft (located at 45% of span) and another bending (located at 35% of span).

4.3.1 Wing Calibration in the Wind Tunnel

As with the bench-top tests, a calibration of the strain gauges with the wing in the tunnel was performed to determine the deflection-to-voltage ratio of the bridges as different conditioners were being used. The deflection was produced in a slightly different manner for the tunnel tests. Weights were suspended from the wing at various locations along the chord at 2/3 the span of the wing (Figure 4-37).

Three different tests were performed with these weights, which were suspended from the wing via a hanger (17 gm). The first test used 217 gm (2.13 N) from the wing at points along the wing chord. This test was to locate the elastic axis. The location of the elastic axis

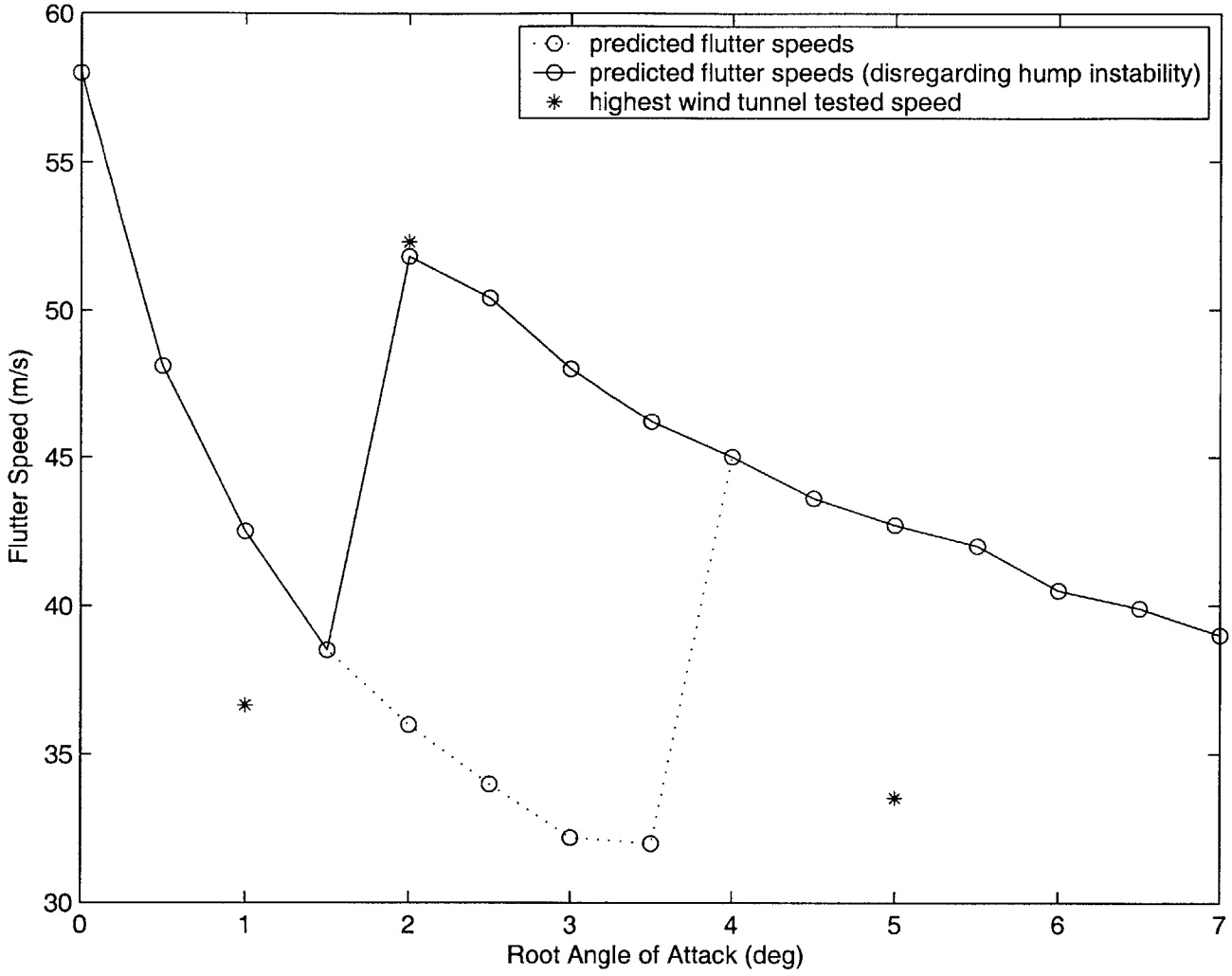

Figure 4-35: Predicted flutter speed for various root angles of attack

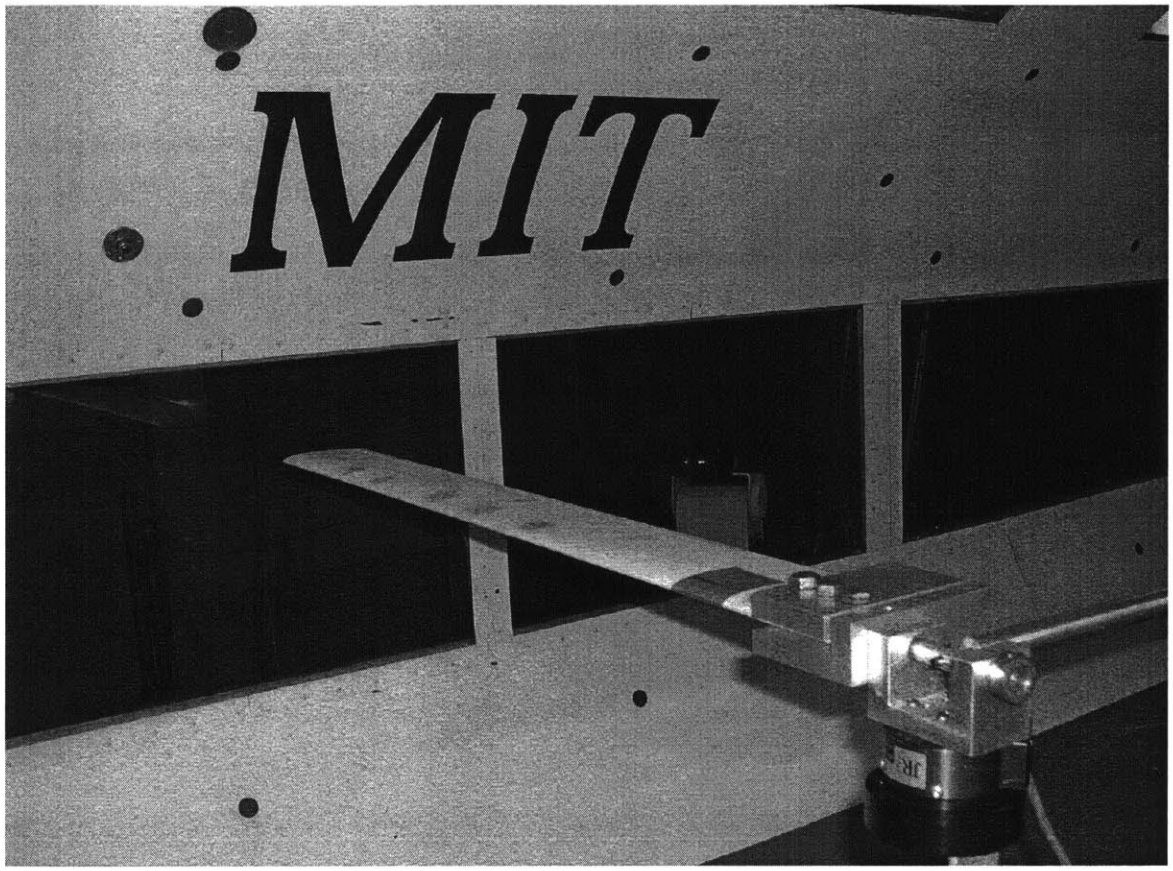

Figure 4-36: Wing set-up in the Wright Brothers wind tunnel

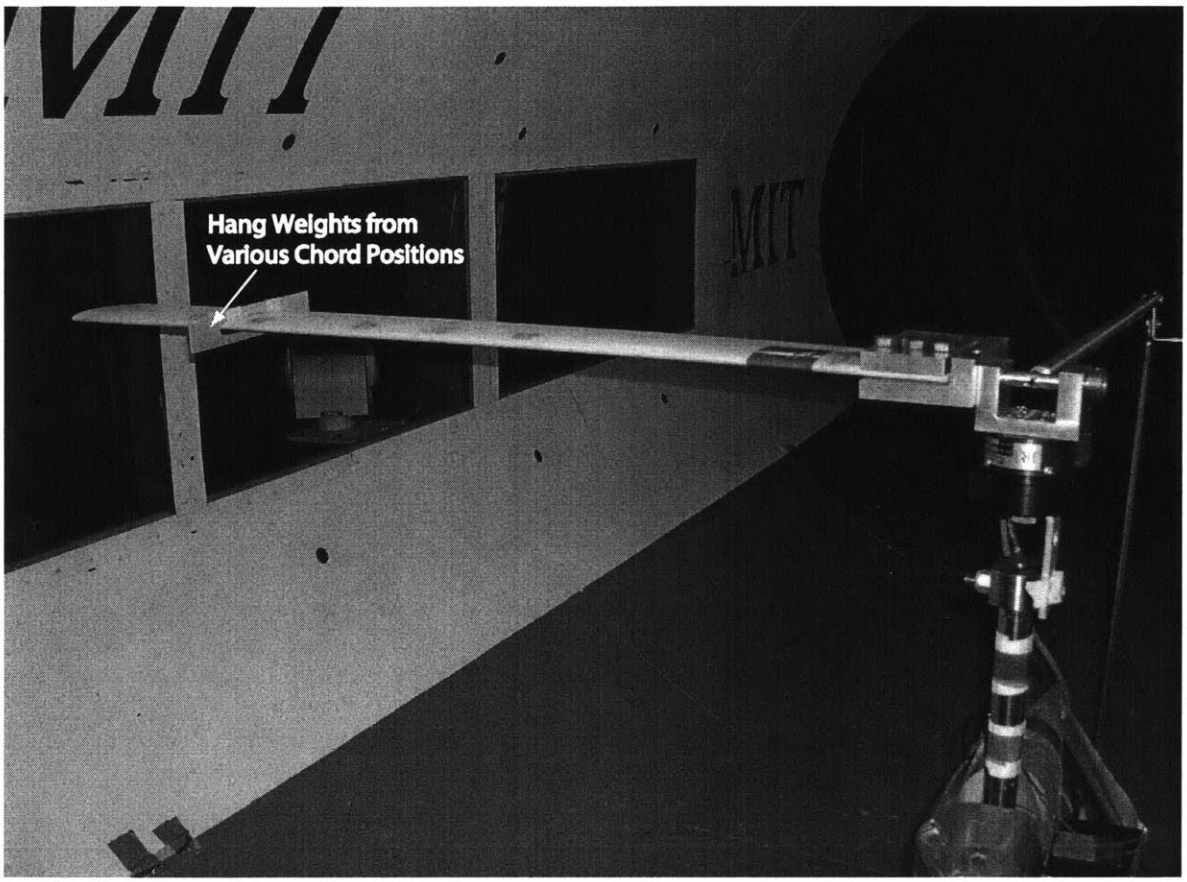

Figure 4-37: Set-up for hanging weights to calibrate strain gauges

was determined to be at 73% of the chord from the leading edge. This result contradicts the analytical expectation of 30% of the chord. This is due to the location of the strain gauge used to calculate this result. The root torsion gauge was used and is located about 10 mm from the clamp. The area near the clamp is subjected to end effects and does not behave according to St. Venant's principle. If the gauge was located at least a chord-length away from the clamp, the results would more accurately reflect the analytical value. A plot of the resulting strain gauge output is provided in Figure 4-38.

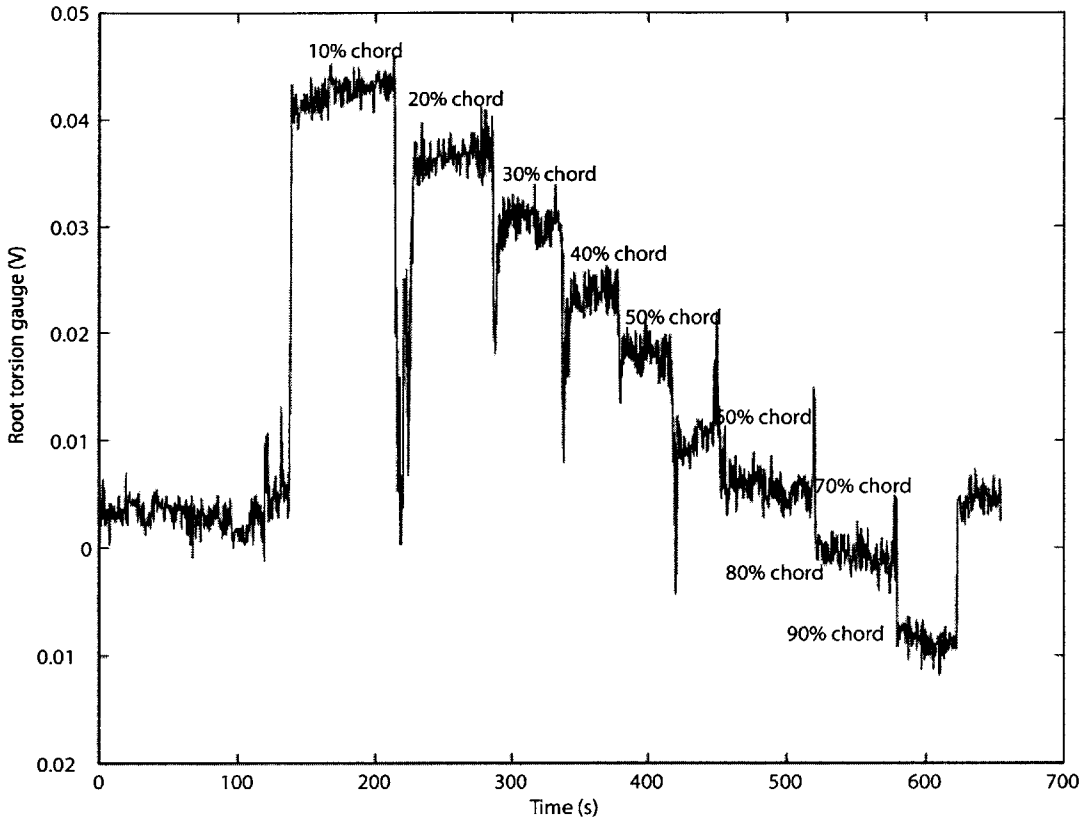

Figure 4-38: Time trace for elastic axis determination

The second test was to hang weights— 117 gm (1.147 N), 217 gm (2.128 N), and 317 gm (3.109 N)— at 50% of the chord to calibrate the strain gauge output due to bending. The locations of the leading and trailing edges at the wing tip were recorded for each weight as well. This was accomplished by first measuring the height of the unloaded wing tip (leading

and trailing edge) and then the height for all subsequent loadings. A time trace of the strain gauge data is provided in Figure 4-39.

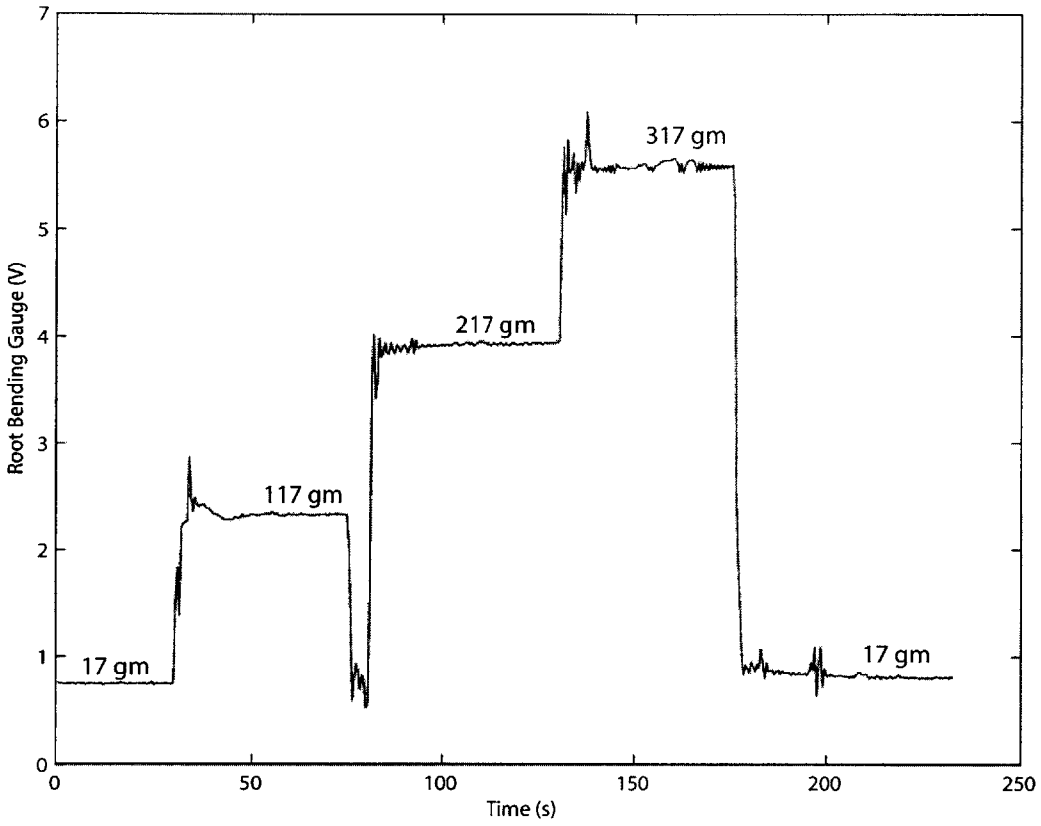

Figure 4-39: Time trace for wing loaded at 50% chord in wind tunnel

Finally this second test was repeated, except the weights were hung from 90% of the chord. This provided a second calibration for the gauges. A time trace of this data is shown in Figure 4-40.

A calibration curve for the root bending gauge as a function of voltage-to-bending moment at the root is provided in Figure 4-41. A curve for the root torsion gauge depicting the voltage-to-pitch moment at the root relation is given in Figure 4-42. To get the data from both loading cases to agree, the moment was found about an axis at 63.81% chord line. A curve for the other bending gauge provides the voltage-to-bending moment at 35% span (gauge location) and is shown in Figure 4-43.

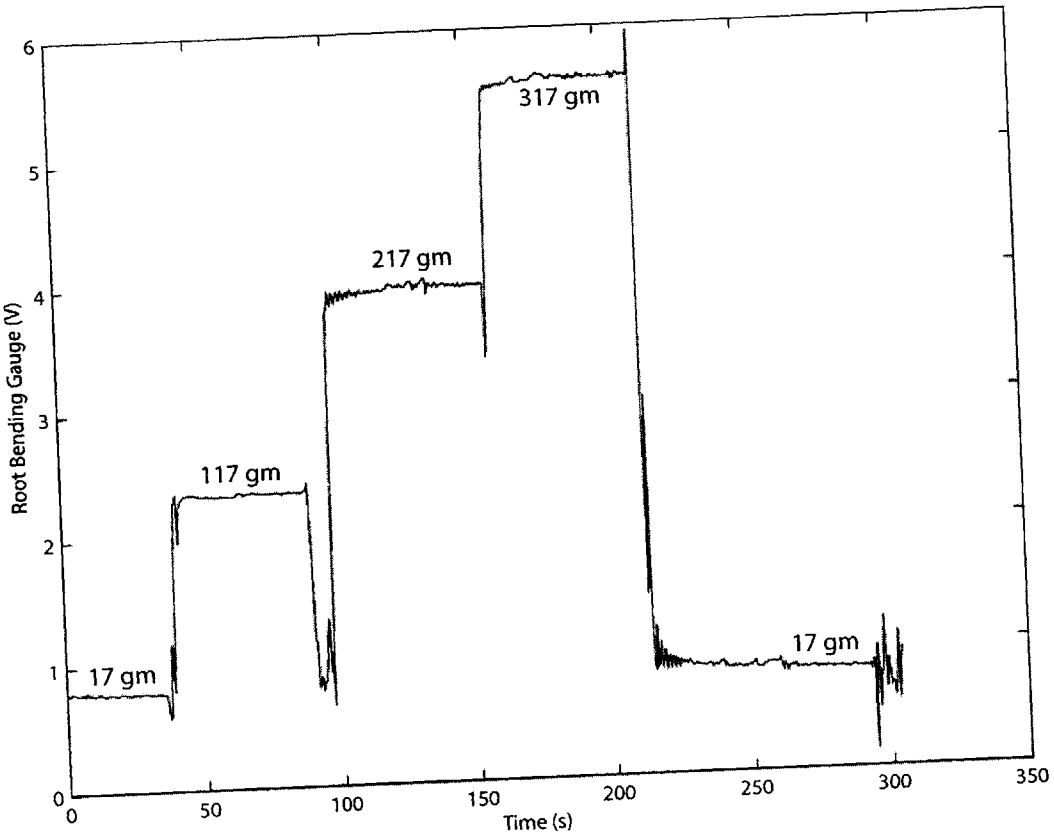

Figure 4-40: Time trace for wing loaded at 90% chord in wind tunnel

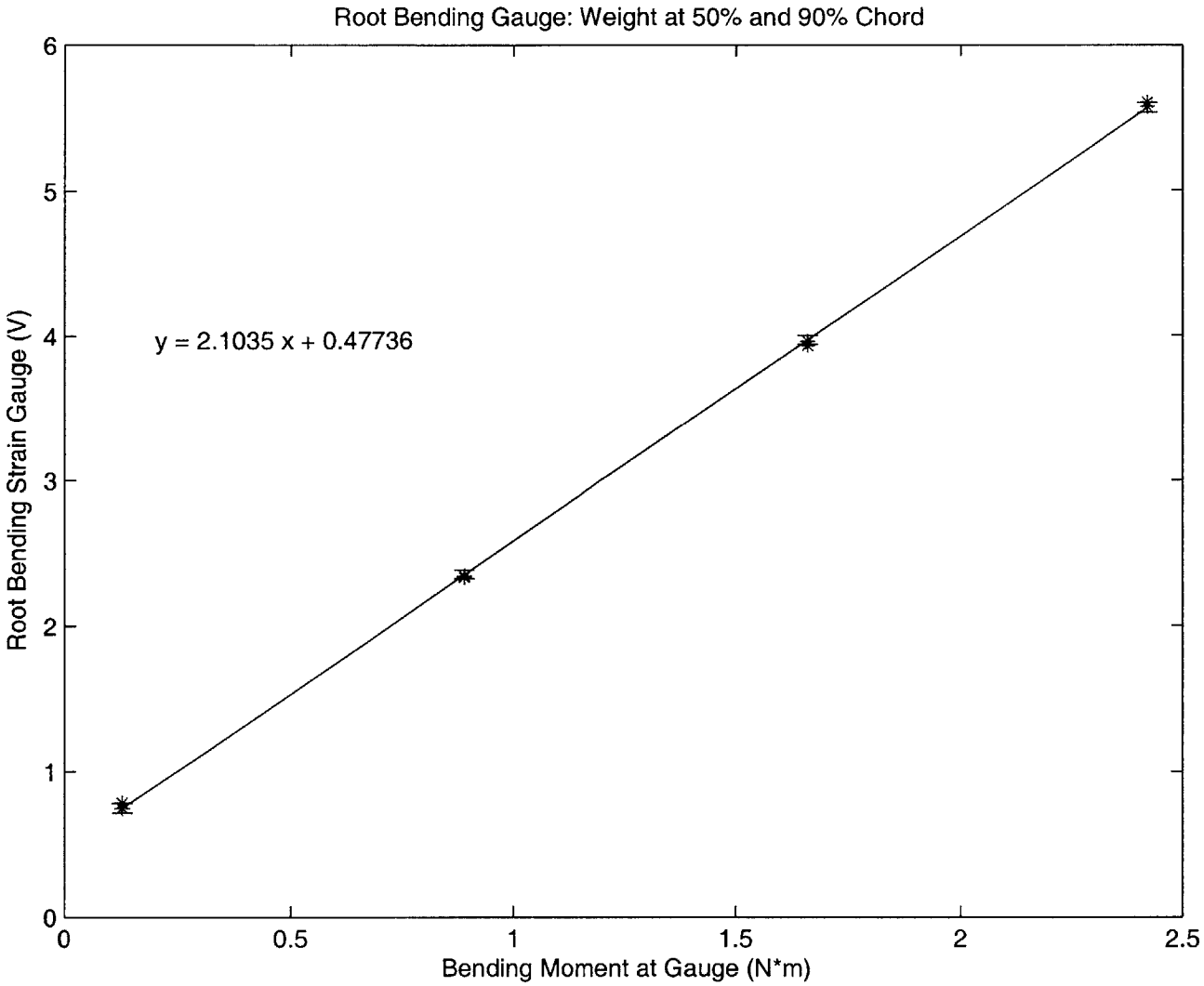

Figure 4-41: Calibration of root bending gauge from both 50% and 90% chord load cases

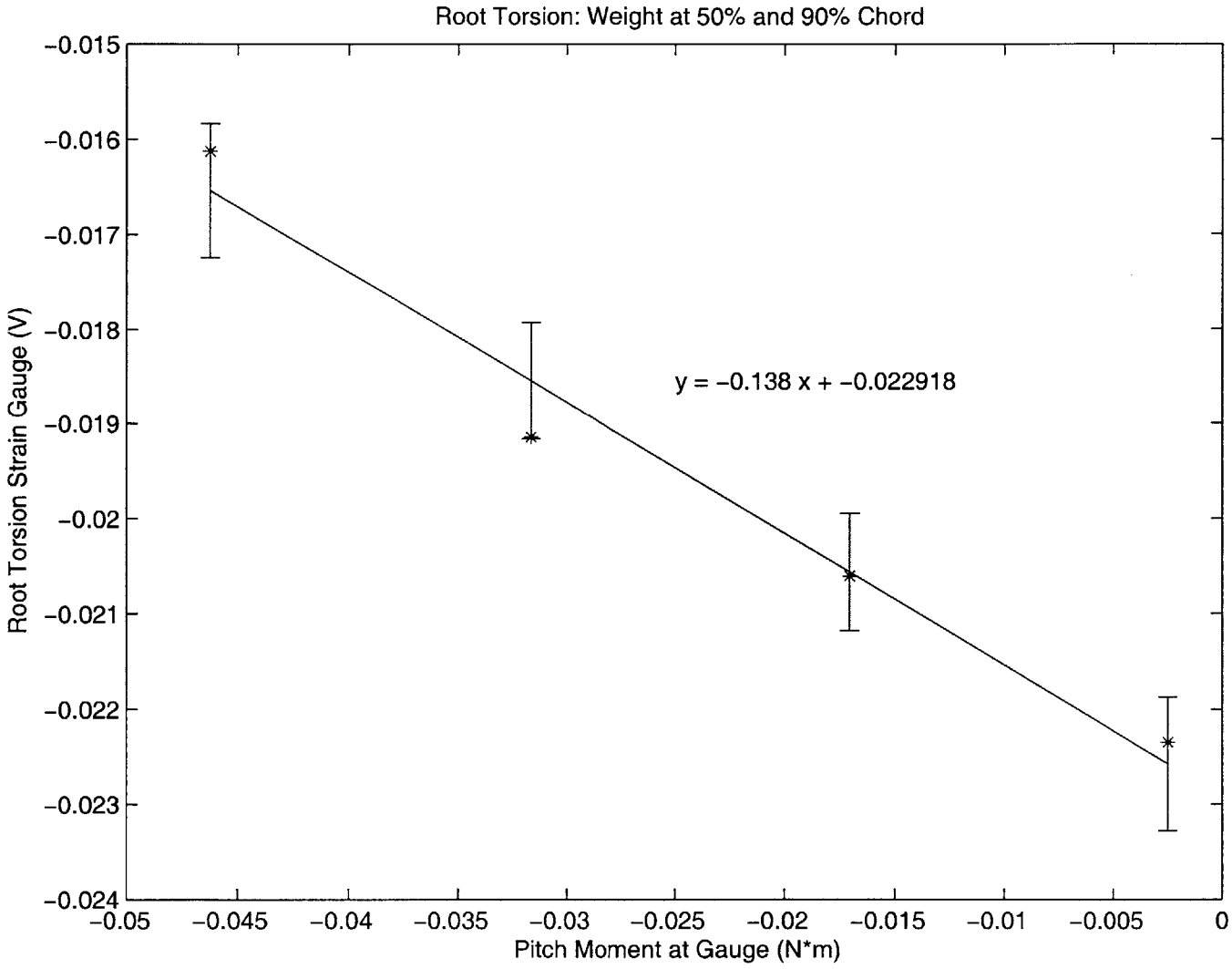

Figure 4-42: Calibration of root torsion gauge from both 50% and 90% chord load cases

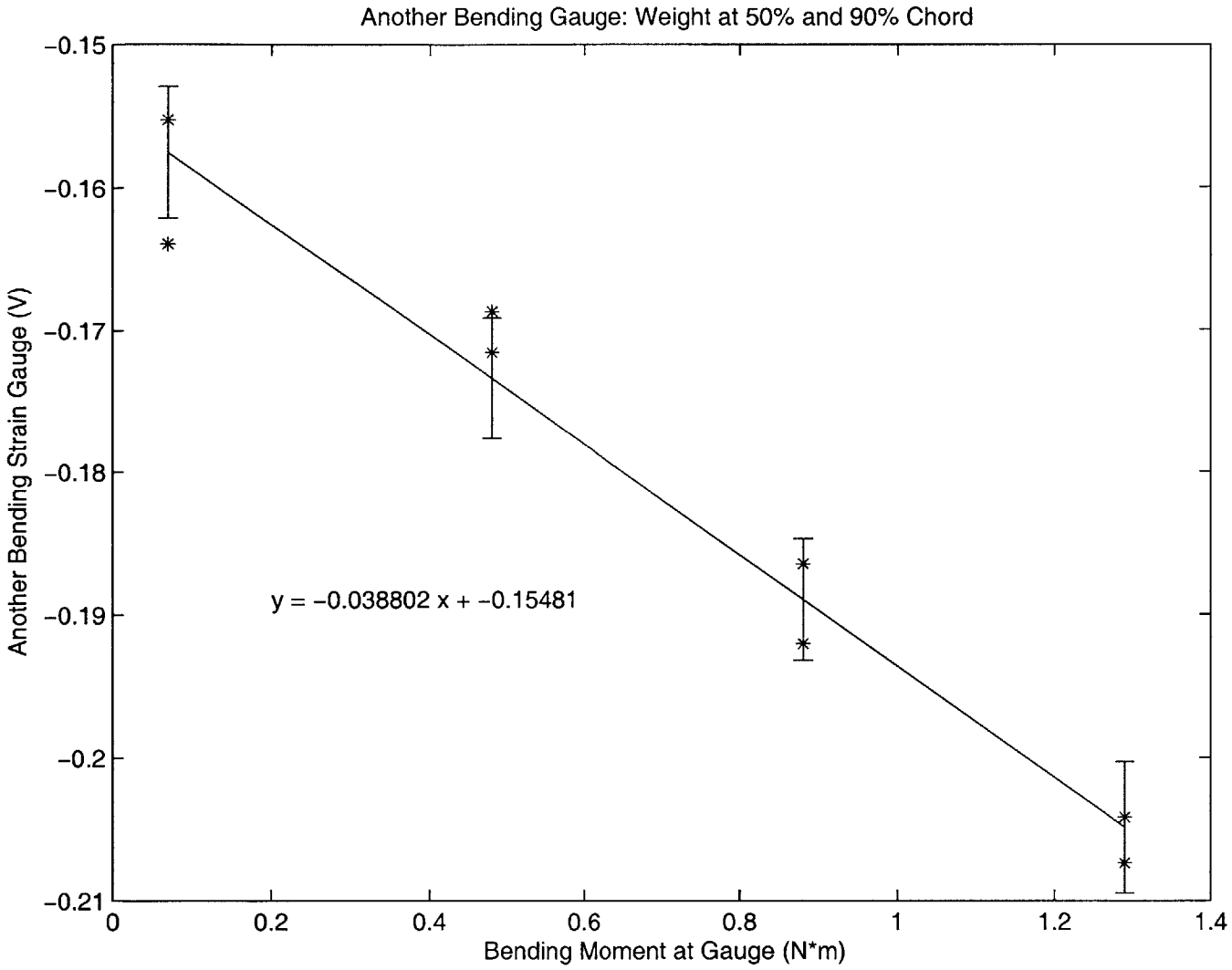

Figure 4-43: Calibration of other bending gauge (located at 35% span) from both 50% and 90% chord load cases

In addition to these static tests, the tap tests were also repeated. From these tap tests, the frequencies of the wing were confirmed with the new mounting set-up to be the same as in the bench, with the addition of three unexpected frequencies detected. A 15-Hz chorwise bending mode was introduced, due to flexibility of the load cell mounting. A mode at 20 Hz is present in most of the tunnel data, this is also believed to be associated with the flexibility of the load cell mounting. Another possibility is that some larger motors produce a 20-Hz dynamic disturbance. The 60-Hz mode is often found in dynamic data and is due to electricity noise. Data from the undisturbed system is provided in Figure 4-44. The 100 Hz dynamics is also believed to be either noise from the tunnel environment, as its magnitude is quite large, even in the undisturbed wing data. The graphs for the bending, torsion, and forward/aft taps are provided in Figure 4-45 through Figure 4-47.

The data from the root bending gauge shows the expected 6-Hz 1^{st} bending mode and the 38-Hz 2^{nd} bending mode. It also shows significant dynamics at 15 Hz and 20 Hz.

The data from the root torsion gauge shows the 6-Hz 1^{st} bending mode and the 38-Hz 2^{nd} bending mode again, but also shows the 70-Hz 1^{st} torsion mode. Again, an unexpected dynamics at 15 Hz, 20 Hz, and 100 Hz can be seen from the data.

The data from the forward/aft strain gauge shows the first two bending modes as well, and also shows the 45 Hz 1^{st} chordwise bending mode. The dynamics at 15 Hz was again detected.

4.3.2 Wind Tunnel Tests

With the natural frequencies of the wing confirmed, the wind tunnel tests were conducted. The first wind tunnel test was to determine the lift curve for the wing. The wing was then flown at three different root angles of attack (1°, 2°, and 5°). The starting speed for each of these root angles of attack tests was 20.1 m/s (45 mph) with the upper limits varing according to the behavior of the wing.

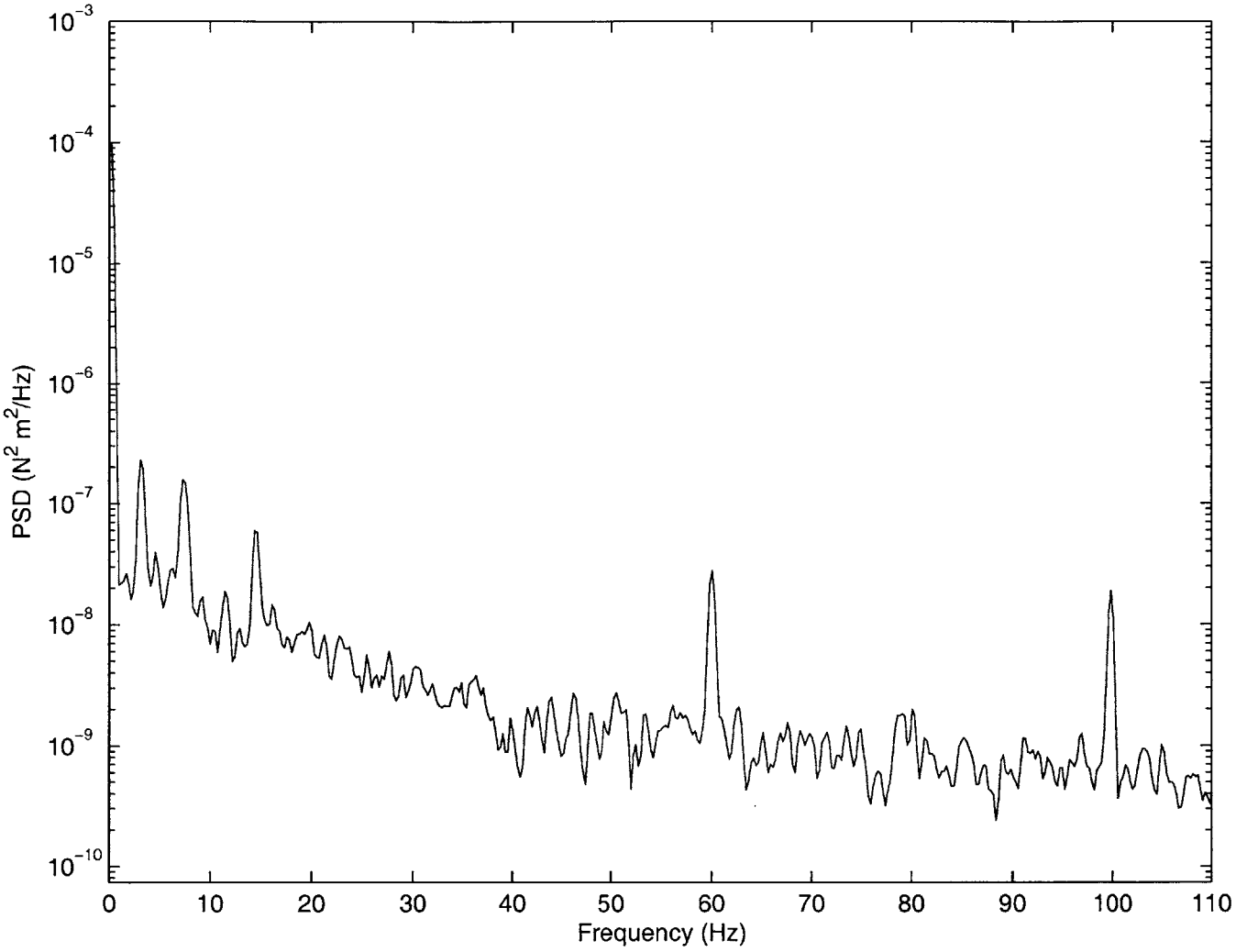

Figure 4-44: Other bending gauge readings from undisturbed wing mounted in tunnel

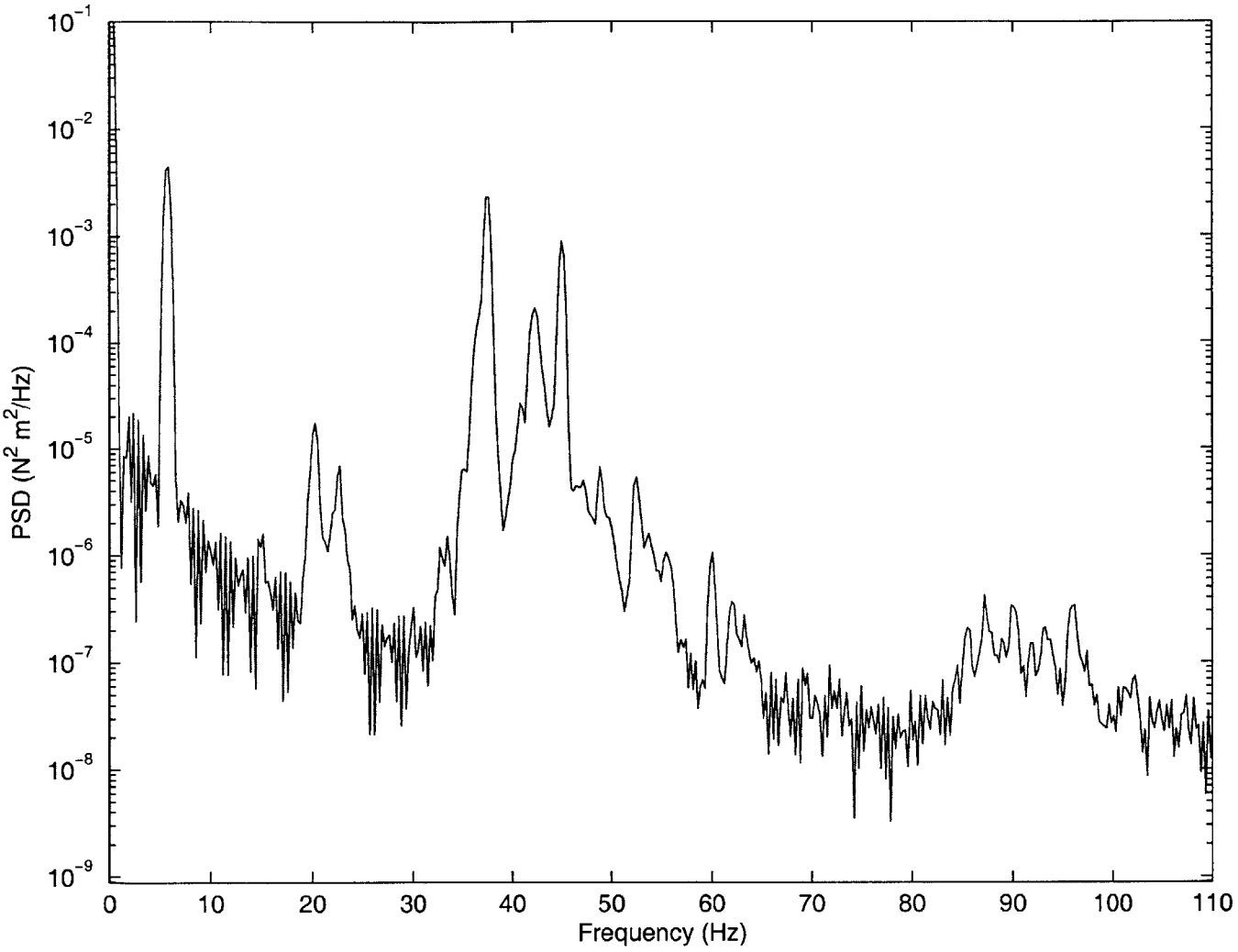

Figure 4-45: Root bending gauge readings from tap test—wing mounted in tunnel

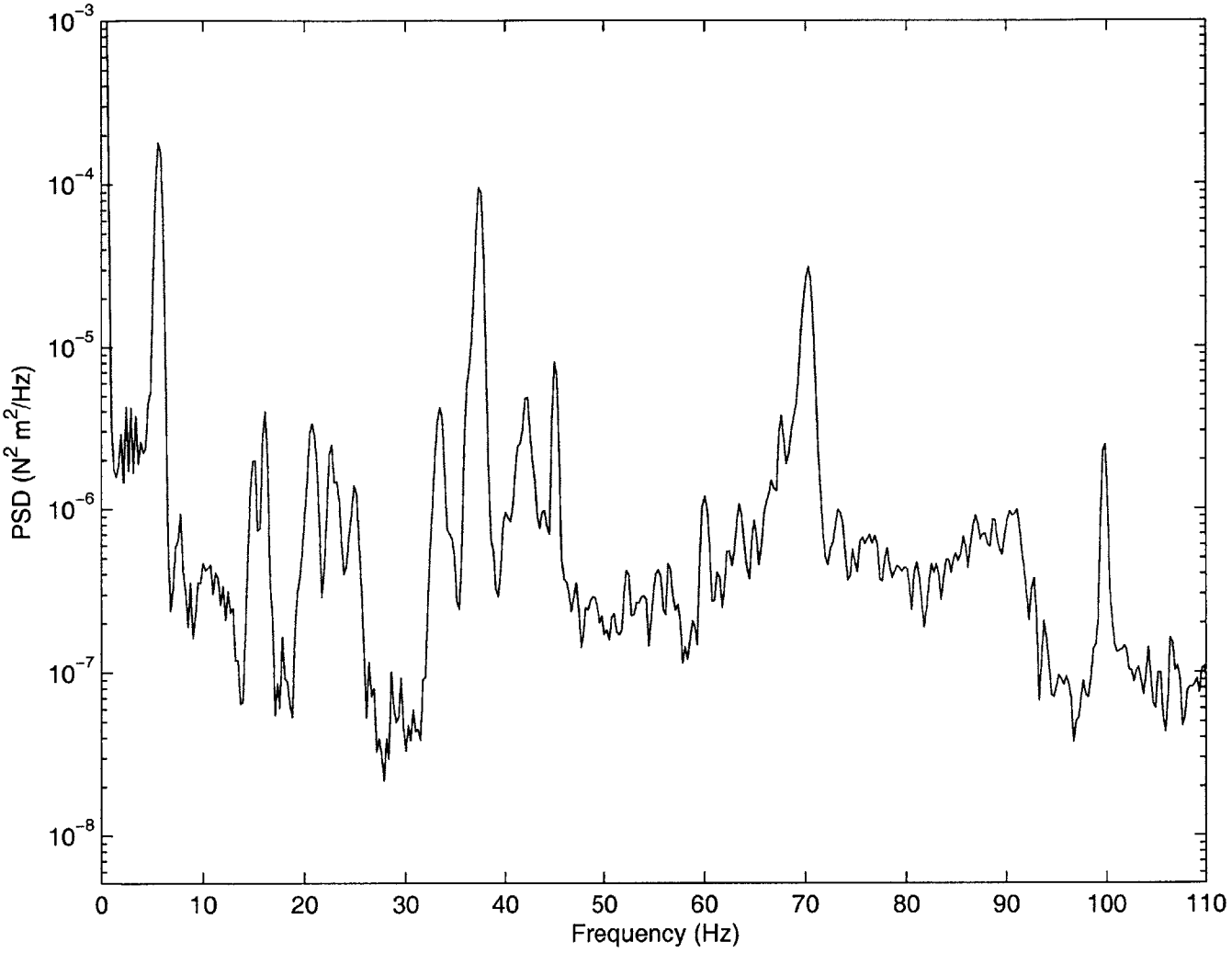

Figure 4-46: Root torsion gauge readings from tap test—wing mounted in tunnel

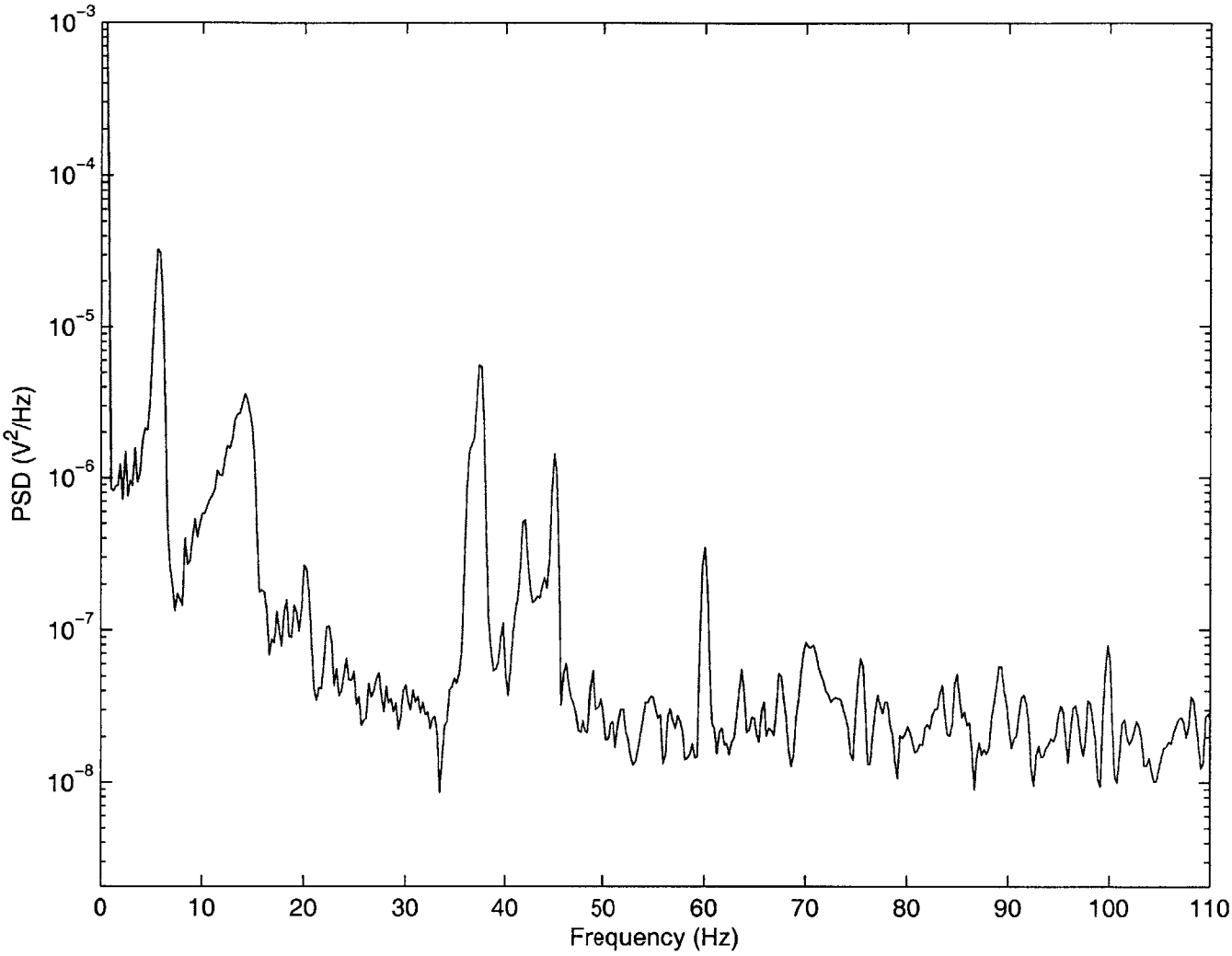

Figure 4-47: Forward/Aft bending gauge readings from tap test—wing mounted in tunnel

Wing Lift Curve

The lift curve was generated by flying the wing at 20 m/s (33.6 mph) and incrementing the angle of attack from 0° to 12°. The lift generated was monitored through the load cell. Both the theoretical and experimental lift curves are provided in Figure 4-48. The symbols represent the experimental data and the solid line is the theoretical curve generated from [3]. In addition to the calibration matrix coefficient, the load cell data was multiplied by a constant factor of 10. The exact reason for this multiplier is unknown to the author. A further calibration of the load cell is necessary to properly identify the correct calibration term.

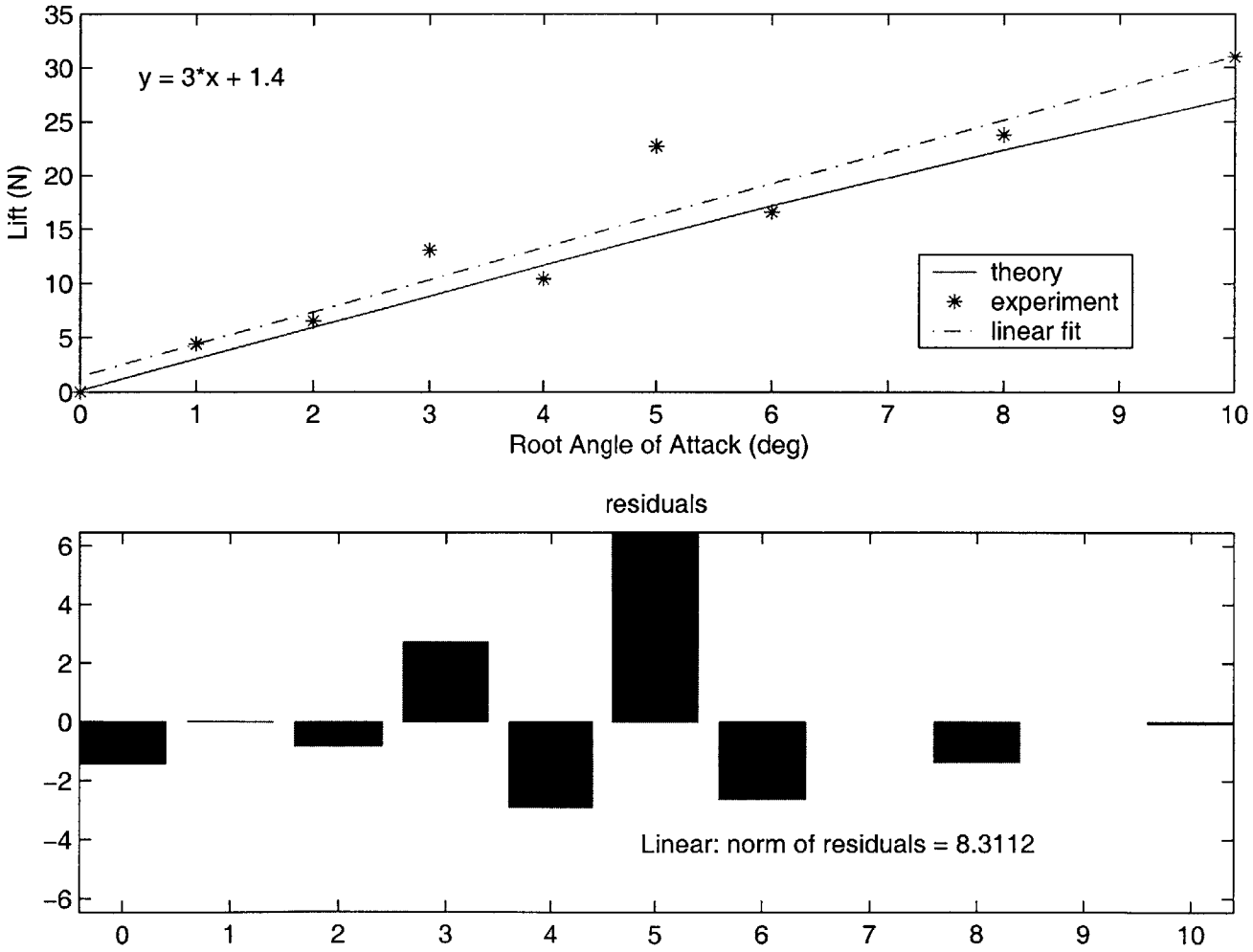

Figure 4-48: Lift curve for wing

1° Root Angle of Attack Tests

The 1° test were conducted from 20.1 m/s (45 mph) to 36.7 m/s (82 mph). Since this was the first round of tests, the flight speed was not driven up near flutter to ensure that data would be collected for all three angles of attack.

The data from the sensors at 20.1 m/s (45 mph) show many of the natural frequencies and is provided in Figure 4-49 through Figure 4-52. This data was processed through a Welsh averaging scheme with a 125 data point window and an overlap of 63 data points. At a minimum, all flight data was processed through this scheme.

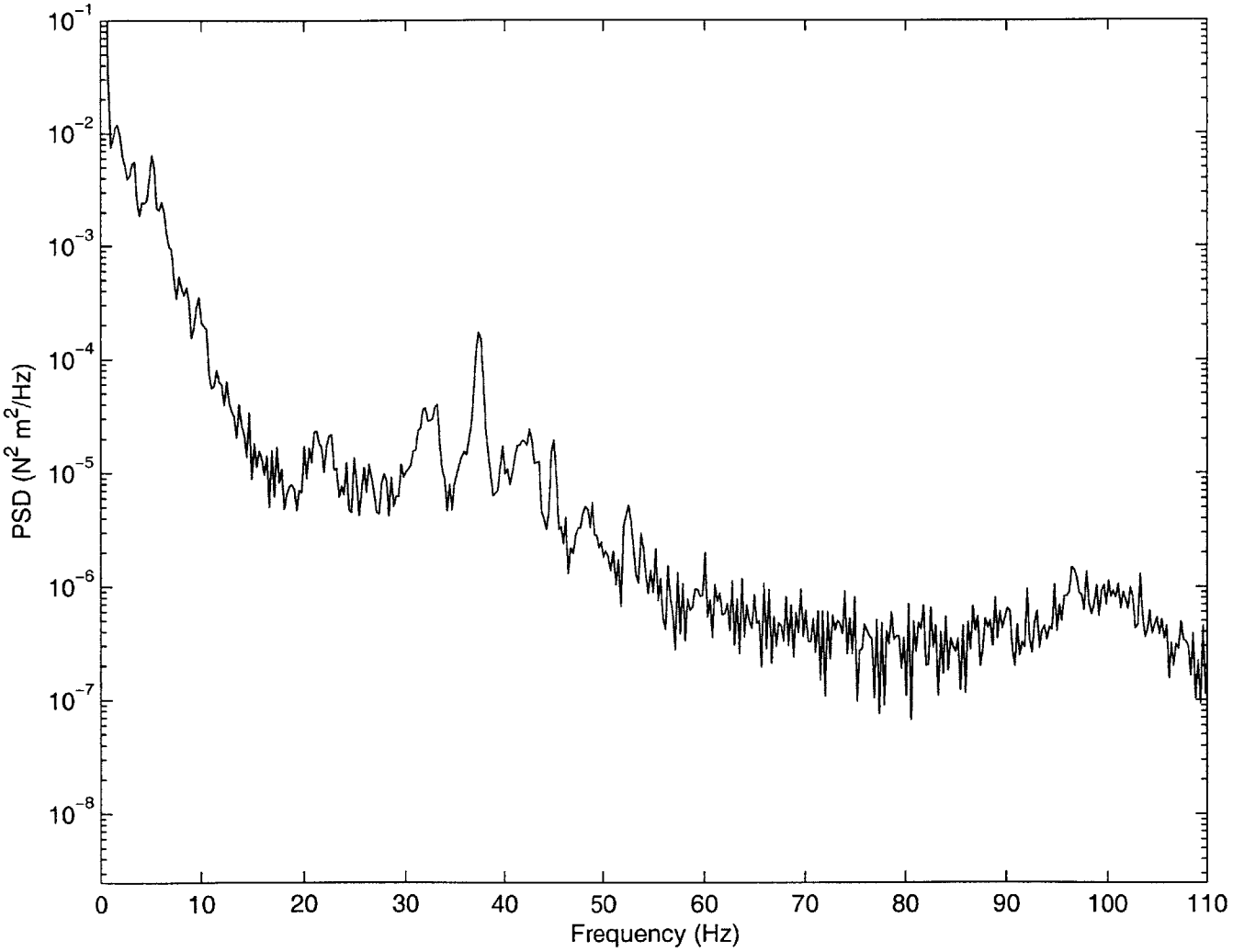

Figure 4-49: Frequency plot from root bending gauge at 20.1 m/s for 1° root angle of attack

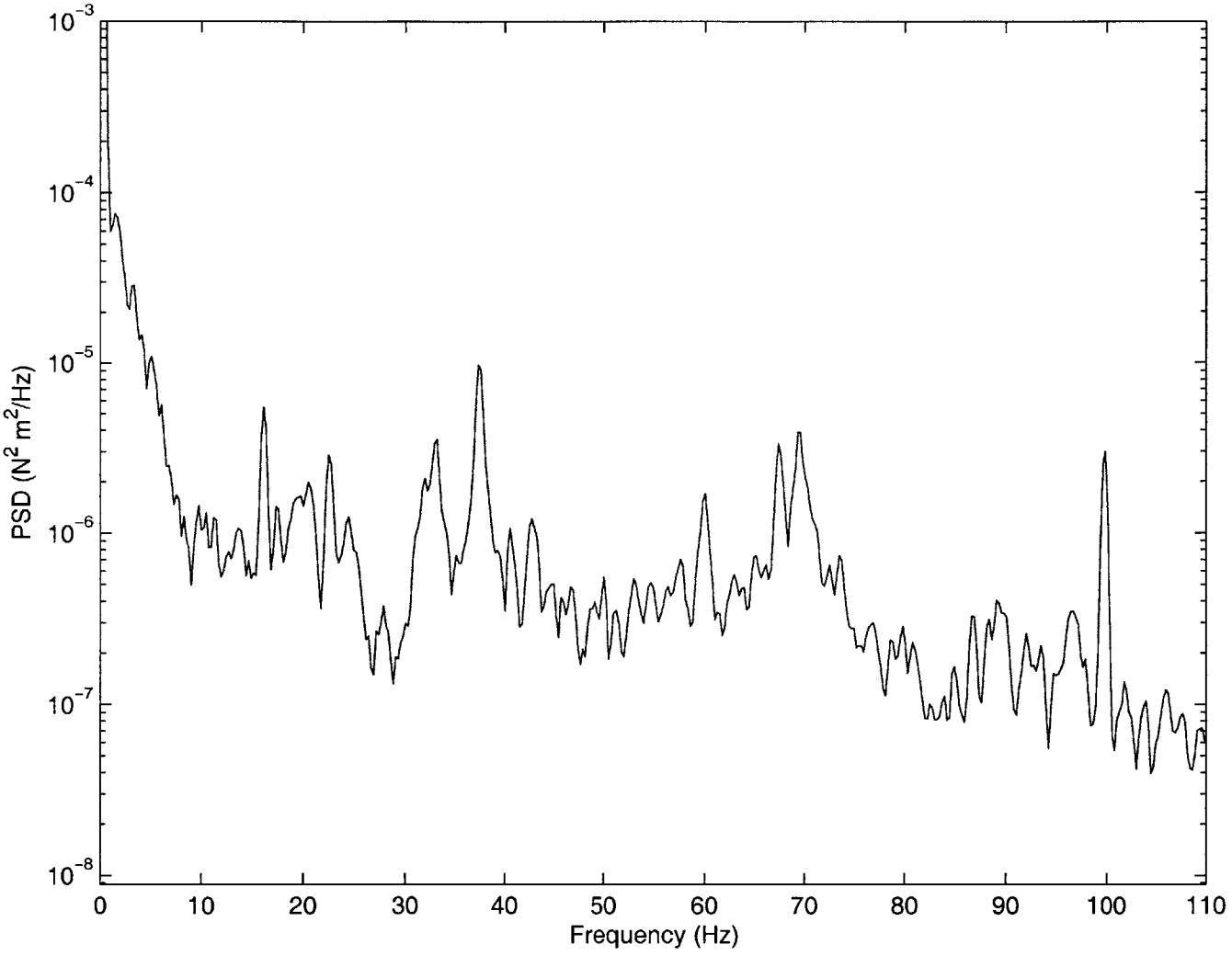

Figure 4-50: Frequency plot from root torsion gauge at 20.1 m/s for 1° root angle of attack

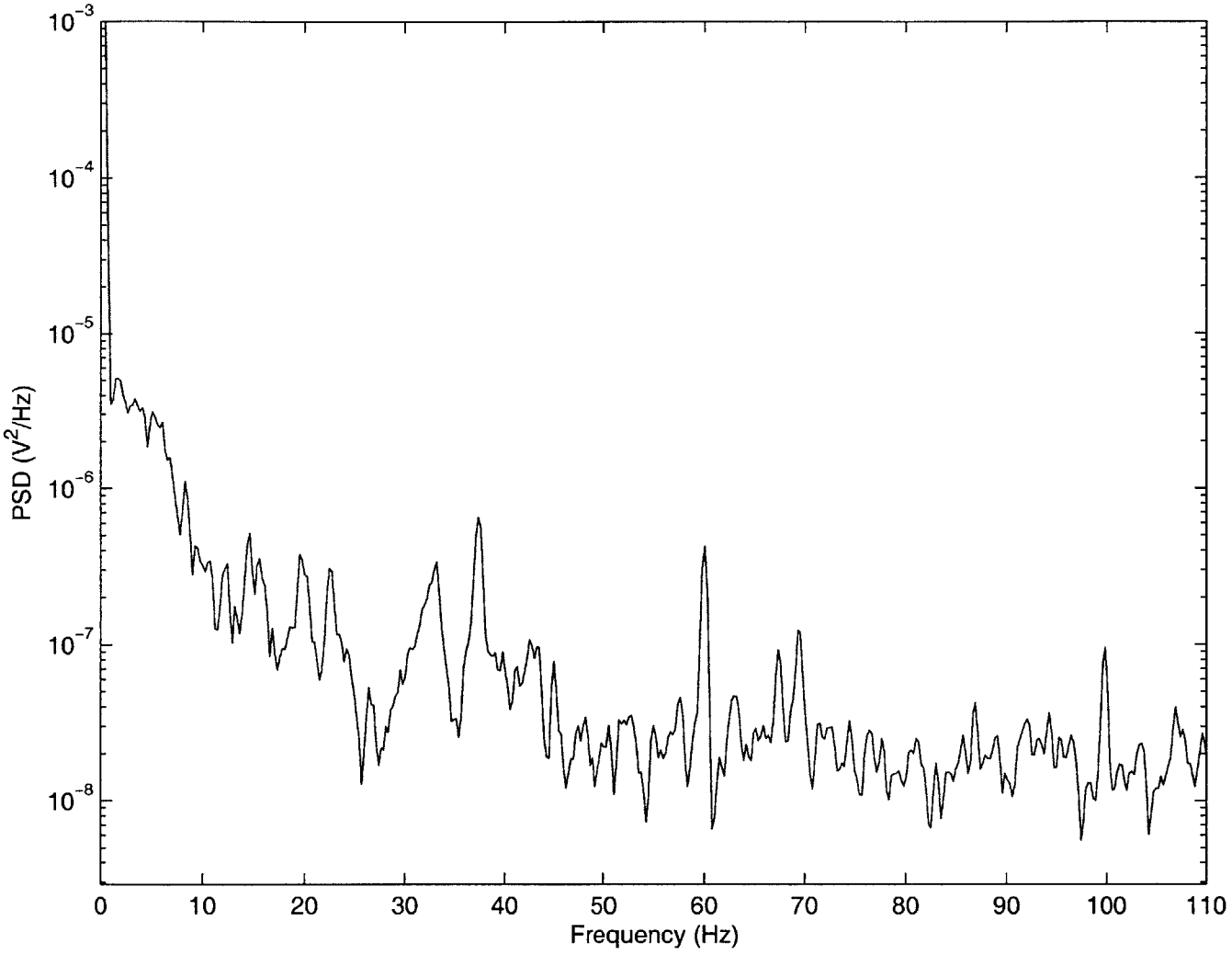

Figure 4-51: Frequency plot from forward/aft gauge at 20.1 m/s for 1° root angle of attack

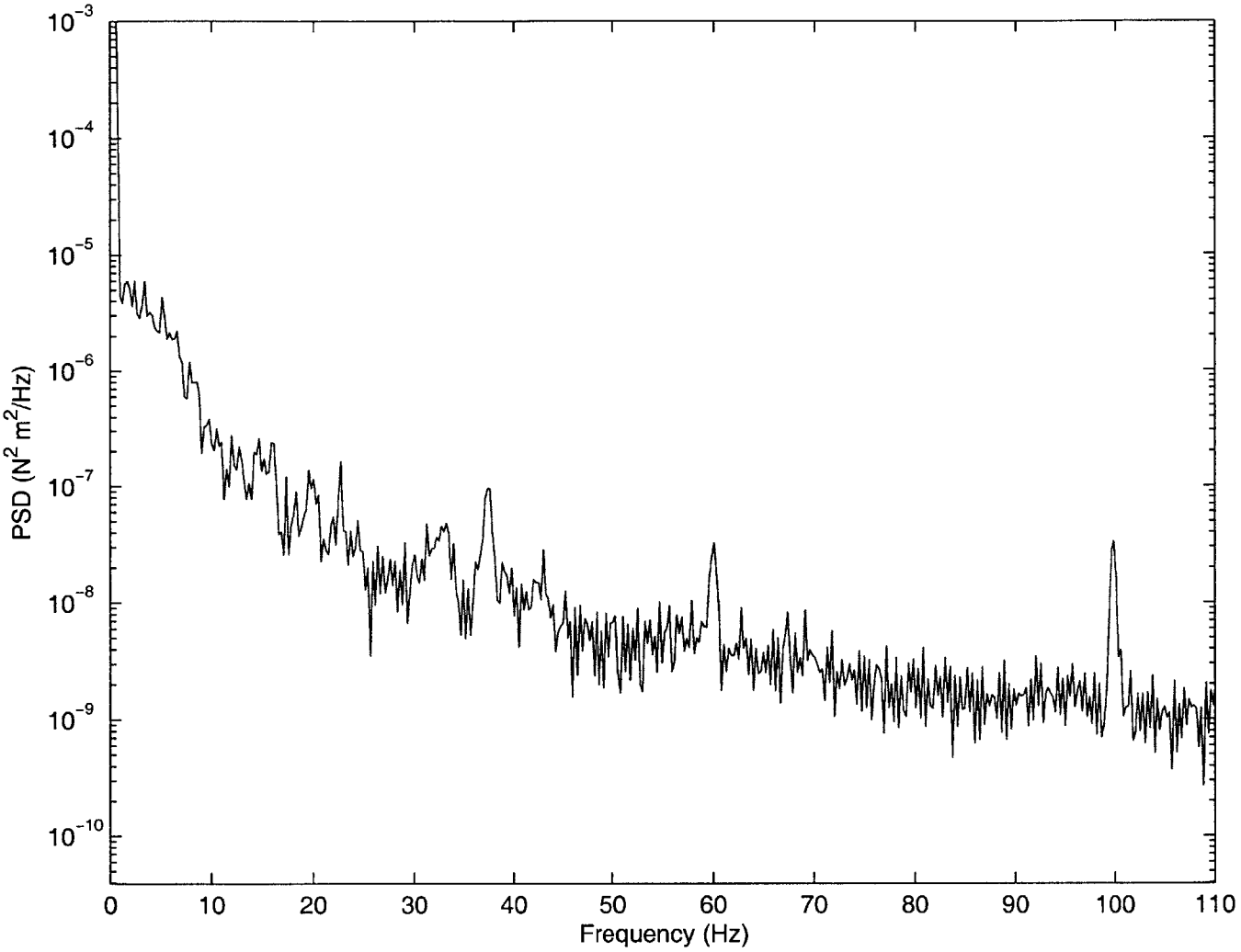

Figure 4-52: Frequency plot from the other bending gauge at 20.1 m/s for 1° root angle of attack

The data from the sensors at 36.7 m/s (82 mph) is noisier and the natural frequencies are harder to detect. These results are shown in Figure 4-53 through Figure 4-56.

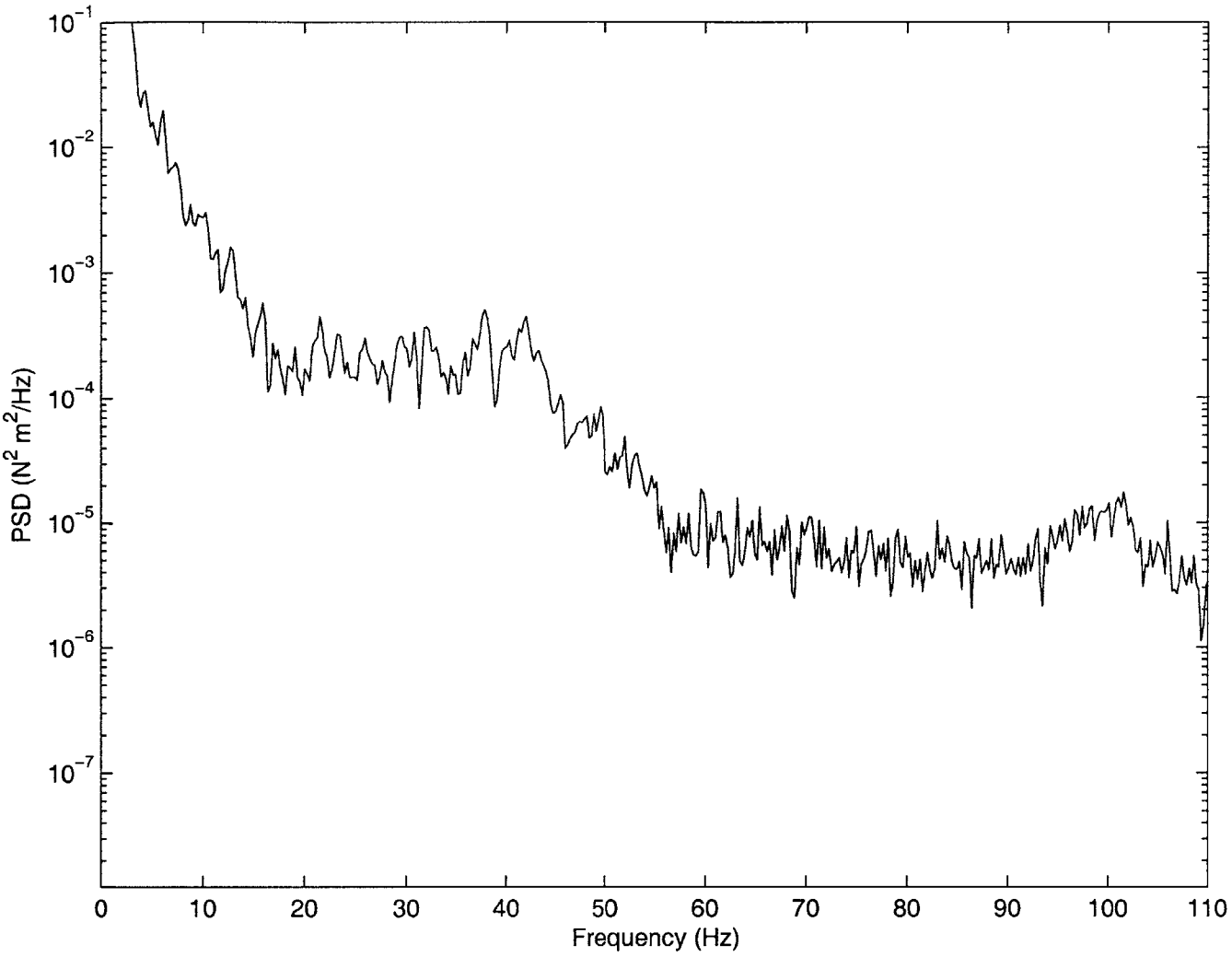

Figure 4-53: Frequency plot from root bending gauge at 36.7 m/s for 1° root angle of attack

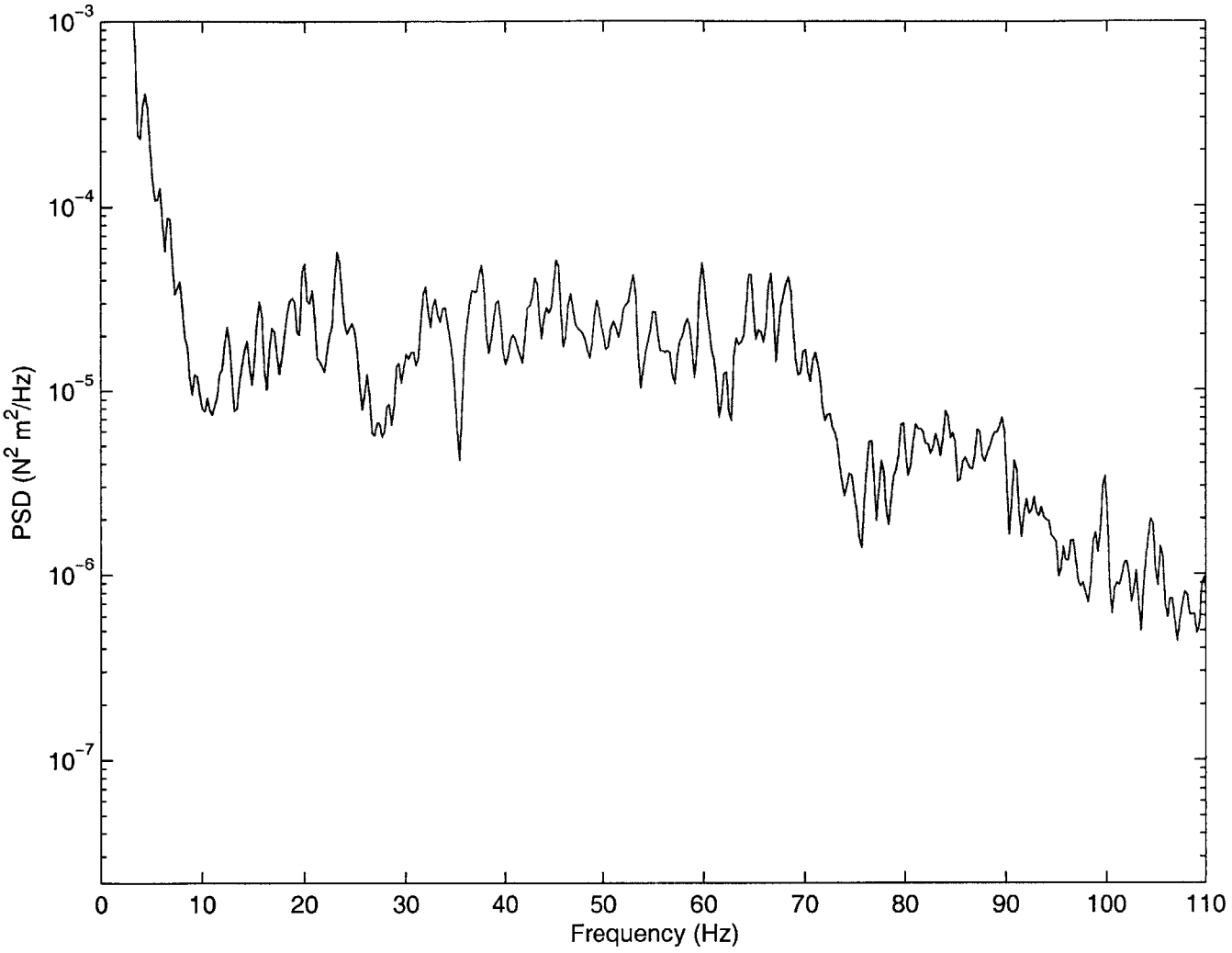

Figure 4-54: Frequency plot from root torsion gauge at 36.7 m/s for 1° root angle of attack

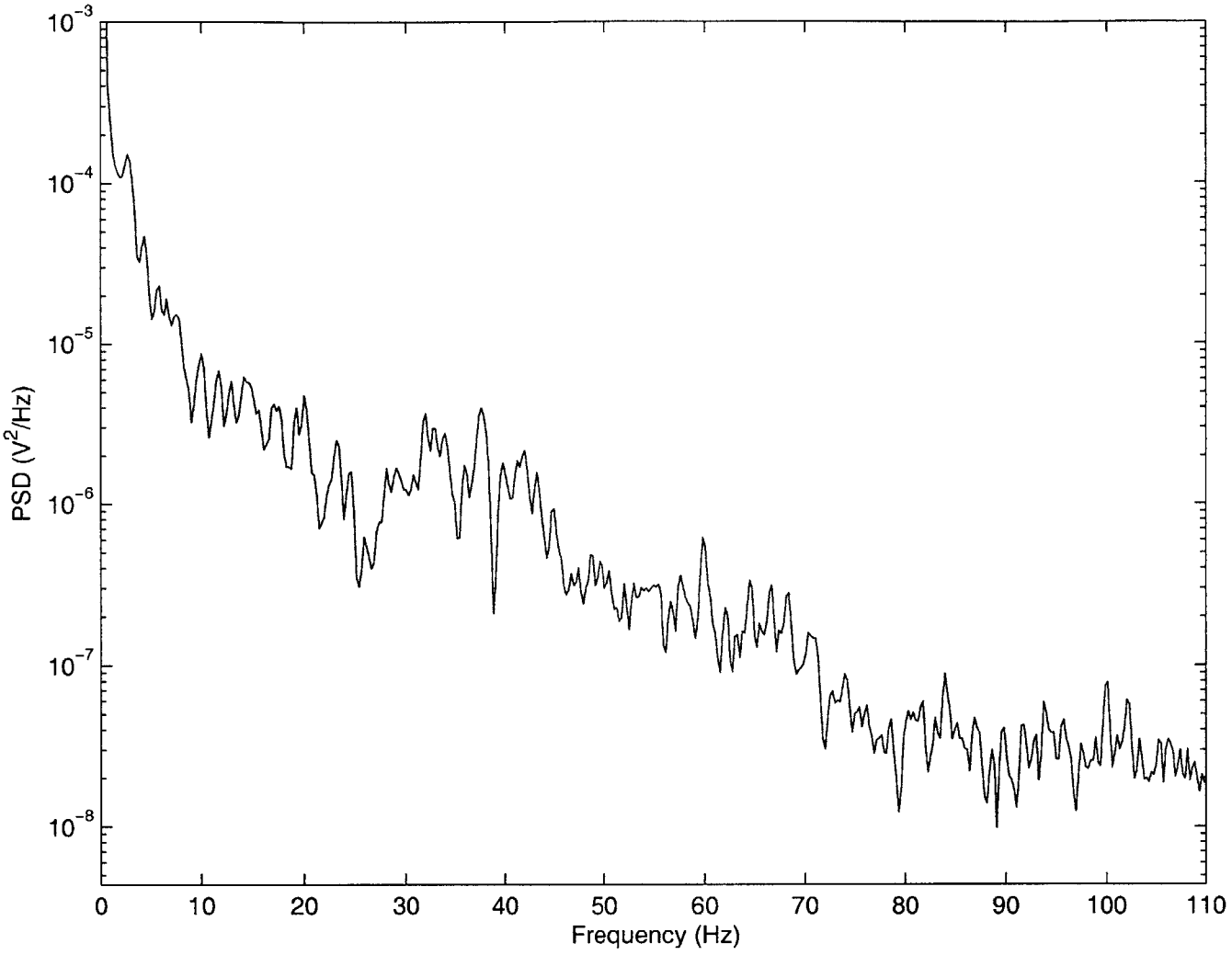

Figure 4-55: Frequency plot from forward/aft gauge at 36.7 m/s for 1° root angle of attack

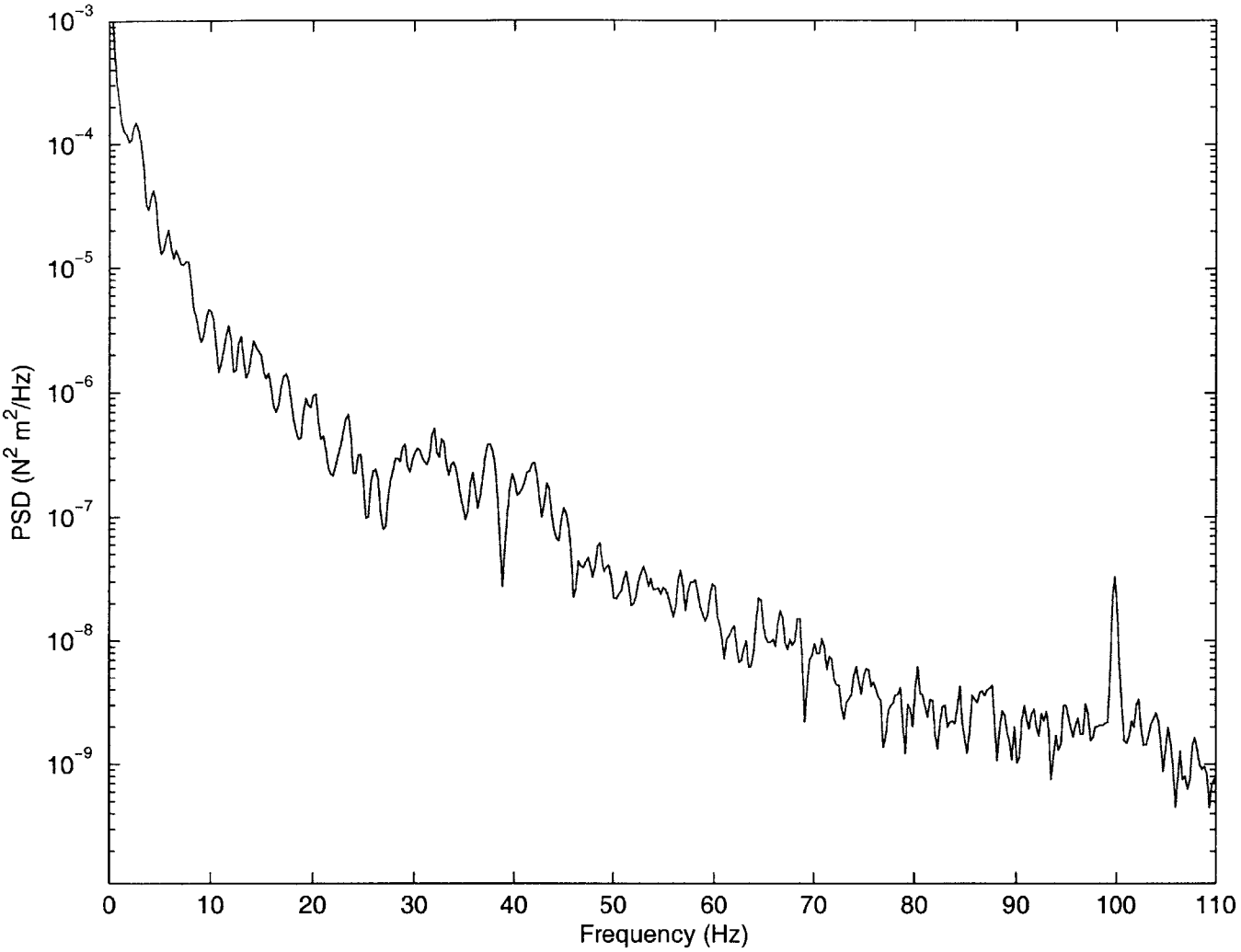

Figure 4-56: Frequency plot from the other bending gauge at 36.7 m/s for 1° root angle of attack

2° Root Angle of Attack Tests

The 2° tests were conducted from 20.1 m/s (45 mph) to 36.7 m/s (82 mph) and then from 20.1 m/s (45 mph) to 52.3 m/s (117 mph) after the 5° case was completed.

The natural frequencies at 20.1 m/s were fairly straight forward to determine. The added turbulence from the wind tunnel did not interfere with this 10 s data collect, so this data did not require extensive processing or filtering. The time trace from the root bending gauge is provided in Figure 4-57 to show how clean the data looks.

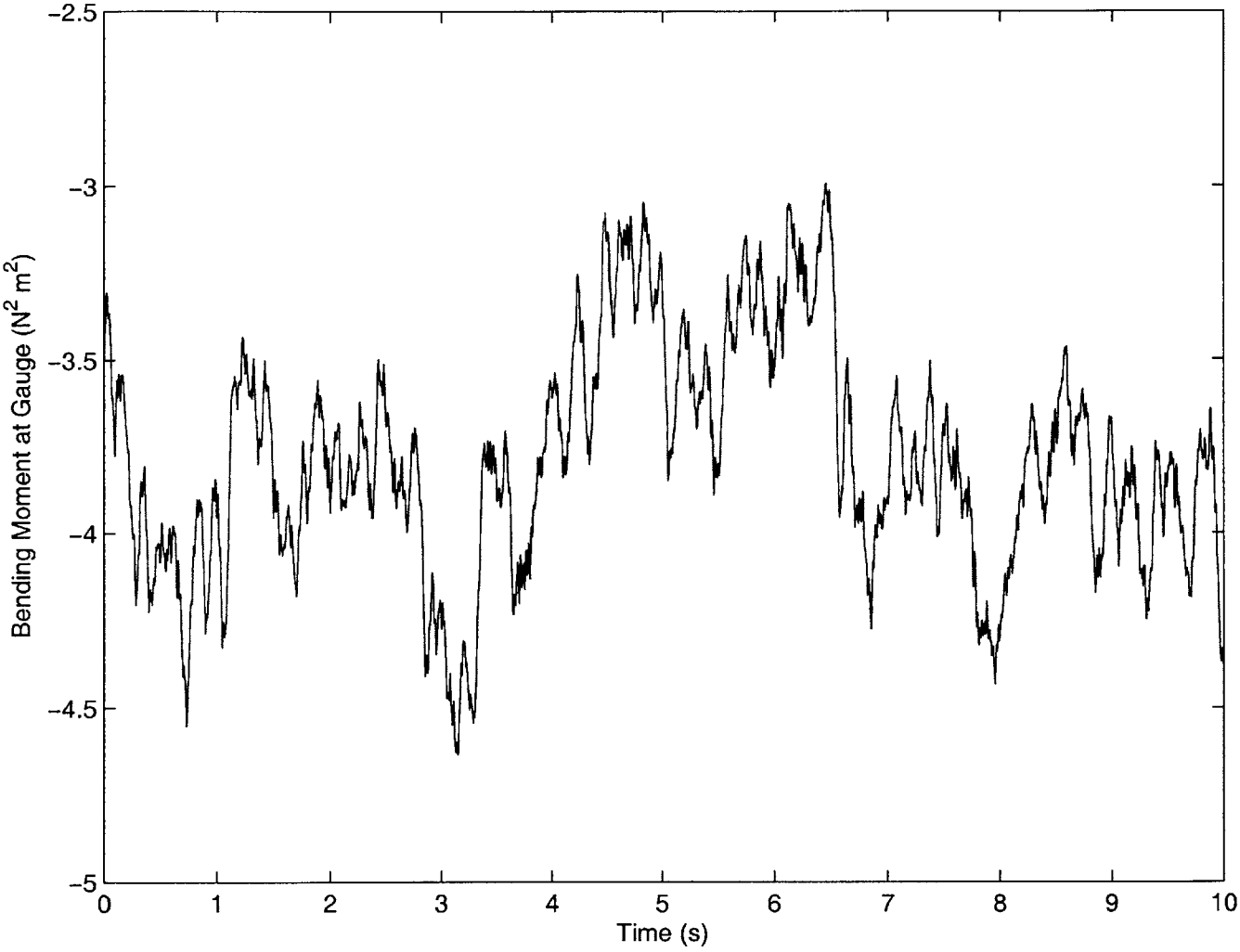

Figure 4-57: Time trace of data from root bending gauge at 20.1 m/s for 2° root angle of attack

The data from the four strain gauges with the aforementioned averaging technique are provided in Figure 4-58 through Figure 4-61.

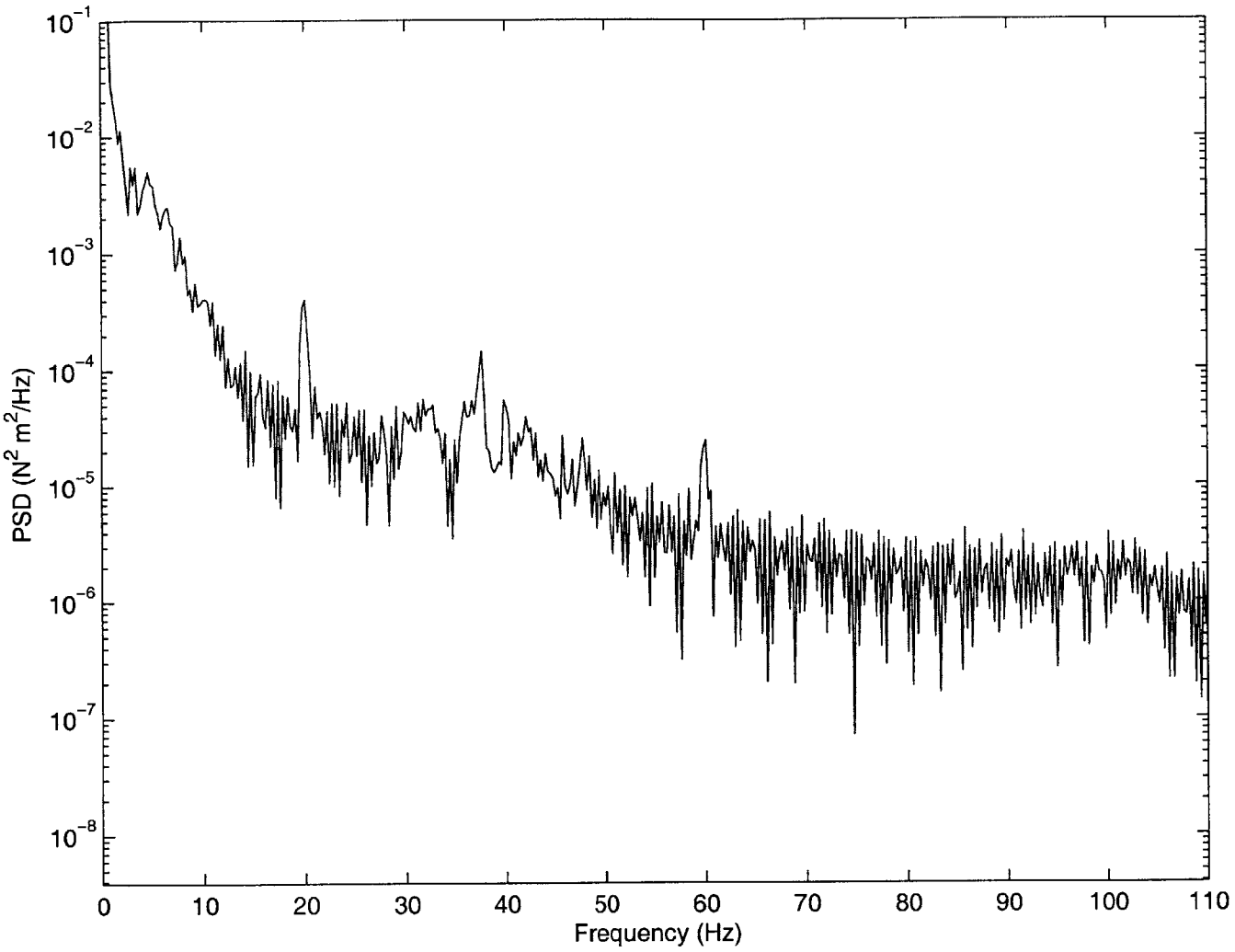

Figure 4-58: Frequency plot from root bending gauge at 20.1 m/s for 2° root angle of attack

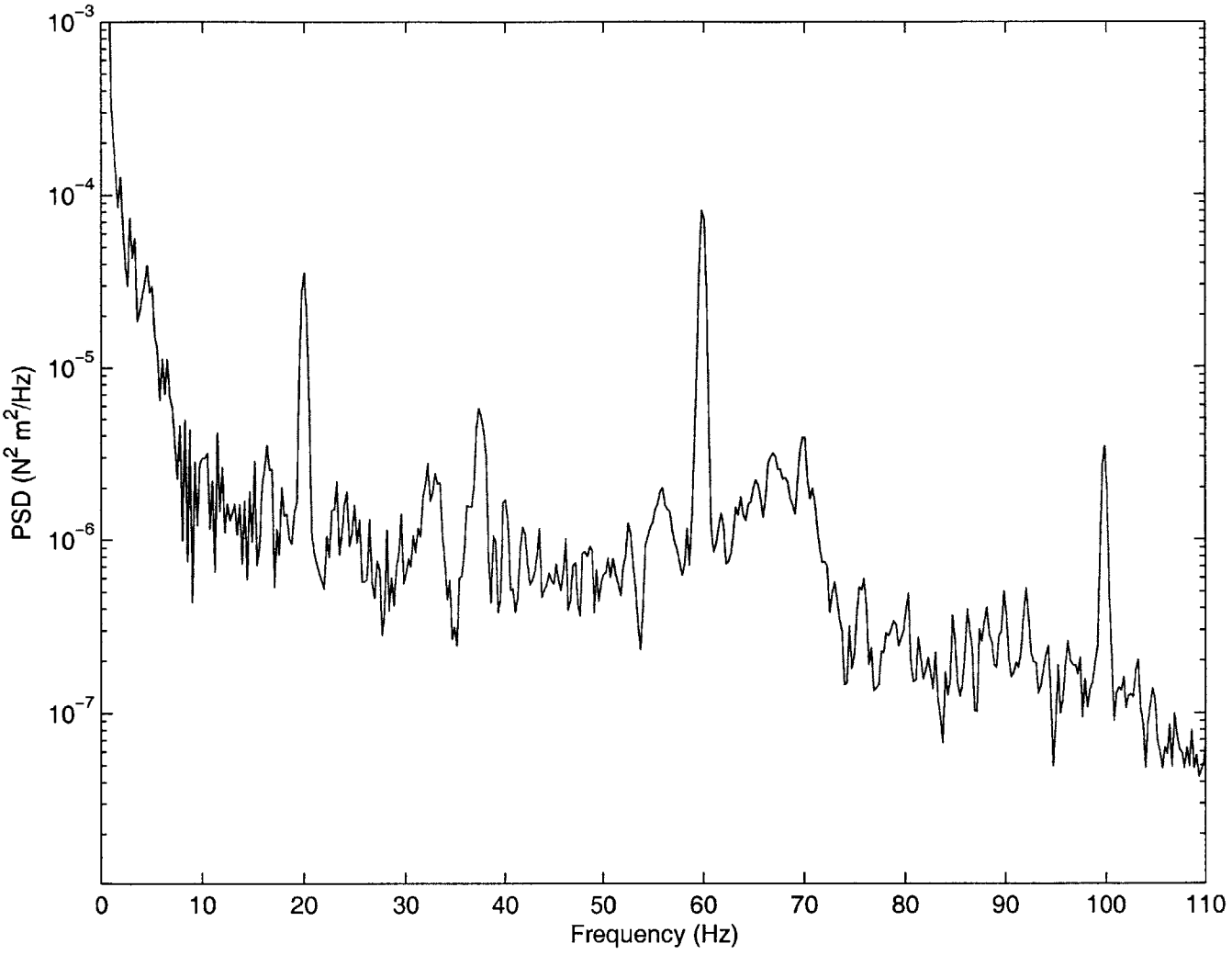

Figure 4-59: Frequency plot from root torsion gauge at 20.1 m/s for 2° root angle of attack

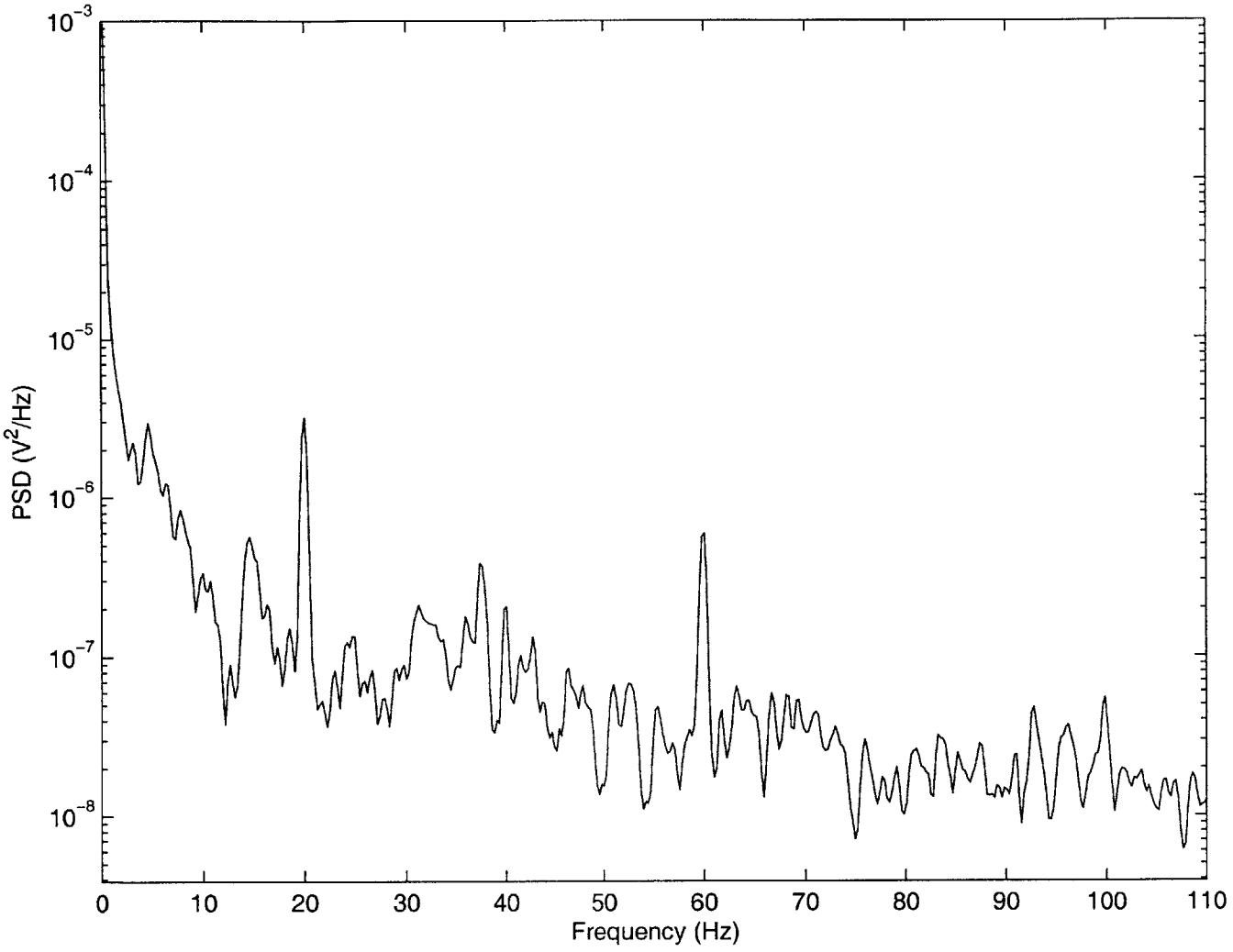

Figure 4-60: Frequency plot from forward/aft gauge at 20.1 m/s for 2° root angle of attack

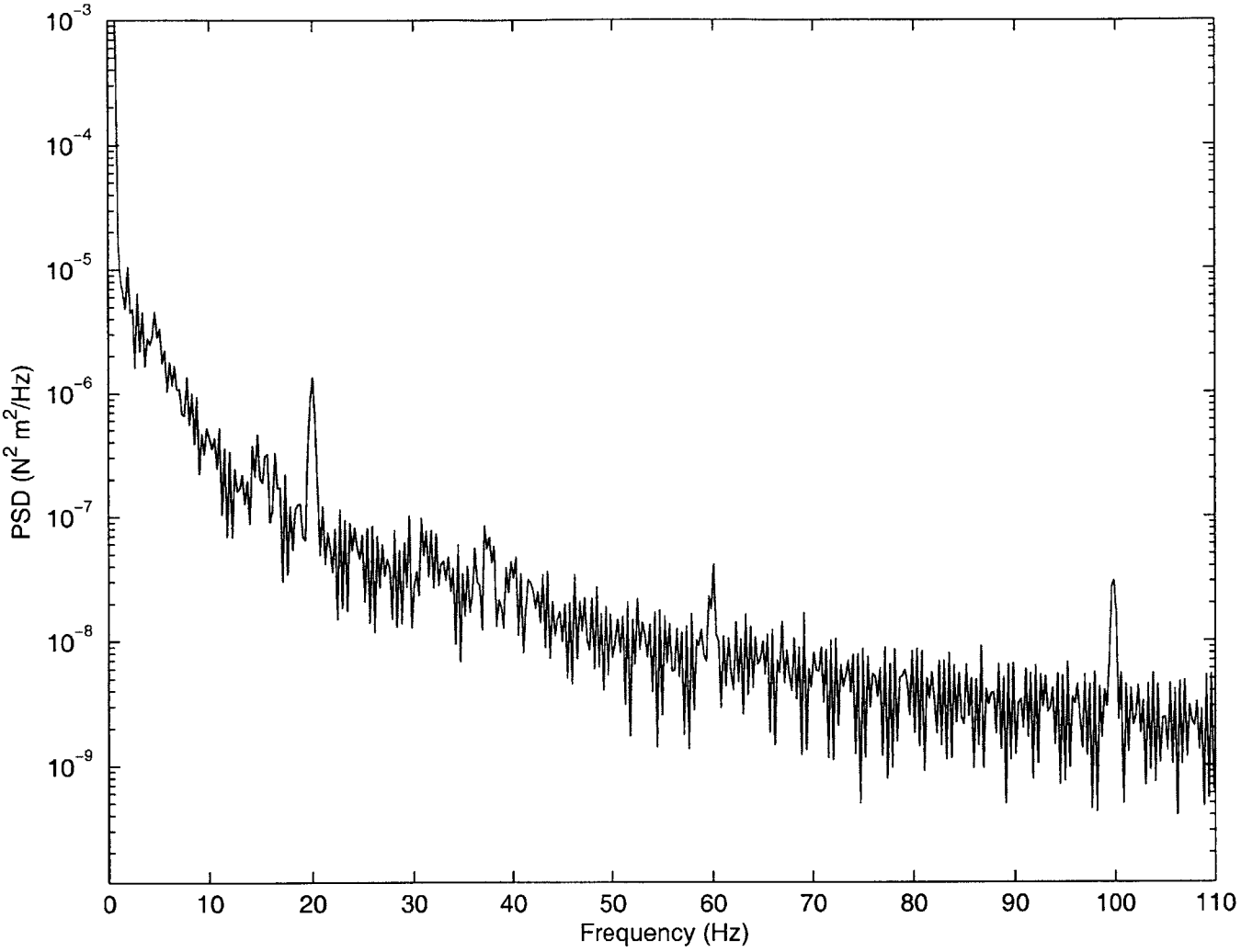

Figure 4-61: Frequency plot from the other bending gauge at 20.1 m/s for 2° root angle of attack

All four bridges detected a 20-Hz disturbance as well as one at 37-Hz. The additional bending gauge only slightly detected the 37 Hz signal. A summary of which gauge detected which frequencies is provided in Table 4.8.

Table 4.8: Frequencies detected from strain gauges at 20.1 m/s for 2° root angle of attack

Gauge	6 Hz	20 Hz	37 Hz	70 Hz	100 Hz
Root Bending	X	X	X		
Root Torsion		X	X	X	X
Chordwise Bending		X	X		
Additional Bending		X	X		X

A data set of importance from the 2° root angle of attack tests is at 52.3 m/s. Through visual observation of the wing behavior, it is believed that the wing was operating just below the flutter speed. Two root torsion gauge time traces of the wing operating at this speed are provided in Figure 4-62 and Figure 4-63. The data from the sensors is provided in Figure 4-64 through Figure 4-66.

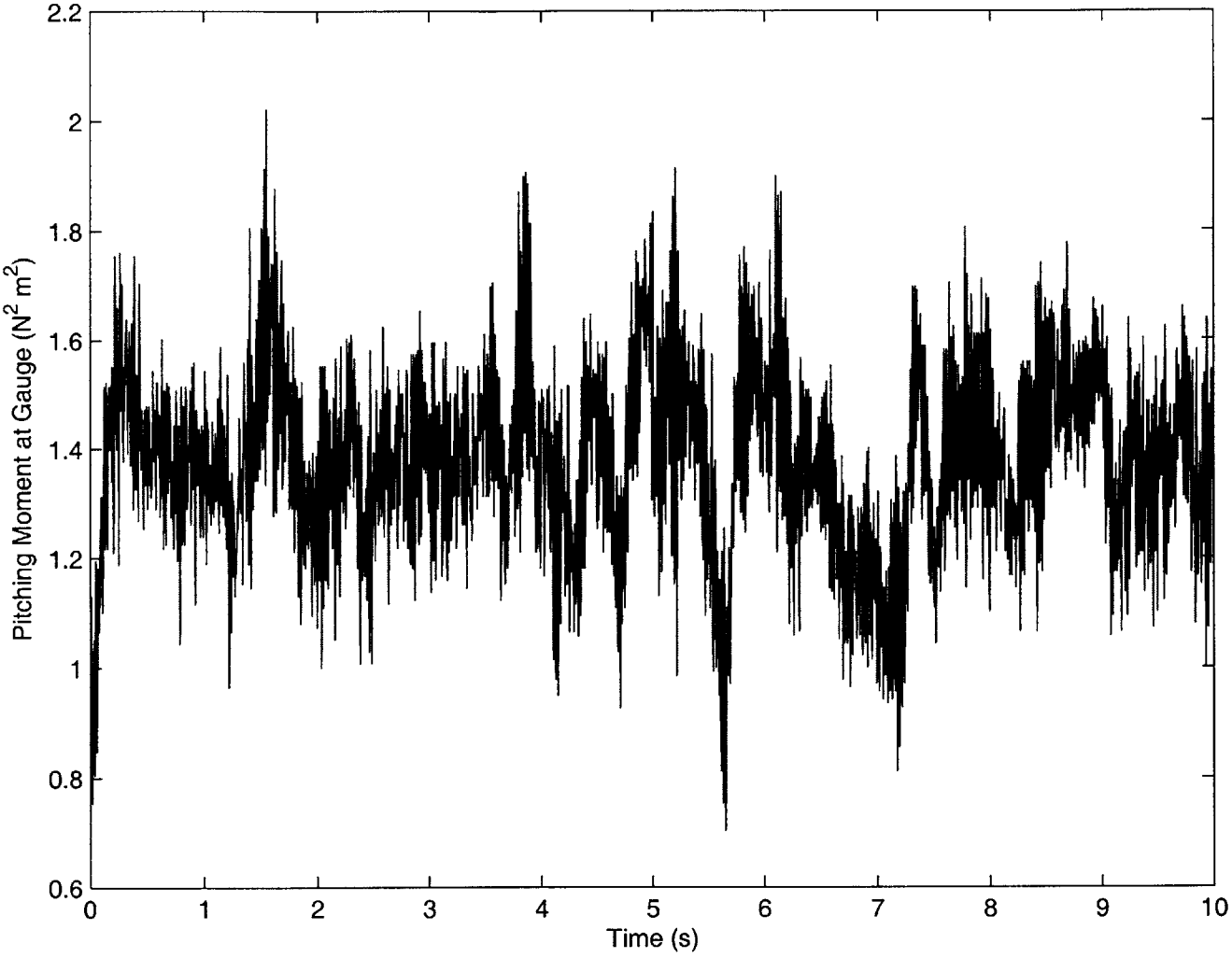

Figure 4-62: Time trace of data from root torsion gauge at 52.3 m/s for 2° root angle of attack

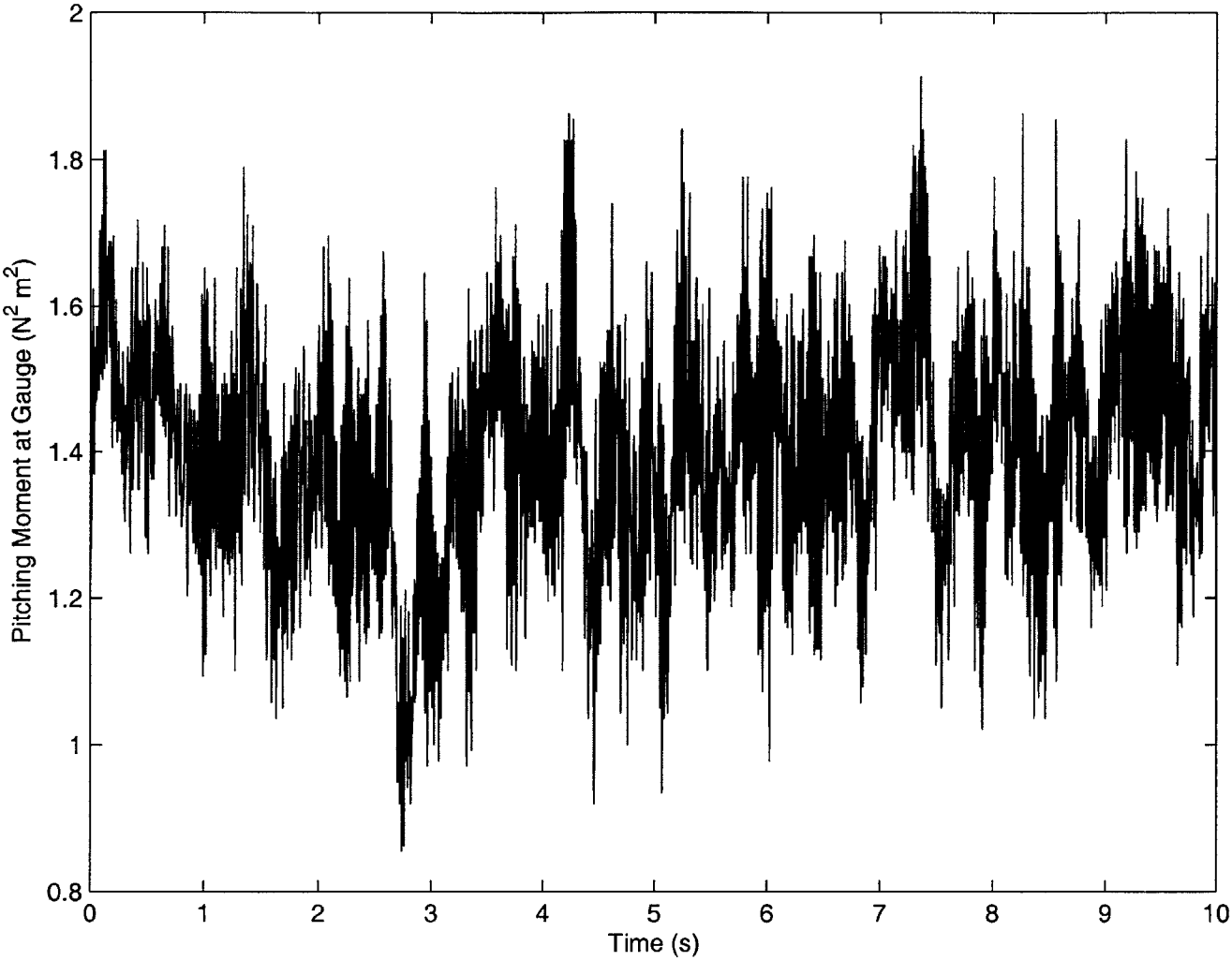

Figure 4-63: Time trace of data from root torsion gauge at 52.3 m/s for 2° root angle of attack

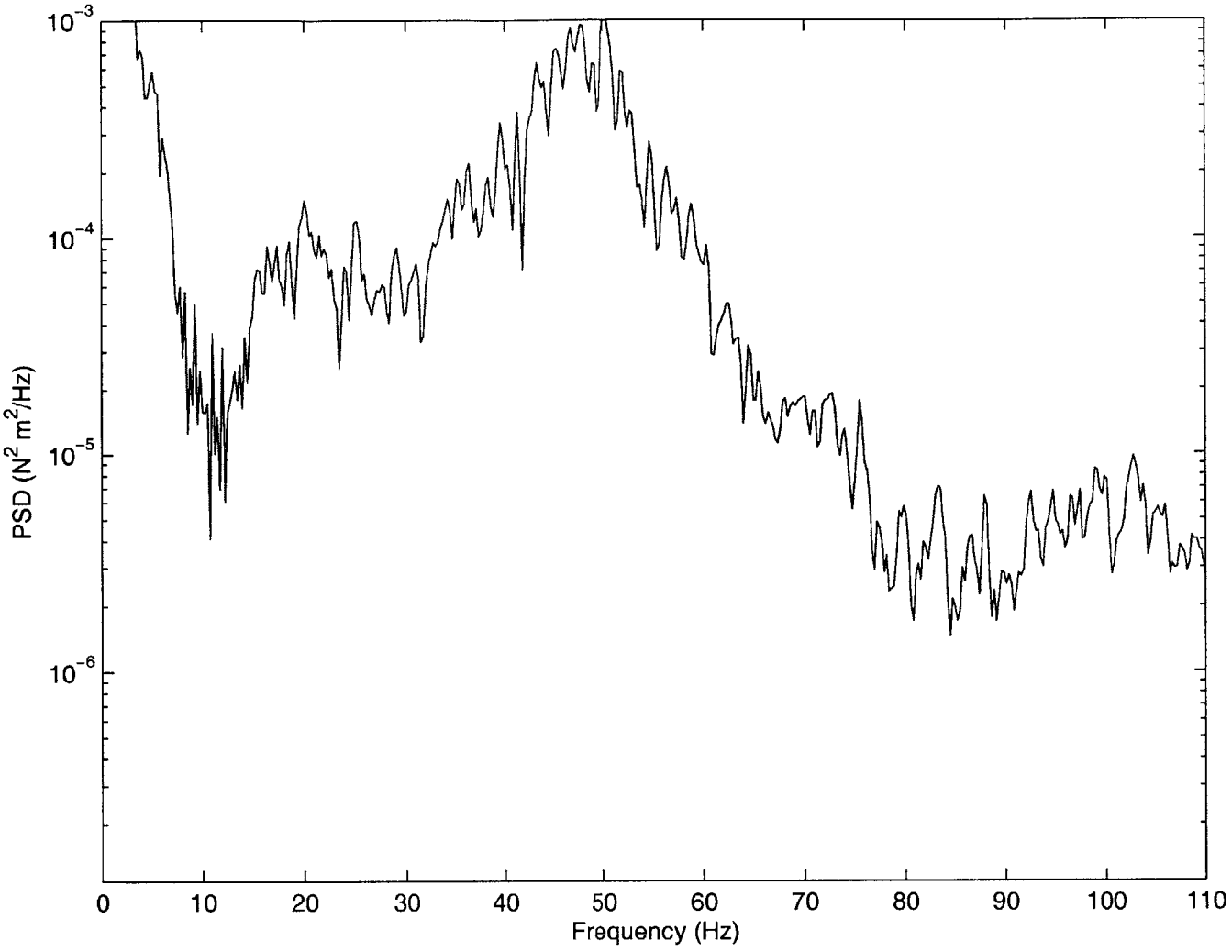

Figure 4-64: Frequency plot from root torsion gauge at 52.3 m/s for 2° root angle of attack

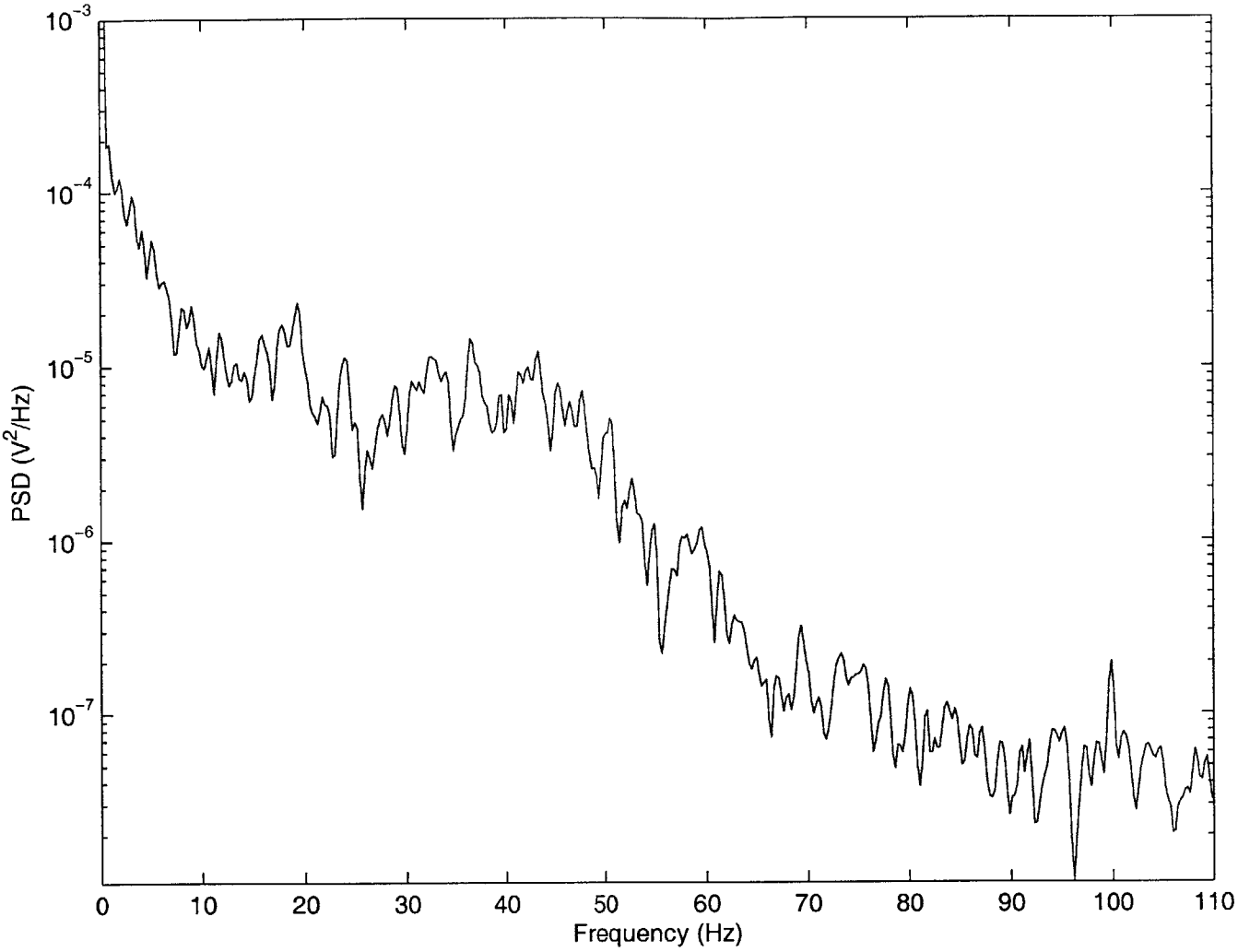

Figure 4-65: Frequency plot from forward/aft gauge at 52.3 m/s for 2° root angle of attack

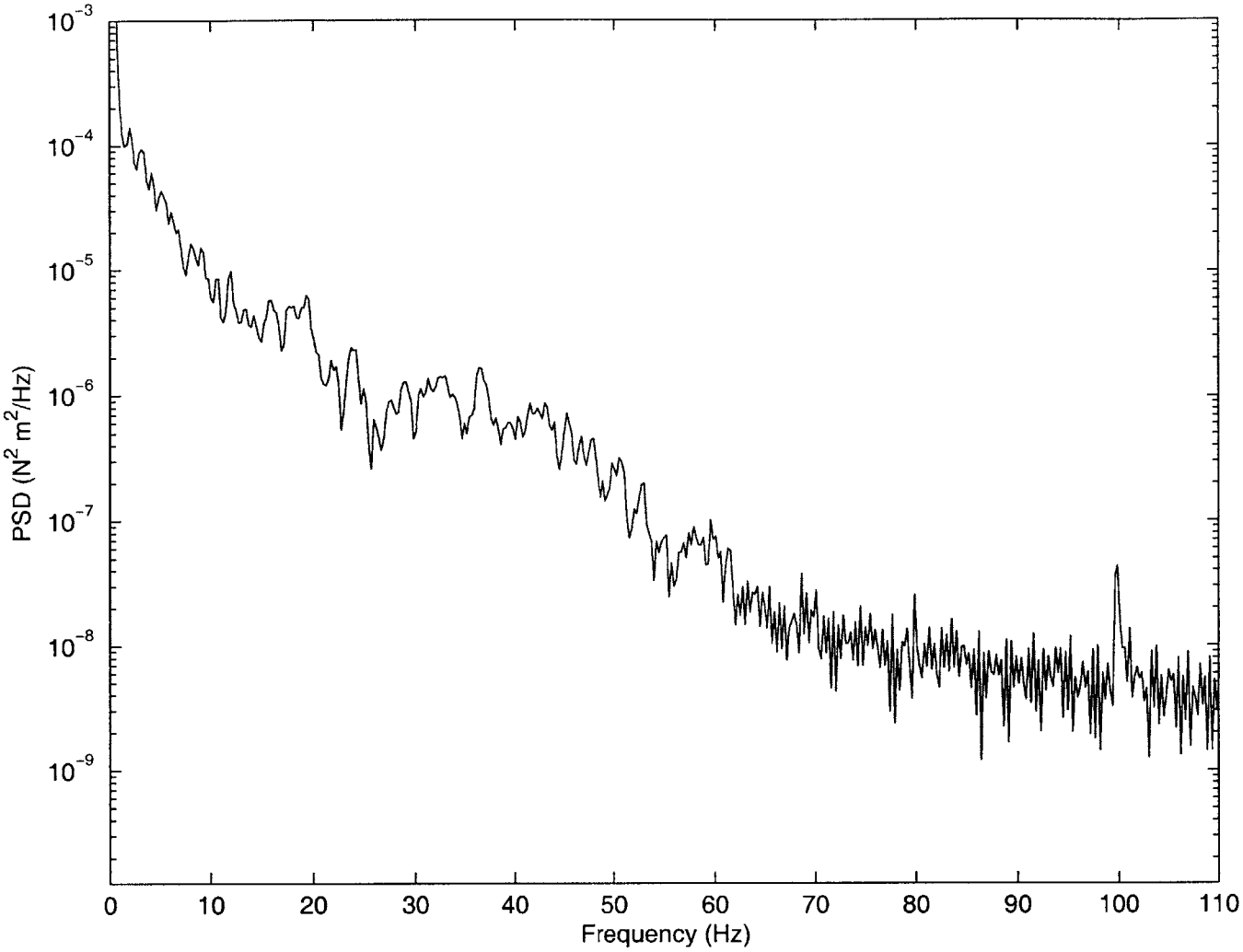

Figure 4-66: Frequency plot from the other bending gauge at 52.3 m/s for 2° root angle of attack

5° Root Angle of Attack Tests

The 5° tests were conducted from 20.1 m/s (45 mph) to 33.5 m/s (75 mph). The wing at this root angle of attack produced very large tip deflections. Therefore, the wing was not flown up to 36.7 m/s (82 mph) as originally desired because of fear that the wing would break and damage the tunnel.

The data from a 20.1-m/s case is provided in Figure 4-67 through Figure 4-69. The data from the root bending gauge is not provided as the signal exceeded the recording limits.

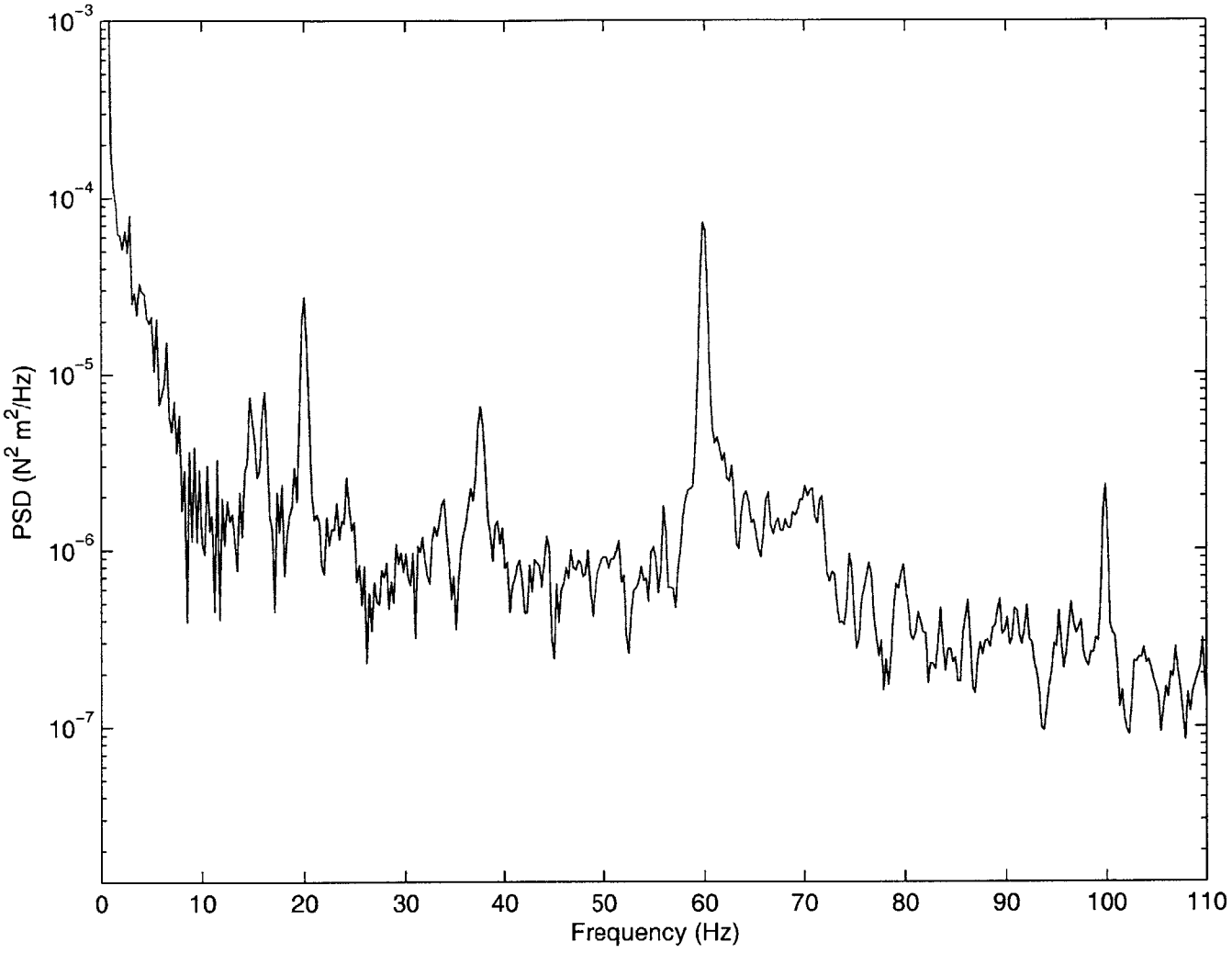

Figure 4-67: Frequency plot from root torsion gauge at 20.1 m/s for 5° root angle of attack

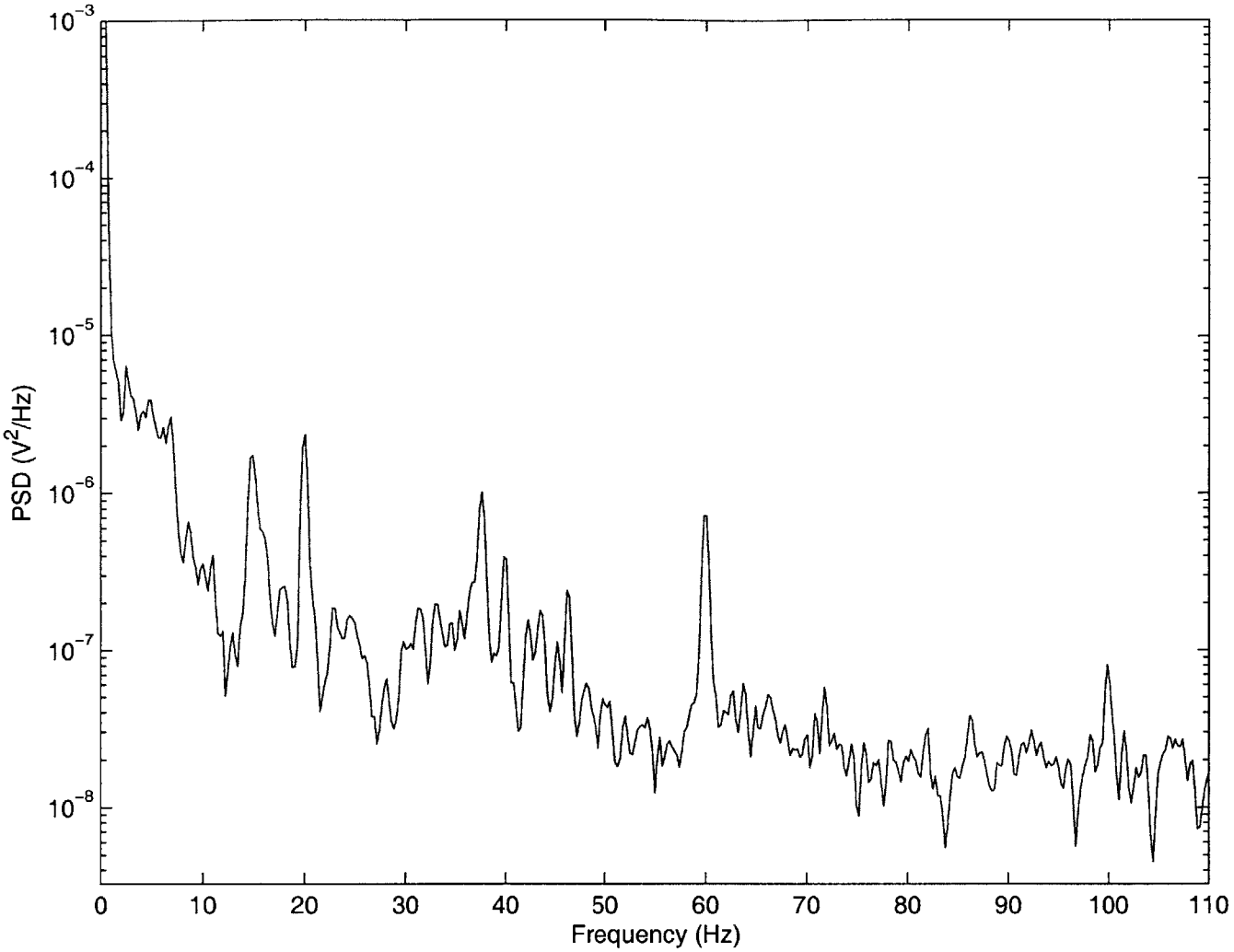

Figure 4-68: Frequency plot from forward/aft gauge at 20.1 m/s for 5° root angle of attack

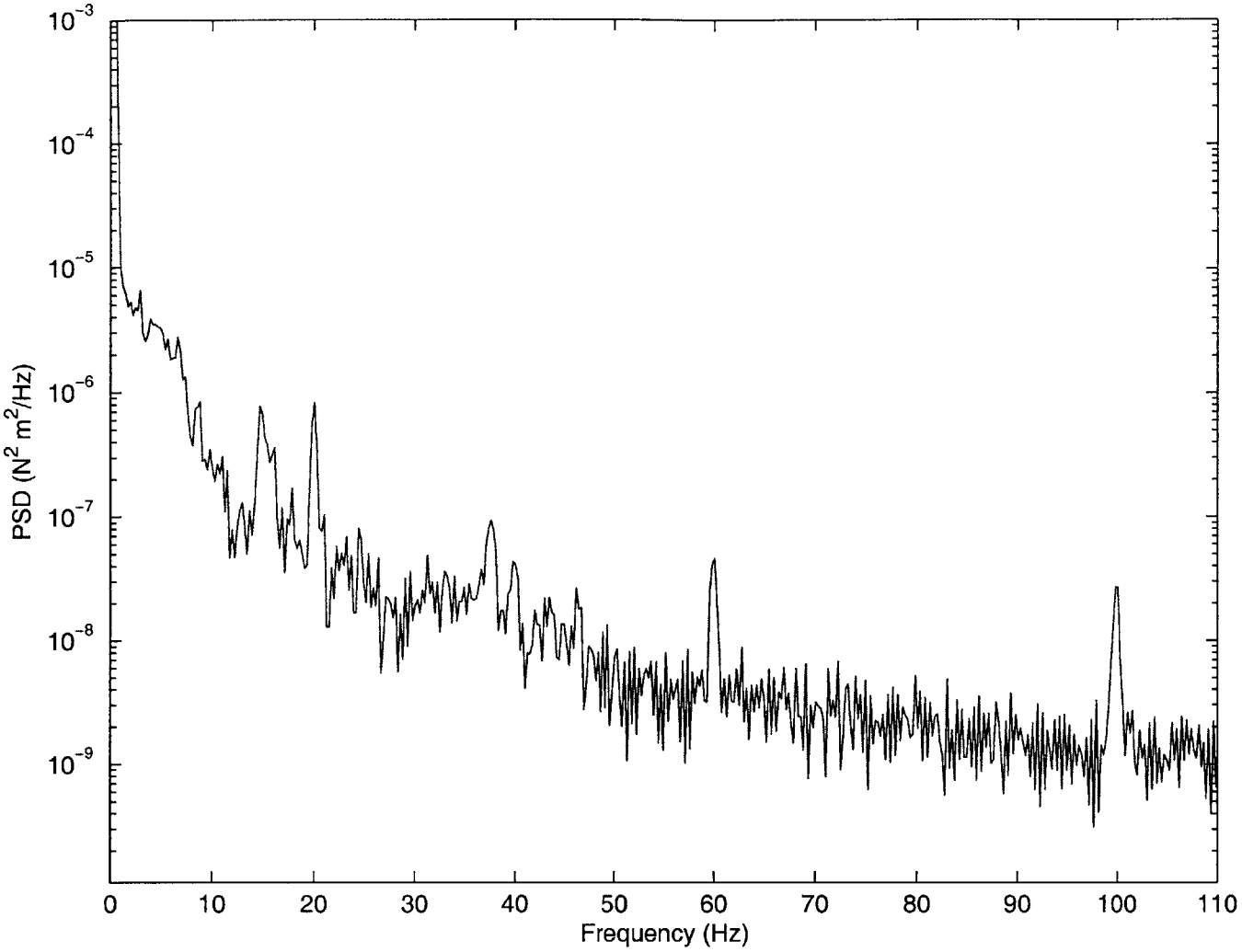

Figure 4-69: Frequency plot from the other bending gauge at 20.1 m/s for 5° root angle of attack

The data from the 33.5-m/s (75-mph) case shows some interesting frequency results. This data is provided in Figure 4-70 through Figure 4-72. There are three dynamics present in the root torsion gauge that were not targeted as noise from the tunnel environment: 34 Hz, 42 Hz, and 46 Hz. The forward/aft gauge and the bending gauge at 35% chord have dynamics at 34 Hz, 38 Hz, and 40 Hz. This range of frequencies is where the root locus plot (Figure 4-32) predicts both the 2^{nd} bending and the 1^{st} chordwise bending to be interacting.

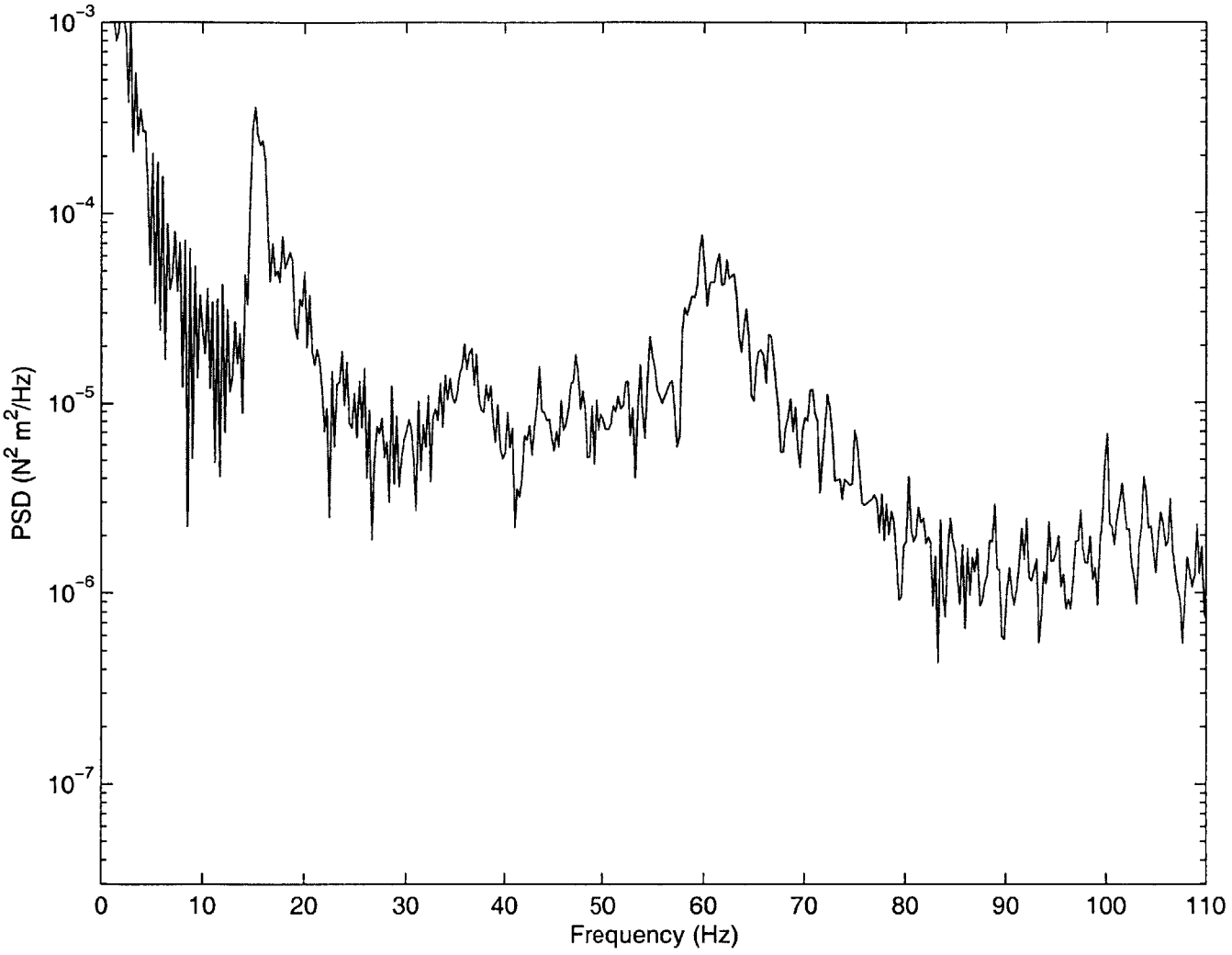

Figure 4-70: Frequency plot from root torsion gauge at 33.5 m/s for 5° root angle of attack

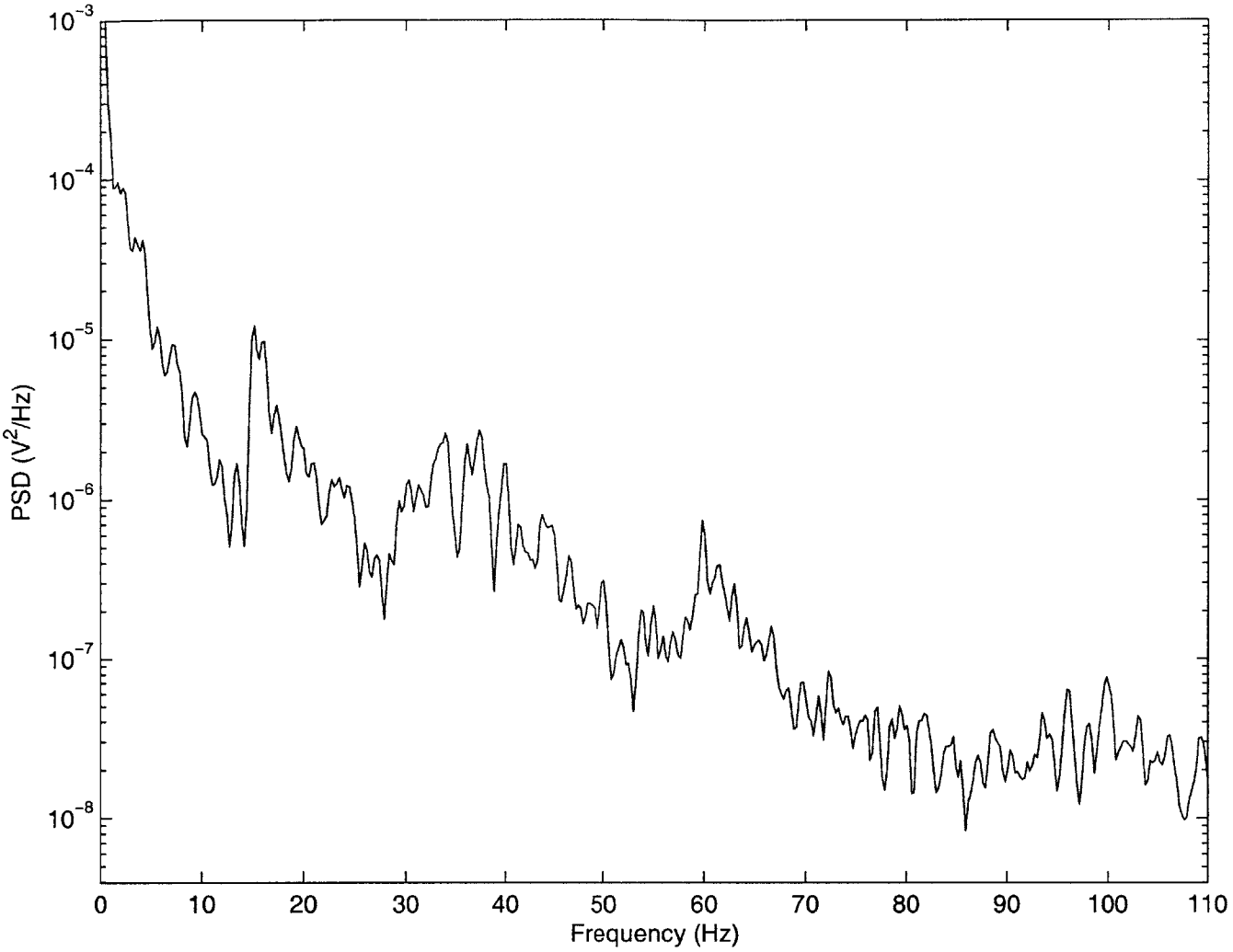

Figure 4-71: Frequency plot from forward/aft gauge at 33.5 m/s for 5° root angle of attack

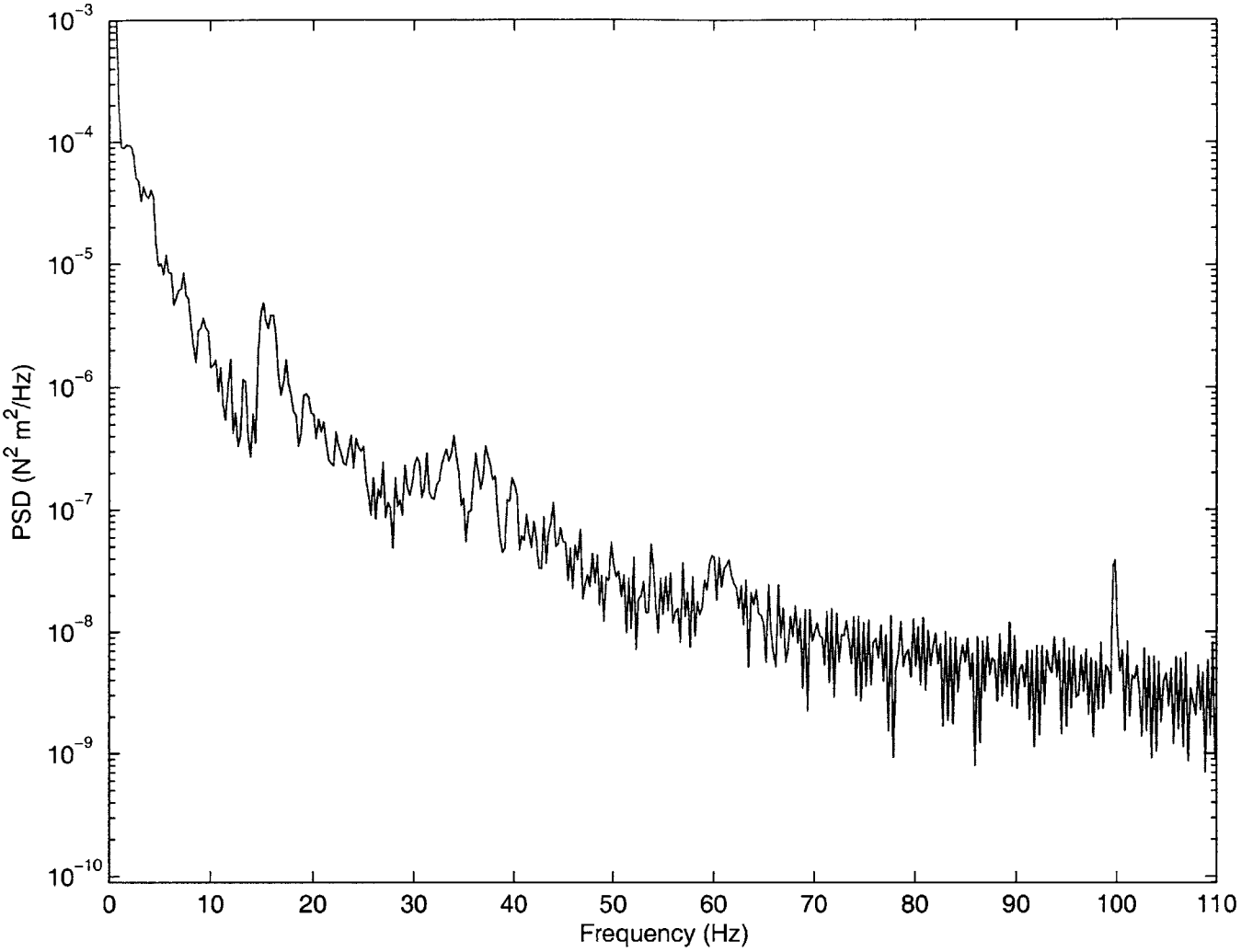

Figure 4-72: Frequency plot from the other bending gauge at 33.5 m/s for 5° root angle of attack

Post-Tunnel Tap Tests

After the tests in the tunnel were completed, a follow-up tap test was conducted to determine if anything changed during flight. The results from a bending excitation tap are provided in Figure 4-73. This tap test captured the 6-Hz 1^{st} bending mode, the 38-Hz 2^{nd} bending mode, the 45-Hz 1^{st} chordwise bending mode, and the 70-Hz 1^{st} torsion mode. The torsion mode was excited through a twisting tap. The data from the torsion strain gage is provided in Figure 4-74. This graph shows the 60-Hz 1^{st} bending mode and the 70-Hz 1^{st} torsion mode. A mode at 100 Hz is also being excited. The forward/aft tap test is not provided as the tap

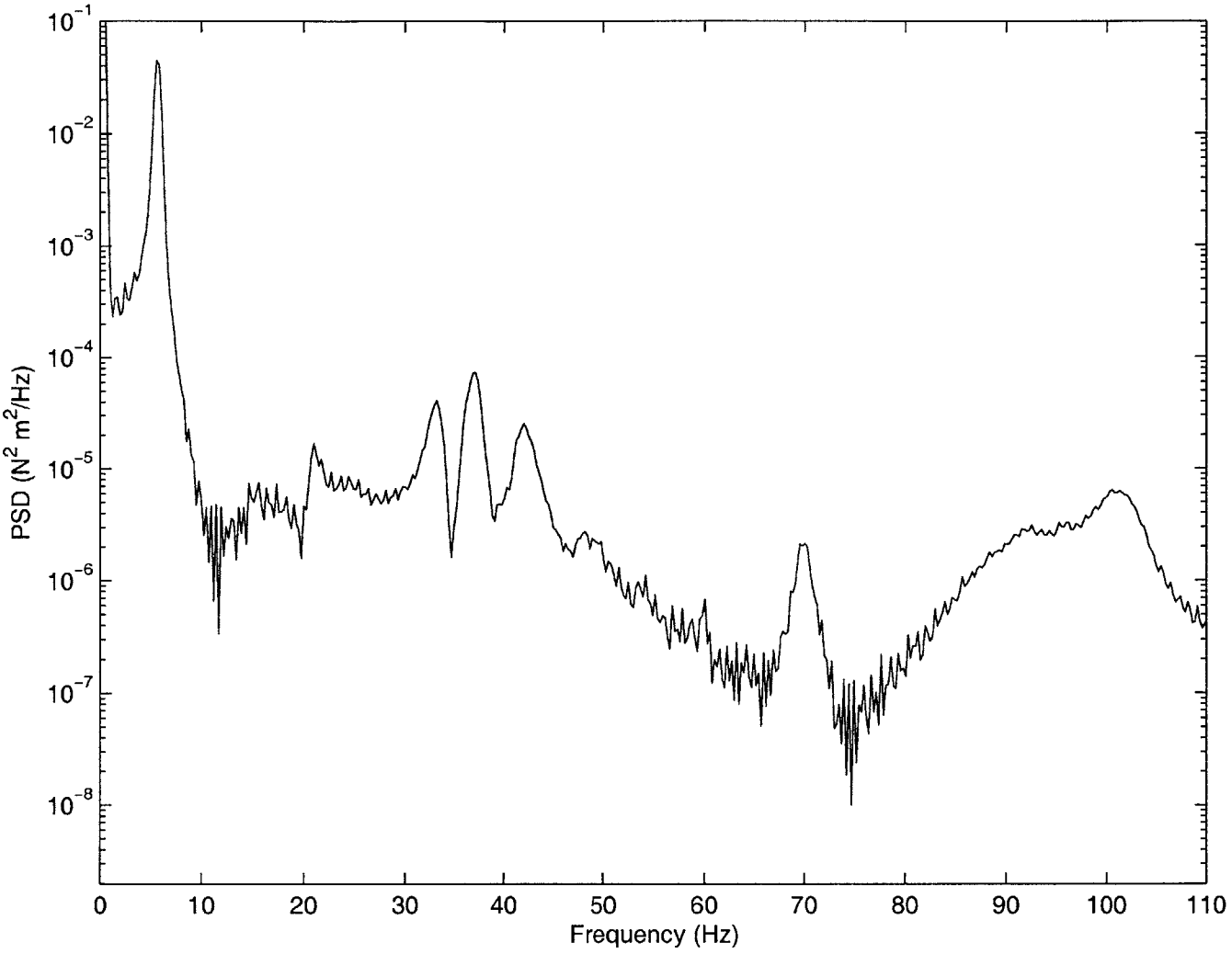

Figure 4-73: Root bending gauge readings from tap test—wing mounted in tunnel

was not recorded at the correct time. However, the chordwise bending mode was seen in the bending tap. The chordwise bending mode was excited through a tap on the leading edge.

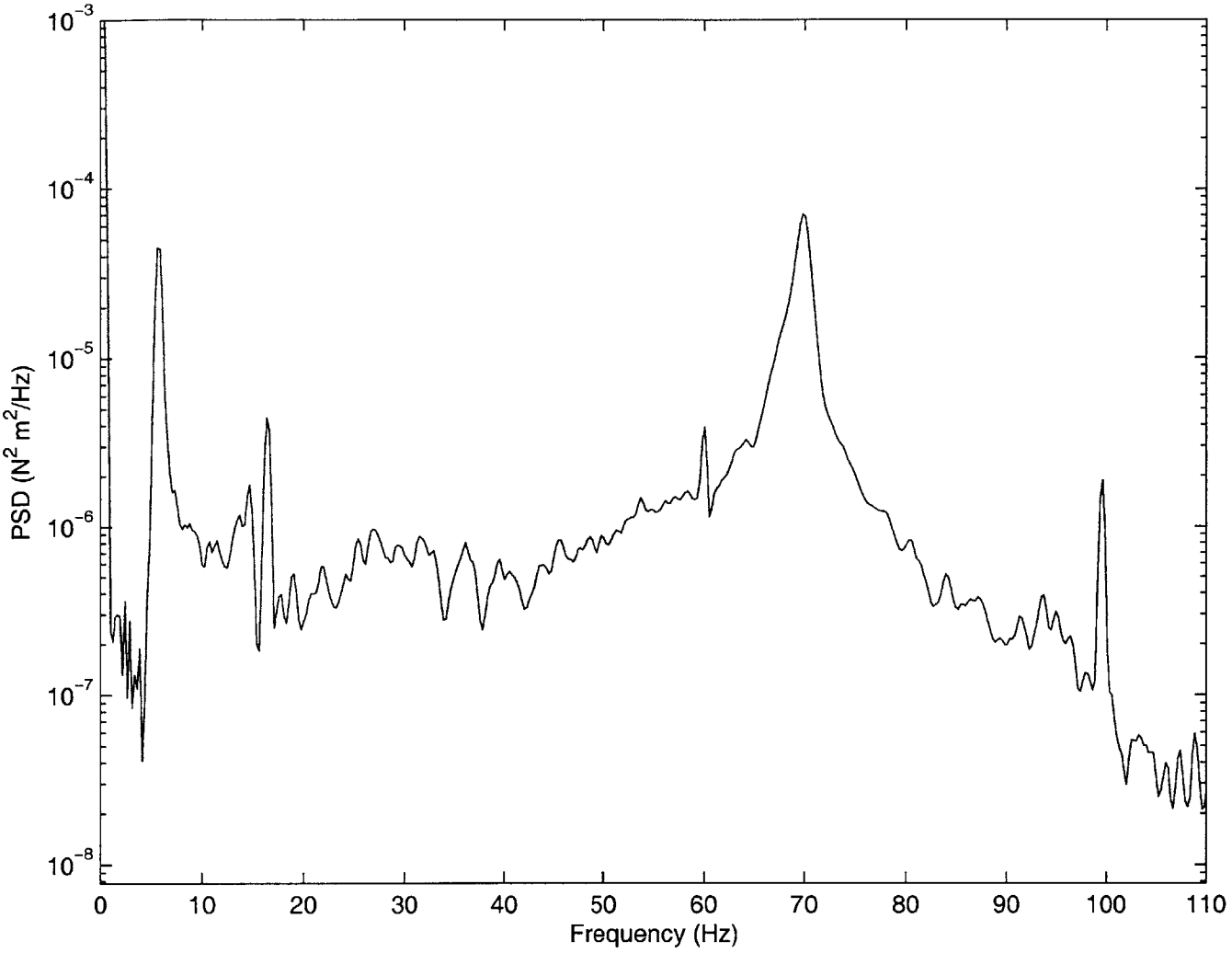

Figure 4-74: Root torsion gauge readings from tap test—wing mounted in tunnel

The data from the forward/aft gauge is shown in Figure 4-75. This data yields the 45 Hz 1^{st} chordwise bending mode. This dynamic is masked quite a bit by the noise from the tunnel, especially the 15-Hz and 60-Hz signal.

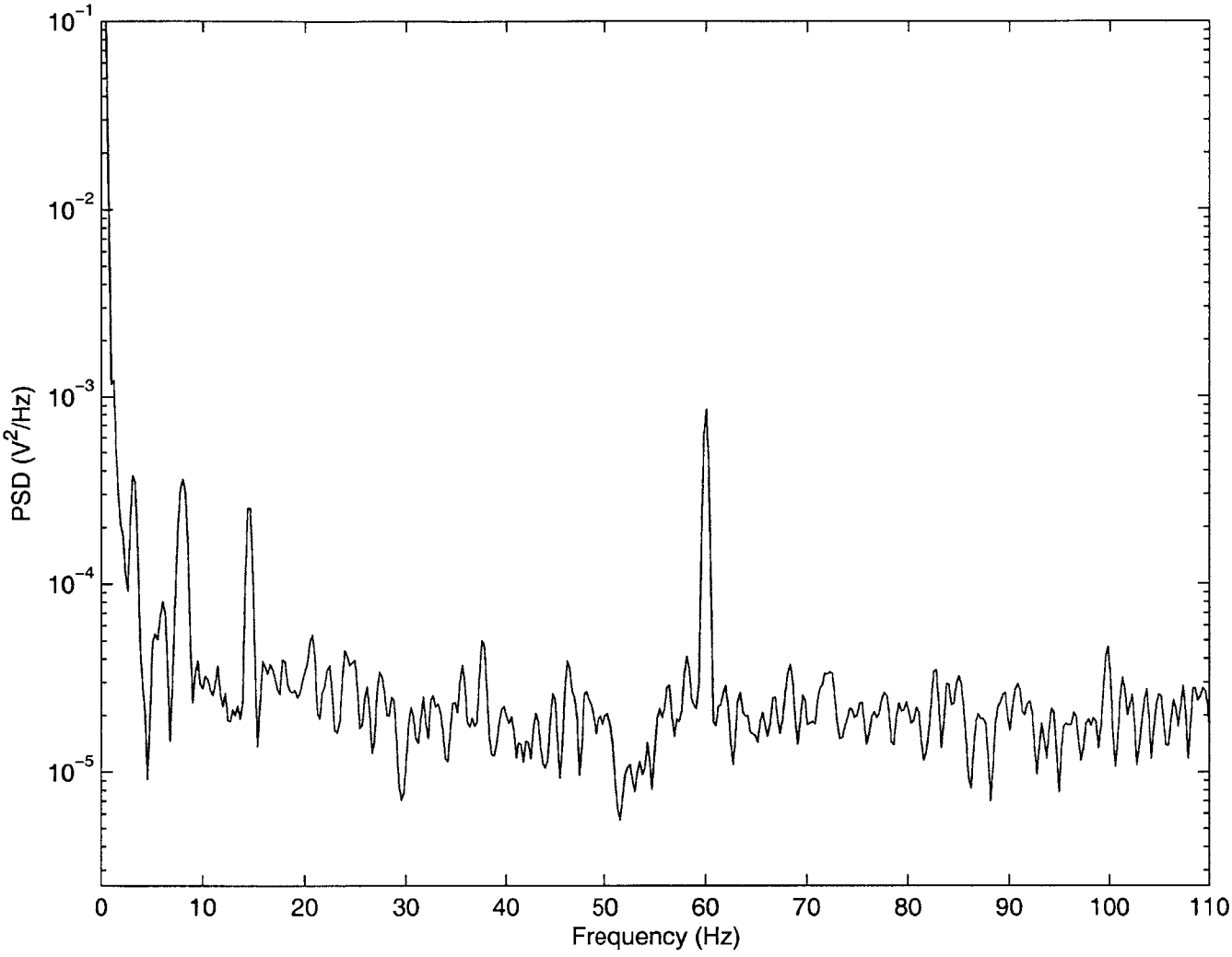

Figure 4-75: Average tip accelerometer readings from tap test—wing mounted in tunnel

Chapter 5

Concluding Remarks

This chapter presents a summary of the findings from the analytical and experimental portions of this thesis. Along with the summary are sections on the conclusions drawn from the research as well as recommendations for future work. The recommendations section suggests improvements to the manufacture of the wing and the test set-up.

5.1 Summary

The aeroelastic behavior of high-aspect ratio wings was studied via a new numerical formulation [11] which encompasses a non-linear, large deflection beam model with strain-based finite element representation and finite-state unsteady airloads. Using this formulation, a wing was designed, built, and its structural behavior evaluated under a variety of conditions. Bench-top tests were performed to understand the structural dynamic behavior of the wing. The first four natural frequencies at zero wind speed measured during bench-top 'tap' testing were in good agreement with the analytical model. The wing was then tested within the Wright Brothers Wind Tunnel to further understand the changes in dynamic behavior due to flight speed and root angle of attack. The wing was flown at speeds ranging from 20 m/s to 51.8 m/s and at 1°, 2°, and 5° root angles of attack. The tip deflections and natural frequencies were recorded for these cases.

5.2 Conclusions

The results presented herein validate the analytical model of the wing's aeroelastic behavior under a variety of angle of attacks and wind speeds. Few parameter changes were introduced to the model to reproduce the actual dynamic behavior. The need for these changes can be associated with complexities resulting from the manufacturing process. With these changes implemented, the predicted flutter speed is within 99% of the estimated flutter speed from observations in the wind tunnel. Experimental validation of the analytical model provides confidence in the ability of the code to predict the behavior of other systems under similar conditions. This capability would be useful for predicting the theoretical performance of high aspect ratio wings currently under consideration for upcoming remote sensing and reconnaissance vehicle programs.

5.3 Recommendations for Future Work

The manufacture and test of the active wing presented in Appendix C would further validate the capabilities of the analysis code. This would also demonstrate the capabilities of embedded piezoelectric actuators (in the composite wing skin) to increase the flight envelope of HALE vehicles. Note that a stress analysis, similar to the one conducted for the passive wing, will still have to be performed for the active wing design.

Several areas of improvement in the wing manufacturing and the test set-up have been identified that would facilitate future evaluations. First, although it would be more difficult, the foam core should be manufactured as a single piece, rather than four seperate ones. This would provide for more uniform cross-sectional properties. Second, the use of tip accelerometers was of limited value and could have been eliminated without a large impact on the results. The omission of the accelerometers would aleviate one of the reasons for using four seperate pieces of foam for the core—there would no longer be a need to run wires through the center of the wing. Omitting the accelerometers also helps with the homogeneity of the cross section. Finally, the load cell added unwanted noise into the data and had little practical value in the experiment. If a lift curve is desired it could be attained via a separate

set-up. During the dynamic tests of the wing, where mode shapes and frequencies are important, the flexibility of the load cell mounting fixture added undesirable dynamics to the system.

References

[1] Patil, M. J., D. H. Hodges, and C. E. S. Cesnik, "Nonlinear Aeroelasticity and Flight Dynamics of High-Altitude Long-Endurance Aircraft," *Journal of Aircraft*, Vol. 38, No. 1, 2001, pp. 88–94.

[2] Patil, M. J., D. H. Hodges, and C. E. S. Cesnik, "Characterizing the Effects of Geometrical Nonlinearities on Aeroelastic Behavior of High Aspect-Ratio Wings," in *Proceedings of the International Forum on Aeroelasticity and Structural Dynamics*, 1999.

[3] Cesnik, C. E. S. and E. L. Brown, "Modeling of High Aspect Ratio Active Flexible Wings for Roll Control," in *Proceedings of AIAA/ASME/ASCE/AHS/ASC Structures, Structural Dynamics, and Materials Conference and Exhibit, 43rd, AIAA-2002-1719*, 2002.

[4] Ortega-Morales, M. and C. E. S. Cesnik, "Modeling and Control of the Aeroelastic Responce of Highly Flexible Active Wings," Tech. Rep. AMSL # 00-2, Massachusetts Institute of Technology, February 2000.

[5] Patil, M. J., D. H. Hodges, and C. E. S. Cesnik, "Nonlinear Aeroelasticity Analysis of High Aspect Ratio Wings," in *Proceedings of the 39th Structures, Structural Dynamics, and Materials Conference*, 1998.

[6] Cesnik, C. E. S., D. H. Hodges, and M. J. Patil, "Aeroelastic Analysis of Composite Wings," in *Proceedings of the 37th Structures, Structural Dynamics, and Materials Conference*, 1996.

[7] Minguet, P. and J. Dugundji, "Experiments and Analysis for Composite Blades Under Large Deflections Part II: Dynamic Behavior," *AIAA Journal*, Vol. 28, No. 9, 1990, pp. 1580–1588.

[8] Patil, M. J. and D. H. Hodges, "On the Importance of Aerodynamic and Structural Geometrical Nonlinearities in Aeroelastic Behavior of High-Aspect-Ratio Wings," in *Proceedings of AIAA/ASME/ASCE/AHS/ASC Structures, Structural Dynamics, and Materials Conference and Exhibit, 41st, AIAA-2000-1448*, 2000.

[9] Tang, D. and E. H. Dowell, "Experimental and Theoretical Study on Aeroelastic Response of High-Aspect-Ratio Wings," *AIAA Journal*, Vol. 39, No. 8, 2001, pp. 1430–1441.

[10] Tang, D. and E. H. Dowell, "Experimental and Theoretical Study on Gust Response of High-Aspect-Ratio Wings," *AIAA Journal*, Vol. 40, No. 3, 2002, pp. 419–429.

[11] Brown, E. L., *Integrated Strain Actuation in Aircraft with Highly Flexible Composite Wings*, Ph.D. thesis, Massachusetts Institute of Technology, January 2003.

[12] Rodgers, J. P., *Development of an Integral Twist Actuated Rotor Blade for Individual Blade Control*, Ph.D. thesis, Massachusetts Institute of Technology, October 1998.

[13] Juhl, B., "Roehm America, Inc. - Rohacell." email, 2002. personal communication.

[14] Peters, D. A. and M. J. Johnson, "Finite-State Airloads for Deformable Airfoils on Fixed and Rotating Wings," in *Symposium on Aeroelasticity and Fluid/Structure Interaction, Proceedings of the Annual Winter Meeting*, November 1994.

[15] Peters, D. A., S. Karunamoorthy, and W. M. Cao, "Finite State Induced Flow Models Part I: Two-Dimensional Thin Airfoil," *Journal of Aircraft*, Vol. 32, No. 2, 1995, pp. 313–322.

[16] Jones, R. M., *Mechanics of Composite Materials*, Hemisphere Publishing Corporation, 1975.

Appendix A

Mathematical Formulation

A.1 Introduction

This appendix provides a summary of the mathematical modeling used in this research. A brief description of the geometrical, structural, and aerodynamic issues is presented. A detailed description of the mathematical formulation can be found in [3] and [11].

The main features of this code are:

- nonlinear, large deflection beam model ,
- strain-based finite element representation , and
- finite-state unsteady airloads .

A.2 Geometrical Lay-out

There are three reference frames governing the wing and its interactions with the environment. The first being the global coordinate system through which the wind speed and gravity affect the wing. The undeformed reference frame of the wing is measured with respect to the cross section area centroid along the 30% chord line of the wing. Finally the deformed reference frame follows the deformation of the beam reference line. A diagram of these coordinate frames with respect to the wing is provided in Figure A-1.

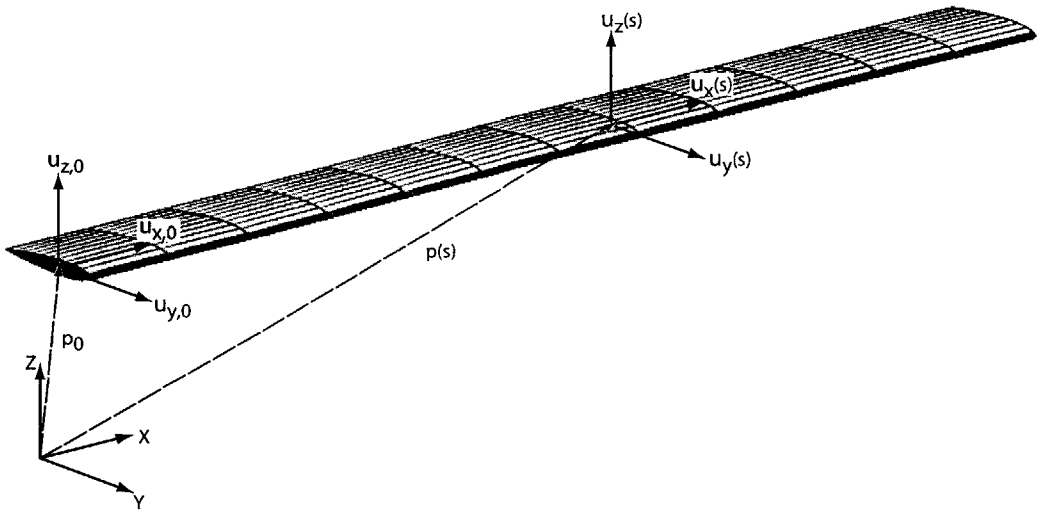

Figure A-1: Coordinate systems for the wing

A.3 Structural Formulation

The structural analysis of the wing is based on the principles of virtual work. These principles yield the following general equation:

$$\delta W = \int_V (f(x,y,z)\delta u(x,y,z))dV$$

where δW is the virtual work done by a force, $f(x,y,z)$, to move an object a virtual distance, $\delta u(x,y,z)$. Separating this equation into individual forces yields the general equation:

$$\delta W = F_{1u}\delta u + F_{2u}\delta u + \cdots + F_{nu}\delta u$$

For an object to be in equilibrium, the above equation must be zero, that is, $\delta W = 0$.

Within the program, the wing is allowed to move through three-dimensional bending and twisting deformations, while extension and shear deformations are assumed negligible and thus ignored. With this assumption, the virtual work equation becomes [3]:

$$\delta W = \int_{s=0}^{L} (\delta p^T F + \delta\theta^T M + \delta\kappa^T M^{int})du$$

In this equation, δp^T is the change in the position of the reference line, p(s), see Figure A-1. The term $\delta\theta^T$ represents the virtual rotation about the reference line, and $\delta\kappa^T$ denotes the virtual curvature of the wing. The variable F stands for the external forces on the wing, M

represents the external moments, and M^{int} represents the internal moments acting on the wing.

When the vector q is defined to be the curvatures,κ in (x,y,z) and the variable R is defined as all the generalized loads, the equation becomes [3]:

$$\delta W = \delta \underline{q}^T(-M_q \ddot{\underline{q}} - C_q \dot{\underline{q}} - K_q \underline{q} + \underline{R}_q)$$

In this equation, M_q denotes the mass matrix, C_q symbolizes the damping matrix, and K_q is the stiffness matrix. Setting this system into equilibrium, yields:

$$M_q \ddot{\underline{q}} + C_q \dot{\underline{q}} + K_q \underline{q} = \underline{R}_q$$

The stiffness matrix, K_q, is defined as:

$$K_q = \begin{bmatrix} K_{11} & K_{12} & K_{13} & K_{14} \\ K_{12} & K_{22} & K_{23} & K_{24} \\ K_{13} & K_{23} & K_{33} & K_{34} \\ K_{14} & K_{24} & K_{34} & K_{44} \end{bmatrix}$$

where K_{11} is the extension stiffness, K_{22} is the torsional stiffness, K_{33} is the bending stiffness about y, and K_{44} is the bending stiffness about z (or the chordwise bending stiffness). The off-diagonal terms are the cross-coupling terms, e.g., K_{14} is the extension-chordwise-bending stiffness term.

A.4 Aerodynamic Formulation

The aerodynamic model used in this aeroelastic formulation comes from the theory derived in [14] and [15]. A full discussion on this is provided in [11] and [3]. The theory accounts for thin deformable airfoil cross section undergoing large deformations at subsonic speeds. It also includes small deformations about this large deflected state.

The lift, L, moment, M, and drag, D, are defined by the following equations:

$$L = 2\pi\rho b(\dot{y}[(\tfrac{1}{2}b - d)\dot{\alpha} - \dot{z} - \lambda_0] - \tfrac{1}{2}b\ddot{z} - \tfrac{1}{2}bd\ddot{\alpha})$$
$$M = 2\pi\rho b(\dot{y}[-(d + \tfrac{1}{2}b)\dot{z} - (d + \tfrac{1}{2}b)\lambda_0 - d^2\dot{\alpha}] - \tfrac{1}{2}bd\ddot{z} - \tfrac{1}{2}b(d^2 + \tfrac{1}{8}b^2)\ddot{\alpha})$$
$$D = -2\pi\rho b(\dot{z}^2 + d^2\dot{\alpha}^2 + \lambda_0^2 + 2d\dot{\alpha}\dot{z} + 2\lambda_0\dot{z} + 2d\dot{\alpha}\lambda_0)$$

Within these equations, b is the semichord, d is the distance between the reference axis and the mid-chord, and λ_0 represents the inflow term due to free vorticity [3]. The term, ρ denotes the air density. The variables which represent the motion: y, $\dot{y}$, z, $\dot{z}$, $\ddot{z}$, α, $\dot{\alpha}$, and $\ddot{\alpha}$ are defined in Figure A-2.

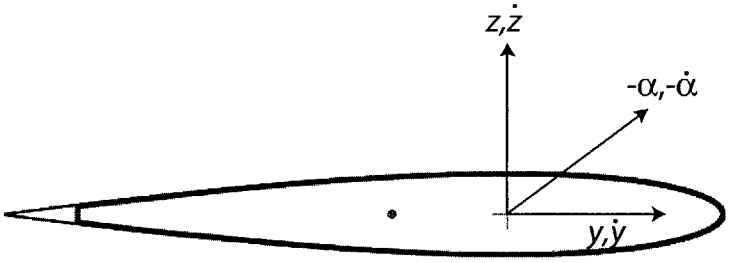

Figure A-2: Variables defining airfoil motion [3]

These equations are linearized with respect to time, t_a, by the following equations [3]:

$$\dot{y} = (\dot{y}_a + \Delta\dot{y})$$
$$\dot{z} = (\dot{z}_a + \Delta\dot{z} - \dot{y}_a\Delta\alpha)$$
$$\dot{\alpha} = (\dot{\alpha}_a + \Delta\dot{\alpha})$$
$$\dot{\lambda_0} = (\dot{\lambda_{0,a}} + \Delta\dot{\lambda_0})$$

Applying these perturbations to the equation of virtual work yields:

$$\delta W = \int_{s=0}^{L}(L\delta z + D\delta y + M\delta\alpha)ds$$

A.5 Aeroelastic Formulation

The structural and aerodynamic formulations combine to produce the aeroelastic equations [3].

$$M\underline{\ddot{q}} + C\underline{\dot{q}} + K\underline{q} + D\underline{\lambda} = \underline{F}$$
$$\underline{\dot{\lambda}} = F_1\underline{\ddot{q}} + F_2\underline{\dot{q}} + F_3\underline{\lambda}$$

In this equation, the mass, M, and damping, C, matrices are functions of the strains. The structural stiffness, K, matrix is constant for a given geometry and material distribution. The force vector, $\underline{F}$, contain the inertial and aerodynamic forces and is a function of initial values of $\dot{q}$, q, and λ. It also contains the effects of the active material layers in the wing construction. See [11] for further details.

Appendix B

Material Properties

The material file associated with the MATLAB code needs material properties to be converted from engineering moduli (E_l, E_t, ν_{lt}, G_{lt}) in the local ply coordinate system to the plane-stress stiffness constants, Q [16]. Equations B.1 through B.5 show the relations. The subscripts 'l' and 't' represent longitudinal and transverse directions, respectively. The two Poisson's ratios are related via Equation B.6. The material properties for the foam core are provided in the standard nomenclature.

$$Q_{11} = \frac{E_l}{1 - \nu_{lt}\nu_{tl}} \tag{B.1}$$

$$Q_{12} = \frac{\nu_{lt}E_t}{1 - \nu_{lt}\nu_{tl}} \tag{B.2}$$

$$Q_{22} = \frac{E_t}{1 - \nu_{lt}\nu_{tl}} \tag{B.3}$$

$$Q_{16} = Q_{26} = 0 \tag{B.4}$$

$$Q_{66} = G_{lt} \tag{B.5}$$

$$\nu_{tl} = \frac{E_t}{E_l\nu_{lt}} \tag{B.6}$$

Table B.1: Properties of the materials used in this study

	E-glass/epoxy	Piezocomposite
Q_{11}	19.7 GPa	33.6 GPa
Q_{12}	2.92 GPa	7.54 GPa
Q_{22}	19.7 GPa	16.6 GPa
Q_{66}	4.10 GPa	5.13 GPa
d_{11}	n/a	309 pm/V
d_{12}	n/a	-129 pm/V
$t_{electrode}$	n/a	0.0011 m
thickness	0.1143 mm	0.127 mm
ρ	1716 kg/m^3	4060 kg/m^3
$\epsilon_{11}^u, \epsilon_{22}^u$	10000 μm/m	4000 μm/m
ϵ_{12}^u	15000 μm/m	5500 μm/m

	Rohacell 31
E	36 MPa
G	14 kPa
ρ	30 kg/m^3
$\epsilon_{11}^u, \epsilon_{22}^u$	27000 μm/m
ϵ_{12}^u	30000 μm/m

Appendix C

Active Wing Design

This appendix describes the design and analysis of the active flexible wing that is proposed as a follow-on to the passive wing built for this thesis. Stress analysis will still have to be conducted for this design.

C.1 Active Design

The active wing design is composed of three layers of E-glass/epoxy fabric oriented at 0° around an inner foam core, with two active layers embedded within the E-glass. There is no spar in this design. The goal is to have a flexible wing with low flutter speeds, for the reasons mentioned during the passive design. This design provides a flexible wing while still maintaining closed cell properties. A drawing of the wing lay-up is provided in Figure C-1.

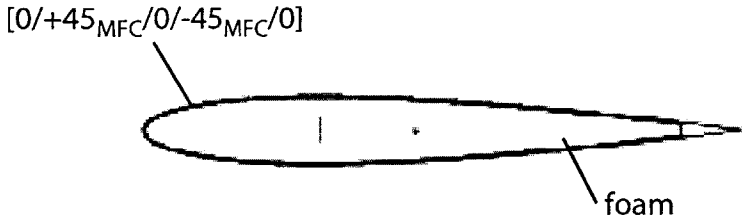

Figure C-1: Cross section of active wing

C.1.1 Basic Static and Dynamic Properties

The cross-sectional properties for the active design are provided below. The stiffness matrix terms for this cross section are given in Table C.1. Detailed definitions of the elements of the matrix are provided in Appendix A. The inertia matrix for this cross-section is provided in Table C.2. The center of gravity for the cross-section is located 0.0214 m aft of the reference line (located at 30% chord). This places the center of gravity at 49.9% of the chord.

Table C.1: Non-zero stiffness matrix terms for the active wing design: 1 = Extension, 2 = Torsion, 3 = Flatwise Bending, 4 = Chordwise Bending

K_{11}	$2.27 * 10^6$ N
K_{14}= K_{41}	$-4.78 * 10^4$ N*m
K_{22}	57.72 N*m^2
K_{33}	57.00 N*m^2
K_{44}	$2.69 * 10^3$ N*m^2

Table C.2: Non-zero inertial matrix terms for active wing design

I_{11}	$0.244 * 10^{-3}$ m^4
I_{22}	$0.998 * 10^{-5}$ m^4
I_{33}	$0.234 * 10^{-3}$ m^4

The dynamic properties of the wing are important to its aeroelastic response. The first six natural frequencies of the wing are summarized in Table C.3. The corresponding mode shapes are provided in Figure C-2.

Table C.3: Natural frequencies of the active wing design in vacuum

Mode	Frequency	Mode Shape
1	6.8 Hz	1^{st} Bending
2	36.8 Hz	1^{st} Chordwise Bending
3	44.1 Hz	2^{nd} Bending
4	121. Hz	1^{st} Torsional
5	133. Hz	3^{rd} Bending
6	232. Hz	2^{nd} Torsional

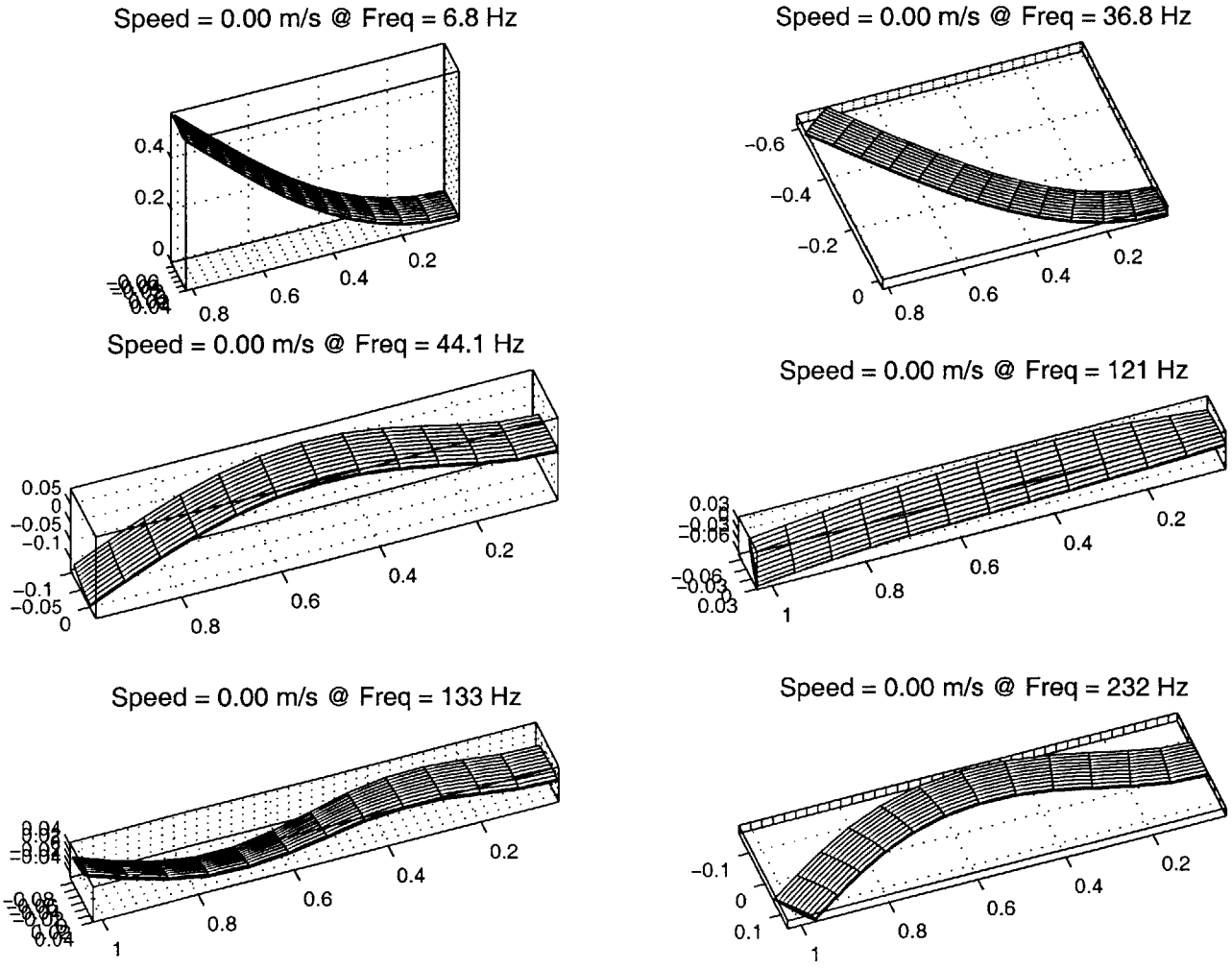

Figure C-2: First six normal modes for active wing design (in vacuum)

C.1.2 Wing Non-linear Characteristics

As seen in the passive wing designs, different root angles of attack of the wing result in different wing tip deflections once the wing is exposed to airloads. The change in tip deflection is graphed in Figure C-3 for the range of root angles of attack of interest: 1° to 5°. The tip deflection increases with increased angle of attack.

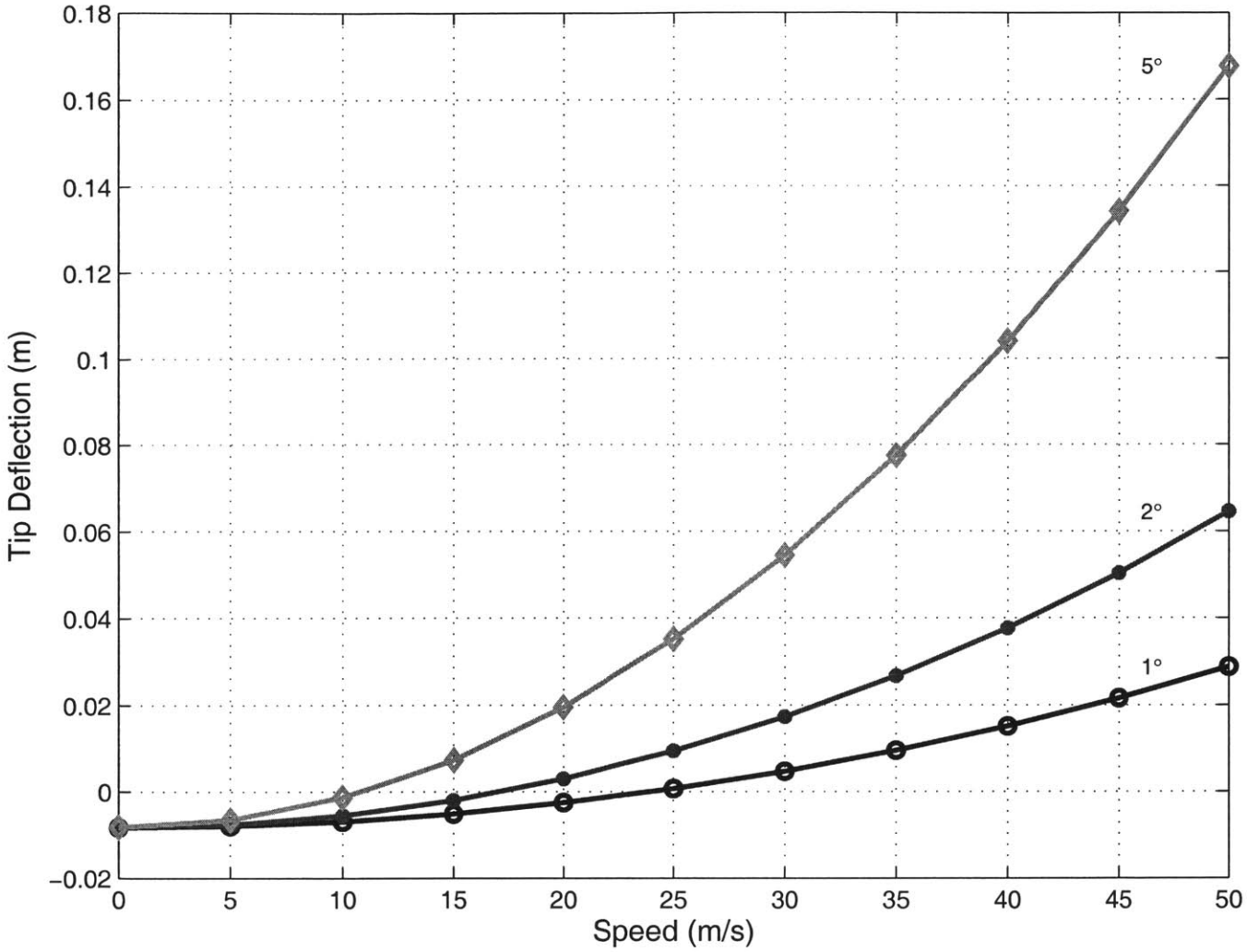

Figure C-3: Static tip deflection for increasing speed at different root angles of attack

The wing tip twist also changes with increased root angle of attack. This data is provided in Figure C-4. To better illustrate this effect, the initial root angle of attack has been subtracted from the total tip twist, yielding only the elastic angle change due to gravitational and aero-loading.

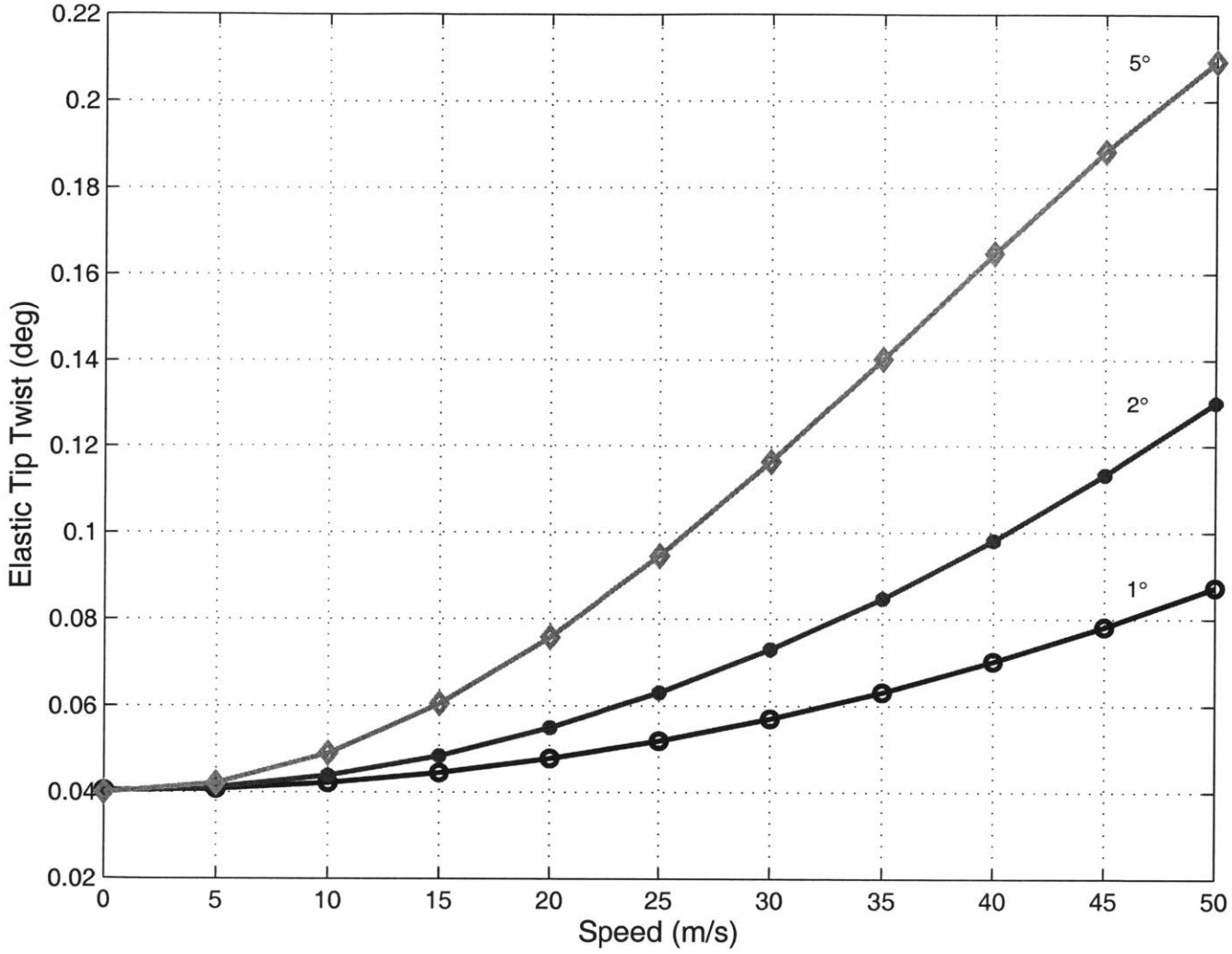

Figure C-4: Elastic tip twist for increasing speed at different root angles of attack

The changes in tip deflection and twist result in a change in the dynamic behavior of the wing, and ultimately a change in the wing's flutter speed. This is shown in the root locus plots for the wing at root angles of attack of 1°, 2° and 5°. The flutter speeds as a function of root angle of attack determined from these plots are provided in Figure C-5.

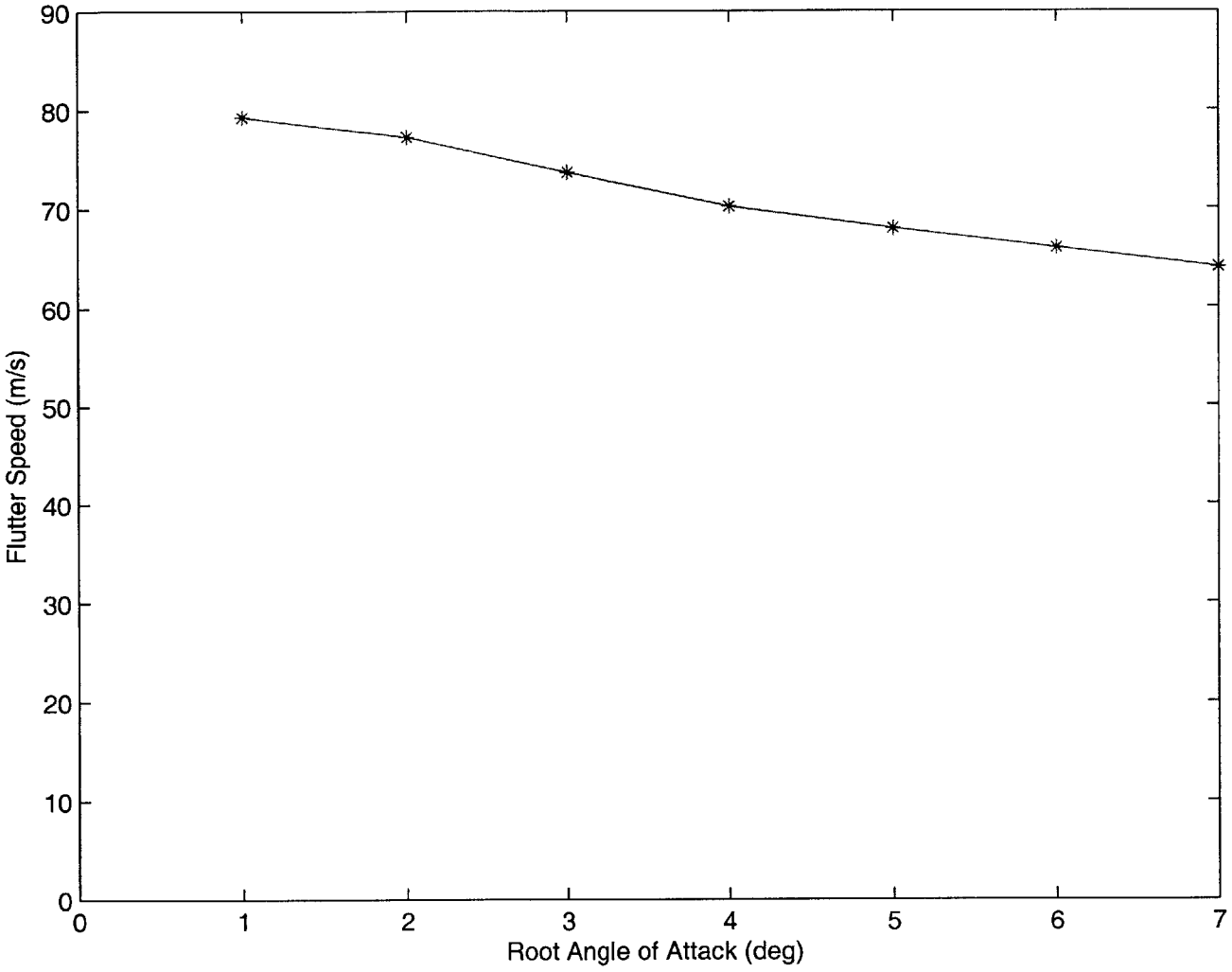

Figure C-5: Flutter speeds for active wing design

One-Degree Root Angle of Attack

The flutter speed for one-degree root angle of attack is determined to be 79.3 m/sec, shown in Figure C-6. The mode of instability is the second mode. A magnified plot of this mode's behavior is provided in Figure C-7. This mode is primarily the first chordwise bending. However, the forces due to air pressure on the tilted wing result in some torsion being present as well. The first six mode shapes at this speed are given in Figure C-8.

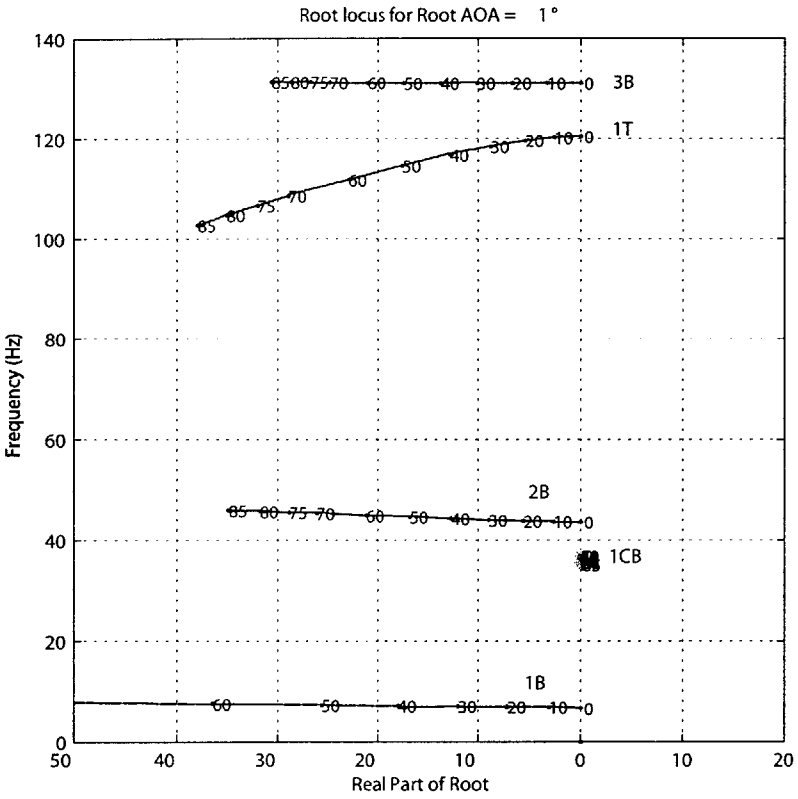

Figure C-6: Root locus plot for 1° root angle of attack

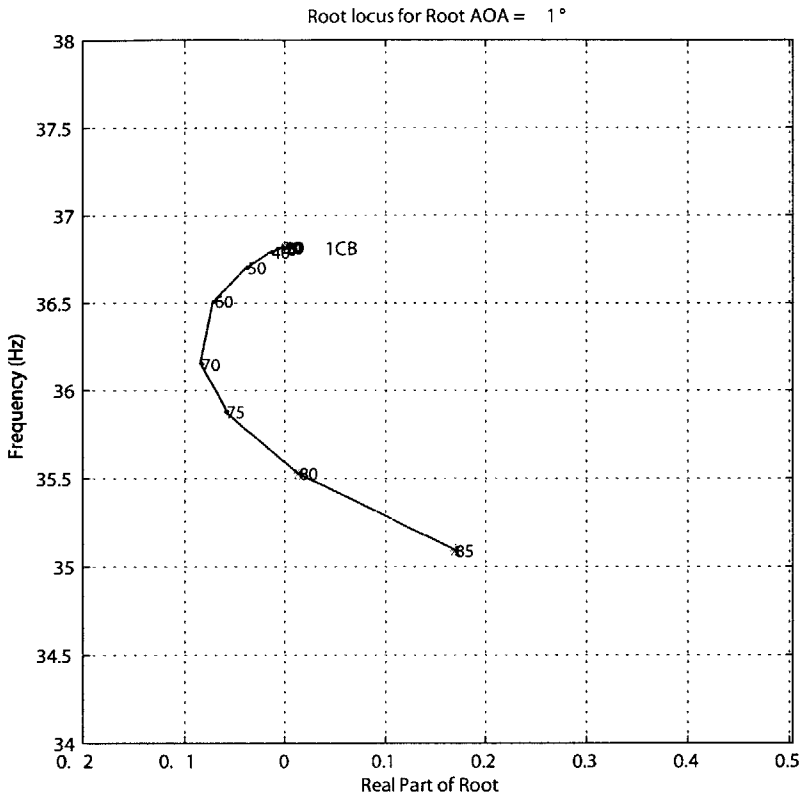

Figure C-7: Magnification of root locus plot for 1° root angle of attack

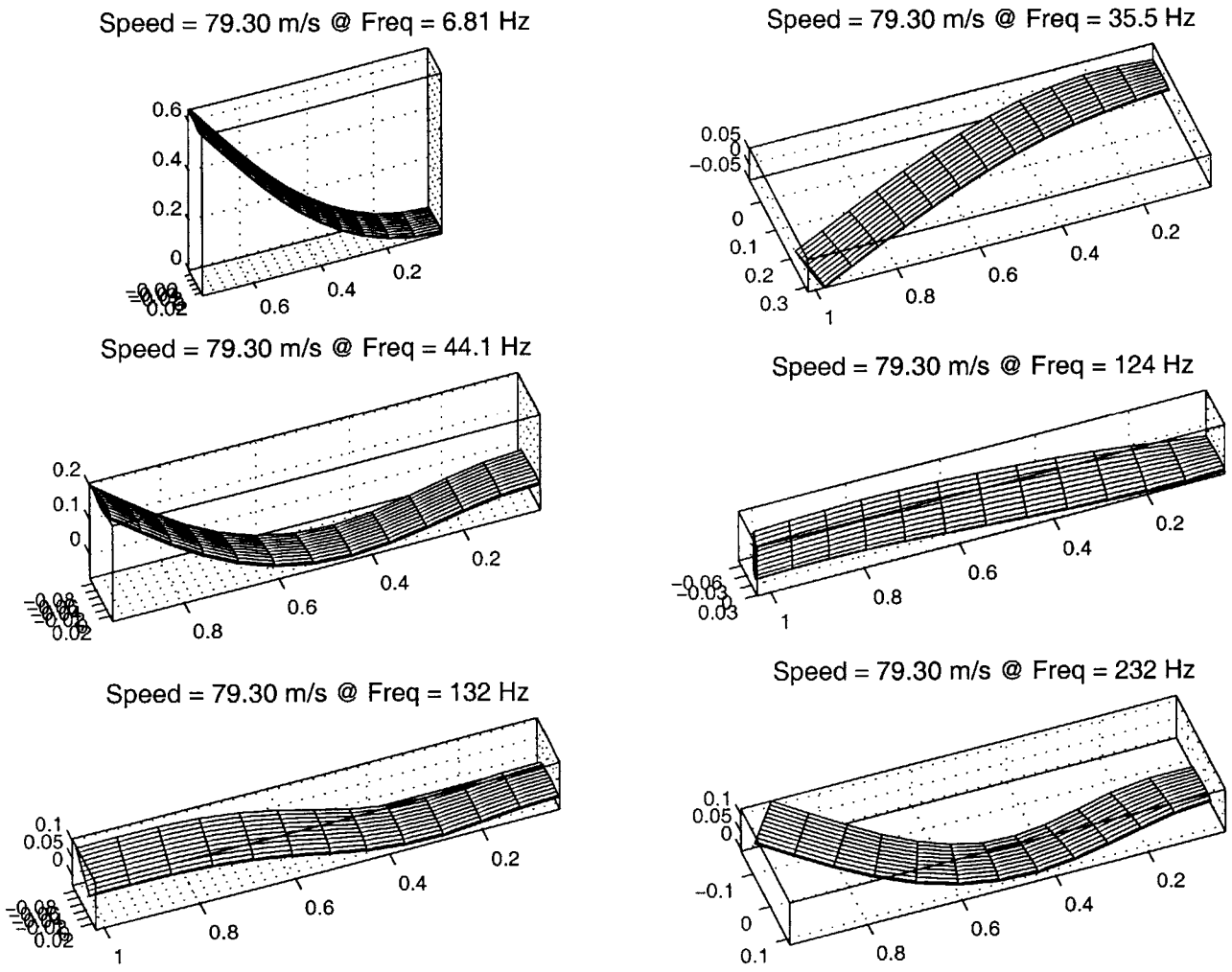

Figure C-8: Mode Shapes for active wing design at 1° root angle of attack and its corresponding flutter speed of 79.3 m/s

When the wing is flown at 10% above the flutter speed for a 1° angle of attack, the wing enters into a Limit Cycle Oscillation (LCO). The tip deflections and the tip twist are plotted for this case up to 1 second. These plots are given in Figure C-9 thru Figure C-11.

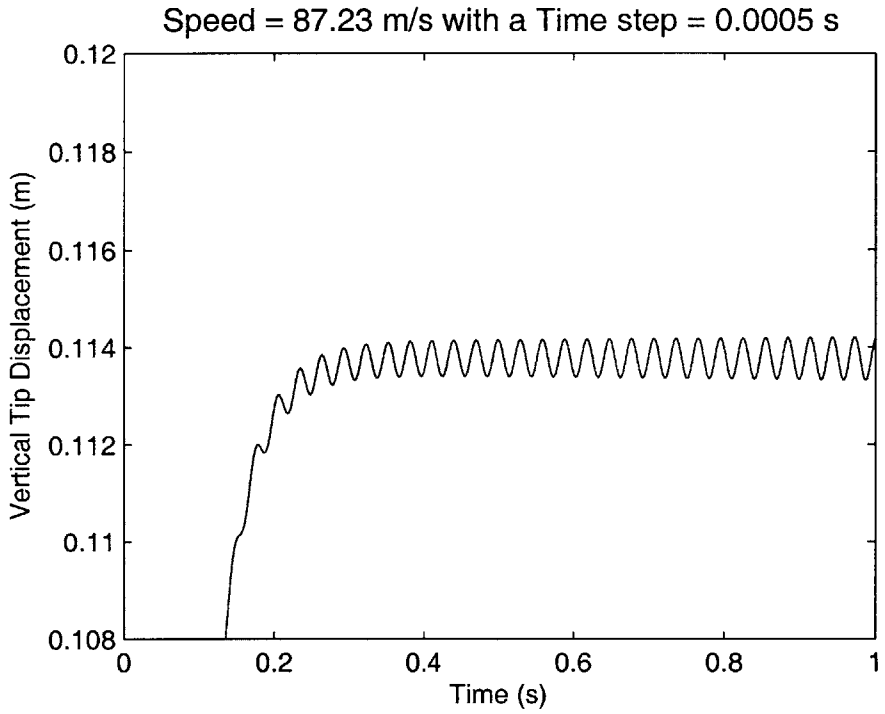

Figure C-9: Nonlinear time simulation of the wing vertical tip displacement at 10% above its flutter speed (1° root angle of attack) for the active wing design

Two-Degree Root Angle of Attack

The flutter speed for two degrees angle of attack is determined to be 77.3 m/s from the root locus plot shown in Figure C-12. The instability mode is the same as for 1°, except the amount of torsion present is increased. The drop in the second natural frequency due to the increased upward bend, also causes the second mode to turn over faster and amplifies the effects of flow over the wing. The first six modes at flutter speed are provided in Figure C-14.

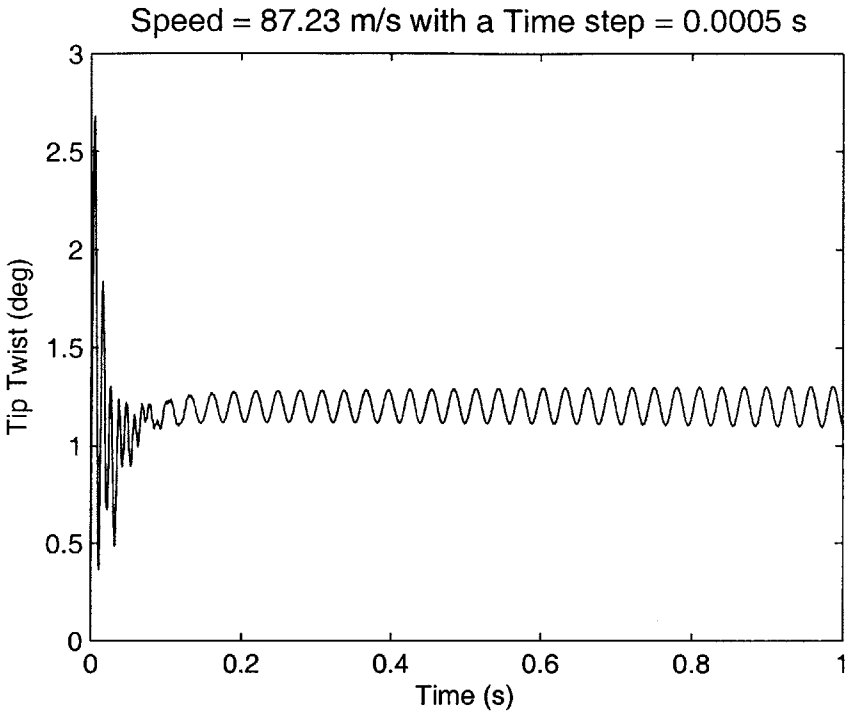

Figure C-10: Nonlinear time simulation of the wing tip twist at 10% above its flutter speed (1° root angle of attack) for the active wing design

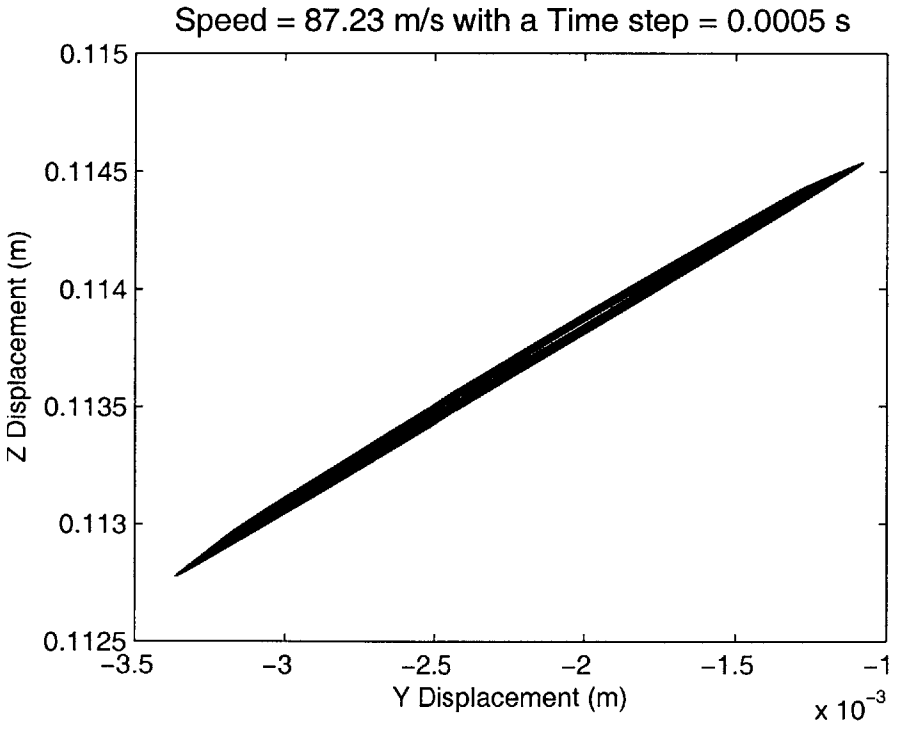

Figure C-11: Nonlinear time simulation of the wing tip displacement motion at 10% above its flutter speed (1° root angle of attack) for the active wing design

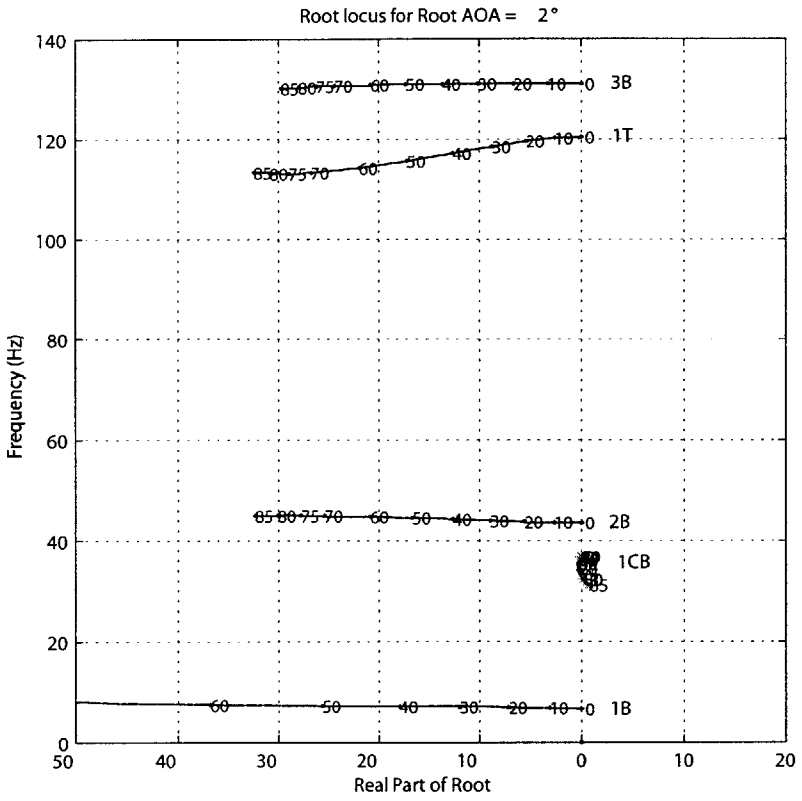

Figure C-12: Root locus plot for 2° root angle of attack

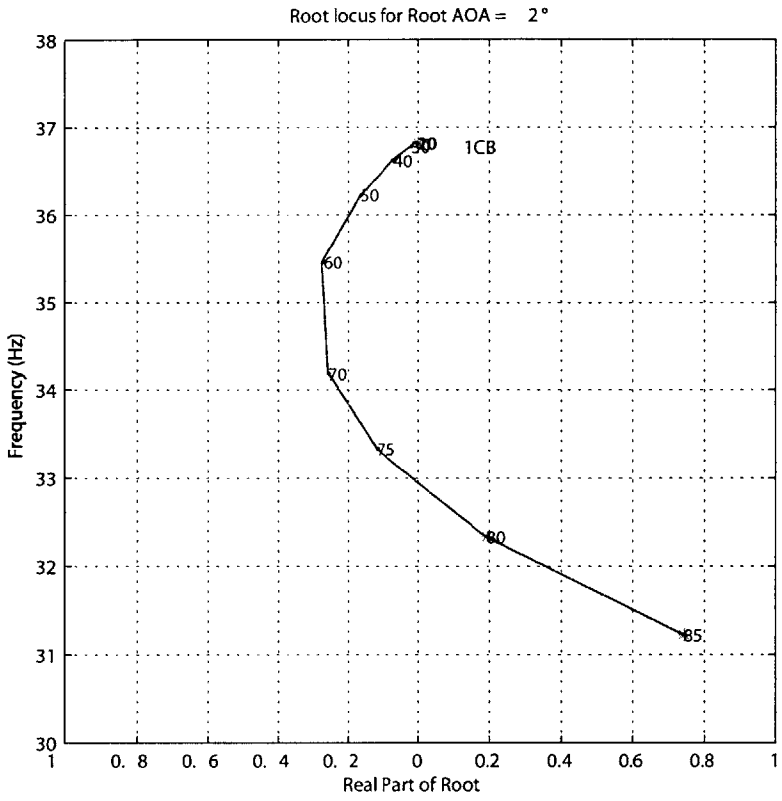

Figure C-13: Magnification of root locus plot for 2° root angle of attack

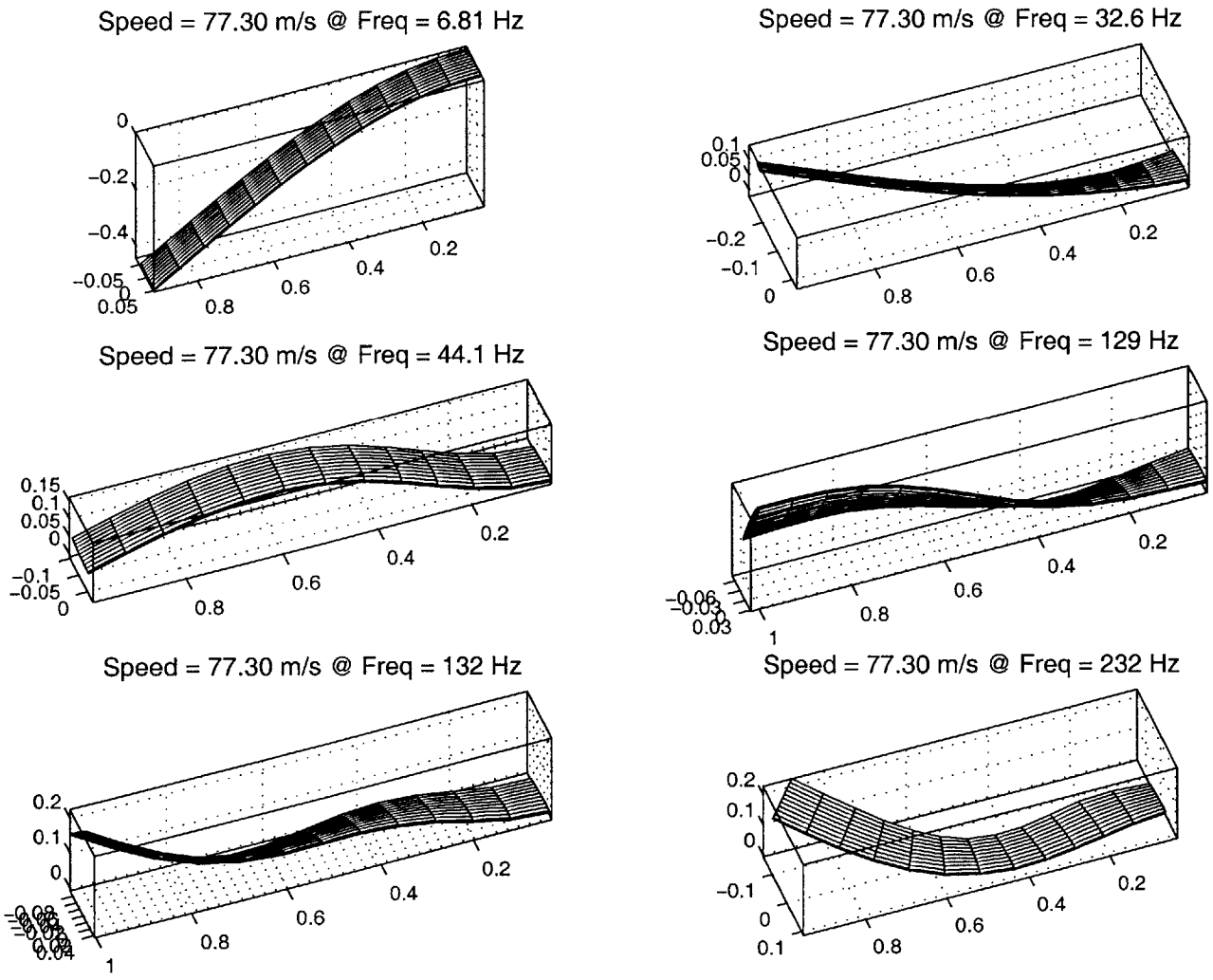

Figure C-14: Mode shapes for active wing design at 2° root angle of attack and its corresponding flutter speed of 77.3 m/s

For 2° angle of attack, the wing also enters a LCO when flown at 10% above the flutter speed. The tip deflections and the tip twist are plotted for this case up to 3 seconds. These plots are given in Figure C-15 thru Figure C-17.

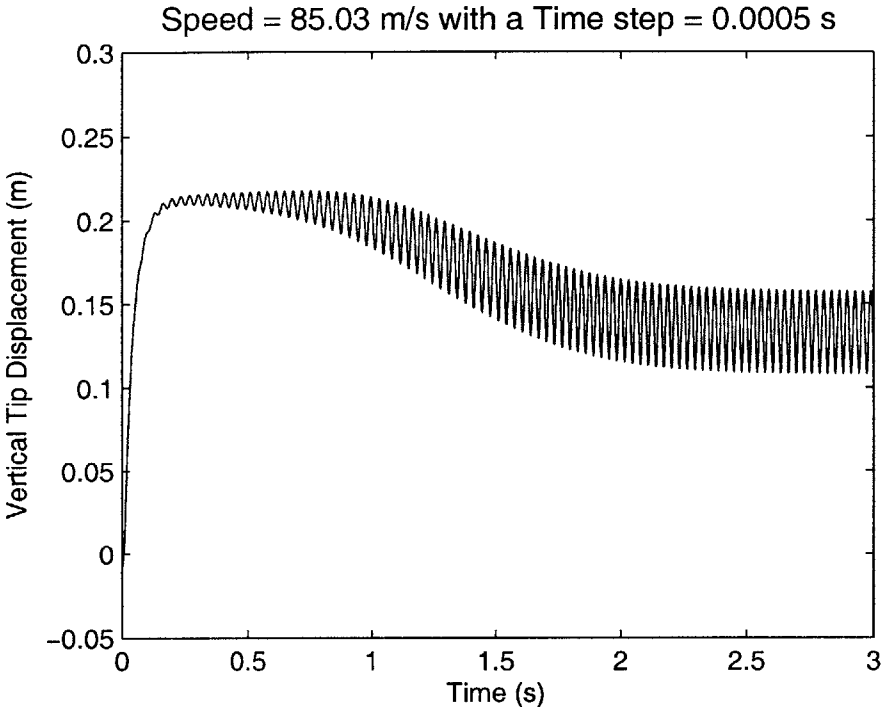

Figure C-15: Nonlinear time simulation of the wing vertical tip displacement at 10% above its flutter speed (2° root angle of attack) for the active wing design

Five-Degree Root Angle of Attack

The flutter speed for five degrees angle of attack is shown to be 68 m/s in the root locus plot provided in Figure C-18. As with the 1° and 2° cases, the mode of instability is the second mode, which is the 1^{st} chordwise bending with some torsional effects. The changes in the dynamic behavior due to the increased upward bend result in the second mode rolling over faster to the positive dampening axis. The fourth mode (1^{st} torsion) has curved upward and now interacts with the fifth mode (3^{rd} bending mode). This interaction between the fourth and fifth mode has caused the fifth mode to turn towards the instability line as well. The first six mode shapes for this case are provided in Figure C-19.

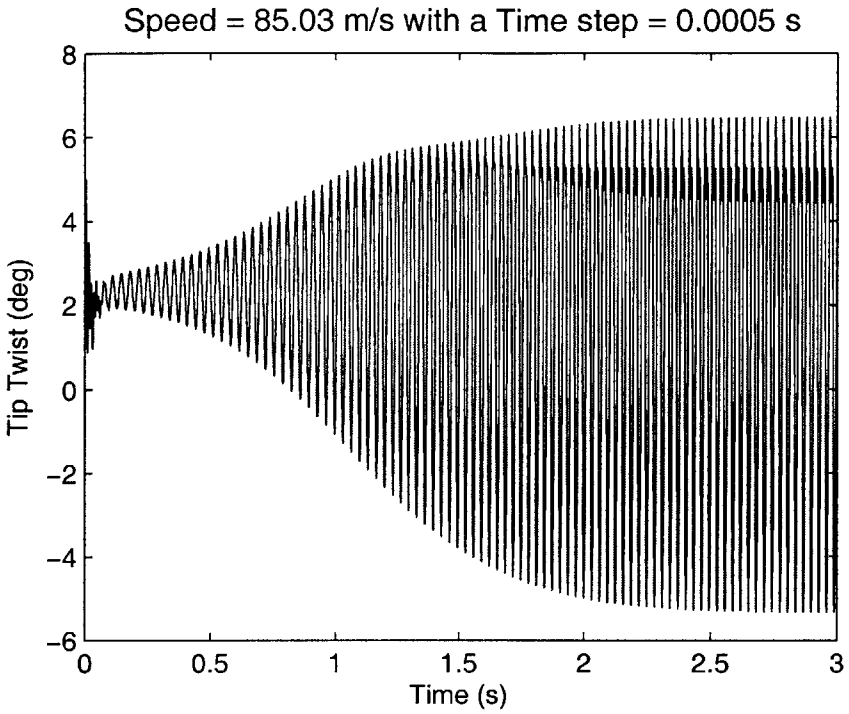

Figure C-16: Nonlinear time simulation of the wing tip twist at 10% above its flutter speed (2° root angle of attack) for the active wing design

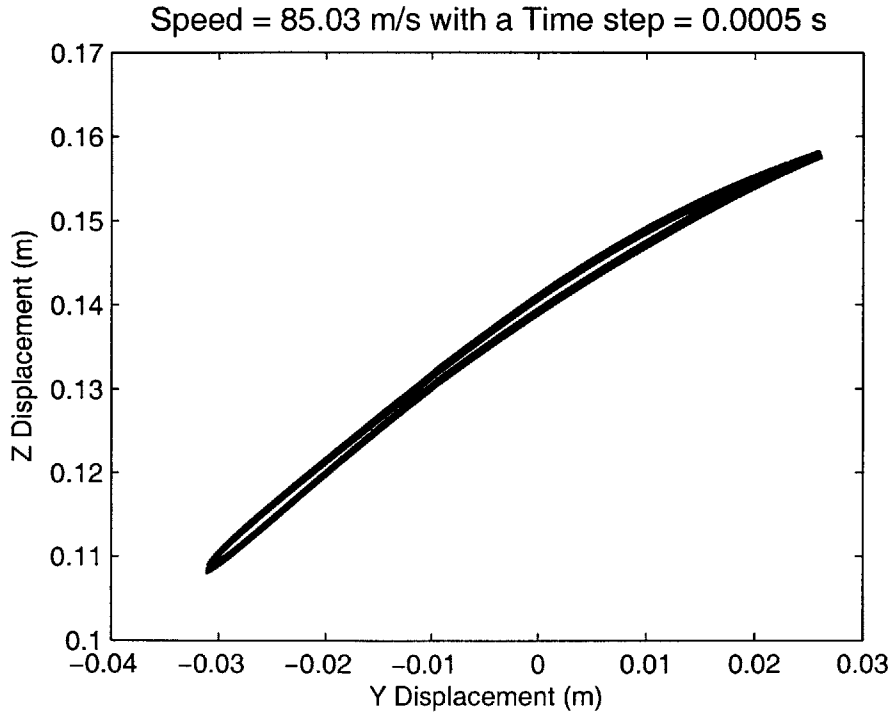

Figure C-17: Nonlinear time simulation of the wing tip displacement motion at 10% above its flutter speed (2° root angle of attack) for the active wing design

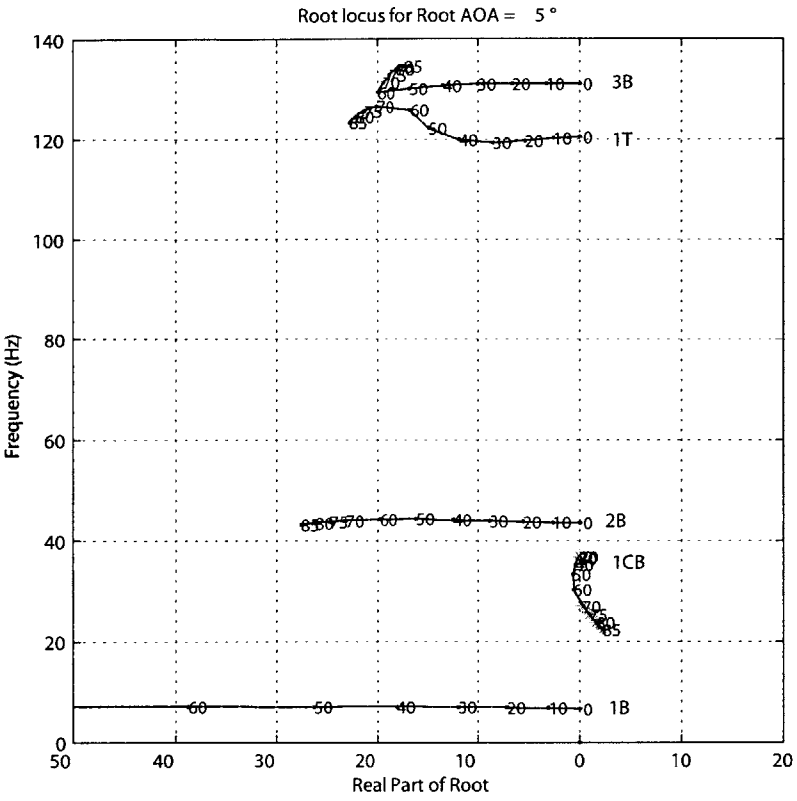

Figure C-18: Root locus plot for 5° root angle of attack

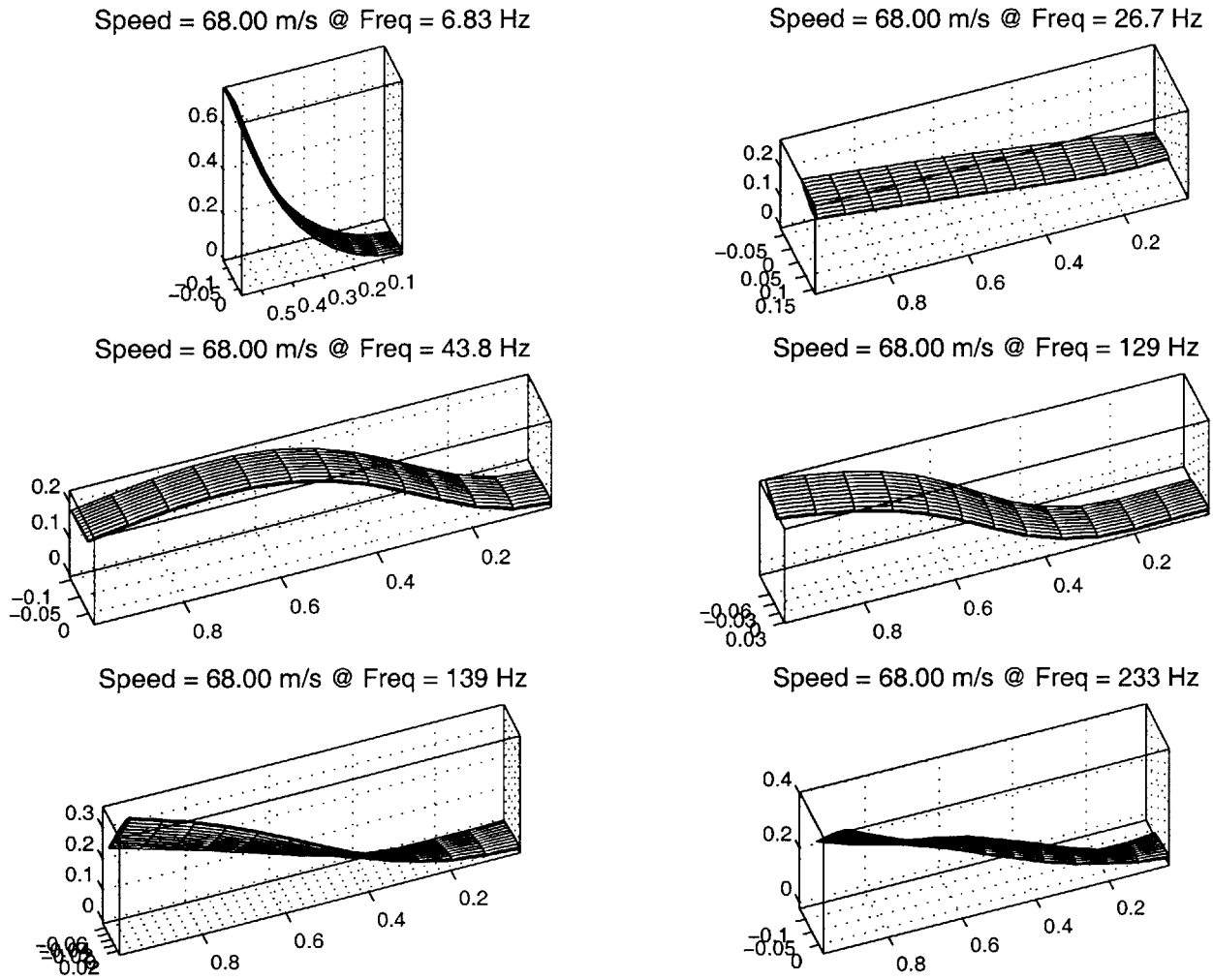

Figure C-19: Mode shapes for active wing design at 5° root angle of attack and its corresponding flutter speed of 68 m/s

For 5° angle of attack, the wing also enters a LCO when flown at 10% above the flutter speed. The tip deflections and the tip twist are plotted for this case up to 1 second. These plots are given in Figure C-20 thru Figure C-22.

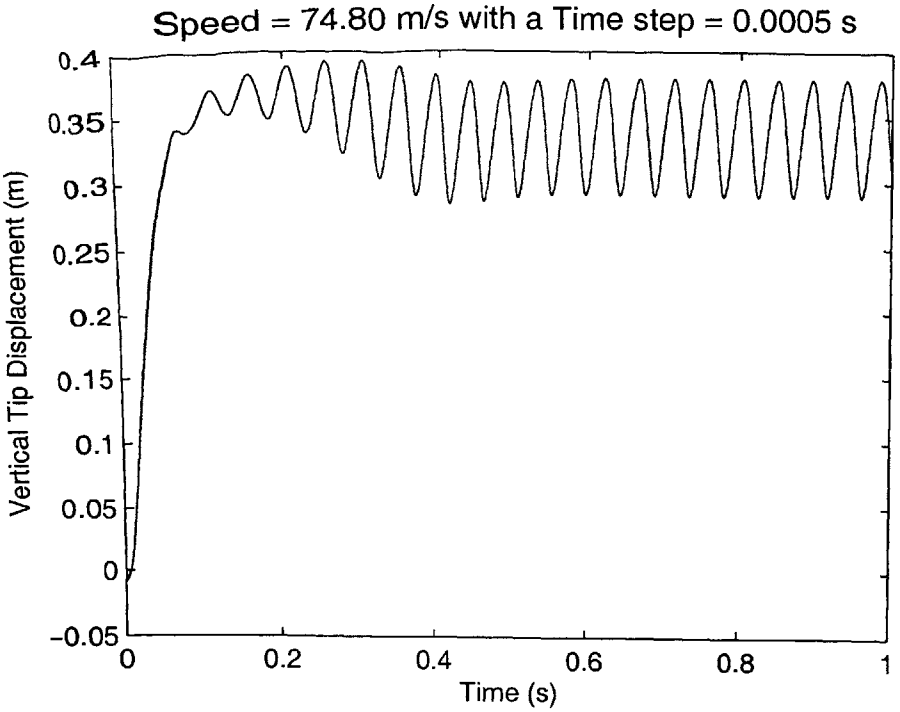

Figure C-20: Nonlinear time simulation of the wing vertical tip displacement at 10% above its flutter speed (5° root angle of attack) for the active wing design

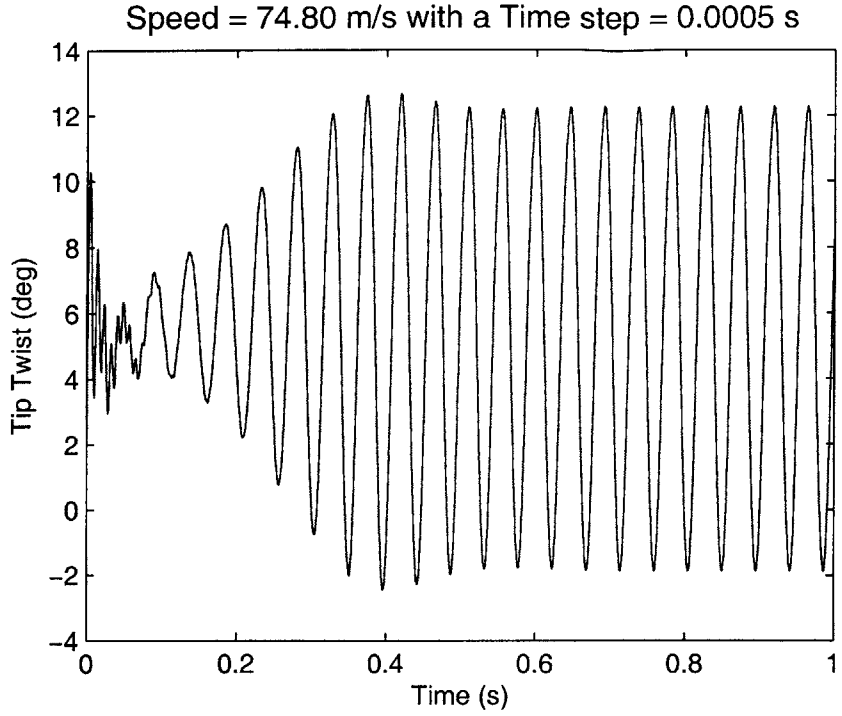

Figure C-21: Nonlinear time simulation of the wing tip twist at 10% above its flutter speed (5° root angle of attack) for the active wing design

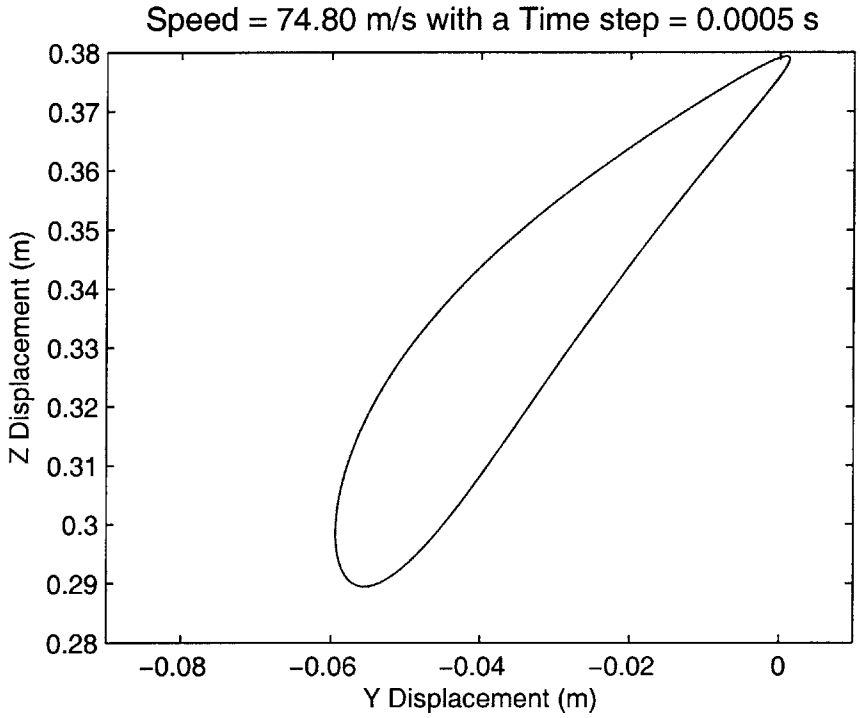

Figure C-22: Nonlinear time simulation of the wing tip displacement motion at 10% above its flutter speed (5° root angle of attack) for the active wing design